Polaritonics:
An Intermediate Regime Between Electronics and Photonics

by

David W. Ward

B.S. Physics, College of Charleston, 1999

Submitted to the Department of Chemistry
in partial fulfillment of the requirements for the degree of

Doctor of Philosophy at the Massachusetts Institute of Technology

at the

MASSACHUSETTS INSTITUTE OF TECHNOLOGY
[February 2005]
January 2005

Author .....
Department of Chemistry
Jan 18, 2005

Certified by .....
Keith A. Nelson
Professor
Thesis Supervisor

Accepted by .....
Robert W. Field
Chairman, Departmental Committee of Graduate Students

This doctoral thesis has been examined by a committee of the Department of Chemistry as follows:

Professor Robert W. Field .....

Chairman

Professor Keith A. Nelson .....

Thesis Supervisor

Professor Robert G. Griffin .....

Polaritonics:

An Intermediate Regime Between Electronics and Photonics

by

David W. Ward

Submitted to the Department of Chemistry
on Jan 18, 2005, in partial fulfillment of the
requirements for the degree of
Doctor of Philosophy at the Massachusetts Institute of Technology

Abstract

This thesis contains the foundational work behind the field of polaritonics. Corresponding to a frequency range from roughly 100 gigahertz up to 10 terahertz, polaritonics bridges the gap between electronics and photonics. In this regime, signals are carried by an admixture of electromagnetic and lattice vibrational waves known as phonon-polaritons, rather than currents or photons.

Impulsive stimulated Raman scattering (ISRS) is employed for phonon-polariton generation, whereby lattice vibrations are driven by optical femtosecond laser pulses directed into ferroelectric $LiNbO_3$ or $LiTaO_3$. The vibrational amplitude is proportional to the intensity of the excitation pulses. Due to the high dielectric constants of these crystals, phonon-polaritons travel in a predominantly lateral direction away from the excitation region. Lateral propagation is further facilitated by employing crystals whose thickness is on the order of the phonon-polariton wavelength, such that propagation occurs within one or more of the slab waveguide modes of the crystal. Direct observation of phonon-polaritons is achieved using real-space imaging, which monitors and records the spatiotemporal evolution of phonon-polaritons within a ferroelectric crystal.

The details of both broadband and narrowband phonon-polariton generation and propagation in bulk and thin film crystals are presented. Additionally, robust polaritonic waveform generation is illustrated that relies on temporal or spatial shaping of the optical excitation pulses. Guidance, control, and other types of signal processing are demonstrated by patterning of the host crystal using femtosecond laser micromachining. Waveguides that direct propagation, resonators that confine polaritonic signals, reflectors that direct, shape, and focus polaritonic waveforms, and periodic photonic crystal structures that restrict phonon-polaritons to a narrow band of frequencies are fabricated and their functionality demonstrated. The details of the laser micromachining employed for fabrication of these structures in a variety of crystal thicknesses are also presented here.

Experimental measurements are supported by a novel implementation of finite-difference-time-domain (FDTD) simulations that accurately model both phonon-polariton generation

and propagation in bulk, thin film, and patterned crystals. Additionally, numerical experiments are performed to predict functionality that will enable advanced polaritonic bistable devices for use in digital polaritonics and negative refractive polaritonic materials for unique waveform generation, signal processing, and sub-diffraction terahertz imaging.

Polaritonics offers lower signal-to-noise than photonics and higher bandwidth signals than electronics, with generation, propagation, guidance, and control integrated into a single all-optical platform. Direct visualization of signal propagation makes device design and testing substantially easier than in either electronics or photonics. With continued development, fabrication of polaritonic materials should prove less demanding than traditional photonic structures, as it requires feature sizes on the order of micrometers rather than nanometers. Due to the high terahertz electric field strengths associated with ISRS phonon-polariton generation and the robust signal processing tool chest presented here, polaritonics promises to be useful in various spectroscopic applications including, but not limited to, linear and nonlinear terahertz spectroscopy and terahertz near field microscopy.

Thesis Supervisor: Keith A. Nelson
Title: Professor

Acknowledgments

I would first like to thank my research advisor, Keith Nelson, and colleagues, Eric Statz, Jaime Choi, Thomas Feurer, Kevin Webb, and Nikolay Stoyanov, with whom I have worked closely and have enjoyed much fruitful collaboration. I must also thank the other members of the Nelson group who have contributed positively to my experience at MIT. They are Cindy Bolme, Timothy Crimmins, Michael Gleason, Christ Glorieux, Kenji Katayama, Christoph Klieber, Richard Koehl, Benjamin Paxton, Peter Poulin, Rebecca Slayton, Kathy Stone, Darius Torchinsky, Joshua Vaughan, Gregory Wakeham, Masashi Yamaguchi, and Ka-Lo Yeh.

I would also like to thank the other MIT professors with whom I interacted regularly. Among them are John Deutch, Robert Field, Robert Griffin, Robert Silbey, and Richard Lester.

A great deal of this thesis work can be attributed to the fantastic UROPs with whom I have had the privilege to work with. In no particular order, they are Rishi Roy, Dustin Ledbetter, Jordan Rubinstein, Sabine Volkmer, and Isabell Thomann.

I owe a great deal to the collaborators that made this thesis possible. Those not already mentioned here are James Scott, Finlay Morrison, Ryan Roth, Siavash Yazdanfar, Kerwyn Casey Huang, John Joannopoulos, Ming-chuan Yang, and Richard Osgood.

A lot of the success I have enjoyed as a graduate student I owe to earlier influences. Special thanks are due to William Loman, who nurtured my early scientific curiosity. An incomplete list of those who had a significant influence prior to graduate school are Jim Kinsey, Carter Kittrell, Linh Le, the Quattrochi family, Gordon Jones, Jeff Wragg, Kristin Krantzman, Barbara J. Garrison, Linda Jones, and my first grade teacher Mrs. Mills.

I could not have done this thesis work without having lived through the Navy years that preceded it. Thanks to all my Navy shipmates for keeping me alive—Hooyah!

I have thoroughly enjoyed the time I spent with friends on the conference circuit. They have contributed to my understanding of fields outside my own, and have provided much needed relief from the rigors of graduate school. An incomplete list is Manu Sharma, Malliga Suewattana (aka Cherry), Dan Dan Mao (aka Bam Bam), Faith Coldren, and Delmar Larson.

I would also like to thank my closest friends and roommates Ryan Thom, Serhan Altunata, Abigail Haka, Joel Eaves, Michiko Uozumi, Connie Chung, Robert Smith, Jennifer Lockman, Nicole Levi, Debra Bowen, Tai Nguyen, Edwin Culp, and Lara Kirkham.

There have been numerous pleasant distractions from graduate school, without which I may not have maintained my sanity. I would like to acknowledge the girls of Spearmint Rhino in Las Vegas; Gavin and the rest of crew from the Pink Palace in Corfu, Greece; Alita and the rest of the waitresses at King's College who made my stay in Cambridge and London very enjoyable, Sabine Volkmer and her family who were my hosts in Germany, and the performers at the American Repertory Theater.

Finally, I would like to thank my ex-wives and family who have exhibited infinite patience and provided support in all my endeavors. This thesis is dedicated to the memory of my dog Rusty, who spent more than twenty years with me before dying in 2000, and to my grandfather, James K. Cox, whose death was the darkest hour in all my life.

We are at the very beginning of time for the human race. It is not unreasonable that we grapple with problems. But there are tens of thousands of years in the future. Our responsibility is to do what we can, learn what we can, improve the solutions, and pass them on.

—Richard P. Feynman

Contents

List of Figures

List of Tables

Chapter 1

Introduction

This thesis contains the foundational work of the field of polaritonics, in which signals are carried by phonon-polaritons, an admixture of electromagnetic waves and lattice vibrations, through patterned materials, rather than alternating currents, as in electronics, or photons, as in photonics [95]. Since phonon-polaritons propagate with frequencies in the range of hundreds of gigahertz to several terahertz, polaritonics bridges the gap between electronics and photonics. A compelling motivation for polaritonics is the demand for high speed signal processing and linear and nonlinear terahertz spectroscopy. Polaritonics has distinct advantages over electronics, photonics, and traditional terahertz spectroscopy in that it offers a fully integrated platform that supports terahertz wave generation, guidance, manipulation, and readout in a single patterned material.

Polaritonics, like electronics and photonics, requires three elements: robust waveform generation, detection, and guidance and control. Without all three, polaritonics would be reduced to just phonon-polaritons, just as electronics and photonics would be reduced to just electromagnetic radiation. These three elements can be combined to enable device functionality similar to that in electronics and photonics. This chapter identifies the obstacles to and scientific questions posed by each of these three elements, and highlights some of the key results. Additionally, a theoretical model manifest in a novel implementation of the finite-difference-time-domain (FDTD) algorithm is presented that not only models phonon-

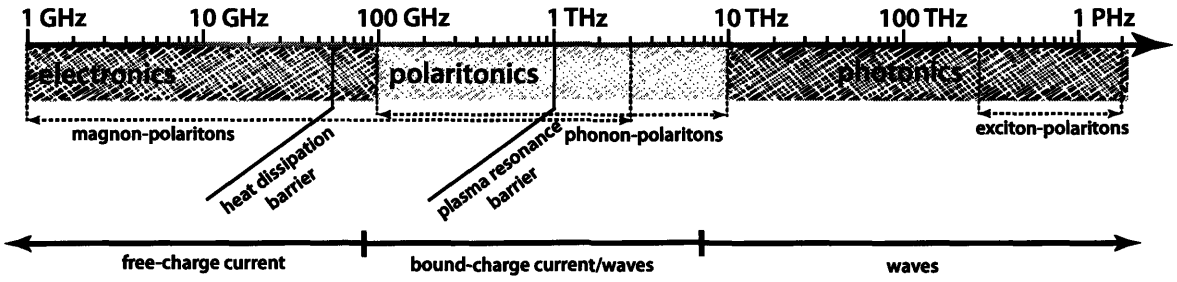

Figure 1-1: Polaritonics may resolve the incongruence between electronics, which suffers technological and physical barriers to increased speed, and photonics, which requires lossy integration of light source and guiding structures. Other quasiparticles/collective excitations such as magnon-polaritons and exciton-polaritons, their location identified above, may be exploitable in the same way that phonon-polaritons have been for polaritonics.

polariton generation, detection, and guidance, but also aids in the design of advanced materials that may lead to digital polaritonic devices and nonlinear terahertz spectroscopy.

1.1 Electronics, Photonics, and Polaritonics

The simplest way to understand the relevance of polaritonics is by identifying its proximity to electronics and photonics in the electromagnetic spectrum (See Fig. 8-16). Conveniently, it lies directly between photonics and electronics and spans two decades of frequencies. Roughly, this range/span corresponds to frequencies between 100 gigahertz and 10 terahertz.

In electronics, signals are manifest in alternating electrical currents and disseminated via a transverse electromagnetic (TEM) radiation field, in which both the electric and magnetic fields may have components in the direction of signal propagation through a transmission line. Familiar examples, both digital and analog, abound. For example, coaxial cable is a common transmission line for kilohertz-gigahertz signal transmission. The transistor and other solid state electronic bistable devices comprise the realm of digital electronics, which facilitated the microprocessor revolution. A classic electronic analog circuit is the LRC filter, which exploits resonance in LRC circuits to provide frequency selectivity to electronic devices. We show the realization of the polaritonic equivalent of this circuit, a phonon-polariton resonator, in chapter 7.

The photonics technology explosion that has taken place over the last twenty years was a result of exponential growth in demand for higher bandwidth communications. The use of the term optical communications as a synonym for photonics is evidence to the importance of photonics to this industry. In photonics, guidance is necessary because even the most well collimated laser beam propagating in free space will diverge considerably over long distances. Fiber optic technology overcomes this obstacle by transmitting signals through waveguide modes in the fiber, which serve to control the direction of propagation. The fiber consists of a cylindrical core surrounded by a lower index cladding that facilitates total internal reflection of light within the core. When the fiber diameter is on the order of the wavelength of light within it, total internal reflection results in a number of waveguide modes in which the light may propagate. As the name implies, signals in photonics are carried by photons, and take the form of either transverse magnetic (TM) or transverse electric (TE) optical radiation fields in guided wave structures. The TE and TM notation refer to either a single electric (TE) or magnetic (TM) field component normal to the direction of propagation.

The importance of high speed signal processing is growing as the demand for higher bandwidth and faster processing in communications and computing continues to increase exponentially. Present technology is insufficient to satisfy these growing demands. A major part of the problem is the bottleneck that results from the integration of optical fiber, which is capable of terahertz bandwidth, and relatively slow electronic switching technologies. Most photonic signal processing devices rely on electro-optic technology in which device bandwidth and speed are limited by reliance on electronics. It may be possible to circumvent, or at least ameliorate, integration problems by overcoming the present technological barriers in electronics (50 gigahertz heat dissipation barrier) but physical barriers intrinsic to electronics ($\sim$1 terahertz plasma resonance barrier) preclude higher-bandwidth throughput. These barriers also hinder the desired performance increases in electronic computing. The industry metric for processor speed growth is Moore's law, which stipulates that the number of transistors per integrated circuit will double every two years. So far the semiconductor industry has been able to sustain this growth, but this is unlikely to continue as the afore-

mentioned barriers are approached. Polaritonics provides an attractive solution to many of the problems in optical communications and computing.

To illustrate the functionality of polaritonic devices, consider the hypothetical circuit in Fig. 1-2. The optical excitation pulses that generate phonon-polaritons, in the top left and bottom right of the crystal, enter normal to the crystal face (into the page). The resulting phonon-polaritons will travel laterally away from the excitation regions. Entrance into the waveguides is facilitated by reflective and focusing structures. Phonon-polaritons are guided through the circuit by terahertz waveguides carved into the crystal. Circuit functionality resides in the interferometer structure at the top [83] and the coupled waveguide structure at the bottom of the circuit [61]. The latter employs a photonic bandgap structure with a defect (yellow) that could provide bistability for the coupled waveguide [78]. Though no polaritonic circuits of this type are presented in this thesis, many of the individual elements comprising the circuit are demonstrated.

1.2 A Brief History of Polaritons

Polaritons are quasiparticles/collective excitations that result from the coupling of light to an elementary excitation in a solid through an electric-dipole or magnetic-dipole interaction. In this regime, light can be thought of as "dressed" in the material excitation, the light dragging the material excitation along with it as it propagates through the crystal. Thus, polaritons have energy density distributed between electromagnetic energy associated with the radiation field and mechanical or electrical energy associated with the elementary excitation.

Whenever the polariton picture is valid, the usual treatment of photons in a crystal lattice is insufficient, because the strong coupling to the material gives rise to an avoided crossing between light dispersion and elementary excitation dispersion. The net result is that polaritons exhibit a strong frequency dependence in which propagation slows as the material excitation resonance frequency is approached, and terminates at the polaritonic bandgap. Propagation at frequencies in the bandgap is forbidden, much in the same way that electrons are forbidden within an electronic bandgap. Above resonance, as the coupling

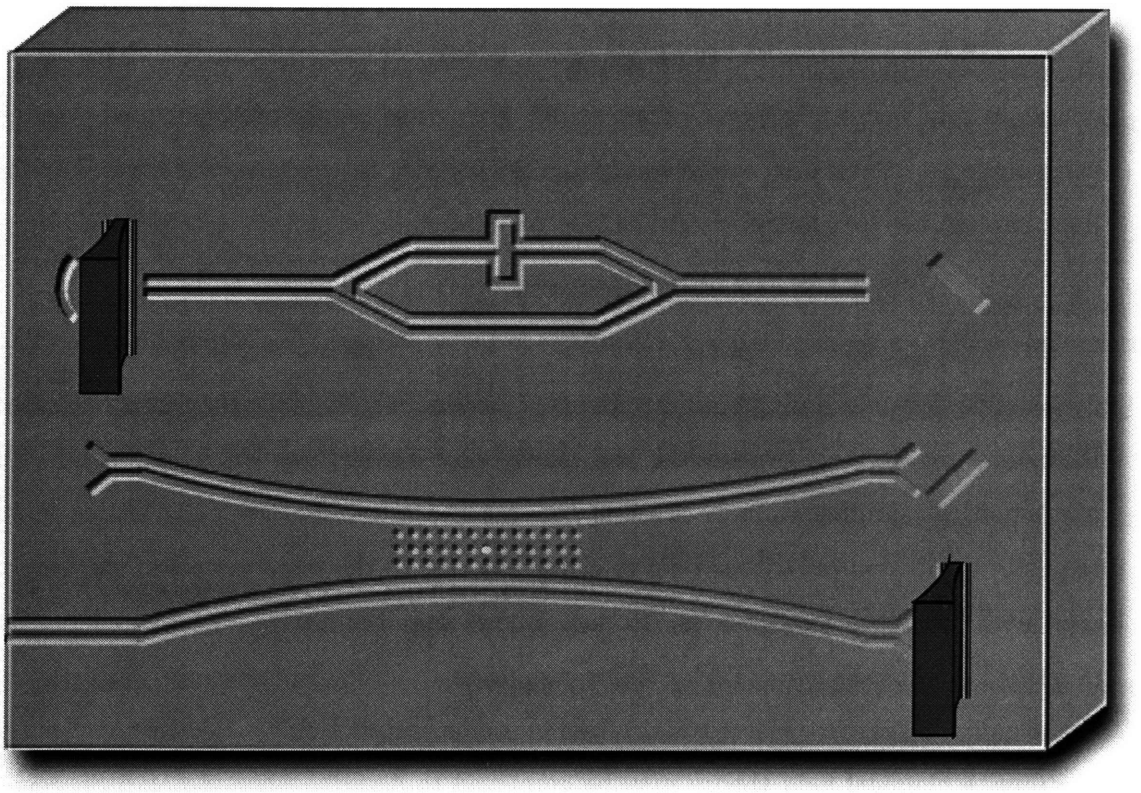

Figure 1-2: Fanciful depiction of a polaritonic circuit illustrating fully integrated terahertz wave generation, guidance, manipulation, and readout in a single patterned material. Phonon-polaritons are generated in the upper left and lower right hand corners by focusing femtosecond optical excitation pulses into the crystal near waveguide entrances. Phonon-polaritons propagate laterally away from the excitation region and into the waveguides. Signal processing and circuit functionality is facilitated by resonant cavities, reflectors, focusing elements, coupled waveguides, splitters, combiners, interferometers, and photonic bandgap structures created by milling channels that fully extend throughout the thickness of the crystal.

becomes weaker, propagation is restored and approaches the regime in which the ordinary description of light in a crystal lattice is valid. Polariton dispersion is discussed in more detail in chapter 4.

Since there are a variety of elementary excitations in solids that may possess an electric or magnetic dipole moment, there are also a variety of polariton species. Microwaves can couple to spin waves in a ferromagnetic solid, giving rise to magnon-polaritons. Visible light can couple to excitons in a semiconductor, giving rise to exciton-polaritons. Far infrared light can couple to transverse optic (TO) phonons in a ferroelectric crystal, giving rise to phonon-polaritons. The last variety is central to this thesis.

Since the quasiparticle picture is one in which many interacting bodies may be replaced by a single non-interacting entity, phonon-polaritons may be described in a simplified way that does not need to account for the many-body interactions within the solid. Further mathematical simplification is possible because the infrared-active (IR) lattice vibrations requisite to phonon-polaritons behave classically due to the large masses of the ions associated with the vibrational modes. It then follows that the lattice potential energy may be described adequately by a Taylor series expansion in ionic displacement. Note that this is not usually the case for electronic orbitals in atoms and molecules. Because of these simplifications, a classical field theory may be employed to describe phonon-polariton generation and propagation. Such a theory was developed in the 1940's—an extension of Maxwell's field theory to account for polariton dispersion [9, 39]. A similar model is presented in detail in chapter 2. Prior to this model, the propagation of light through dispersive materials was treated phenomenologically without accounting for the material excitation directly [14, 79].

The first true quasiparticle description of polaritons was a quantum field theory for phonon-polaritons developed in the 1950's [26]. Soon afterwards, a similar approach was taken to describe excition-polaritons, in which the term "polaritons" appeared for the first time [37]. With the advent of lasers in the 1960's, Raman scattering by phonon-polaritons in $LiNbO_3$ and $LiTaO_3$ was presented during this period [55, 6, 5], and provides most of what is known today about phonon-polariton modes in ferroelectric crystals.

1.3 Polaritonic Modeling and Simulation

To facilitate the engineering of polaritonic devices like the one shown in Fig. 1-2, the science of polaritonics must be fully understood, and models capable of predicting phonon-polariton behavior in a patterned material must be used. This thesis addresses these points directly. The system of equations necessary to describe phonon-polariton generation and propagation in $LiNbO_3$ and $LiTaO_3$ is presented in chapter 2. These equations are analytically solvable in only a limited number of cases. To remedy this, a novel implementation of the finite-difference-time-domain (FDTD) method suitable for simulation of phonon-polariton generation and propagation in arbitrary patterned materials is presented in chapter 3. The utility of these simulations is demonstrated in chapter 4, where experimental measurements of phonon-polaritons are compared to theory and simulation. FDTD simulations are employed throughout this thesis to provide insight into polaritonic behavior.

1.4 Waveform Generation

It was the advent of femtosecond laser technology [80] that made possible the development of polaritonics. In the 1980's, scientists at Bell Labs generated what they termed as "terahertz electrical transients," which we now know to be phonon-polaritons, in ferroelectric $LiTaO_3$ using optical femtosecond lasers. A ferroelectric crystal is an ionic crystal that possesses a permanent polarization in the unit cells, which may be aligned through poling with a static electric field, and is required for efficient phonon-polariton generation and propagation. An ultrashort optical pulse focused into a ferroelectric crystal like $LiNbO_3$ or $LiTaO_3$ generates phonon-polaritons in the terahertz frequency range through impulsive stimulated Raman scattering (ISRS) [23] and difference frequency mixing (DFM) [3]. The primary contribution to nonlinear optical phonon-polariton generation is ISRS, which acts on lattice vibrations directly through the Raman force [11].

The early ISRS experiments in ferroelectric crystals were motivated by a desire to understand the dynamics of ferroelectric phase transitions and nonlinear lattice dynamics [24].

The continued use of ferroelectric crystals in the work in this thesis and elsewhere is primarily due to their extraordinarily large electro-optic coefficients, which facilitates intense phonon-polariton generation and easy detection.

Auston was the first to describe terahertz generation as analogous to Cherenkov radiation, an effect recently confirmed through direct observation [91]. The Cherenkov effect is described in more detail in chapter 4, but an important consequence of it deserves mention here. Phonon-polaritons generated in ferroelectric crystals propagate nearly laterally to the excitation pulse due to the high dielectric constants of ferroelectric crystals, facilitating easy separation of phonon-polaritons from the excitation pulses that generated them. Phonon-polaritons are therefore available for direct observation, as well as coherent manipulation, as they move from the excitation region into other parts of the crystal [3, 51, 91]. Lateral propagation is paramount to a polaritonic platform in which generation and propagation take place in a single crystal. A full treatment of the Cherenkov-like terahertz wave response reveals that in general, there is also a forward propagation component that must be considered in many cases.

The advent of programmable temporal pulse shaping with spatial light modulators [108], which occurred in the early 1990's, created new opportunities for phonon-polariton generation through ISRS. Phonon-polaritons can also be shaped temporally through the optical excitation pulses, allowing for facile narrowband phonon-polariton generation [107]. A simpler method described recently uses a phase-grating to facilitate the crossing of two excitation pulses to from an intensity gradient, which excites phonon-polaritons with a wavelength equal to the grating periodicity [20]. Even more recently, robust techniques for programmable phonon-polariton waveform generation were demonstrated by shaping the optical excitation pulse not only temporally but spatially as well, using a two-dimensional spatial light modulator [29, 52].

Techniques of phonon-polariton waveform generation through temporal and spatial pulse shaping of optical excitation pulses are demonstrated in chapter 4. This chapter also provides foundational work that characterizes broadband and narrowband phonon-polariton gener-

ation, assesses the electric field strengths and ionic displacements associated with phonon-polaritons, and illustrates phonon-polariton dispersion in bulk crystals.

1.5 Signal Detection

Direct observation of phonon-polariton propagation was made possible by real-space imaging [51], in which the spatial and temporal profiles of phonon-polaritons are imaged onto a CCD camera using Talbot phase-to-amplitude conversion [88]. This by itself was an extraordinary breakthrough. It was the first time that electromagnetic waves were imaged directly, appearing much like ripples in a pond when a rock plummets through the water's surface. Real-space imaging is the preferred detection technique in polaritonics, though other more conventional techniques like optical Kerr-gating, time resolved diffraction, interferometric probing, and terahertz field induced second harmonic generation are useful in some applications where real-space imaging is not easily employed. For example, patterned materials with feature sizes on the order of a few tens of microns cause parasitic scattering of the imaging light. Phonon-polariton detection is then only possible by focusing a more conventional probe, like those mentioned before, into an unblemished region of the crystal. These techniques are discussed in chapter 4.

1.6 Guidance and Control

The last element requisite to polaritonics is guidance and control, which is the central topic of this thesis. Complete lateral propagation parallel to the crystal plane is achieved by generating phonon-polaritons in crystals of thickness on the order of the phonon-polariton wavelength [103]. This forces propagation to take place in one or more of the available slab waveguide modes. However, dispersion in these modes can be radically different than in bulk propagation, and in order to exploit this, the dispersion must be understood. Experimental measurements and modeling of phonon-polariton generation and propagation in thin films is presented in chapter 5.

Control and guidance of phonon-polariton propagation may also be achieved by guided wave [31, 83, 85], reflective [100], diffractive [81], and dispersive elements [84], as well as photonic and effective index crystals [101, 102] that can be integrated directly into the host crystal. However, $LiNbO_3$, $LiTaO_3$, and other perovskites are impermeable to the standard techniques of material patterning. In fact, the only etchant known to be even marginally successful is hydrofluoric acid (HF), which etches slowly and predominately in the direction of the crystal optic axis.

In this thesis, femtosecond laser micromachining is used for device fabrication by milling "air" holes and/or troughs into ferroelectric crystals by directing them through the focus region of a femtosecond laser beam. This is the first demonstration of convenient, controllable, and rapid large scale damage induced in $LiNbO_3$ and $LiTaO_3$. The advantages of femtosecond laser micromachining for a wide range of materials have been well documented [74]. In brief, free electrons are created within the beam focus through multiphoton excitation. Because the peak intensity of a femtosecond laser pulse is many orders of magnitude higher than that from longer pulse or continuous wave lasers, the electrons are rapidly accelerated and heated to form a plasma. The electrostatic instability, produced by the plasma, of the remaining lattice ions results in ejection of these ions and hence ablation of the material, leaving a material void in the laser focus region. Since multiphoton excited free electrons are always available at the beam focus, highly uniform and repeatable damage confined to the laser focus region results. Also, since the pulse duration and ablation time scales are much faster than thermalization time, femtosecond laser micromachining does not suffer from the adverse effects of a heat-affected-zone, like cracking and melting in regions neighboring the intended damage region. Fabrication of several structures on a variety of size scales is discussed in detail in chapter 6, and propagation within them is discussed in chapter 7.

1.7 Advanced Materials

The last chapter of this thesis is devoted to theoretical considerations of advanced polaritonic devices and functionalities that are presently out of reach experimentally. Chapter 8 develops

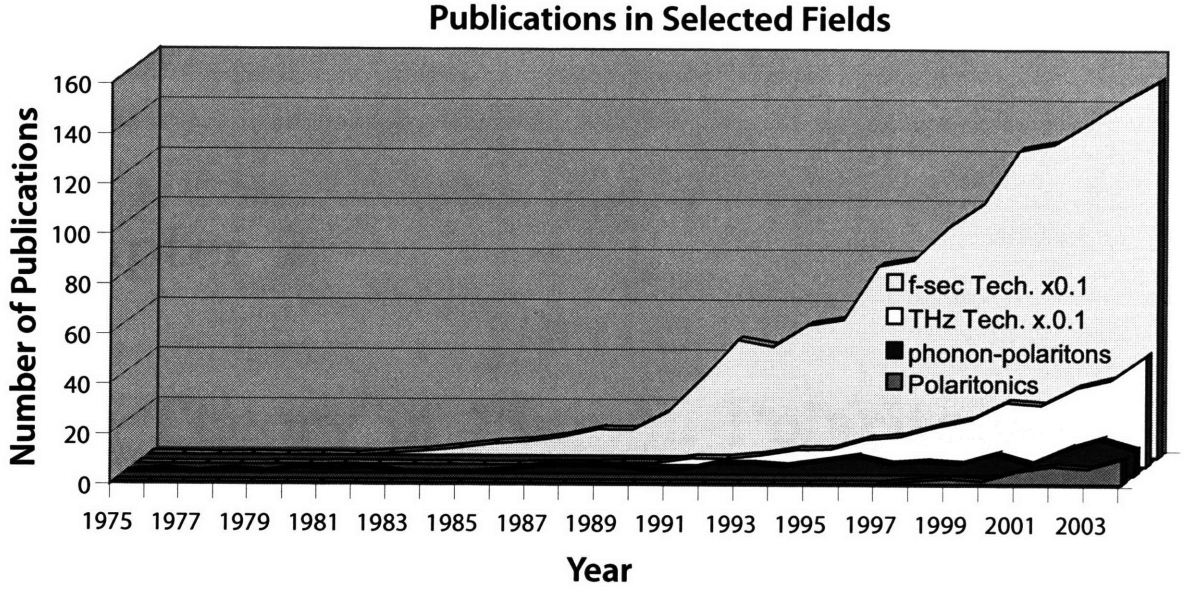

Figure 1-3: Data collected from ISI Web of Knowledge on the number of publications each year in femtosecond laser technology, terahertz radiation, phonon-polaritons, and terahertz polaritonics. Femtosecond laser and terahertz technology are scaled down by a factor of ten.

a theoretical model of the phenomenon of negative refraction, in which light refracts opposite to normal refraction at an interface. It is already known that the simultaneous existence of negative permittivity and permeability will result in negative refraction when the electric and magnetic resonances overlap in frequency. The theory presented here explains why this is so and puts negative refraction on equal footing with attenuation and dispersion. The theory is then used to extend negative refraction into the polariton regime, illustrating the role of negative index materials in ISRS and DFM generation of phonon-polaritons. Negative index waveguides are also briefly considered.

The final chapter of this thesis, chapter 8, concludes this study by considering the merger of the science and technology developed here with other emerging technologies, rendering a perhaps wishful, but likely, realistic prognosis of what lies ahead. The graph in Fig. 1-3 represents the rise in publications in several fields including and related to polaritonics, and indicates that continued growth and development is likely to occur. Though no commercial applications of polaritonics yet exist, the dawn of polaritonics is clearly upon us.

Chapter 2

The Theory of Phonon-Polaritons

In this chapter, the basic theory of phonon-polaritons is presented. More practical matters and particulars of phonon-polariton generation, propagation, and detection are deferred until chapters 4 and 7, as they are closely allied with the experimental techniques employed to generate, guide, and detect them. Instead, consideration is given here to how phonon-polaritons arise in a simple cubic ionic crystal. In this case, a simplified illustration of polariton dispersion emerges, which will facilitate understanding later when the more complex situations of phonon-polaritons in $LiNbO_3$ and $LiTaO_3$ are explored experimentally and in simulation. At the end of this chapter, the system of equations used for modeling of phonon-polariton generation and propagation in $LiNbO_3$ and $LiTaO_3$ is presented. Though analytically insoluble, except under the crudest assumptions, these equations provide the basis for numerical solution via a modified version of the finite-difference-time-domain (FDTD) method, presented in chapter 3.

The model developed in this chapter is essentially an oscillator that undergoes transverse vibrations when driven by an external electromagnetic field. These vibrations cause the oscillator to radiate electromagnetic waves that can interfere with the externally applied driving field. Radiation passing back and forth from electromagnetic wave to vibrational wave comprises a coupled system that results in the polariton dispersion presented in section 2.2.

2.1 Phonon-Polaritons in a Cubic Ionic Crystal

Assuming cubic lattice symmetry, several simplifications arise that make the theory of phonon-polaritons more easily presented. Since the ultimate goal is to apply this theory to phonon-polaritons in $LiNbO_3$ and $LiTaO_3$, which are of tetragonal symmetry, discrepancies that arise under the assumption of cubic symmetry will be pointed out. The objective of this section is to arrive at a macroscopic optical theory to replace the usual theory of light propagation in a crystal lattice. The derivations below closely follow those given previously by Born and Huang [9, 39], which contain a more complete account of the phenomenon. We begin by deriving the coupling of electromagnetic radiation to a transverse polar optic phonon mode using a microscopic model. We then adapt this model to a macroscopic field model using Maxwell's equations to derive the optical properties of phonon-polaritons, which we use to illustrate polariton dispersion, the defining characteristic of the polariton regime.

2.1.1 Microscopic Model for a Single Polar Mode

Here a microscopic model of a diatomic polar ionic crystal in the presence of an external electric field is considered. The fields contributing to the ion motion are categorized using the theory of the local field [2]. According to this theory, the local field is the field at an ion's lattice position minus the field from the ion itself. It is equal to the contributions from the local near field, attributed to dipole moments of nearby ions, the external applied field, and the near macroscopic field, which is the contribution from dipole moments far enough away to be treated as an external macroscopic polarization. Under conditions of high lattice symmetry, local near field contributions to the ions are negligible, but in the case of $LiNbO_3$ and $LiTaO_3$, which have a rhombohedral lattice, there will be a contribution. The local near field, E^{loc}, is given by the Lorentz relation [10],

$$E^{\mathrm{loc}} = E + \frac{1}{3\epsilon_0} P, \tag{2.1}$$

where E is the macroscopic electric field, and P is the macroscopic polarization. Only a single polarization component is assumed, for simplicity, which has no effect on the generality of the results since cubic symmetry is assumed.

The microscopic polarizability, α, which is assumed linear in the external applied field, contributes to the local field in the form of an atomic polarizability, α_∞, associated with electronic energy levels of the unit cell atoms, and a displacement polarizability, α_{ion}, associated with ionic displacements, which can be written:

$$\begin{aligned} p_\infty + Ze\mathrm{w} &= \alpha E, && (2.2)\\ p_\infty &= \frac{\alpha_\infty}{E^{\text{loc}}}, && (2.3)\\ Ze\mathrm{w} &= \frac{\alpha_{\text{ion}}}{E^{\text{loc}}}. && (2.4)\\ \mathrm{w} &= (\mathrm{w}^+ - \mathrm{w}^-), && (2.5) \end{aligned}$$

where p_∞ is the microscopic atomic polarization, Ze is the dipolar charge in Z units of discrete charge e, and w is the net ionic displacement defined in terms of the positive and negative ionic displacements from equilibrium, w^+ and w^-, respectively.

The microscopic polarizability can be related to a macroscopic total polarization ($P = P_\infty + P_{\text{ion}}$), which can also be written in terms of a macroscopic susceptibility:

$$\begin{aligned} P &= N\alpha E, && (2.6)\\ &= \epsilon_0 \chi E, && (2.7) \end{aligned}$$

where N is the oscillator density, which is inversely proportional to the unit cell volume, and ϵ_0 is the permittivity of free space.

Invoking the rigid ion approximation, the atomic polarizability is neglected and only the ionic displacement is accounted for. The equation of motion for the unit cell ions is expressed in accordance with Newton's second law as:

$$M\ddot{\mathrm{w}} = -K\mathrm{w} + ZeE^{\text{loc}}, \qquad (2.8)$$

where

$$M = \frac{M^+M^-}{M^+ + M^-}. \tag{2.9}$$

K is the linear restoring force coefficient between the ions, and M is the reduced mass of the charge centers of the normal mode.

Application of an external electromagnetic field, $E = E_0 e^{-i\omega t}$, results in plane wave solutions for the relative ionic displacements,

$$\mathrm{w} = \mathrm{w}_0 e^{-i\omega t}, \tag{2.10}$$

$$\mathrm{w}_0 = \frac{eE_0}{M}\frac{1}{\omega_{\mathrm{TO}}^2 - \omega^2}, \tag{2.11}$$

$$\omega_{\mathrm{TO}} = \sqrt{\frac{K}{M}}, \tag{2.12}$$

where ω_{TO} is the transverse optic (TO) phonon frequency, and ω is the frequency of the driving field. The microscopic displacement polarizability is then found to be,

$$\alpha_{\mathrm{ion}} = \frac{Ze\mathrm{w}_0}{E_0} = \frac{Ze^2}{M(\omega_{TO}^2 - \omega^2)}. \tag{2.13}$$

Assuming now that the ions are immobile, it is easy to show that the atomic polarizability takes a form similar to that in Eq. (2.13),

$$\alpha_\infty = \frac{Ze^2}{m_e(\omega_0^2 - \omega^2)}, \tag{2.14}$$

where ω_0 is the electronic resonance frequency, and m_e is the mass of an electron. ω_{TO} is typically in the far infrared, while ω_0 is typically in the ultraviolet.

A crude correction to the rigid ion model can be made by simply summing the ionic polarizability from the rigid ion approximation with the atomic polarizability from the immobile ion approximation,

$$\alpha = \alpha_\infty + \alpha_{\mathrm{ion}}. \tag{2.15}$$

An expression for the macroscopic polarization can then be obtained by using the microscopic

polarizability, Eq. (2.2), with Eq. (2.6) and the crude correction above results in,

$$P = \frac{N}{1 - \frac{N}{3}\alpha_\infty}\left(Ze\mathrm{w} + \alpha_\infty E^{\mathrm{loc}}\right). \tag{2.16}$$

Using the Lorentz relation from Eq. (2.1) to eliminate the local field, a general expression for the polarization, similar to that derived elsewhere [9], is obtained:

$$P = b_{21}Q + b_{22}E, \tag{2.17}$$

$$b_{21} = \frac{Ze\sqrt{N/M}}{1 - \frac{N}{3}\alpha_\infty}, \tag{2.18}$$

$$b_{22} = \frac{N\alpha_\infty}{1 - N\alpha_\infty}, \tag{2.19}$$

where Q is the normalized ionic displacement defined as,

$$Q \equiv \sqrt{NM}\mathrm{w}. \tag{2.20}$$

Eliminating the local field from Eq. (2.8) and substituting in for Q from Eq. (2.16), the ionic equation of motion can be written, including a phenomenological damping term, as,

$$\ddot{Q} = b_{11}Q - \Gamma\dot{Q} + b_{12}E, \tag{2.21}$$

where

$$b_{11} = -\frac{K}{M} + \frac{\frac{N(Ze)^2}{3M}}{1 - \frac{N}{3}\alpha_\infty}, \tag{2.22}$$

and

$$b_{12} = \frac{Ze\sqrt{N/M}}{1 - \frac{N}{3}\alpha_\infty}. \tag{2.23}$$

Equations (2.17) and (2.21) describe the coupling between mechanical ion motion and an applied electric field, and vice versa, respectively. Although isotropy was assumed in the derivation, these two equations are valid for anisotropic crystals as well, though the relations for the coupling coefficients (Eqs. (2.18), (2.19), (2.22) and (2.23)) are not. As will be shown

later in section 2.1.2, the b-coefficients are taken from spectroscopic data, and the local near field, which was neglected here, is included in the measured values.

2.1.2 Macroscopic Field Model of Phonon-Polaritons

One of the crowning achievements of twentieth century physics was the development of non-abelian gauge theories, sometimes called Yang-Mills theories, or simply gauge theories. These theories are based on the principle of gauge symmetry. The prototype gauge theory is Maxwell's theory of electromagnetism, in which the symmetry is Lorentz invariance, from which the electromagnetic force arises naturally. In this section, Maxwell's field theory is extended to the polariton regime. Carrying out this extension, the wave equation and dispersion relation governing phonon-polariton propagation in bulk crystals are obtained.

The key distinction of the model developed here is that the material excitation, manifest in the mechanical component Q, is associated with a field, and the same gauge as applies to the electric field, E, and magnetic field, H, is imposed. Then, any point in the host crystal is characterized by an electric, magnetic, and mechanical field.

The phonon-polariton equations of motion, Eqs. (2.17) and (2.21), are introduced into Maxwell's equations through the displacement field $\vec{D}$. Maxwell's equations can then be written as:

$$\nabla \times \vec{E} = -\mu_0 \ddot{\vec{H}} \tag{2.24}$$

$$\nabla \times \vec{H} = \dot{\vec{D}}, \tag{2.25}$$

$$\vec{D} = \epsilon_0 \vec{E} + \vec{P}, \tag{2.26}$$

$$\nabla \cdot \vec{D} = 0, \tag{2.27}$$

$$\nabla \cdot \vec{B} = 0, \tag{2.28}$$

where μ_0 is the permeability of free space, P is the total macroscopic polarization, including both ionic and electronic contributions, and we assume a non-magnetic material, $\vec{B} = \mu_0 \vec{H}$, for simplicity.

Substituting P from Eq. (2.17) into Eq. (2.26), the constitutive relation becomes,

$$\vec{D} = (\epsilon_0 + b_{22})\vec{E} + b_{21}\vec{Q}, \tag{2.29}$$

where the vector components of $\vec{Q}$ refer to the polarization in the same way as for $\vec{E}$, $\vec{D}$, and $\vec{H}$. Taking the time derivative of the constitutive relation and eliminating $\dot{\vec{D}}$ in Eq. (2.25), the field equations governing phonon-polariton propagation in an ionic cubic crystal may be written as:

$$\ddot{\vec{Q}} = b_{i11}\vec{Q} - \Gamma_i\dot{\vec{Q}} + b_{i12}\vec{E}, \tag{2.30}$$

$$\dot{\vec{E}} = \frac{1}{\epsilon_0 + b_{i22}}\left(\nabla \times \vec{H} - b_{i21}\dot{\vec{Q}}\right), \tag{2.31}$$

$$\dot{\vec{H}} = -\frac{1}{\mu_0}\nabla \times \vec{E}, \tag{2.32}$$

$$\nabla \cdot \vec{D} = 0, \tag{2.33}$$

$$\nabla \cdot \vec{B} = 0, \tag{2.34}$$

where we have allowed for polarization dependent coupling coefficients and damping denoted by the subscript i. Phonon-polaritons must satisfy all five equations simultaneously.

Dielectric Function $\varepsilon(\omega)$

The dielectric function $\varepsilon(\omega)$ governs the phonon-polariton phase velocity, and may be derived by considering plane wave solutions to Eq. (2.30):

$$E = |E|e^{-i\omega t}, \tag{2.35}$$

$$Q = |Q|e^{-i\omega t}, \tag{2.36}$$

$$\dot{Q} = -i\omega|Q|e^{-i\omega t} = -i\omega Q, \tag{2.37}$$

$$\ddot{Q} = -\omega^2|Q|e^{-i\omega t} = -\omega^2 Q, \tag{2.38}$$

where the displacement of magnitude $|Q|$ and electric field of magnitude $|E|$ is polarized along a single arbitrary direction. Substitution into Eq. (2.30) yields:

$$Q = \frac{b_{12}E}{-b_{11} - \omega^2 - i\omega\Gamma}. \tag{2.39}$$

Next, we eliminate Q in Eq. (2.17) to obtain:

$$P = \Big(\frac{b_{12}b_{21}}{-b_{11} - \omega^2 - i\omega\Gamma} + b_{22}\Big)E. \tag{2.40}$$

Recall that the polarization is related to a susceptibility, as given in Eq. (2.7), which can be related to the dielectric function, also known as the relative permittivity, through the relation $\varepsilon_r = 1 + \chi$. Using Eq. (2.40), the dielectric function can then be written as:

$$\varepsilon_r(\omega) = \Big(1 + \frac{b_{22}}{\epsilon_0}\Big) + \frac{1}{\epsilon_0}\Big(\frac{b_{12}b_{21}}{-b_{11} - \omega^2 - i\omega\Gamma}\Big). \tag{2.41}$$

The coupling coefficients b_{11} and b_{22} may be discerned in terms of the measurable crystal optical properties by considering limiting cases of Eq. (2.41). Taking the limit as $\omega \to \infty$, the high frequency dielectric constant is obtained,

$$\varepsilon_\infty = \Big(1 + \frac{b_{22}}{\epsilon_0}\Big), \tag{2.42}$$

or solving for b_{22}:

$$b_{22} = \epsilon_0(\varepsilon_\infty - 1). \tag{2.43}$$

Neglecting damping and taking the limit as $\omega^2 \to b_{11}$, a resonance is observed and the transverse optic phonon frequency is obtained,

$$b_{11} = -\omega_{\mathrm{TO}}^2. \tag{2.44}$$

Taking the limit as $\omega \rightarrow 0$, the static field dielectric constant is found to be,

$$\varepsilon_0 = \varepsilon_\infty + \frac{b_{12}b_{21}}{\epsilon_0 \omega_{\mathrm{TO}}^2}. \tag{2.45}$$

Further, conservation of energy requires that $b_{12} = b_{21}$ [9], which we apply to Eq. (2.45) to determine the remaining coupling coefficients:

$$b_{12} = b_{21} = \omega_{\mathrm{TO}} \sqrt{\epsilon_0(\varepsilon_0 - \varepsilon_\infty)}. \tag{2.46}$$

Inserting Eqs. (2.43), (2.44) and (2.46) into Eq. (2.41), the dielectric function is obtained in terms of the observable optical properties,

$$\varepsilon_r(\omega) = \varepsilon_\infty + \frac{\omega_{\mathrm{TO}}^2(\varepsilon_0 - \varepsilon_\infty)}{\omega_{\mathrm{TO}}^2 - \omega^2 - i\omega\Gamma}. \tag{2.47}$$

It is well known from Maxwell's electromagnetic field theory that the dielectric function must vanish for any longitudinal electromagnetic disturbance. Accordingly, $\varepsilon(\omega_{\mathrm{LO}}) = 0$, where ω_{LO} is the longitudinal optic phonon frequency. Inserting $\varepsilon(\omega_{\mathrm{LO}})$ into Eq. (2.47) results in the celebrated Lyddane-Sachs-Teller relation [58],

$$\omega_{\mathrm{LO}} = \sqrt{\frac{\varepsilon_0}{\varepsilon_\infty}} \omega_{\mathrm{TO}}. \tag{2.48}$$

The relations derived in this section are valid for any polar ionic crystal regardless of symmetry, as they are discerned from measurable macroscopic optical properties of the crystal. In the case of a cubic polar ionic crystal, the optical properties can be related to the parameters from the microscopic model in the previous section by eliminating the b-coefficients.

2.1.3 The Wave Equation

We first derive the scalar wave equation appropriate for propagation in a uniform dielectric, followed by the vector and scalar potential wave equations which are required for treating

propagation in non-uniform dielectrics such as the photonic bandgap materials of chapter 7.

The Scalar Wave Equation

The wave equation governing phonon-polariton propagation in bulk polar ionic crystals can be derived by considering Eqs. (2.30)-(2.26) for a uniform, isotropic, non-magnetic material with no free charges. First, we apply the curl operator to the left and right hand side of Eq. (2.32) and substitute in for $\vec{H}$ from Eq. (2.31) to obtain:

$$\nabla \times \nabla \times \vec{E} = -\mu_0(\epsilon_0 + b_{22})\ddot{\vec{E}} - \mu_0 b_{21}\ddot{\vec{Q}}. \tag{2.49}$$

Using the vector identity $\nabla \times (\nabla \times \vec{E}) = \nabla(\nabla \cdot \vec{E}) - \nabla^2\vec{E}$ and asserting $\nabla \cdot \vec{E} = 0$, which is appropriate for a uniform dielectric in the absence of free charges, we arrive at the wave equation:

$$\left(\nabla^2 - \frac{1}{c_0^2/\varepsilon_\infty}\right)\vec{E} = -\mu_0\omega_{\mathrm{TO}}\sqrt{\epsilon_0(\varepsilon_0 - \varepsilon_\infty)}\ddot{\vec{Q}}, \tag{2.50}$$

where

$$\ddot{\vec{Q}} = -\omega_{\mathrm{TO}}^2\vec{Q} - \Gamma\dot{\vec{Q}} + \omega_{TO}\sqrt{\epsilon_0(\varepsilon_0 - \varepsilon_\infty)}\vec{E}, \tag{2.51}$$

and b_{11}, b_{22} and b_{12}/b_{21} have been substituted from Eqs. (2.44), (2.43) and (2.46), respectively.

The Vector and Scalar Potential Coupled Wave Equations

The scalar wave equation is not appropriate for non-uniform dielectric materials like those presented in chapter 7. Instead, two coupled wave equations can be derived, one for the scalar potential and the other for the vector potential. In the case of a uniform dielectric, these equations reduce to the scalar wave equation from the previous section.

To derive the coupled wave equations, we introduce the vector potential $\vec{A}$ and scalar potential ϕ. Because we are assuming a non-magnetic material, the vector potential may be written as:

$$\mu_0\vec{H} = \nabla \times \vec{A}. \tag{2.52}$$

Inserting this into Eq. (2.32) and introducing the, as yet unspecified ,scalar potential ϕ, we find for $\vec{E}$ that

$$\vec{E} = -\dot{\vec{A}} - \nabla\phi. \tag{2.53}$$

Introducing Eqs. (2.52) and (2.53) into Eq. (2.31) with the aid of the constitutive relation (Eq. (2.29)), we obtain

$$\left(\nabla^2\vec{A} - \frac{1}{c_0^2/\varepsilon_\infty}\ddot{\vec{A}}\right) - \nabla\cdot\left((\nabla\cdot\vec{A}) + \frac{1}{c_0^2/\varepsilon_\infty}\dot{\phi}\right) = -\mu_0\omega_{\mathrm{TO}}\sqrt{\epsilon_0(\varepsilon_0-\varepsilon_\infty)}\dot{\vec{Q}}. \tag{2.54}$$

A vector field requires both its curl and divergence to be specified. The curl criterion is specified in Eq. (2.52). The divergence criterion comes from Eq. (2.27). Inserting Eq. (2.53) into the divergence criterion, we find that

$$\nabla^2\phi + \frac{\partial}{\partial t}(\nabla\cdot\vec{A}) = \omega_{\mathrm{TO}}\sqrt{\frac{\varepsilon_0/\varepsilon_\infty^2 - 1}{\epsilon_0}}(\nabla\cdot\vec{Q}). \tag{2.55}$$

If a field theory is to be used for phonon-polaritons, then the field component Q must be described as a vector field, which is uniquely determined by its solenoidal and irrotational parts, defined as $\nabla\cdot\vec{Q}_t = 0$ and $\nabla\times\vec{Q}_l = 0$ respectively. Inserting both parts in Eq. (2.55), the electric field $\vec{E}$ is found to be:

$$\vec{E} = -\frac{\omega_{\mathrm{TO}}\sqrt{\epsilon_0(\varepsilon_0-\varepsilon_\infty)}}{\epsilon_0\varepsilon_\infty}\vec{Q}_l. \tag{2.56}$$

The solution is unique since $\vec{E}$ must be irrotational. Inserting the solenoidal and irrotational parts into the ionic equation of motion (Eq. (2.30)) yields two equations,

$$\ddot{\vec{Q}}_t = -\omega_{\mathrm{TO}}^2\vec{Q}_t, \tag{2.57}$$

$$\ddot{\vec{Q}}_l = -\frac{\varepsilon_0}{\varepsilon_\infty}\omega_{\mathrm{TO}}^2\vec{Q}_l, \tag{2.58}$$

where we have neglected damping. If we again consider plane wave solutions for the solenoidal

and irrotational parts,

$$\vec{Q}_t = |Q_t|e^{-i\omega_t t} \tag{2.59}$$

$$\vec{Q}_l = |Q_l|e^{-i\omega_l t} \tag{2.60}$$

we find that the solenoidal frequency is associated with the transverse optic phonon mode and the irrotational frequency is associated with the longitudinal optic phonon mode as follows:

$$\omega_t = \omega_{\mathrm{TO}}, \tag{2.61}$$

$$\omega_l = \sqrt{\frac{\varepsilon_0}{\varepsilon_\infty}}\omega_{\mathrm{TO}} = \omega_{\mathrm{LO}}, \tag{2.62}$$

where the latter follows from Eq. (2.48).

Equations (2.54) and (2.55) constitute the vector and scalar coupled wave equations, which may be simplified by choosing an appropriate gauge. We choose the polariton gauge, defined as

$$\nabla \cdot \vec{A} = -\frac{\varepsilon_\infty}{c_0^2}\dot{\phi}. \tag{2.63}$$

Introducing this equation into Eqs. (2.54) and (2.55), we arrive at the simplified coupled vector and scalar potential wave equations:

$$\left(\nabla^2\vec{A} - \frac{1}{c_0^2/\varepsilon_\infty}\ddot{\vec{A}}\right) = -\mu_0\omega_{\mathrm{TO}}\sqrt{\epsilon_0(\varepsilon_0 - \varepsilon_\infty)}\dot{\vec{Q}}, \tag{2.64}$$

$$\nabla^2\phi - \frac{\varepsilon_\infty}{c_0^2}\dot{\phi} = \omega_{\mathrm{TO}}\sqrt{\frac{\varepsilon_0/\varepsilon_\infty^2 - 1}{\epsilon_0}}(\nabla \cdot \vec{Q}). \tag{2.65}$$

For simple problems involving uniform polaritonic material, and even for waveguides and resonators, the coupling between scalar and vector equations can be ignored with little loss of accuracy, in which case Eqs. (2.64) and (2.65) reduce to the scalar wave equation. In more complicated non-uniform polaritonic materials such as photonic bandgap materials or scattering elements, the scalar wave equation is not a viable option. The FDTD method

described in chapter 3, and used throughout this thesis, overcomes this difficulty by working directly with Maxwell's equations, rather than the wave equation, which is only approximate in most circumstances considered here.

2.2 Polariton Dispersion

It is easy to verify that solutions to Eqs. (2.50) and (2.51) take the form,

$$E = E_0 e^{i(k\cdot r - \omega t)}, \tag{2.66}$$

$$Q = Q_0 e^{i(k\cdot r - \omega t)}, \tag{2.67}$$

where an arbitrary relative phase may be introduced through either E_0 or Q_0. We address this phase later in section 3.7.1. Eqs. (2.66) and (2.66) satisfy the scalar wave equation if and only if the spatial frequency k, or wavevector as it is usually termed, and the temporal frequency ω are related by the wave propagation speed:

$$\frac{\omega}{k} = \frac{c_0}{n}, \tag{2.68}$$

where n is the index of refraction. Phonon-polaritons become highly dispersive as the transverse optic phonon frequency is approached, and hence the index of refraction is dependent on the frequency. In this case, it is related to the dielectric function, Eq. (2.47):

$$\varepsilon(\omega) = n^2. \tag{2.69}$$

Combining this with Eq. (2.68) using the relation in Eq. (2.69), we find that

$$\varepsilon_\infty \omega^4 - (\omega_{\mathrm{TO}}^2 \varepsilon_0 + c_0^2 k^2)\omega^2 + \omega_{\mathrm{TO}}^2 c_0^2 k^2 = 0, \tag{2.70}$$

where damping has been neglected for simplicity. This fourth order equation can be factored by making the substitution $\omega^2 = \omega'$, to give

$$\omega' = \frac{\omega_{\mathrm{TO}}^2 \varepsilon_0 + c_0^2 k^2}{2\varepsilon_\infty} \pm \frac{1}{2}\sqrt{\left(\frac{c_0^2 k^2 + \omega_{\mathrm{TO}}^2 \varepsilon_0}{\varepsilon_\infty}\right)^2 - \frac{4\omega_{\mathrm{TO}}^2 c_0^2 k^2}{\varepsilon_\infty}}. \tag{2.71}$$

Substituting in $\omega' = \omega^2$ and taking only the positive root, since negative frequencies are non-physical, we arrive at the phonon-polariton dispersion relation,

$$\omega = \sqrt{\frac{\omega_{\mathrm{TO}}^2 \varepsilon_0 + c_0^2 k^2}{2\varepsilon_\infty} \pm \frac{1}{2}\sqrt{\left(\frac{c_0^2 k^2 + \omega_{\mathrm{TO}}^2 \varepsilon_0}{\varepsilon_\infty}\right)^2 - \frac{4\omega_{\mathrm{TO}}^2 c_0^2 k^2}{\varepsilon_\infty}}}. \tag{2.72}$$

The two roots arise due to an avoided crossing between the uncoupled electromagnetic wave dispersion and the phonon dispersion. The positive root corresponds to the upper polariton branch, and the negative root to the lower polariton branch. The two roots of Eq. (2.72) and the relative permittivity associated with polariton dispersion are illustrated in Fig. 2-1(a) and (b), respectively.

At low polariton wavevectors ($\omega << \omega_{\mathrm{TO}}$), the lower branch is "light-like," while the upper branch ($\omega \gtrapprox \omega_{\mathrm{LO}}$) is "phonon-like." Consequently, the coupling of the electromagnetic polariton component is relatively weak for lower branch polaritons and relatively high for upper branch polaritons. The $k \rightarrow 0$ asymptote is $\omega = 0$ for the lower branch and $\omega = \omega_{\mathrm{LO}}$ for the upper branch (this is not a longitudinal oscillation).

The situation reverses as the wavevector increases ($\omega \lessapprox \omega_{\mathrm{TO}}$ for the lower branch and $\omega >> \omega_{\mathrm{LO}}$). As the frequency approaches the TO phonon frequency, the energy density for lower branch polaritons resides increasingly in the mechanical component (phonons), while for the upper branch it is increasingly in the electromagnetic component (photons).

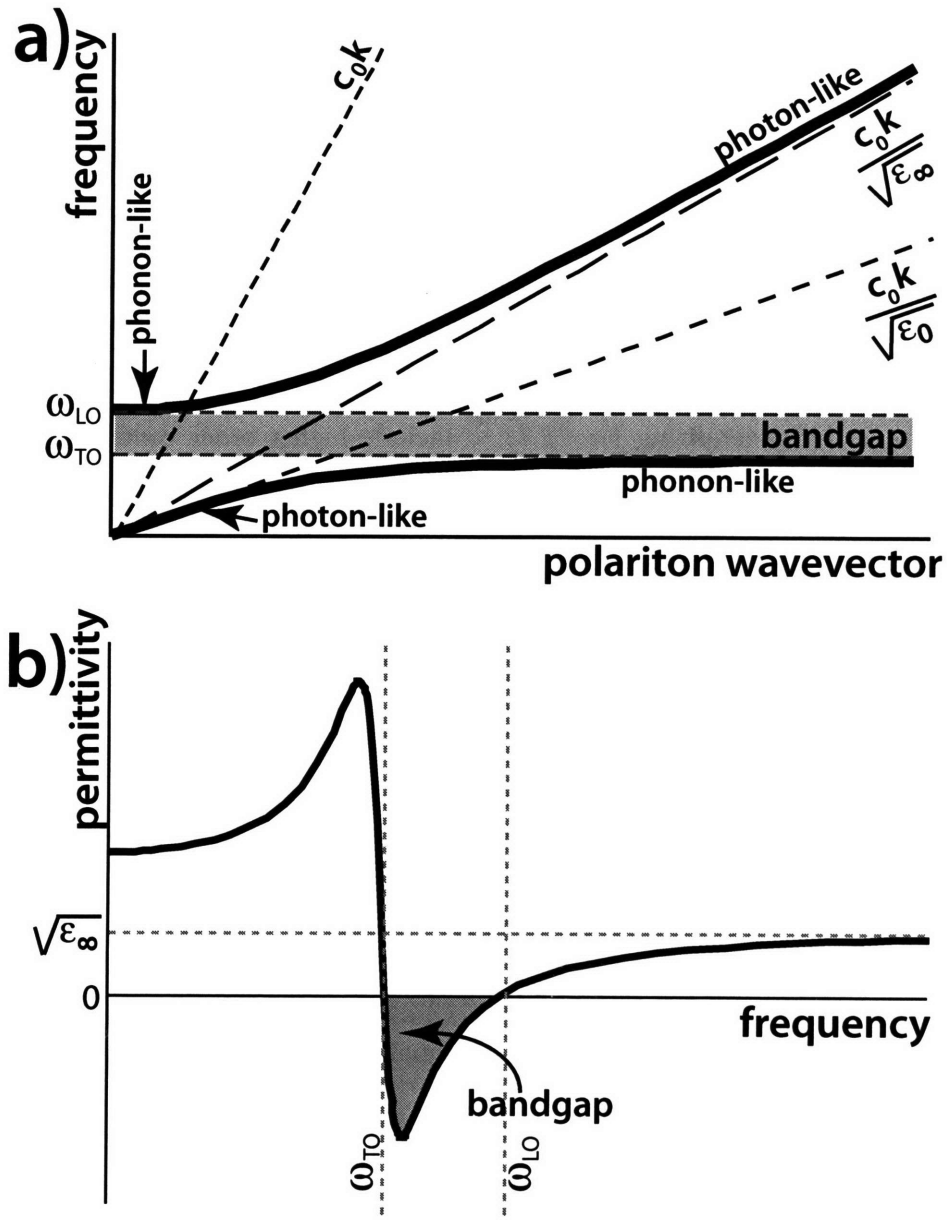

Figure 2-1: a) Dispersion relation characteristic of the polariton regime. A bandgap separates the TO and LO frequencies of the mixed mode excitation (photon+phonon). The lower branch has photon-like dispersion for low wavevectors and phonon-like dispersion for high wavevectors, while the upper branch exhibits the opposite behavior. Also shown are the light line for free space, and light lines for the low and high frequency limits in the crystal. b) Relative permittivity associated with a polariton mode. The bandgap in part a) and b) is shaded in gray.

2.3 Phonon-Polariton Generation

Phonon-polaritons can be generated by simply transmitting far-infrared (FIR) radiation into a ferroelectric crystal externally, but as mentioned in chapter 1, most of the recent work involves polariton generation through nonlinear coherent optical interactions in which the phonon-polaritons are generated directly in the ferroelectric crystal. Since optical fields are of larger frequency than FIR fields, only difference mixing near a phonon-polariton mode is possible ($\omega_1^{\rm FIR} = \omega_3^{\rm opt} - \omega_2^{\rm opt}$).

We begin by generalizing Eq. (2.7) to include higher order contributions to the total macroscopitc polarization:

$$P = \epsilon_0\Big(\chi^{(1)}E(\omega_1) + \chi^{(2)}\mathbb{E}(\omega_2)\cdot\mathbb{E}(\omega_3) + \ldots\Big), \tag{2.73}$$

where $E(\omega_1)$ is a FIR field, and $\mathbb{E}(\omega_2)$ and $\mathbb{E}(\omega_3)$ are optical fields. Just as we divided the polarization into ionic and electronic contributions in Eq. (2.2), we do so again for the nonlinear susceptibility, which can be written as,

$$\chi^{(2)}(\omega) = \chi_\infty^{(2)}(\omega) + \chi_{\rm ion}^{(2)}(\omega), \tag{2.74}$$

where $\chi_\infty^{(2)}$ and $\chi_{\rm ion}^{(2)}$ are the second-order electronic and ionic susceptibilities, respectively. We can then write the coupled scalar wave equations, one for each frequency ω_1, ω_2 and ω_3, as follows [44]:

$$\Big(\nabla^2 + \frac{\omega_3^2 n_3^2}{c_0^2}\Big)\mathbb{E}(\omega_3) = -\frac{\omega_3^2}{c_0^2}\Big(\chi_\infty^{(2)}(\omega_3)E(\omega_1)\mathbb{E}(\omega_2) + \alpha'\mathbb{E}(\omega_2)Q(\omega_1)\Big), \tag{2.75}$$

$$\Big(\nabla^2 + \frac{\omega_2^2 n_2^2}{c_0^2}\Big)\mathbb{E}(\omega_2) = -\frac{\omega_2^2}{c_0^2}\Big(\chi_\infty^{(2)}(\omega_2)\mathbb{E}(\omega_3)E^*(\omega_1) + \alpha'\mathbb{E}(\omega_3)Q^*(\omega_1)\Big), \tag{2.76}$$

$$\Big(\nabla^2 + \frac{\omega_1^2 n_1^2}{c_0^2}\Big)E(\omega_1) = -\frac{\omega_1^2}{c_0^2}\Big(\chi_\infty^{(2)}(\omega_1)\mathbb{E}(\omega_3)\mathbb{E}^*(\omega_2) + \frac{b_{21}}{\epsilon_0}Q(\omega_1)\Big), \tag{2.77}$$

and

$$\Big(\omega_{\rm TO}^2 - \omega_1^2 - i\omega_1\Gamma\Big)Q(\omega_1) = b_{12}E(\omega_1) + \alpha'\mathbb{E}(\omega_3)\mathbb{E}^*(\omega_2), \tag{2.78}$$

where $*$ indicates the complex conjugate, α' is a second-order coupling constant, which is yet to be determined, and n_1, n_2, and n_3 are the indices of refraction for frequencies ω_1, ω_2, and ω_3, respectively.

Eliminating $Q(\omega_1)$ in Eqs. (2.75)-(2.77) with Eq. (2.78), we find the following: Equation (2.77) becomes,

$$\left(\nabla^2 + \frac{\omega_1^2}{c_0^2}(1 + \chi^{(1)}(\omega_1))\right)E(\omega_1) = -\frac{\omega_1^2}{c_0^2}\chi(\omega_1 : \omega_3 - \omega_2)\mathbb{E}(\omega_3) \cdot \mathbb{E}^*(\omega_2), \tag{2.79}$$

with

$$\chi^{(2)}(\omega_1 : \omega_3 - \omega_2) = \chi^{(2)}_{\infty}(\omega_1) + \chi^{(2)}_{\text{ion}}(\omega_1), \tag{2.80}$$

and

$$\chi^{(2)}_{\text{ion}}(\omega_1) = \frac{\alpha' b_{12}/\epsilon_0}{\omega_{\text{TO}}^2 - \omega_1^2 - i\omega_1\Gamma}. \tag{2.81}$$

Equation (2.76) becomes,

$$\begin{aligned}\left(\nabla^2 + \frac{\omega_2^2 n_2^2}{c_0^2}\right)\mathbb{E}(\omega_2) &= -\frac{\omega_2^2}{c_0^2}\Big(\chi^{(2)*}(\omega_2 : \omega_3 - \omega_1)\mathbb{E}(\omega_3)E^*(\omega_1) \\ &+ \chi^{(3)*}(\omega_2 : \omega_3, -\omega_3, \omega_2)|\mathbb{E}(\omega_3)|^2\mathbb{E}(\omega_2)\Big),\end{aligned} \tag{2.82}$$

with

$$\chi^{(2)}(\omega_2 : \omega_3 - \omega_1) = \chi^{(2)}_{\infty}(\omega_2) + \chi^{(2)}_{\text{ion}}(\omega_2), \tag{2.83}$$

and

$$\chi^{(3)}(\omega_2 : \omega_3, -\omega_3, \omega_2) = \frac{\alpha'^2/\epsilon_0}{\omega_{\text{TO}}^2 - \omega_1^2 - i\omega_1\Gamma}. \tag{2.84}$$

$\chi^{(3)}$ in Eq. (2.84) is known as the Raman susceptibility, which can be measured from Raman scattering experiments. Equation (2.75) is similar to Eq. (2.82), and repeating it here adds nothing new.

Assuming low conversion efficiency, we can calculate the terahertz intensity generated by

plane waves of frequencies ω_2 and ω_3 propagating in the x direction from the equation,

$$\frac{dE(\omega_1)}{dx} = -\frac{i\omega_1}{2n_1c_0}\chi^{(2)}(\omega_1)\mathbb{E}(\omega_3)\mathbb{E}^*(\omega_2)e^{i\Delta k_x x}, \tag{2.85}$$

where the complex wavevector phase matching condition is,

$$\Delta k_x = \Delta k_x' + i\Delta k_x'', \tag{2.86}$$

$$\Delta k_x' = k_{3x}' - k_{2x}' - k_{1x}', \tag{2.87}$$

$$\Delta k_x'' = k_{3x}'' + k_{2x}'' - k_{1x}''. \tag{2.88}$$

The solution to Eq. (2.85) is similar to that for second harmonic generation, which is well known [11]. The solution is,

$$I(\omega_1, x_l) = \frac{I(\omega_3)I(\omega_2)\omega_1^2}{2n_1n_2n_3\epsilon_0c_0^3}\left(\frac{|\chi^{(2)}(\omega(1))|^2|e^{-\Delta k_x'' x_l} - 1|^2}{(\Delta k_x'')^2}\right), \tag{2.89}$$

where x_l is the interaction length. It is evident above that both phase matching and conversion efficiency are important. We will address the former in chapter 4 and the latter is taken up in chapter 7.

The ionic susceptibility, χ_{ion}, is an order of magnitude larger than the electronic susceptibility, χ_∞, for the experiments in this thesis because the optical excitation light has a central frequency of approximately 374 THz, which is nearer the ionic resonance (7.6 and 6.0 THz in $LiNbO_3$ and $LiTaO_3$, respectively) than any electronic resonances [48]. We can then assume that the electronic polarization is in phase with the optical driving field, and χ_∞ can be assumed to be constant.

It is possible for the second-order ionic and electronic susceptibilities to interfere with each other. Interference will be greatest when the difference frequency, ω_3, is near the ionic resonance. In this case, the ionic polarization will be out of phase with the optical excitation light, and since we are already considering that the electronic polarization is in phase with the excitation light, the two polarizations will be out of phase with each other. However, since

we are assuming that the electronic polarization is small relative to the ionic polarization, then interference effects will be negligible.

When the difference mixing is with electronic states, i.e., a $\chi_{\infty}^{(2)}$ interaction, the second-order generation of terahertz radiation is simply called difference frequency mixing (DFM). When it is with vibrational states. i.e., a $\chi_{\text{ion}}^{(2)}$ interaction, however, generation is called stimulated Raman scattering. In the case of femtosecond optical excitation light, it is called impulsive stimulated Raman scattering (ISRS), where impulsive refers to the fact that the pulse duration is shorter than the period of the phonon-polaritons generated. We discuss ISRS in detail in the next section, where we determine the second-order coupling constant through consideration of the ISRS mechanism.

2.3.1 Impulsive Stimulated Raman Scattering (ISRS)

Assuming the polarization of a dipole oscillator is proportional to an applied optical field and a time dependent molecular polarizability,

$$\alpha(t) = \alpha_0 + \left(\frac{\partial \alpha}{\partial \mathrm{w}}\right)_0 \vec{\mathrm{w}}(t) + ..., \tag{2.90}$$

where α_0 is the permanent polarization experienced at $\vec{\mathrm{w}}(t) = 0$, then the microscopic displacement field can be written as,

$$\vec{d} = \epsilon_0 \vec{e} + \mathbf{p} = \epsilon_0 \Big(1 + \alpha_0 + \left(\frac{\partial \alpha}{\partial \mathrm{w}}\right)_0 \mathrm{w}(t)\Big)\vec{e}(t), \tag{2.91}$$

to second order in the Taylor expansion of molecular polarizability. The microscopic Maxwell equations can then be written for a non-magnetic, charge-free system as,

$$\nabla \times \vec{e} = -\mu_0 \frac{\partial}{\partial t}\vec{h}, \tag{2.92}$$

$$\nabla \times \vec{h} = \epsilon_0 \Big(\frac{\partial \alpha}{\partial \mathrm{w}}\Big)_0 \frac{\partial}{\partial t}[\vec{\mathrm{w}}(t) \cdot \vec{e}(t)], \tag{2.93}$$

where lowercase vectors ($\vec{e}$, $\vec{h}$, $\vec{d}$) are employed to denote these as the microscopic electric, magnetic, and displacement fields, respectively. The electromagnetic potential may then be written using Poynting's theorem,

$$\nabla \cdot (\vec{e} \times \vec{h}) + \frac{\partial}{\partial t}\Big[\frac{1}{2}\mu_0 |\vec{h}(t)|^2\Big] - \frac{\partial}{\partial t}\Big[\frac{1}{2}\epsilon_0 \Big(\frac{\partial \alpha}{\partial \mathrm{w}}\Big)_0 \vec{\mathrm{w}}(t)|\vec{e}(t)|^2\Big] = 0. \tag{2.94}$$

The bracketed terms in Eq. (2.94) are identified as the magnetic (U_h) and electric energy density (U_e), respectively, from the relation $\nabla \cdot S = -[\dot{U}_h + \dot{U}_e]$, which relates the Poynting vector S to the energy densities.

The force is defined as the negative gradient of the potential. Hence, the stimulated Raman force applied by an optical electric field is,

$$f_{\mathrm{ISRS}}(t) = \frac{1}{2}\epsilon_0 \Big(\frac{\partial \alpha}{\partial \mathrm{w}}\Big)|\vec{e}(t)|^2. \tag{2.95}$$

The macroscopic force in an ordered crystal with unit cell volume V and oscillator density $N = 1/V$ in terms of the macroscopic electric field, and the normal mode reduced mass M is,

$$F_{\mathrm{ISRS}}(t) = \frac{1}{2}\epsilon_0 \sqrt{\frac{N}{M}} \Big(\frac{\partial \alpha}{\partial \vec{\mathrm{w}}}\Big)|\vec{\mathbb{E}}(t)|^2. \tag{2.96}$$

Comparing Eq. (2.96) with the driven oscillator in Eq. (2.78), we can discern the second-order coupling coefficient,

$$\alpha' = \frac{1}{2}\epsilon_0 \sqrt{\frac{N}{M}} \Big(\frac{\partial \alpha}{\partial \vec{\mathrm{w}}}\Big). \tag{2.97}$$

2.4 Phonon-Polaritons in $LiNbO_3$ and $LiTaO_3$

$LiNbO_3$ and $LiTaO_3$ are both uniaxial crystals of C_{3v} symmetry, characterized by two ordinary axes that have the same optical properties, and an extraordinary (optic) axis that is

different [12, 38]. The total macroscopic polarization then takes the uniaxial form,

$$\begin{pmatrix} P_1 \\ P_2 \\ P_3 \end{pmatrix} = \begin{pmatrix} \varepsilon_o & 0 & 0 \\ 0 & \varepsilon_o & 0 \\ 0 & 0 & \varepsilon_e \end{pmatrix} \begin{pmatrix} E_1 \\ E_2 \\ E_3 \end{pmatrix}, \tag{2.98}$$

where the permittivities ε_o and ε_e are just the relative permittivities for each axis times the permittivity of free space.

2.4.1 Phonon Modes in $LiNbO_3$ and $LiTaO_3$

Terahertz frequency radiation polarized along either ordinary axis couples to E symmetry Raman and infrared active phonon modes to form phonon-polaritons. If instead, terahertz radiation is polarized along the optic axis, then coupling is with the A_1 symmetry Raman and infrared active phonon mode.

As long as only linear interactions with the terahertz frequency fields are considered, then there is no coupling between phonon modes, as they are normal modes of the crystal, and are orthogonal to each other. In this case, the formalism developed in this chapter can be applied to each individual phonon mode independently, or since these modes are related to the polarization of the radiation fields, Eqs. (2.30)-(2.34) are applied for each polarization—ordinary and extraordinary. Mixed polarizations are dealt with elsewhere [86].

The normal mode vector $\vec{Q}$ for $LiNbO_3$ and $LiTaO_3$ is similar to the general scalar form in Eq. (2.20) except that it has components for displacements along the two ordinary axes and another for the extraordinary axis. It is defined in terms of the positions of the constituent ions:

$$\vec{Q} \equiv \sqrt{NM}\vec{\mathrm{w}}, \tag{2.99}$$

$$\vec{\mathrm{w}} = \vec{\mathrm{w}}^{+} - \vec{\mathrm{w}}^{-} \equiv \left(\sqrt{\frac{\sum m_p (r_{x,p})^2}{M}}\hat{i}, \sqrt{\frac{\sum m_p (r_{y,p})^2}{M}}\hat{j}, \sqrt{\frac{\sum m_p (r_{z,p})^2}{M}}\hat{k}\right). \tag{2.100}$$

The components of $\vec{r}$=($r_x\hat{i}$,$r_y\hat{j}$,$r_z\hat{k}$) are the displacements of each atom in the unit cell from

Crystal	M(amu)	N(m^{-3})
$LiTaO_3$	11.7	$6.307x10^{27}$
$LiNbO_3$	11.4	$6.285x10^{27}$

Table 2.1: Unit cell information for $LiTaO_3$ and $LiNbO_3$. Mass M is from Eq. (2.102). Oscillator density N comes from Eq. (2.101) and crystallographic data [12].

equilibrium along $\hat{x}$, $\hat{y}$, and $\hat{z}$, and p =1, 2, and 3 correspond to the Li, Nb or Ta, and O atoms, respectively.

The oscillator densities, N, for $LiNbO_3$ and $LiTaO_3$ are calculated by considering the inverse of a 10-atom unit cell volume with hexagonal lattice coordinates a and c in a rhombohedral setting,

$$N = \frac{4}{\sqrt{3}} \frac{1}{a^2 c}. \tag{2.101}$$

The A_1 modes oscillate parallel to the c lattice coordinate, and the E modes oscillate along either axis a.

The lattice coordinates are taken from x-ray and neutron scattering data [12, 38]. The oscillator mass, M, is the reduced mass of the unit cell given from the inverse relation,

$$\frac{1}{M} = \sum \frac{1}{m_p}. \tag{2.102}$$

The values for the reduced mass and oscillator density in $LiNbO_3$ and $LiTaO_3$ are given in Table 2.1.

For the sake of simplicity, only the strongest A_1 and E modes are treated. In $LiNbO_3$ and $LiTaO_3$, these correspond to the lowest frequency resonances for each symmetry. The contribution from higher frequency resonances may be accommodated by refining the high frequency permittivity as follows,

$$\varepsilon_\infty = \varepsilon_\infty^{(e)} \prod_{q=2}^{R} \frac{(\omega_{\mathrm{LO}}^2)_q}{(\omega_{\mathrm{TO}}^2)_q}, \tag{2.103}$$

where $\varepsilon_\infty^{(e)}$ is the off-resonance electronic permittivity, R is the total number of phonon

modes in the crystal for a particular polarization, and $q > 1$ corresponds to the $R-1$ higher frequency phonon modes of either A_1 or E symmetry.

2.4.2 Equations of Motion

Though the modes are uncoupled through linear interactions with terahertz frequency fields, they may be excited by mixed polarization optical excitation light, not necessarily polarized along the same axis as the phonon-polaritons generated. We can then write the complete set of equations for the mechanical component of phonon-polaritons and the polarizations induced:

$$\begin{pmatrix} \ddot{Q}_i + \Gamma_i \dot{Q}_i \\ P_i \end{pmatrix} = \begin{pmatrix} b_{i11}(Q_i) & b_{i12} & \alpha'_{il} \\ b_{i21} & b_{i22} & 0 \end{pmatrix} \begin{pmatrix} Q_i \\ E_i \\ \mathbb{E}_j \mathbb{E}_k \end{pmatrix}, \tag{2.104}$$

$$\bar{\bar{\alpha}}' = \begin{pmatrix} \alpha'_{22} & -\alpha'_{22} & 0 & 0 & \alpha'_{31} & -\alpha'_{22} \\ -\alpha'_{22} & \alpha'_{22} & 0 & \alpha'_{31} & 0 & -\alpha'_{22} \\ \alpha'_{31} & \alpha'_{31} & \alpha'_{33} & 0 & 0 & \alpha'_{31} \end{pmatrix}, \tag{2.105}$$

where i, j, and k correspond to the polarizations of the electric fields and polar ionic displacements—the i, j, k=1 and 2 polarizations correspond to the ordinary axes of the crystal in the $\hat{x}$ and $\hat{y}$ directions respectively, and the i, j, k=3 polarization corresponds to the extraordinary (optic) axis in the $\hat{z}$ direction. α' is the tensor form of the second-order coupling coefficient given in Eq. (2.97). The second subscript, l, on the α' tensor is a contracted notation similar to that of the second-order nonlinear susceptibilities [11] and corresponds to the columns, $l = 1...6$, in Eq. (2.105). The polarization subscripts, i, on the b-coefficients correspond to constants related to the normal modes that oscillate in the i direction. For $i = 1, 2$ they are taken from the E symmetry constants, and for $i = 3$, from the A_1 symmetry constants, specified in Table 2.2 for $LiNbO_3$ and $LiTaO_3$.

	ν_{TO}(THz)	γ(THz)	ε_0	ε_∞
$LiTaO_3$(A_1 mode)	6.0	0.84	37.6	7.6
$LiTaO_3$(E mode)	4.3	0.42	41.5	17.4
$LiNbO_3$(A_1 mode)	7.6	0.84	26.0	10.0
$LiNbO_3$(E mode)	4.6	0.51	41.5	19.5

Table 2.2: Phonon frequencies used in simulations. Raman and IR data extracted from data reported by Barker and Louden [6, 5]

2.4.3 Second-Order Coupling Tensor: $\bar{\bar{\alpha}}'$

The form of $\bar{\bar{\alpha}}'$ is identical and proportional to the nonlinear coefficients d_{ijk}, familiar in nonlinear optics [11], where i is the polarization of the induced field and j and k are the polarizations of the excitation fields. The usual contracted notation α'_{il} is employed, where jk=11(l=1); jk=22(l=2); jk=33(l=3); jk=23,32(l=4); jk=13,31(l=5), and jk=12,21(l=6). The values for the differential polarizabilities may be calculated directly from the second-order nonlinear optical susceptibilities for $LiNbO_3$ and $LiTaO_3$. The tensor components of $\bar{\bar{\alpha}}'$ are,

$$\alpha'_{i,l} = \frac{1}{2}\sqrt{\frac{N}{M}}\epsilon_0\left(\frac{\partial\alpha}{\partial \mathrm{w}}\right)_{il}. \tag{2.106}$$

To determine the differential polarizabilities, we consider the ionic contribution to the polarization in Eq. (2.104), $P_i = b_{i12}Q_i$. Using plane wave solutions, Eqs. (2.66) and (2.67), it can be shown that,

$$P_i = \epsilon_0\frac{\omega_{TO}^2(\varepsilon_0-\varepsilon_\infty)}{\omega_{TO}^2-\omega^2+i\omega\Gamma}E_i + \epsilon_0\frac{\frac{1}{2}\omega_{TO}\sqrt{\epsilon_0(\varepsilon_0-\varepsilon_\infty)}\sqrt{\frac{N}{M}}\left(\frac{\partial\alpha}{\partial \mathrm{w}}\right)_{il}}{\omega_{TO}^2-\omega^2+i\omega\Gamma}\mathbb{E}_j\mathbb{E}_k, \tag{2.107}$$

where ω_{TO}, ε_0, ε_∞, and Γ are associated with the phonon normal mode polarized along i. Comparison of Eq. (2.107) with Eq. (2.73) reveals that the linear and second-order ionic

	$\left(\frac{\partial\alpha}{\partial w}\right)_{33}(\mathrm{m}^2)$	$\left(\frac{\partial\alpha}{\partial w}\right)_{13}(\mathrm{m}^2)$	$\left(\frac{\partial\alpha}{\partial w}\right)_{22}(\mathrm{m}^2)$
$LiTaO_3$	$4.42\text{x}10^{-19}$	$5.65\text{x}10^{-20}$	$2.73\text{x}10^{-20}$
$LiNbO_3$	$1.14\text{x}10^{-18}$	$8.43\text{x}10^{-20}$	$4.46\text{x}10^{-20}$

Table 2.3: Differential polarizability calculated from Eq. (2.110). Second order susceptibilities for $LiNbO_3$ are from Boyd [11], and $LiTaO_3$ from the Handbook of Nonlinear Optical Crystals [22]

susceptibilities can be written as,

$$\chi_{ii}^{(1)} = \frac{\omega_{TO}^2(\varepsilon_0-\varepsilon_\infty)}{\omega_{TO}^2-\omega^2+i\omega\Gamma}, \tag{2.108}$$

$$\chi_{il}^{(2)} = \frac{\frac{1}{2}\omega_{TO}\sqrt{\epsilon_0(\varepsilon_0-\varepsilon_\infty)}\sqrt{\frac{N}{M}}\left(\frac{\partial\alpha}{\partial \mathrm{w}}\right)_{il}}{\omega_{TO}^2-\omega^2+i\omega\Gamma}. \tag{2.109}$$

These susceptibilities include the frequency dependence of the susceptibilities. However, since we include these terms in the driven oscillator equation of Eq. (2.104), which can oscillate phase shifted to the radiation field, we can use frequency independent terms in our model without explicitly accounting for the frequency dependence. The values for the differential polarizabilities can be determined from the second-order nonlinear optical susceptibilities. Recognizing that $d_{ijk}=\frac{1}{2}\chi_{ijk}^{(2)}$, they are determined as follows,

$$\left(\frac{\partial\alpha}{\partial \mathrm{w}}\right)_{il} = 4\omega_{TO}\sqrt{\frac{M}{\epsilon_0(\varepsilon_0-\varepsilon_\infty)N}}d_{il}. \tag{2.110}$$

From the second-order nonlinear optical susceptibility tensor d_{il}, the nonlinear driving terms influence ion motion as follows,

$$\ddot{Q}_1 \propto d_{22}\Big(|\mathbb{E}_1|^2-|\mathbb{E}_2|^2-|\mathbb{E}_1\mathbb{E}_2|\Big)+d_{31}|\mathbb{E}_1\mathbb{E}_3|, \tag{2.111}$$

$$\ddot{Q}_2 \propto d_{22}\Big(-|\mathbb{E}_1|^2+|\mathbb{E}_2|^2-|\mathbb{E}_1\mathbb{E}_2|\Big)+d_{31}|\mathbb{E}_2\mathbb{E}_3|, \tag{2.112}$$

$$\ddot{Q}_3 \propto d_{31}\Big(|\mathbb{E}_1|^2+|\mathbb{E}_2|^2+|\mathbb{E}_1\mathbb{E}_2|\Big)+d_{33}|\mathbb{E}_3|^2, \tag{2.113}$$

where the last terms terms in Eqs. (2.111) and (2.112) are due to Kleinman symmetry, which is valid only for lossless susceptibilities. However, since loss and phase are accounted for in $\vec{Q}$, the resulting susceptibility is still valid. The values for the differential polarizabilities may be determined by considering the limit that $\omega \rightarrow 0$ in Eq. (2.110). Using the values for the second-order nonlinear optical susceptibilities [48, 22], the differential polarizabilities used in $\bar{\bar{\alpha}}'$ are tabulated in Table 2.3.

Chapter 3

Finite-Difference-Time-Domain (FDTD) Simulations of Phonon-Polariton Generation, Propagation, and Detection

This work was done in collaboration with Eric Statz and Nikolay Stoyanov of the Massachusetts Institute of Technology.

Analytic solutions to the equations governing phonon-polariton propagation in chapter 2 can be obtained only in limited cases. Of more practical concern are solutions that account for anharmonicity, phonon mode coupling, nonlinear generation through impulsive stimulated Raman scattering (ISRS) and difference frequency mixing (DFM), and propagation in non-uniform ferroelectric materials like the patterned materials of chapter 7. These solutions, however, require a computational approach.

As a result of ever-increasing computational power, the finite-difference-time-domain (FDTD) method has become a popular tool to simulate propagation of electromagnetic radiation through arbitrary media [110, 87, 113, 112, 53]. The accuracy of FDTD and the

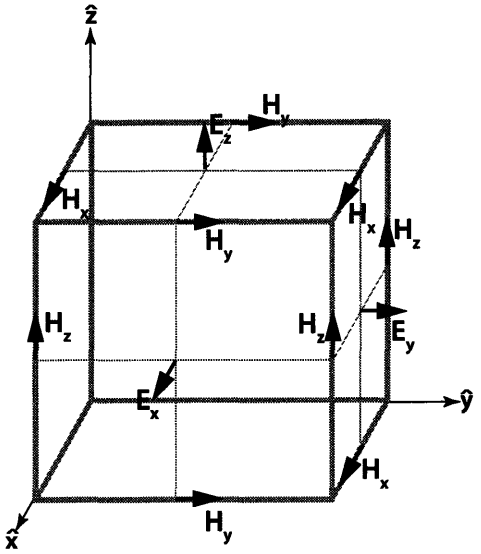

Figure 3-1: Positions of the electric and magnetic field components in a Yee cell. When Maxwell's equations are evaluated in difference equation form, staggering is necessary to satisfy the divergence requirements $\nabla \cdot \vec{D} = 0$ and $\nabla \cdot \vec{B} = 0$. In polaritonic FDTD simulations, the mechanical field components Q_x, Q_y, and Q_z are in the same locations as the electric field components.

ease with which it is parallelized make it even more attractive for larger, more realistic simulations [64, 72, 89]. However, most applications are in the engineering sciences with few major applications in problems of a purely scientific nature—though there are exceptions [8].

The FDTD simulations developed here are based on the method developed by Yee [110], which involves staggering of the mesh grid for the electric and magnetic fields to satisfy Maxwell's electrostatic divergence equation (See Fig. 3-1). In brief, the algorithm starts from an initial condition for either the electric or magnetic field, and discrete forms of Eqs. (2.24) and (2.25) are evaluated iteratively a sufficient number of times to accommodate the desired propagation time to be simulated. Polariton dispersion is included through an auxiliary parameter manifest in the displacement field $\vec{D}$. This method is similar to other methods in which the free charge is used as an auxiliary parameter [113]. In our case, the auxiliary parameter is the ionic displacement associated with a polar optic phonon normal mode, and can be related in a convenient way to the phonon potential energy function, giving it an intuitive physical explanation. Though other methods of including dispersion in FDTD are

available [53, 112, 87], the implementation used here is physically more intuitive and robust, relying on fewer approximations and capable of nonlinear as well as linear dispersion.

In this chapter, phonon-polariton generation, propagation, and probing in ferroelectric $LiNbO_3$ and $LiTaO_3$ crystals are simulated with a novel implementation of the FDTD method, which is modified to account for polariton dispersion, lattice anharmonicty, and generation by ISRS and DFM. Results are compared with theoretical results from chapter 2. Later, in chapters 4, 5, and 7, simulations are compared with time-resolved measurements of phonon-polaritons generated through ISRS.

3.1 FDTD in One Spatial Dimension

To illustrate the method, we consider a one-dimensional implementation with an analytically specified ISRS optical driving field of the form in Eq. (2.96). If we choose the polarization of the excitation pulses and polaritons to be along $\hat{x}$ and the direction of propagation to be $\hat{z}$, then it follows that the magnetic field is polarized along $\hat{y}$. To discretize the equations of propagation, central difference approximations are taken for the derivatives of time and space. Temporal steps are indexed by the integer g and related to continuous time by the relation $t = g\Delta t$. Spatial steps are indexed by the integer m and related to continuous space by the relation $z = m\Delta z$. The temporal discretization method using central differences can then be written as

$$\frac{\partial f(z,t)}{\partial t} \longrightarrow \frac{\Delta f}{\Delta t} \equiv \frac{f(z,g+1/2) - f(z,g-1/2)}{\Delta t}, \tag{3.1}$$

and spatial discretization as,

$$\frac{\partial f(z,t)}{\partial z} \longrightarrow \frac{\Delta f}{\Delta z} \equiv \frac{f(m+1/2,t) - f(m-1/2,t)}{\Delta z}. \tag{3.2}$$

A consequence of the spatial interleaving required in the Yee cell is that the fields must also be interleaved in time, known as "leapfrog", since the temporal response of one field is

proportional to the spatial variation of the other at the previous time step. Implementing Eqs. (2.24), (2.25) and (2.104) as indicated in Eqs. (3.1) and (3.2), and interleaving spatially and temporally yields the difference equation form of Maxwell's equations:

$$\frac{Q_x(m)^{g+\frac{1}{2}} - Q_x(m)^{g-\frac{1}{2}}}{\Delta t} = \dot{Q}_x(m)^{g-\frac{1}{2}} \tag{3.3}$$

$$\frac{\dot{Q}_x(m)^{g+\frac{1}{2}} - \dot{Q}_x(m)^{g-\frac{1}{2}}}{\Delta t} = \tag{3.4}$$
$$-\Gamma_x \dot{Q}_x(m)^{g-\frac{1}{2}} + b_{111} Q_x(m)^{g-\frac{1}{2}} + b_{112} E_x^{g-\frac{1}{2}}(m) + F_{\text{ISRS}}$$

$$\frac{E_x^{g+\frac{1}{2}}(m) - E_x^{g-\frac{1}{2}}(m)}{\Delta t} = \tag{3.5}$$
$$-\frac{H_y^g(m+\frac{1}{2}) - H_y^g(m-\frac{1}{2})}{\epsilon_0 \Delta z} - \frac{b_{121}}{\epsilon_0 + b_{122}} \dot{Q}_x(m)^{g-\frac{1}{2}},$$

$$\frac{H_y^{g+1}(m+\frac{1}{2}) - H_y^g(m+\frac{1}{2})}{\Delta t} = -\frac{E_x^{g+\frac{1}{2}}(m+1) - E_x^{g+\frac{1}{2}}(m)}{\mu_0 \Delta z}, \tag{3.6}$$

where F_{ISRS} is analytically specified by Eq. (2.96) and the second order differential equation in Eq. (2.104) has been separated into two first order differential equations in the variable Q and $\dot{Q}$.

At a given position in space, the fields at each time step can be calculated from their values at the previous time step. Solving for the fields at the latest time step in Eqs. (3.3)-(3.6) yields,

$$Q_x(m)^{g+\frac{1}{2}} = Q_x(m)^{g-\frac{1}{2}} + \Delta t \dot{Q}_x(m)^{g-\frac{1}{2}} \tag{3.7}$$

$$\dot{Q}_x(m)^{g+\frac{1}{2}} = \tag{3.8}$$
$$(1 - \Delta t \Gamma_x) \dot{Q}_x(m)^{g-\frac{1}{2}} + \Delta t (b_{111} Q_x(m)^{g-\frac{1}{2}} + b_{112} E_x^{g-\frac{1}{2}}(m) + F_{\text{ISRS}})$$

$$E_x^{g+\frac{1}{2}}(m) = \tag{3.9}$$
$$E_x^{g-\frac{1}{2}}(m) - \frac{\Delta t}{\epsilon_0 \Delta z}\Big(H_y^g(m+\frac{1}{2}) - H_y^g(m-\frac{1}{2})\Big) - \frac{\Delta t b_{121}}{\epsilon_0 + b_{122}} \dot{Q}_x(m)^{g-\frac{1}{2}},$$

$$H_y^{g+1}(m+\frac{1}{2}) = H_y^g(m+\frac{1}{2}) - \frac{\Delta t}{\mu_0 \Delta z}\Big(E_x^{g+\frac{1}{2}}(m+1) - E_x^{g+\frac{1}{2}}(m)\Big). \tag{3.10}$$

In this fashion, known as Euler forward, the solution of Maxwell's equations proceeds

in much the same way that we envision electromagnetic wave propagation—an electric field induces a magnetic field, which induces an electric field, ad infinitum. The time step and grid size parameters are chosen based on the highest frequency and shortest wavelength propagating waves in the simulation. For stability, the general rule is that at least ten grid points sum to less than the smallest wavelength $\lambda_{\min}$ considered, and the Courant condition then determines the time step [87]:

$$\Delta z \leq \frac{\lambda_{\min}}{10}, \tag{3.11}$$

$$\Delta t \leq \frac{\Delta z}{2c_0}. \tag{3.12}$$

The computer algorithm based on Eqs. (3.7)-(3.10) requires four one-dimensional arrays to be allocated in memory, one for each variable (Q_x, $\dot{Q}_x$, E_x, and H_y). The amount of memory required is then the number of field components to be evaluated times the problem space size, where a problem space of size $\mathbb{M}$ corresponds to the discretized spatial extent to be simulated. After specifying the initial condition, with the analytic driving term F_{ISRS}, each time step is calculated with the following algorithm:

$$\begin{aligned}
Q_x[m] &= Q_x[m] + \Delta t \dot{Q}_x[m] \\
\dot{Q}_x[m] &= (1 - \Delta t \Gamma_x)\dot{Q}_x[m] + \Delta t(b_{111}Q_x[m] + b_{112}E_x[m] + F_{\text{ISRS}}) \\
E_x[m] &= E_x[m] + \frac{\Delta t}{\epsilon_0 \Delta z}\Big(H_y[m-1] - H_y[m]\Big) - \frac{\Delta t b_{121}}{\epsilon_0 + b_{122}}\dot{Q}_x[m] \\
t &= t_0 + g\frac{\Delta t}{2} \\
H_y[m] &= H_y[m] + \frac{1}{2}\Big(E_x[m] - E_x[m+1]\Big) \\
t &= t_0 + g\frac{\Delta t}{2}
\end{aligned} \tag{3.13}$$

The algorithm above is repeated for the desired number of time steps. Note that iteration of Eq. (3.13) results in an implicit time formulation, i.e., time is not made explicit in the equations for the fields and appears in the algorithm above only for bookkeeping purposes.

3.2 FDTD in Two Spatial Dimensions

Two-dimensional simulations are computationally more expensive than the one-dimensional simulation from the previous section because the problem space becomes $\mathbb{M} \times \mathbb{N}$, or the area, rather than just the length. In a two-dimensional problem space, there are two modes that may be considered: the transverse electric (TE) and transverse magnetic (TM) modes. In the TM mode for a plane defined by the spatial dimensions x and y, the electric and mechanical fields have a single polarization component along the z direction, and the magnetic field has two polarization components, one along x and the other along y. In the TE mode for the same plane, the magnetic field has a single polarization component along the z direction and the electric and mechanical fields have two polarization components, one along x and one along y.

The FDTD algorithm in two dimensions is similar to the one-dimensional implementation. The field equations, given below, are evaluated in a fashion similar to that in Eq. (3.13). Since there are two dimensions now, the subscripts m and n refer to the $\hat{x}$ and $\hat{y}$ directions, respectively.

The two- and three-dimensional simulations employed in this thesis use perfectly matched layer (PML) boundary conditions to truncate an infinite problem space to one of manageable size [87]. This method is based on the physical notion of index matching in optics. Near the edges of the problem space, a gradient of increasing loss is encountered, resulting in drastically reduced reflections over that of perfect electric or perfect magnetic boundary conditions. The PML boundary conditions are not present in the field equations in this chapter, which are provided for illustration only, but they are included in the sample code contained in the appendices.

TM Mode

The simulated field solutions at any moment in time for the TM mode, with respect to z, are characterized by the quintuple $(E_z, Q_z, \dot{Q}_z, H_x, H_y)$. The five field equations to be evaluated

are given below.

$$
\begin{aligned}
Q_z[m,n] &= Q_z[m,n] + \Delta t \dot{Q}_z[m,n] \\
\dot{Q}_z[m,n] &= (1 - \Gamma_z \Delta t)\dot{Q}_z[m,n] + \Delta t\Big(b_{311}Q_z[m,n] + b_{312}E_z[m,n]\Big) + F_{\text{ISRS}} \cdot \hat{z} \\
E_z[m,n] &= E_z[m,n] + \frac{\Delta t}{(\epsilon_0 + b_{322})\Delta x}\Big(H_y[m,n] - H_y[m-1,n]\Big) \\
&\quad + \frac{\Delta t}{(\epsilon_0 + b_{322})\Delta y}\Big(H_x[m,n-1] - H_x[m,n]\Big) - \frac{\Delta t}{(\epsilon_0 + b_{322})}\dot{Q}_z[m,n] \\
H_x[m,n] &= H_x[m,n] + \frac{\Delta t}{\mu_0 \Delta y}\Big(E_z[m,n] - E_z[m,n+1]\Big) \\
H_y[m,n] &= H_y[m,n] + \frac{\Delta t}{\mu_0 \Delta x}\Big(E_z[m+1,n] - E_z[m,n]\Big)
\end{aligned}
\tag{3.14}
$$

TE Mode

The simulated field solutions at any moment in time for the TE mode, with respect to z, are characterized by the septuple $(H_z, E_x, E_y, Q_x, Q_y, \dot{Q}_x, \dot{Q}_y)$. Since the ISRS excitation beam may now be polarized along $\hat{x}$ or $\hat{y}$, it is projected onto each axis. The seven field equations to be evaluated are given below.

$$
\begin{aligned}
Q_x[m,n] &= Q_x[m,n] + \Delta t \dot{Q}_x[m,n] \\
Q_y[m,n] &= Q_y[m,n] + \Delta t \dot{Q}_y[m,n] \\
\dot{Q}_x[m,n] &= (1 - \Gamma_x \Delta t)\dot{Q}_x[m,n] + \Delta t\Big(b_{111}Q_x[m,n] + b_{112}E_x[m,n]\Big) + F_{\text{ISRS}} \cdot \hat{x} \\
\dot{Q}_y[m,n] &= (1 - \Gamma_y \Delta t)\dot{Q}_y[m,n] + \Delta t\Big(b_{211}Q_y[m,n] + b_{212}E_y[m,n]\Big) + F_{\text{ISRS}} \cdot \hat{y} \\
E_x[m,n] &= E_x[m,n] + \frac{\Delta t}{(\epsilon_0 + b_{122})\Delta y}\Big(H_z[m,n] - H_z[m,n-1]\Big) \\
&\quad - \frac{\Delta t}{(\epsilon_0 + b_{122})}\dot{Q}_x[m,n]
\end{aligned}
\tag{3.15}
$$

$$
\begin{aligned}
E_y[m,n] &= E_y[m,n] + \frac{\Delta t}{(\epsilon_0 + b_{222})\Delta x}\Big(H_z[m-1,n] - H_z[m,n]\Big) \\
&\quad - \frac{\Delta t}{(\epsilon_0 + b_{222})}\dot{Q}_y[m,n] \\
H_z[m,n] &= H_z[m,n] + \frac{\Delta t}{\mu_0 \Delta x}\Big(E_y[m,n] - E_y[m+1,n]\Big) \\
&\quad + \frac{\Delta t}{\mu_0 \Delta y}\Big(E_x[m,n+1] - E_x[m,n]\Big)
\end{aligned}
$$

3.3 FDTD in Three Spatial Dimensions

Though most of the experiments simulated in this thesis are amenable to one- and two-dimensional simulations, sometimes a three-dimensional simulation is required. The one- and two-dimensional reductions, however, are preferable if the simulation geometry allows for it. For example, if the field along any single dimension has little spatial variation, then a two-dimensional simulation can be employed. Similarly, if spatial variation along two dimensions is minimal, then a one-dimensional simulation may be used with little loss of information and accuracy.

Three-dimensional FDTD simulations are the most general, and the one- and two-dimensional simulations discussed above are merely a reduction from the three-dimensional case. Three-dimensional FDTD is also the most computationally expensive, comprising an $\mathbb{M} \times \mathbb{N} \times \mathbb{O}$ problem space, and requiring the duodecuple (Q_x, Q_y, Q_z, $\dot{Q}_x$, $\dot{Q}_y$, $\dot{Q}_z$, E_x, E_y, E_z, H_x, H_y, H_z) to characterize the fields at any moment in time.

Just as was the case in two dimensions, the three-dimensional algorithm is identical except for the number of field equations to be evaluated and the number of terms in each equation. The field equations for a three-dimensional simulation are given below. The three

spatial dimensions along $\hat{x}$, $\hat{y}$, and $\hat{z}$ are denoted by the letters m, n, and o, respectively.

$$
\begin{aligned}
Q_x[m,n,o] &= Q_x[m,n,o] + \Delta t \dot{Q}_x[m,n,o] \\
Q_y[m,n,o] &= Q_y[m,n,o] + \Delta t \dot{Q}_y[m,n,o] \\
Q_z[m,n,o] &= Q_z[m,n,o] + \Delta t \dot{Q}_z[m,n,o] \\
\dot{Q}_x[m,n,o] &= (1-\Gamma_x \Delta t)\dot{Q}_x[m,n,o] + \Delta t\Big(b_{111}Q_x[m,n,o] + b_{112}E_x[m,n,o]\Big) + F_{\text{ISRS}} \cdot \hat{x} \\
\dot{Q}_y[m,n,o] &= (1-\Gamma_y \Delta t)\dot{Q}_y[m,n,o] + \Delta t\Big(b_{211}Q_y[m,n,o] + b_{212}E_y[m,n,o]\Big) + F_{\text{ISRS}} \cdot \hat{y} \\
\dot{Q}_z[m,n,o] &= (1-\Gamma_z \Delta t)\dot{Q}_z[m,n,o] + \Delta t\Big(b_{311}Q_z[m,n,o] + b_{312}E_z[m,n,o]\Big) + F_{\text{ISRS}} \cdot \hat{z}
\end{aligned}
$$

$$
\begin{aligned}
E_x[m,n,o] &= E_x[m,n,o] + \frac{\Delta t}{(\epsilon_0 + b_{122})\Delta y}\Big(H_z[m,n,o] - H_z[m,n-1,o]\Big) \\
&\quad + \frac{\Delta t}{(\epsilon_0 + b_{122})\Delta z}\Big(H_y[m,n,o-1] - H_y[m,n,o]\Big) - \frac{\Delta t}{(\epsilon_0 + b_{122})}\dot{Q}_x[m,n,o] \\
E_y[m,n,o] &= E_y[m,n,o] + \frac{\Delta t}{(\epsilon_0 + b_{222})\Delta x}\Big(H_z[m-1,n,o] - H_z[m,n,o]\Big) \\
&\quad + \frac{\Delta t}{(\epsilon_0 + b_{222})\Delta z}\Big(H_x[m,n,o] - H_x[m,n,o-1]\Big) - \frac{\Delta t}{(\epsilon_0 + b_{222})}\dot{Q}_y[m,n,o] \\
E_z[m,n,o] &= E_z[m,n,o] + \frac{\Delta t}{(\epsilon_0 + b_{322})\Delta x}\Big(H_y[m,n,o] - H_y[m-1,n,o]\Big) \\
&\quad + \frac{\Delta t}{(\epsilon_0 + b_{322})\Delta y}\Big(H_x[m,n-1,o] - H_x[m,n,o]\Big) - \frac{\Delta t}{(\epsilon_0 + b_{322})}\dot{Q}_z[m,n,o] \\
H_x[m,n,o] &= H_x[m,n,o] + \frac{\Delta t}{\mu_0 \Delta z}\Big(E_y[m,n,o+1] - E_y[m,n,o]\Big) \\
&\quad + \frac{\Delta t}{\mu_0 \Delta y}\Big(E_z[m,n,o] - E_z[m,n+1,o]\Big) \\
H_y[m,n,o] &= H_y[m,n,o] + \frac{\Delta t}{\mu_0 \Delta x}\Big(E_z[m+1,n,o] - E_z[m,n,o]\Big) \\
&\quad + \frac{\Delta t}{\mu_0 \Delta z}\Big(E_x[m,n,o] - E_x[m,n,o+1]\Big) \\
H_z[m,n,o] &= H_z[m,n,o] + \frac{\Delta t}{\mu_0 \Delta x}\Big(E_y[m,n,o] - E_y[m+1,n,o]\Big) \\
&\quad + \frac{\Delta t}{\mu_0 \Delta y}\Big(E_x[m,n+1,o] - E_x[m,n,o]\Big)
\end{aligned}
\tag{3.16}
$$

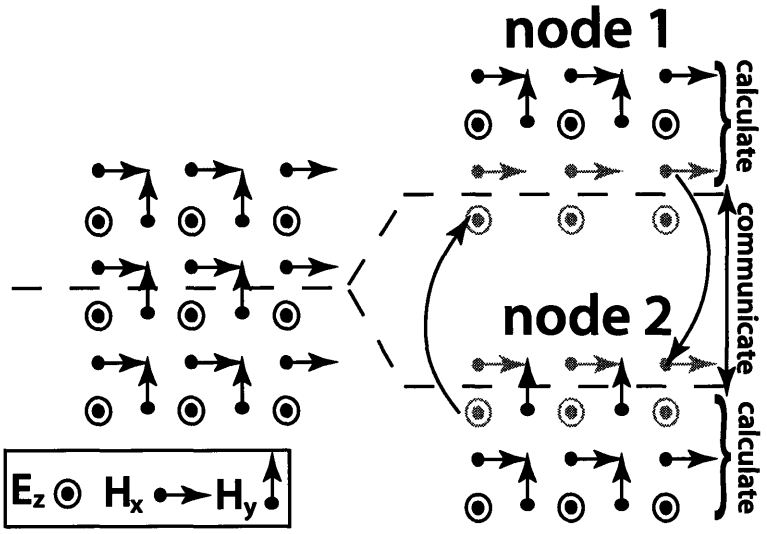

Figure 3-2: Parallelization of a two-dimensional TM problem space. The un-split problem space, as it would be for serial computation, is shown on the left, and the split problem space, as it would be for parallel computation, is shown on the right. Interprocess communication is limited to fields at the edge of the problem space, making FDTD "embarrassingly" parallelizable. In the figure, node 1 calculates H_x and receives E_z from node 2, while node 2 calculates E_z and is communicated the values for H_x from node 1.

3.4 Parallelization of the FDTD Algorithm

Since many of the applications of Eqs. (3.13)-(3.16) require problem spaces larger than that afforded by a single computer, the simulations are parallelized by distributing equal portions of the problem space over the nodes of a Beowulf computer cluster. In the simple 1D case, parallelization is trivial, as both E_x, Q_x, and H_y at the beginning and end of the distributed problem space are passed between nodes. The procedure for two-dimensional simulation is more illustrative of the general technique and more easily depicted than the three-dimensional case.

Figure (3-2) illustrates parallelization in two dimensions. Parallelization of the FDTD simulations onto $\mathbb{A}$ nodes is done by subdividing the problem space along one of the spatial axes into $\mathbb{A}$ equal segments. Each node calculates E, Q, $\dot{Q}$, and H in the same way as for a serial simulation, passing the values of E and H along the boundary to the neighboring

segments. Since the Yee cell has an offset E and H grid, only one field needs to be passed in each direction; E fields are passed to subdivisions of greater y, H to subdivisions of smaller y. Each field is passed once per simulation time step. Note that since Q and $\dot{Q}$ are coupled spatially only through the radiation field, no modifications are required for parallelization of the auxiliary parameter. Computation time for parallelized FDTD is linear in the number of cluster nodes. The Beowulf cluster used in this work is composed of 12 dual processor Athlon MP machines, networked via 100-baseT ethernet interconnects. Each processor has 1.5 GB of RAM.

3.5 FDTD in Patterned Materials

Polariton propagation through patterned materials may be performed by specifying the material parameters at each point in the problem space. This is accomplished by loading an array into memory, with the same dimensions as the simulation problem space, the contents of which specify the material type at each spatial position. This array may be generated externally, saved as a file, and read into memory at the beginning of the FDTD simulations. Accurate reflection, transmission, refraction, and diffraction from material specified features are inherent to the algorithm, requiring no further modelling. The structures simulated correspond to actual structures fabricated by femtosecond laser machining, and are presented in chapter 7.

Irregularly shaped structures and diagonal interfaces sometimes result in errors that grow uncontrollably in the FDTD simulations. If present, these errors are amplified and propagated by the algorithm, resulting in large divergences that corrupt the simulation, i.e., the simulation blows up. For example, simulations of tip-shaped structures encounter these problems when the tip angle exceeds 30 degrees. The simplest remedy is to decrease the spatial grid point size until the problem abates. This can be computationally costly, so alternatives to this are desirable. In some cases, material averaging is sufficient. For example, if the problem is at an interface with a dielectric contrast of 5 to 1, then simply inserting an intermediate layer with a dielectric constant of 3 may ameliorate the problem.

Lastly, non-orthogonal grids that better conform to the structure shape may be used, as described in detail elsewhere [87].

3.6 Simulated Polariton Imaging

Probing by polariton imaging or interferometry is also simulated in the FDTD algorithm, but has no effect on the propagating fields as it is manifest through post-processing at the end of each time step and effects only the output data.

For illustration purposes, probing of the normal mode along Q_z is considered. The magnitude of the ionic displacement can be related to a phase shift introduced into an optical probe through the time dependent index of refraction n,

$$\begin{aligned} n(t) &= n_0 + \Delta n, \\ &= \sqrt{1 + N\alpha_0 + \sqrt{\frac{N}{M}}\left(\frac{\partial \alpha}{\partial \mathrm{w}}\right)_{33} Q_z(t)}, \end{aligned} \tag{3.17}$$

where α_0 is the molecular polarizability with internuclear coordinates fixed to the equilibrium value, and the polarization components of $\left(\frac{\partial \alpha}{\partial \mathrm{w}}\right)_{33}$ indicate that two excitation pulses polarized along the z-direction generate a second-order polarization also along z, as explained in chapter 2.

If we assume an optical probe propagating in the $\hat{x}$ direction with polarization along $\hat{z}$ of the form $E_z(x,y,z,t) = E_0(y,z,t)e^{i\omega(t-x/c_0)}\hat{z}$, and that $n(t)$ from phonon-polaritons is small, then the field detected at time t can be written as,

$$E_z(x,y,z,t) \approx E_0(y,z,t)e^{i\omega(t-x/c_0)}\hat{z} - i\frac{\omega}{c_0}E_0(y,z,t)d(n(t)-1)e^{i\omega(t-x/c_0)}\hat{z}, \tag{3.18}$$

where d is the crystal thickness through which the probe propagated. Using experimental methods of phase-to-amplitude conversion, the phase term (the last term in Eq. (3.18)) is

converted to an amplitude such that the probe signal becomes,

$$I_{\text{probe}}(y,z,t) \propto \sqrt{\frac{N}{M}} d^2 \left(\frac{\partial \alpha}{\partial \text{w}}\right)_{33} Q_z(t). \tag{3.19}$$

Because of the linear relationship between phase shift and Q_3, merely summing the values of Q_z from the simulation can yield an effective phase shift for the simulated probe beam. For a simulation of dimension $\mathbb{M}$, probing in direction $\hat{x}$, an array of dimension $\mathbb{M}$ is generated, with the coordinate of x replaced with a time coordinate $t = cx$. The magnitude of t, $t_{\max}$, is equal to the longest temporal period that probe light will remain within the simulation region, in units of Δt. At each time step, the array has a subarray of dimension $\mathbb{M} - 1$ inserted at $t = 0$, and the rest of the array is pushed along t by one index. The subarray with $t = t_{\max}$ is output as the ionic displacement, and removed from the array. Each value in the array is then incremented by the corresponding values in the $\mathbb{M}$-dimensional Q array, with the x coordinate chosen using a lookup table that converts the optical delay given by t to one or more indices in dimension $\hat{x}$.

Upon output, the summed ionic displacements are converted into signal intensity through Eq. (3.19), which is convolved with the probe envelope $I_0(t,z)$ to yield an $(\mathbb{M}-1)$ dimensional probe output vector at each time step Δt. For variations in Q_z, which have characteristic lengths much greater than the pulse width, the probe pulse can be approximated as a delta function, eliminating the convolution.

3.7 Simulation Results

In this section, the FDTD method developed in this chapter is shown to exhibit the correct behavior appropriate to the polariton regime, including polariton dispersion, field retardation, and a polaritonic bandgap. Comparison is made with theory from chapter 2. Two- and three-dimensional simulation results are also shown for illustrative purposes. Simulation parameters are taken from the values tabulated in chapter 2 and reported elsewhere [5].

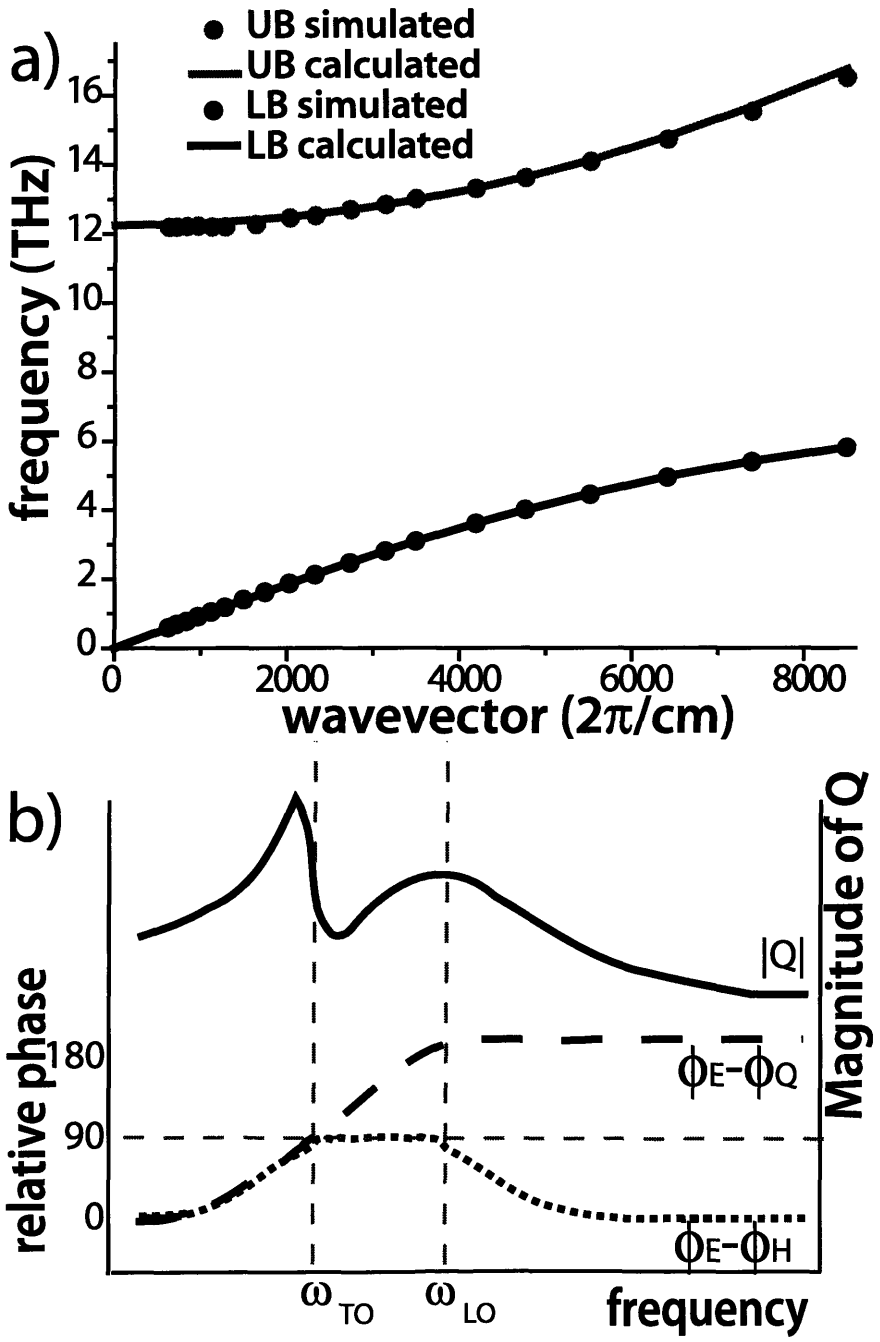

Figure 3-3: a) Dispersion relation for lower and upper branch phonon-polaritons resulting from one-dimensional simulations. b) Relative phases of E, H, and Q and magnitude of Q as a function of polariton frequency. The phase of Q influences the phase of E and the relative phase difference between E and H determines the propagation and attenuation properties of the polariton radiation field.

3.7.1 One Dimensional Simulations

All simulations in this section were performed by specifying an initial electric field, E_z, polarized along the optic axis of $LiNbO_3$ prior to the first simulation time step. The field is propagated in subsequent time steps by the FDTD algorithm.

Polariton Dispersion

The phonon-polariton phase velocity is determined by the dispersion relation, the theoretical values of which may be obtained from Eq. (2.72). Simulated dispersion is compared with theoretical dispersion in Fig. 3-3, and is found to be in good agreement.

By using a spatially periodic excitation pattern, specific phonon-polariton wave vectors, k, may be selected. The dispersion relation was constructed by monitoring a fixed point on the spatial grid of the simulation problem space with a well defined separation from the excitation region so that the temporal evolution of the phonon-polaritons may be recorded as they pass by. The resulting temporal response was Fourier transformed to obtain spectral information, which is graphed versus the excitation wave vector as shown in the figure.

Retardation Effects

To determine the phases of E, H, and Q, a single grid point in the problem space was monitored and recorded for each time step in the simulation, and the temporal evolution of these components was compared. Figure 3-3(b) illustrates the simulation results, where the relative phase of H_x and Q_z is plotted as a function of frequency relative to E_z. Note that the relative phases of H_x and H_y with respect to E_z behave the same, but for convenience only H_x is shown. The normalized ionic displacement Q_z is in phase with E_z for frequencies well below resonance. As resonance is approached, Q_z becomes out of phase with E_z, reaching 90^o at ω_{TO}. The relative phase then quickly becomes 180^o at ω_{LO}, where it remains for all higher frequencies. This phenomenon can be understood in terms of an oscillator driven below, near, or above resonance.

Also shown is the magnitude of Q_z as a function of frequency. For frequencies well below

resonance, the magnitude is small, indicating weak coupling of the electric field to the normal mode. The magnitude increases as resonance is approached, reaching a maximum slightly before ω_{TO}, at which point it rapidly decreases until at ω_{TO} it begins to increase again, reaching another maximum at ω_{LO}. The magnitude then decreases monotonically, such that at frequencies well above ω_{LO}, Q_z is effectively zero.

The relative phase between H_x and E_z, which is a measure of the attenuation rate, is consistent with the results above. As the phonon amplitude increases, so does the phase shift, reflecting increasing energy loss through the phonons. The 90^o phase shift within the gap indicates no propagation there.

Reflection and Transmission at an Interface

The bandgap described by the relative phases of E, H, and Q above should be apparent in transmission/reflection experiments at a crystal interface. Simulations were performed to verify that this behavior is present in our implementation of the FDTD method. Simulations were compared with theoretical transmission/reflection coefficients derived from Eq. (2.47). For a one-dimensional problem, reflection($\mathcal{R}$) and transmission($\mathcal{T}$) coefficients take a simplified form [45],

$$\mathcal{R} = \frac{1-\sqrt{\varepsilon_r}}{1+\sqrt{\varepsilon_r}}, \tag{3.20}$$

$$\mathcal{T} = \frac{2\sqrt{\varepsilon_r}}{1+\sqrt{\varepsilon_r}}. \tag{3.21}$$

In the simulation, terahertz radiation was directed from free space into a $LiNbO_3$ crystal at normal incidence over a decade of frequencies centered about the resonance frequency ω_{TO}. Figure 3-4(a) shows a 1 terahertz pulse incident upon and reflected from the crystal interface. The reflection and transmission coefficients are indicated in the figure. Since the frequency of the incident radiation is well below resonance, there is little dispersion evident in the response, i.e., the reflected wavepacket has the same bandwidth as the incident. In Fig. 3-4(b) the incident radiation frequency is slightly below resonance, giving rise to

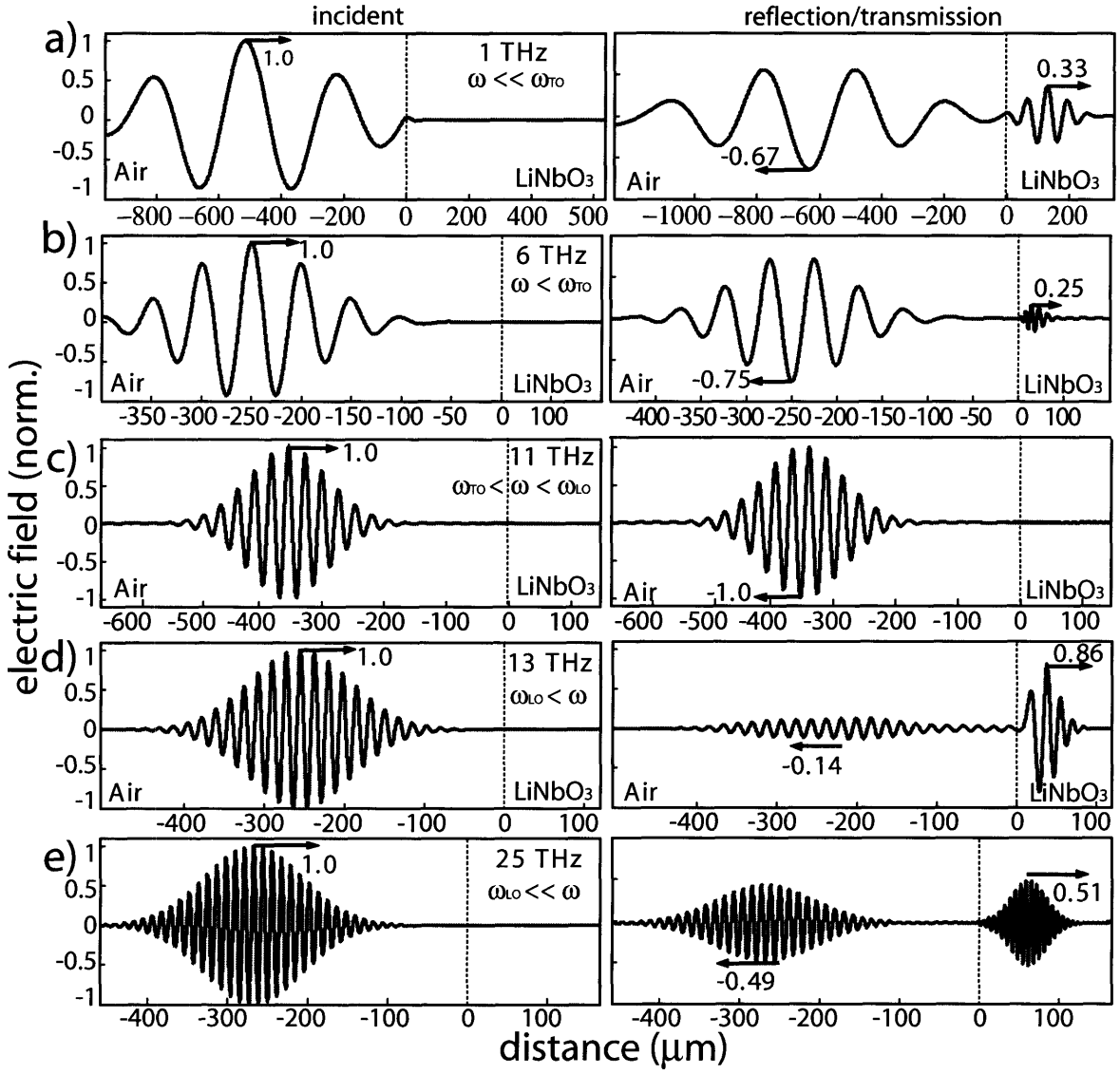

Figure 3-4: Transmission/reflection data from a one-dimensional simulation of terahertz radiation incident upon a $LiNbO_3$ interface. The left hand side illustrates the incident field, and the right hand side illustrates the reflected and transmitted fields. Reflection and transmission illustrating a) non-dispersive and b) dispersive response below ω_{TO}; c) non-propagating response in the bandgap; and d) dispersive and e) non-dispersive response above ω_{LO}.

some dispersion in the transmitted waveform. Also, since the index of refraction is very high near resonance, the reflection coefficient becomes very large. Figure 3-4(c) illustrates an incident frequency that is in the bandgap. Close inspection of the penetration at the interface indicates minimal penetration, analogous to a skin depth in metal, and is on the order of a micron. Simulations were performed at terahertz frequencies above the bandgap as well. They show a return to propagating waves as expected, exhibiting dispersive effects at frequencies near ω_{LO} (Fig. 3-4(d)), but not well above it (Fig. 3-4(e)). Transmission and reflection simulations were found to be in good agreement with Eqs. (2.47), (3.20), and (3.21).

3.7.2 Two and Three-Dimensional Simulation Results

Figure 3-5(a) illustrates a two-dimensional, TM mode simulation of continuous wave (CW) terahertz radiation reflection and transmission at a $LiNbO_3$ interface. The incident field was analytically specified in a small region in the lower left hand corner of the problem space and polarized along the crystal optic axis (out of page). Since the field is analytically specified in an extended spatial region, the radiation field can be pointed in any direction. In the figure, it was directed at the interface with an angle of $\sim$30 degrees to the normal. The analytic region does not extend all the way to the interface, and the wave is seen to diverge as it is propagated by the FDTD algorithm. As it reaches the interface, it is reflected back onto itself, resulting in the interference pattern evident in the last two frames of the figure.

Waves that pass through the interface and into $LiNbO_3$ are phonon-polaritons, but only the electric field is shown in the figure. Since the index of refraction is much higher ($\sim$5) in $LiNbO_3$ than in air, the wavelength is five times shorter in the material. The terahertz radiation refracts at the interface and phonon-polaritons propagate forward with a smaller angle, bent toward the normal, than the incident radiation. The electric fields around the outer edges of the problem space correspond to the PML region. This region contains no physically relevant information, so the fields are masked and appear absent in the figure. This is most apparent in the last frame.

A three-dimensional simulation of broadband ISRS phonon-polariton generation is illustrated in Fig. 3-5(b), where the mechanical field Q_z is shown. An optical excitation pulse with 50 femtosecond pulse duration (FWHM) polarized along the crystal optic axis, $\hat{z}$, was propagated through a $LiNbO_3$ crystal, from top to bottom in the figure, by analytically specifying the pulse at each time step. The excitation pulse group velocity was taken to be $\sim c_0/2.2$ [22]. Since the phonon-polariton phase velocity, $\sim c_0/5.2$ is much slower, the resulting phonon-polariton wavefront is tilted at an angle of ~26 degrees. The tilt is discussed in detail in the next chapter.

To visualize phonon-polaritons in three dimensions, isosurfaces were constructed from the Q_z field output. An isosurface is a region throughout the problem space with the same value for the Q_z field. In the figure, two isosurfaces are shown—one in red and the other in gray. The center region traces the excitation pulse path, in which forward scattered upper branch phonon-polaritons are bouncing back and forth from the front and back face of the crystal. The grey and red isosurfaces to the left and right of the excitation region are lower branch phonon-polaritons with positive and negative displacements, respectively. The figure was taken from a later time step, such that the excitation pulse had already left the crystal and the lower branch polaritons have propagated away from the excitation region.

Narrowband phonon-polariton generation by an intensity grating excitation pulse is illustrated in Fig. 3-5(c). Again, only the mechanical field is shown, and the mechanics of the excitation pulse were the same as before. A front view of the problem space is shown, in which the intensity grating excitation pulse has propagated from back to front in the figure (out of page). An isosurface is shown of the lower branch phonon-polaritons propagating away from the excitation region. Because the frequency is higher than in part (b) of the figure, upper branch phonon-polaritons of comparable amplitude to lower branch phonon-polaritons were not present. In addition to the isosurface, three cross-sections of the mechanical field amplitudes are shown, one for each orthogonal plane in the problem space. The combination of isosurfaces and cross-sections allow for a more complete viewing of the three-dimensional output, as each plane can be arbitrarily moved up and down, left and right, and back to

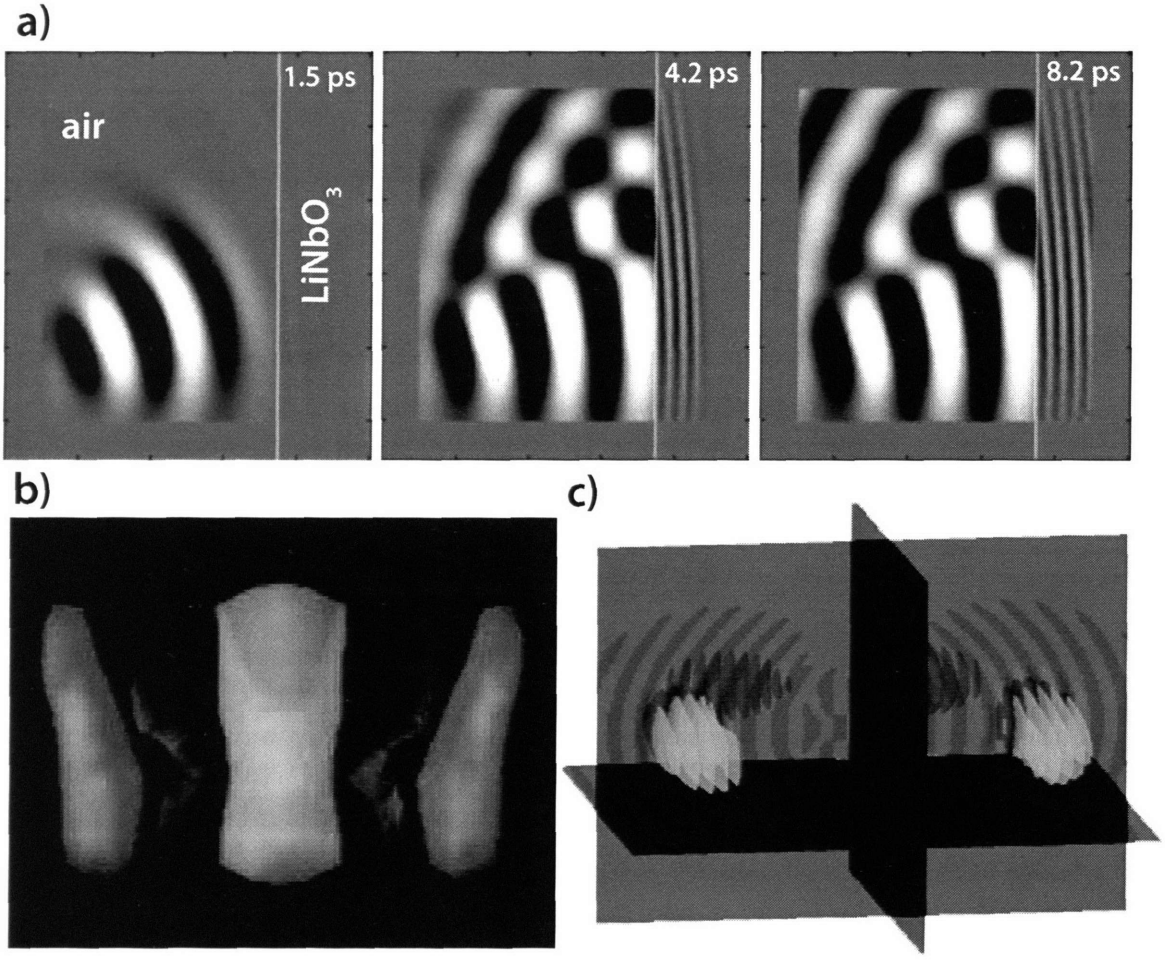

Figure 3-5: a) Two-dimensional TM mode simulation of CW terahertz wave reflection and transmission at a $LiNbO_3$ interface, marked by the white light on the right. E_z is shown. b) Three-dimensional simulation of broadband, b), and narrowband, c), phonon-polariton generation by ISRS. In b), a top-down view is shown in which the excitation pulse has propagated from top to bottom. In c), a front view is shown in which an excitation intensity grating has propagated from back to front (out of page).

front.

The two- and three-dimensional simulations shown here are for illustration only. A more complete description of simulated phonon-polariton generation and propagation is given in chapters 4, 5, and 7.

Chapter 4

Phonon-Polariton Generation, Propagation, and Detection in Bulk Ferroelectric Crystals

This work was done in collaboration with Eric Statz of the Massachusetts Institute of Technology.

This chapter illustrates the experimental details of phonon-polariton generation and detection in bulk crystals. Results of experiments using these methods are presented and compared with theory and simulation. Additionally, using the FDTD simulations of chapter 3 and the theoretical models developed in this chapter, metrics for generation, propagation, and detection are established and tabulated.

4.1 Experimental Methods

Two lasers were utilized for phonon-polariton generation and detection: a home-built Ti:sapphire multi-pass amplifier (800 nm central wavelength, 50 fs, 1 KHz repetition rate, 700 μJ/pulse) seeded by a KM Labs oscillator (790 nm central wavelength, 15 fs, 88 MHz repetition rate, 3

nJ/pulse) and a Coherent RegA Ti:sapphire regenerative amplifier (800 nm, 200 fs FWHM, 250 KHz repetition rate, 6 μJ/pulse) seeded by a Coherent Mira oscillator.

The experimental methods employed in this thesis work are variants of the standard ultrafast pump-probe setup, in which temporal resolution, on a femtosecond time scale, is achieved by separating a laser beam into a pump arm and probe arm, and inserting a mechanical translation stage into either arm to control the relative optical path length between them. Typically, separation into the pump and probe arms is achieved with a beamsplitter (90% pump/10% probe, unless indicated otherwise). Temporal resolution is limited to the smallest step size of the translation stage, which in our case was 1 μm, or 6.67 fs of delay.

All the experiments performed here used poled, X- or Y-cut stoichiometric $LiNbO_3$, congruent MgO:$LiNbO_3$, and congruent $LiTaO_3$ ferroelectric crystals for phonon-polariton generation. These crystals exhibit excellent conversion of optical light to phonon-polaritons due to their high electro-optic coefficients, and are all uniaxial crystals. Whereas $LiTaO_3$ is nearly isotropic, $LiNbO_3$ exhibits a strong anisotropy between the ordinary and the extraordinary axes at optical as well as terahertz frequencies (See Table 4.1). Phonon-polaritons polarized along the optic axis are associated with A_1 vibrational normal modes, and those polarized along either of the ordinary axes, with E symmetry vibrational normal modes, all of which are both Raman and infrared active.

Most of the crystals employed here are commercially available except for the 10 μm thin films, which were fabricated through crystal ion slicing as discussed in chapter 5.

	$LiNbO_3$		$LiTaO_3$	
400 nm	o	eo	o	eo
c_0/c	2.439	2.312	2.282	2.278
c_0/v_g	3.050	2.802	2.620	2.618
800 nm				
c_0/c	2.256	2.164	2.157	2.153
c_0/v_g	2.358	2.250	2.236	2.231
Far Infrared				
ε_0	41.5	26.0	41.5	37.6
ε_∞	19.5	10.0	17.4	7.6
ν_T [THz]	4.6	7.6	4.3	6.0
Γ [THz]	0.51	0.84	0.42	0.84
0.5 THz				
c_0/c_{pol}	6.46	5.11	6.47	6.15
$c_0/v_{g,pol}$	6.50	5.12	6.52	6.18
$1/\alpha$ [mm]	1.6	3.7	5.1	1.0
critical angle [deg]	8.9	11.3	8.9	9.4
Brewster angle [deg]	81.2	78.9	81.2	80.8
forward prop. angle [deg]	21.4	26.0	20.3	21.3
probe angle [deg]		6.1		3.5
1.0 THz				
c_0/c_{pol}	6.53	5.13	6.55	6.20
$c_0/v_{g,pol}$	6.70	5.19	6.77	6.34
$1/\alpha$ [mm]	0.4	0.8	1.2	0.2
critical angle [deg]	8.8	11.3	8.8	9.3
Brewster angle [deg]	81.3	79.0	81.3	80.8
forward prop. angle [deg]	21.2	26.0	20.0	21.1
probe angle [deg]		6.0		3.5

Table 4.1: Material constants and important properties derived or repeated from values available elsewhere [6, 22].

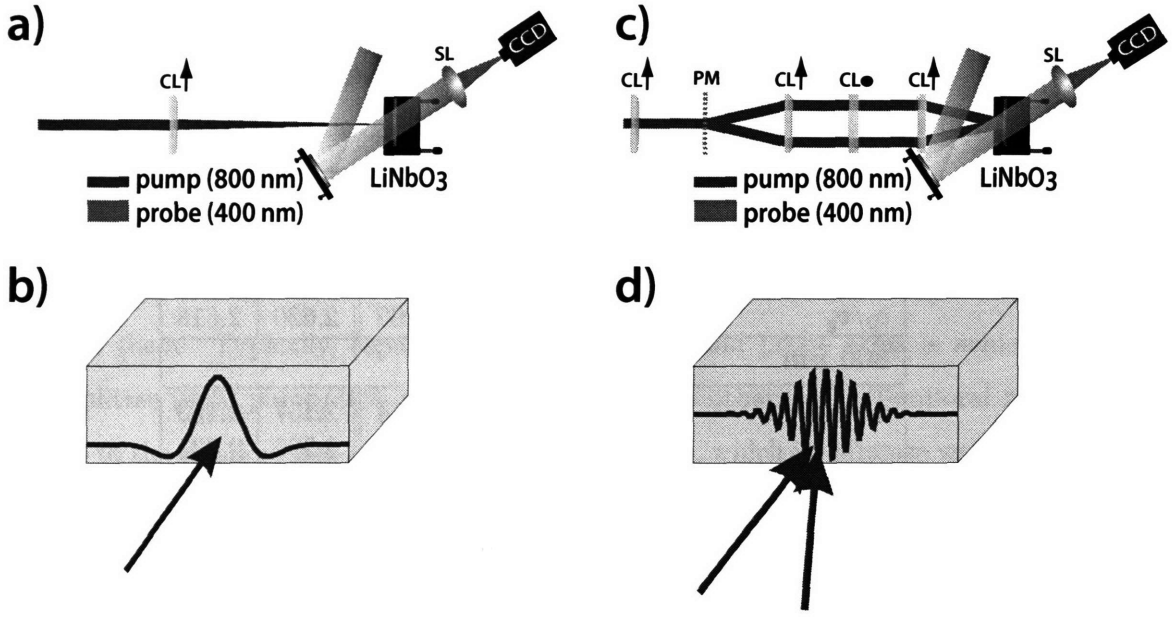

Figure 4-1: a) Broadband phonon-polariton generation by cylindrical lens focusing, and b) the resulting intensity profile in the crystal. c) Narrowband phonon-polariton generation by crossing two beams derived from the ± 1 orders of a diffractive phase grating. The telescope recombines the two diffracted beams at the crystal, resulting in the intensity grating shown in d). Cylindrical lens (CL) orientation is indicated by arrows in the direction of curvature. Detection through real-space imaging is illustrated in both. A diverging lens is used to expand the probe beam to capture phonon-polaritons as they propagate through the crystal. The probe beam makes a small angle ($\sim 10^o$) with respect to the pump beam in order to phase match the excitation and probe beams. It is then imaged through a 0.65 numerical aperture microscope objective onto a CCD camera. The sample is imaged slightly out of focus to facilitate phase-to-amplitude conversion.

4.1.1 Broadband Generation: Line and Point Excitations

Broadband phonon-polaritons were generated by focusing the amplifier output onto a ferroelectric crystal. The use of a spherical lens results in a "point" of light that is circularly symmetric such that phonon-polaritons propagate radially away from the focus region. We refer to phonon-polaritons generated in this way as point excitations. Alternatively, a cylindrical lens makes a "line" of light, referred to hereafter as a line excitation, which is uniform along one dimension and results in quasi-collimated phonon-polaritons which, apart from attenuation due to damping, may propagate with little change across an entire crystal (typ-

ically 3-10 mm). The latter is the most common experimental geometry employed in this thesis, and is illustrated in Fig. 4-1(a) along with the resulting intensity pattern in part (b).

The lens employed for generation is chosen based on the phonon-polariton central frequency desired. Guidelines to facilitate this choice are given later in this chapter (section 4.3.1). The excitation pulse energies for line excitations were typically on the order of 100-200 μJ, and are limited by laser-induced damage in the material.

4.1.2 Narrowband Generation: Intensity Grating Excitations

Narrowband phonon-polaritons were generated by focusing an optical intensity grating onto a ferroelectric crystal. The excitation pulses were split into ± 1 orders of diffraction by a phase grating placed in the pump beam path. All higher orders and the zero order of diffraction were blocked. An imaging telescope was used to cross the two orders in the sample. The crossing angle, determined by the phase grating periodicity, gives the intensity grating fringe spacing [20]. The fringe spacing of the grating gives the phonon-polariton central wavelength, while the number of fringes gives the number of cycles. The phonon-polariton wavevector magnitude k is varied by adjusting the crossing angle, through the use of phase gratings with different periodicity.

The total excitation pulse energy was typically about 100μJ, and the spot-size at the sample was typically about 1 mm in the grating dimension and 600μm in the perpendicular direction. The phase grating setup and the resulting intensity grating are illustrated in Fig. 4-1(c) and (d).

4.1.3 Coherent Control

Temporal Pulse Shaping: Pulse Trains

Coherent control over phonon-polaritons can be exerted by exciting with multiple pulses, separated temporally from each other with the overall temporal window of the pulse train on the order of phonon-polariton response times. Temporal pulse shaping via manipulation

of the excitation pulse spectral content with a spatial light modulator (SLM) has previously been demonstrated [107]. In this case, diffraction gratings are employed to access the spectral content of the excitation pulses, and these limit the overall transmission of the pulse shaper. Further, limitations in SLM pixel size limit the pulse train bandwidth.

We have developed a novel reflection-based pulse shaper, affectionately called the Deathstar, with a higher throughput than is attainable with SLM-based pulse shapers, because it uses no gratings. It also is capable of a broader range of pulse train repetition rates than SLM-based pulse shapers. The Deathstar, illustrated schematically in Fig. 4-2, consists first of a system of two retroreflectors, which divide a single ultrafast laser pulse into seven pulses with temporal spacing that is evenly tunable by moving one of the retroreflectors on a translation stage. Following the photoreflector is a system of mirrors which compensate for the additional ~20 cm round trip that each sequential pulse takes before leaving the pulse shaper. After passing through the pulse shaper, the resulting waveform consists of seven equally spaced pulses with an overall Gaussian envelope, focused onto the sample to a 130 μm spot size.

The lower frequency limit is determined by the maximum separation between retroreflectors--here 7 cm. The upper frequency limit of the pulse shaper is limited by the femtosecond laser input (RegA), which provides pulses of 200 fs FWHM duration. In this case, pulse train repetition rates in excess of 5 THz result in overlap of the constituent pulses, thus smearing out the excitation pulse train.

For phonon-polariton generation, another limitation is incurred. If the repetition rate is high enough that phonon-polaritons from the previous pulse in the pulse train have not had sufficient time to propagate out of the excitation region, then smearing of the resulting phonon-polariton pulse train occurs. For this reason, repetition rates are limited from 0.1 to 0.5 THz for a 130 μm excitation spot size. Higher repetition rates are possible through the alteration of the lateral dimension of the excitation beam at its focus appropriately. The Deathstar is illustrated in Fig. 4-2. Further details of this pulse shaper can be found elsewhere [16].

The Deathstar was used to exert coherent control over a phonon-polariton resonator, which is reported in chapter 7 and elsewhere [93].

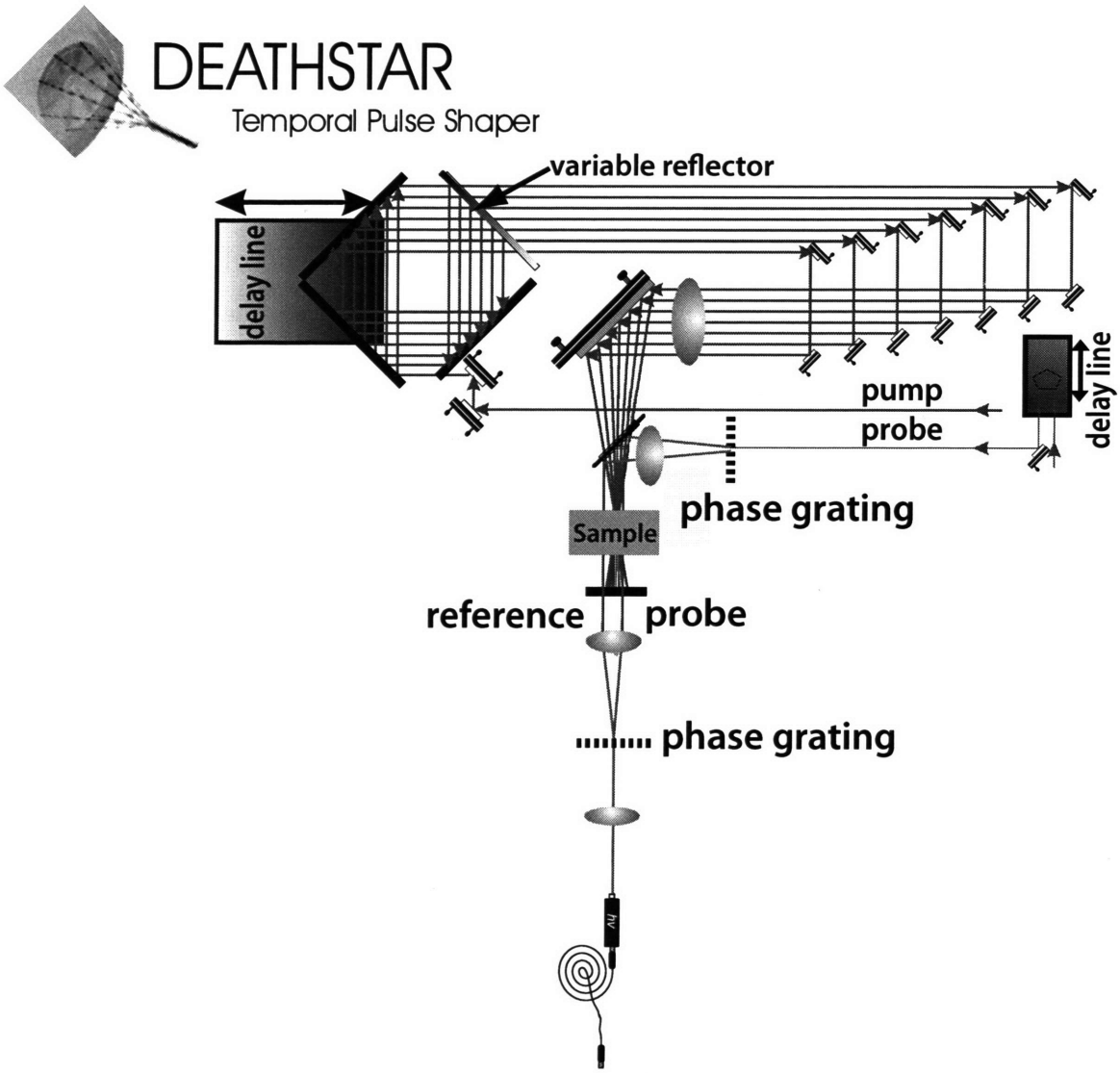

Figure 4-2: Schematic illustration of the Deathstar pulse shaper used to generate narrowband phonon-polaritons. Seven evenly spaced excitation pulses whose repetition rate is adjusted through movement of a single translational stage are all focused to the same spot at the sample. Also shown is an interferometric probing arrangement, in which variably delayed probe pulses are used to monitor the time-dependent phonon-polariton responses through grating-based interferometry.

Spatial Pulse Shaping: Axicon Excitations

Since phonon-polaritons are traveling waves, spatial shaping of the excitation beam profile may also be used to exert coherent control over them. A curved wavefront may be generated to create focusing phonon-polaritons by spatial shaping of the excitation beam profile. One way to achieve a curved wavefront is by including an axicon-lens combination in the pump beam path.

An axicon is a conical biprism that focuses light to a ring. The ring is then imaged to a smaller ring in a ferroelectric crystal which generates a broadband phonon-polariton wavepacket. Part of the wavepacket propagates inward, resulting in focused phonon-polaritons of larger amplitude than can be generated by point excitations [82], and the other part propagates outward, forming an expanding phonon-polariton ring.

Part of the ring can be blocked to form an arc rather than the full ring. The arc results in phonon-polariton focusing that is aberration-free and that has been used to visualize important optical phenomena like the Gouy phase shift [28]. We employed the arc from an axicon excitation to direct and focus phonon-polaritons into transverse waveguides (see chapter 7). The axicon experimental setup is illustrated in Fig. 4-3.

4.2 Phonon-Polariton Detection

In this section, we discuss some details of the detection techniques available for direct observation of phonon-polaritons in ferroelectric crystals. These techniques rely on the ionic displacements associated with phonon-polaritons to induce a phase shift into an optical probe beam, which can give rise to diffraction, birefringence, and phase lags in some or all regions of the probe beam. The majority of data presented in this thesis were taken through real-space imaging, which is presented elsewhere in detail [51, 50], and briefly here, with an emphasis on new techniques not yet described. The probe geometry illustrated in Fig. 4-1 is real-space imaging.

Real-space imaging is preferred when spatiotemporal data is desired but quantitative

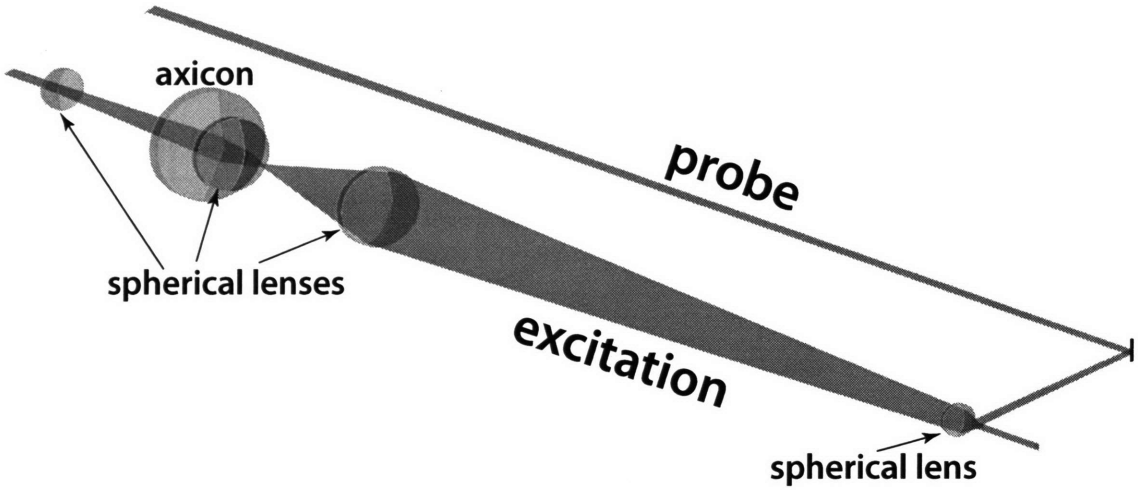

Figure 4-3: Axicon experimental setup. Light passing through an axicon, a conical biprism, forms a ring of light which may be imaged onto a ferroelectric crystal to form a phonon-polariton ring that focuses inward and expands outward. The focusing portion generates phonon-polariton amplitudes not accessible through line and point excitations, due to the damage threshold for optical excitation pulses in $LiNbO_3$ and $LiTaO_3$.

resolution of the signal amplitudes is not required. In some cases, however, quantitative data is required: for example, the direct measurements of terahertz field strengths and ionic displacements presented in chapter 7. In this case, techniques like heterodyned diffraction, grating-based interferometry, and terahertz field induced second-harmonic (TFISH) generation may be used. These are discussed briefly below.

4.2.1 Real-Space Imaging

Real-space imaging relies on an enlarged probe beam that illuminates a region of the crystal significantly larger than the excitation region. The extent of illumination is chosen such that it will fully capture the spatiotemporal evolution of phonon-polaritons in a crystal, which is not possible with a traditional probe that monitors a single point, and is often large enough to encompass the entire crystal (See Fig. 4-4).

As the probe beam propagates through a crystal, regions of large phonon-polariton amplitude induce a phase shift in the probe beam. This phase information can be transformed

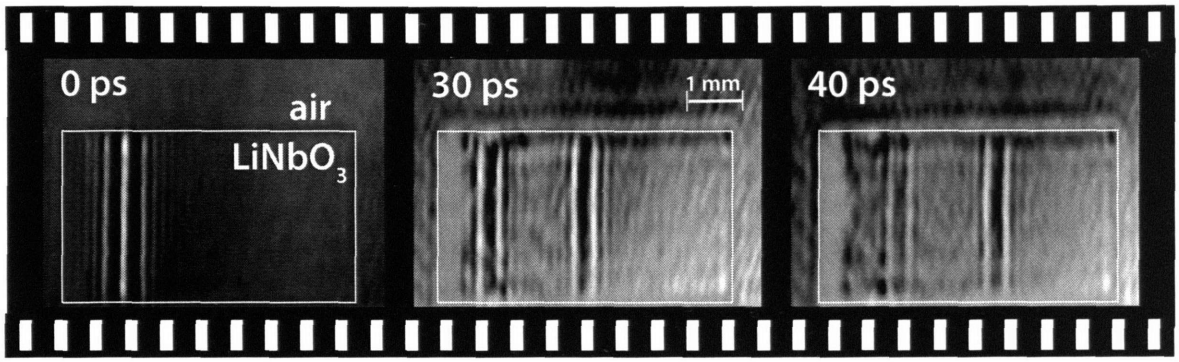

Figure 4-4: Frames from a phonon-polariton "movie" of broadband phonon-polariton generation and propagation in $LiNbO_3$ taken with real-space imaging. The first frame shows the initial phonon-polaritons at the time of generation. Immediately afterwards, wavepackets travel away from the excitation region in both directions. The second frame, taken 30 ps after generation, shows two phonon-polaritons traveling to the right. The first (left) is the reflection of the initial left-going wavepacket and the other was initially traveling to the right.

to amplitude information by imaging the crystal with the probe beam onto a CCD camera with the imaging lens slightly out of focus [88]. By imaging the crystal at subsequent delay times, the series of images may be played back in succession to construct a phonon-polariton "movie" that captures the full spatiotemporal evolution of phonon-polaritons in the crystal.

Frames from a phonon-polariton "movie" are shown in Fig. 4-4 for the case of a broadband phonon-polariton excitation in a 6 x 3 x 1 mm $LiNbO_3$ crystal. Evident in the figure is reflection at the crystal/air interface (left) after the phonon-polaritons propagate away from the excitation region, shown at time zero. Note, the transmitted power resides solely in terahertz radiation, as the requisite coupling to lattice vibrations for phonon-polaritons is unavailable in air.

Blue Light Imaging

The phase contrast accessible through 400 nm imaging is larger than with 800 nm, and stray excitation light, which is parasitic to imaging, is easily removed with color filters when the pump and probe are of different central frequencies. Also, 400 nm probe light is easily produced through frequency doubling of the fundamental 800 nm beam.

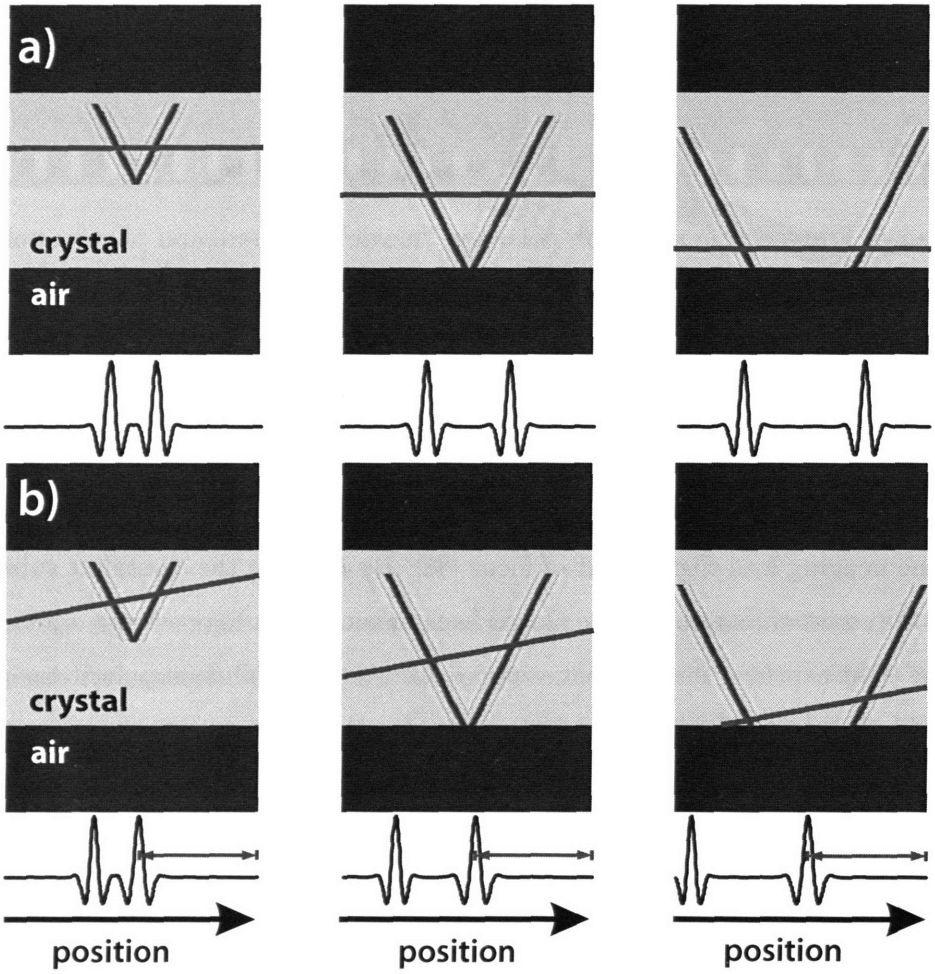

Figure 4-5: a) Because the group velocity of the imaging pulse (red line) is smaller than that of the pump pulse (located at tip of the cone) the signal contributions generated at different times as the pulses travel through the crystal appears at different spatial positions. b) Tilting the imaging pulse results in all signal contributions originating from the phonon-polariton moving to the right to appear at the same spatial position within the coordinate system of the imaging pulse. Therefore, no smearing is observed.

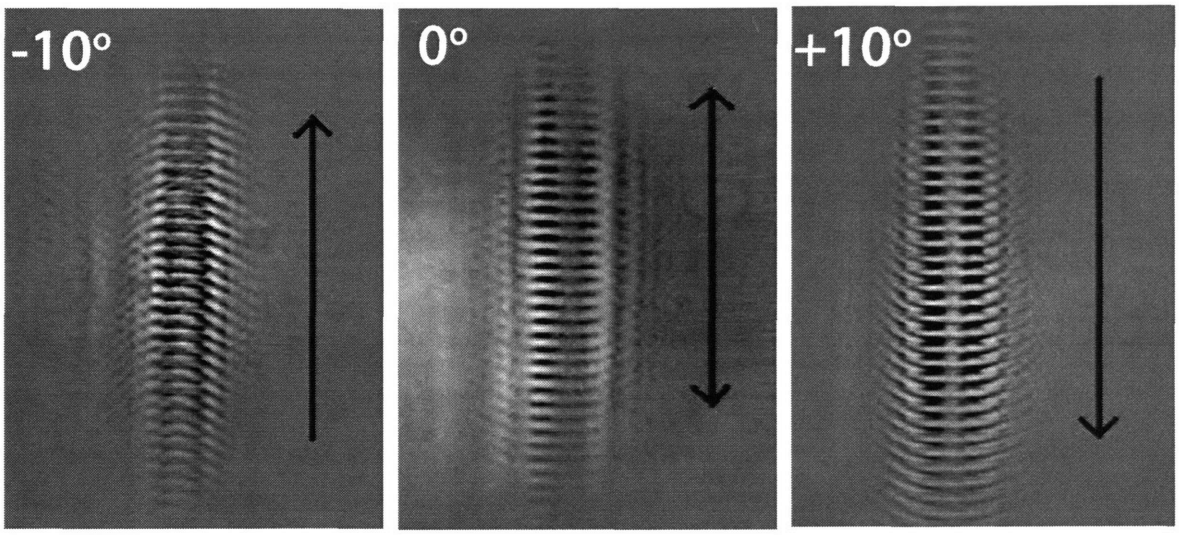

Figure 4-6: Illustration of the preferential detection of propagation in a single direction using tilted 400 nm probe pulses. The tilt angle is indicated in the upper left hand corner. The direction of propagation is discerned by observing the phase front curvature of the phonon-polaritons resulting from a narrow intensity grating.

Despite these advantages, there are drawbacks to 400 nm imaging. The chief limitation is that the probe beam is no longer phase matched to the excitation. In thick crystals, in which the probe beam integrates signal through a significant depth, spatial smearing of the signal will become apparent because contributions to the total signal at different times originate from different spatial positions throughout the thickness of the crystal (see Fig. 4-5(a)).

The probe can be phase matched by transmitting the probe beam through the crystal with a slight tilt with respect to the excitation beam direction. However, tilting only phase matches to phonon-polaritons traveling in one direction. The counter propagating phonon-polaritons will appear substantially weaker and smeared, but in the phase-matched direction, the signal is fully recovered and much stronger as compared to 800 nm imaging (see Fig. 4-5(b))

Experimental results from tilted 400 nm probing are illustrated in Fig. 4-6. Narrowband phonon-polaritons were generated using a phase grating and probed with 400 nm real-space imaging. The intensity grating was intentionally made narrow in one dimension such that

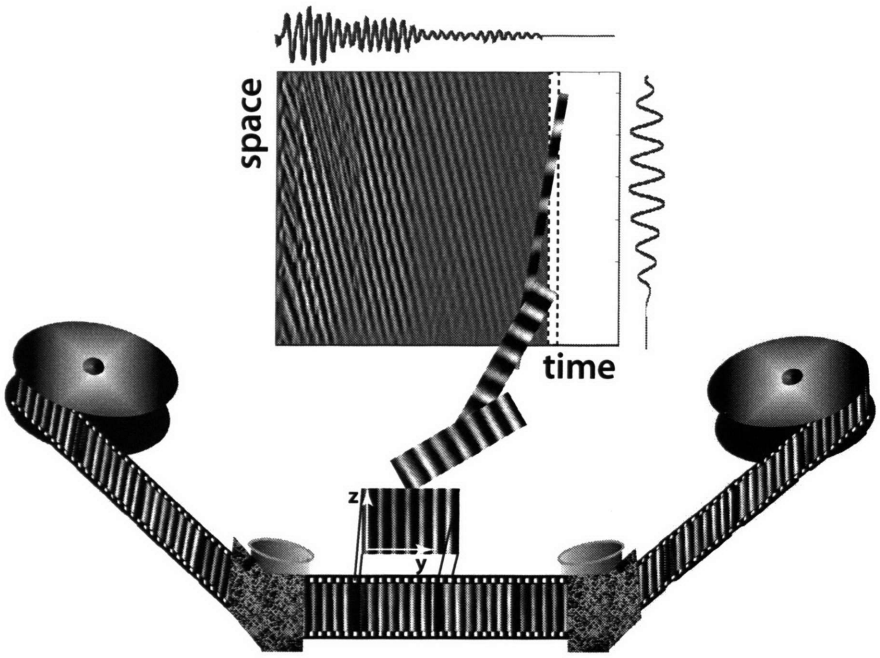

Figure 4-7: When phonon-polaritons are generated by focusing with a cylindrical lens, the amplitude in one dimension is nearly uniform and may be averaged and compressed into a one-dimensional array. Doing so for each frame in a phonon-polariton "movie" results in the space time plot shown above, allowing the full spatiotemporal evolution to be captured in a single two-dimensional graph. Cross-sections are shown along the dimension in which they were taken. The beating evident in the spatial cross-section is explained in chapter 5.

phonon-polaritons generated by the individual fringes in the grating radiate away as if from a point source, the curvature of their phase fronts indicating the direction of propagation. The center image was probed at normal incidence, and phonon-polaritons propagating in both directions are observed. The left and right most frames were taken with the probe pulses tilted at approximately -10 and +10 degrees, respectively. It is clear from the curvature of the phase fronts that with tilted pulses, propagation in a single direction is preferentially detected. The optimal pulse tilt angles in $LiNbO_3$ and $LiTaO_3$ are listed in Table 4.1.

Space-Time Plots

When line excitations are employed, the uniform spatial dimension can be averaged and phonon-polariton "movies" may be compressed into a two-dimensional space-time plot that

captures the full spatiotemporal evolution in a single graph. Since averaging occurs along one spatial dimension, improved signal-to-noise results. Differences in phase and group velocities and wavepacket broadening and dispersion are readily apparent in space-time plots. Slices along the spatial axis yield one-dimensional temporal profiles, and along the temporal axis, one-dimensional spatial profiles. The construction of a space-time plot for narrowband phonon-polaritons in 500 μm thick MgO:$LiNbO_3$ is illustrated in Fig. 4-7.

4.2.2 Grating-Based Interferometry

Interferometric probing has the advantage that it provides precise information regarding the phase shifts induced in an optical probe beam by phonon-polaritons. This technique is employed in chapter 7 for direct measurement of the terahertz field strengths and ionic displacements associated with phonon-polaritons.

The temporal evolution of phonon-polaritons can be monitored through grating-based interferometry (Shown in Fig. 4-2), wherein a beam is split by a phase grating into ± 1 orders of diffraction which serve as probe and reference arms. The probe and reference beams are focused ($2w_0$=25 μm is a typical spot size) and transmitted through a ferroelectric crystal and a reference crystal of the same thickness, and recombined interferometrically at a second phase mask [34]. The probe arm, which is overlapped spatially with the pump, undergoes a time-dependent phase shift due to the phonon-polaritons.

4.2.3 Heterodyned Diffraction

Heterodyned diffraction from laser induced transient gratings have become an important tool in characterizing the low frequency phonon modes characteristic in ferroelectric crystals [20].

Heterodyned diffraction was implemented as follows: The output beam from the amplifier was separated into pump and probe arms, by a 60/40 beamsplitter. The pump was further separated into two excitation beams by a phase grating, collimated by a 15 cm cylindrical lens, and focused onto the sample by a 15 cm spherical lens. These two lenses comprise

a telescope by which the phase mask was imaged onto the sample, similar to narrowband generation as shown in Fig. 4-1(a).

The probe followed a similar path and was split into probe and reference beams, but it was slightly elevated by approximately four beam diameters so that the reference beam side can be attenuated by a neutral density filter and both probe and reference arms can pass through a thin microscope cover slip to adjust the phase between them to facilitate heterodyning. The transmitted portion of the probe diffracts from the transient grating, formed by the crossed excitation beams, throughout the volume of the crystal and was mixed with the transmitted reference beam to produce a transmission heterodyne diffraction probe. The reflected portion of the probe diffracts from the transient grating at the surface of the crystal and was mixed with the reflected portion of the reference beam to form the reflection heterodyne diffracted probe.

Both probe beams were detected with a photodiode for each period of delay between excitation and probe beam. By recording for delay times in excess of the phonon-polariton lifetime, a one-dimensional mapping of the temporal evolution of the phonon-polaritons may be obtained. This technique was used in a simple terahertz spectrometer, which is presented in chapter 7 and elsewhere [21].

4.2.4 Terahertz-Field-Induced Second-Harmonic Generation (TFISH)

Terahertz-field-induced second-harmonic (TFISH) utilizes the electric field of a terahertz pulse to induce a transient anisotropy in a material. TFISH is analogous to electric-field-induced second-harmonic generation (EFISH) in which anisotropy is induced by a permanent distortion in the molecular polarizability or unit cell from the application of a static electric field. Since second harmonic generation is proportional to the degree of anisotropy, it can be monitored to render the temporal evolution of the induced anisotropy. TFISH is effective in not only non-centrosymetric materials but centrosymetric ones as well, and has been previously demonstrated in polar liquids [19].

TFISH is implemented experimentally by focusing a probe beam onto the region of in-

terest and filtering out the fundamental after passing through the sample. It must be tightly focused as the signal is proportional to the probe intensity and second harmonic generation is generally weak. The advantage of TFISH is that probing, in theory, can take place in any material susceptible to displacements or distortions of either the unit cell or the constituent atoms and molecules by terahertz radiation. TFISH probing is not used in this thesis work, though it has been tested, but it is one of the most promising probing techniques for future work.

4.3 Generation, Propagation and Detection of Phonon-Polaritons in Bulk Ferroelectric Crystals: Comparison with Simulation and Theory

In this section we compare phonon-polaritons generated through the methods discussed in the previous section with simulated and theoretical results on phonon-polariton generation, propagation, and detection in $LiNbO_3$ and $LiTaO_3$. The goal is to develop convenient metrics for, and characteristics of, the variety of phonon-polariton waveforms utilized in this thesis. Theoretical issues specific to the experimental geometries of the previous section, and introduced in chapter 2, are taken up here. This section also illustrates the utility and accuracy of the FDTD simulations developed in chapter 3.

4.3.1 Broadband generation

We first consider broadband generation, which corresponds to single or few cycle phonon-polaritons.

Cherenkov Cone

Generation of phonon-polaritons can be conveniently described as Cherenkov radiation emitted by an ultrashort laser pulse propagating through a non-centrosymmetric crystalline ma-

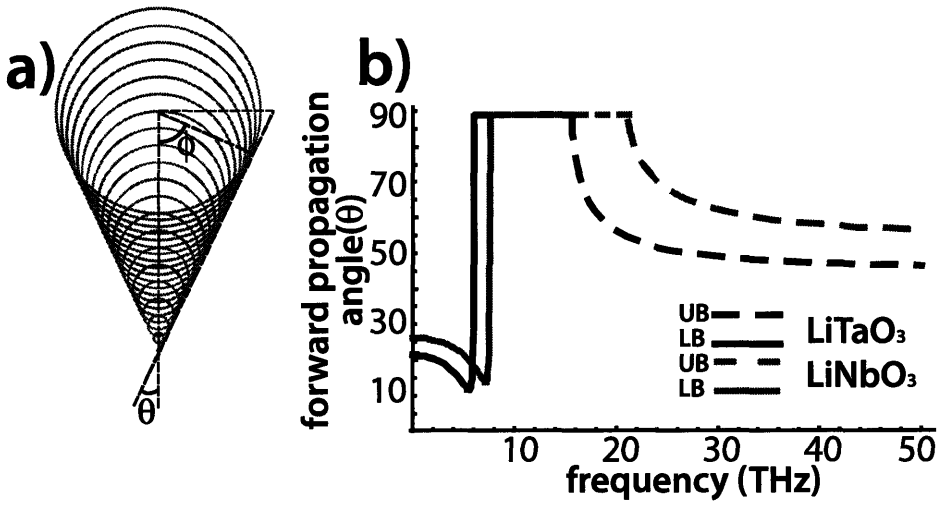

Figure 4-8: a) Cherenkov picture of phonon-polariton generation. An optical excitation pulse "plucks" the ions in a ferroelectric crystal as it propagates through the crystal. The "plucked" ions generate terahertz radiation which provides coupling between ferroelectric unit cells resulting in phonon-polaritons that propagate in the phase-matched direction. This direction is different than that of the excitation pulse due to the disparity between excitation group velocity and phonon-polariton phase velocity, analogous to Cherenkov radiation. b) Calculated forward propagation angles, which are the complements of the traditional Cherenkov angles, in $LiTaO_3$ and $LiNbO_3$ for upper branch (UB) and lower branch (LB) phonon-polaritons.

terial like $LiNbO_3$ and $LiTaO_3$. The excitation pulse generates terahertz radiation by "plucking" the ions via the ISRS force as it traverses the crystal. Because the excitation event at the front surface takes place some time before the excitation at the back surface, the generated phonon-polariton wavefront is tilted and the terahertz radiation generated propagates with a slight forward wavevector component. This process has been compared to Cherenkov radiation [3, 91].

To clarify the origin of the forward wavevector component, consider a single collimated femtosecond laser pulse propagating through a ferroelectric crystal, like that in the Raleigh range of the focused pulses from the previous section. The ions within the vicinity of the excitation pulse respond by radiating uniformly in all directions. Radiation occurs at each point where the excitation pulse is within the crystal. If the excitation pulse group velocity exceeds the phonon-polariton phase velocity, then appreciable phonon-polariton amplitude

results only in the phase matched direction, as illustrated in Fig. 4-8(a). The angle ϕ is the traditional Cherenkov angle; however, shortly we will find the complimentary angle θ, known as the forward propagation angle, more useful in describing the phonon-polariton wavevector. Using the distance $v_g^{\text{pump}}\tau$ traversed by the excitation pulse and $v_p^{\text{pol}}\tau$ traversed by phonon-polaritons in a time interval τ, where v_g^{pump} is the excitation group velocity and v_p^{pol} is the phonon-polariton phase velocity, the Cherenkov and forward propagation angle can be written as

$$\theta = \arcsin\left(\frac{v_p^{\text{pol}}}{v_g^{\text{pump}}}\right), \tag{4.1}$$

$$\phi = \arccos\left(\frac{v_p^{\text{pol}}}{v_g^{\text{pump}}}\right). \tag{4.2}$$

The forward propagation angle θ is indicated for frequencies associated with the A_1 mode in $LiNbO_3$ and $LiTaO_3$ in Fig. 4-8(b). The angle changes because as the resonance frequency is approached, the phonon-polariton phase velocity decreases, giving way to increasingly lateral propagation.

Relationship Between Excitation Spot Size and Phonon-Polariton Waveform Shape and Frequency

To derive the general shape and frequencies of the phonon-polariton waveform produced by a femtosecond optical pulse, we consider a simple model of an ordered sheet of dipolar charge under the influence of an ISRS driving field polarized along the optic axis. The Feynman-Heaviside equation [45] specifies that the radiation field of an oscillating dipole is proportional to the acceleration of the charges in the dipole, but that the radiation from a thin sheet of dipolar charges is proportional instead to the velocity. One can think of the ISRS driving force (Eq. (2.96)) as an impulse that initializes the velocity of the normal mode ionic vibrations, resulting in a radiation field:

$$E_z(t) = \frac{-\eta}{2\epsilon_0 c_0}\frac{\partial P_z(t - x/c_0)}{\partial t}, \tag{4.3}$$

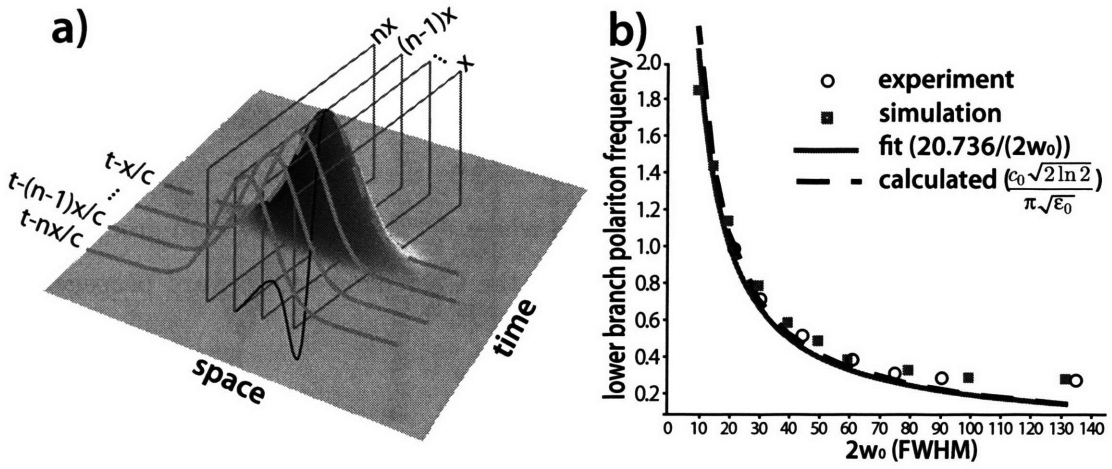

Figure 4-9: The temporal response of phonon-polaritons generated through ISRS can be shown, by an extension of the Feynman-Heaviside equation, to be proportional to the spatial derivative of the excitation pulse profile. b) From the model depicted in a) and described in the text, the central frequency of the terahertz waveform can be shown to depend inversely on the excitation spot-size. Shown here are the calculated, measured, and simulated central frequencies for phonon-polaritons generated with a variety of spot-sizes. Also shown is a fit of the simulated data to the form in Eq. (4.7).

where ϱ is the beam waist (FWHM), η is the inverse of the unit cell area along the two ordinary axes (perpendicular to the optic axis), $t - x/c_0$ is the retarded time, and P_z is the polarization within a sheet of charge. Introducing the substitution $\tilde{x} = ct - x$ and $\partial/\partial t \equiv c_0 \partial/\partial x$ into Eq. (4.3), we find

$$E_z(t) = \frac{-\eta}{2\epsilon_0} \frac{\partial P_z(\tilde{x}/c_0)}{\partial \tilde{x}}, \tag{4.4}$$

where $\tilde{x}$ is in the direction of phonon-polariton propagation and perpendicular to the sheet of dipolar charge. Associating the induced polarization with the ISRS force, Eq. (2.96), the radiated field for a contiguous, non-interacting array of sheets arranged along the longitudinal profile of a temporally impulsive pulse with Gaussian spatial profile (see Fig. 4-9(a)), is

$$E_z(t) = \sqrt{\frac{\epsilon_0(\varepsilon_0 - \varepsilon_\infty)}{NM\varepsilon_0}} \frac{4\eta x \ln 2}{2\omega_{\mathrm{TO}}\varrho^2} \left(\frac{\partial \alpha}{\partial \mathrm{w}}\right)_{33} \mathbb{E}_z^2 e^{\frac{-(4\ln 2)x^2}{\varrho^2}}. \tag{4.5}$$

This equation establishes the link between the spatial profile of the excitation and the temporal profile of the terahertz field, but because it neglects the third dimension, the generated field strengths are a couple of orders of magnitude low. Qualitatively, though, it makes it possible to determine the generated terahertz frequency spectrum due to the spatial profile of the optical excitation pulses. For the case of Gaussian excitation pulses, as above, the spectrum generated can be determined by considering the Fourier transform of the derivative of the excitation profile,

$$FT\Big(\frac{\partial E_z^2(\tilde{x}/c_0)}{\partial \tilde{x}}\Big) = -i\frac{k\varrho}{\sqrt{8\ln 2}}e^{-\frac{\varrho^2 k^2}{16\ln 2}}. \tag{4.6}$$

The center frequency of phonon-polaritons generated by the ISRS driving field is then,

$$\nu_{\max} = \frac{c_0\sqrt{2\ln 2/\varepsilon_0}}{\pi\varrho}. \tag{4.7}$$

For $LiNbO_3$, the relation for the center frequency becomes (22.0 THz-μm)/ϱ, and for $LiTaO_3$, (18.3 THz-μm)/ϱ where ϱ has units of microns. This relationship is illustrated in Fig. 4-9(b) for $LiNbO_3$.

Simulation Results

To illustrate the agreement between the simulated (see Fig. 4-10) and theoretical (Eq. (4.5)) temporal profiles of broadband phonon-polaritons that result from ISRS generation, we consider simulations using the differential polarizabilities in Table 2.3 in which the phonon-polariton temporal profile was recorded by monitoring a single point in space, 1.5 mm off-center from the excitation region, in two different frequency regimes. The optical excitation pulse was 50 fs (FWHM) in duration with a pulse energy of 200 μJ.

Illustrating the non-dispersive regime, which corresponds to frequencies well below resonance (~0.1-1.0 THz in $LiNbO_3$), broadband phonon-polaritons were generated from an optical excitation pulse with a beam waist of 50 μm. The resulting temporal profile, Fig. 4-10(a), corresponds to the spatial derivative of the Gaussian optical excitation pulse profile

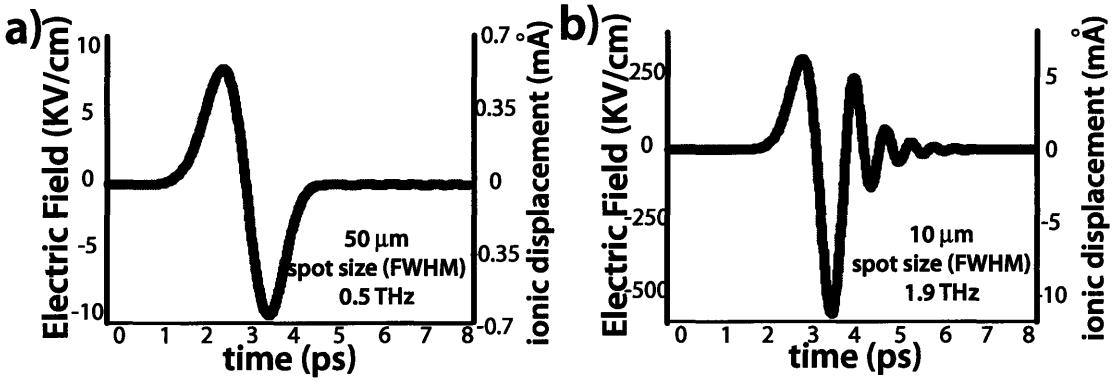

Figure 4-10: Plot of terahertz electric field as a function of time for a broadband phonon-polariton excitation. a) Large spot-size (50 μm) excitation resulting in low frequency phonon-polaritons (500 GHz) and displaying negligible dispersion. b) Small spot-size excitation (10 μm) resulting in high frequency phonon-polaritons (1.9 THz) with significant dispersion. Both excitations were probed at a single grid point in the simulation problem space which was longitudinally displaced 1.5 mm away from the excitation pulse beam-axis.

as predicted by Eq. (4.5).

Considerable dispersion is present in Fig. 4-10(b), in which the excitation pulse spot size was reduced to 10 μm. The general character of the waveform is similar to that in Fig. 4-10(a), but the effects of phonon-polariton group velocity dispersion are apparent. Different frequency components of the phonon-polariton wavepacket propagate at different speeds, and by the time the wave-packet has moved into the monitoring region, it has become significantly distorted. Equation (4.5) does not account for this additional character because it neglects dispersion. There is only a small phase shift between the vibrational and electromagnetic components of phonon-polaritons at these frequencies, so Fig. 4-10 shows both the electric field strengths and vibrational amplitudes associated with the simulated phonon-polaritons.

The spatiotemporal evolution of the phonon-polariton wavefront during the ISRS generation process in $LiNbO_3$ is illustrated for two different excitation pulse spot sizes in Fig. 4-11. Each frame corresponds to the phonon-polariton spatial profile in the simulated two-dimensional plane for a single time step. The series, from top to bottom, illustrates the phonon-polariton wavefront generated as the excitation pulse (not visible in the figure) traverses the crystal from front to back. The resulting phonon-polaritons have appreciable am-

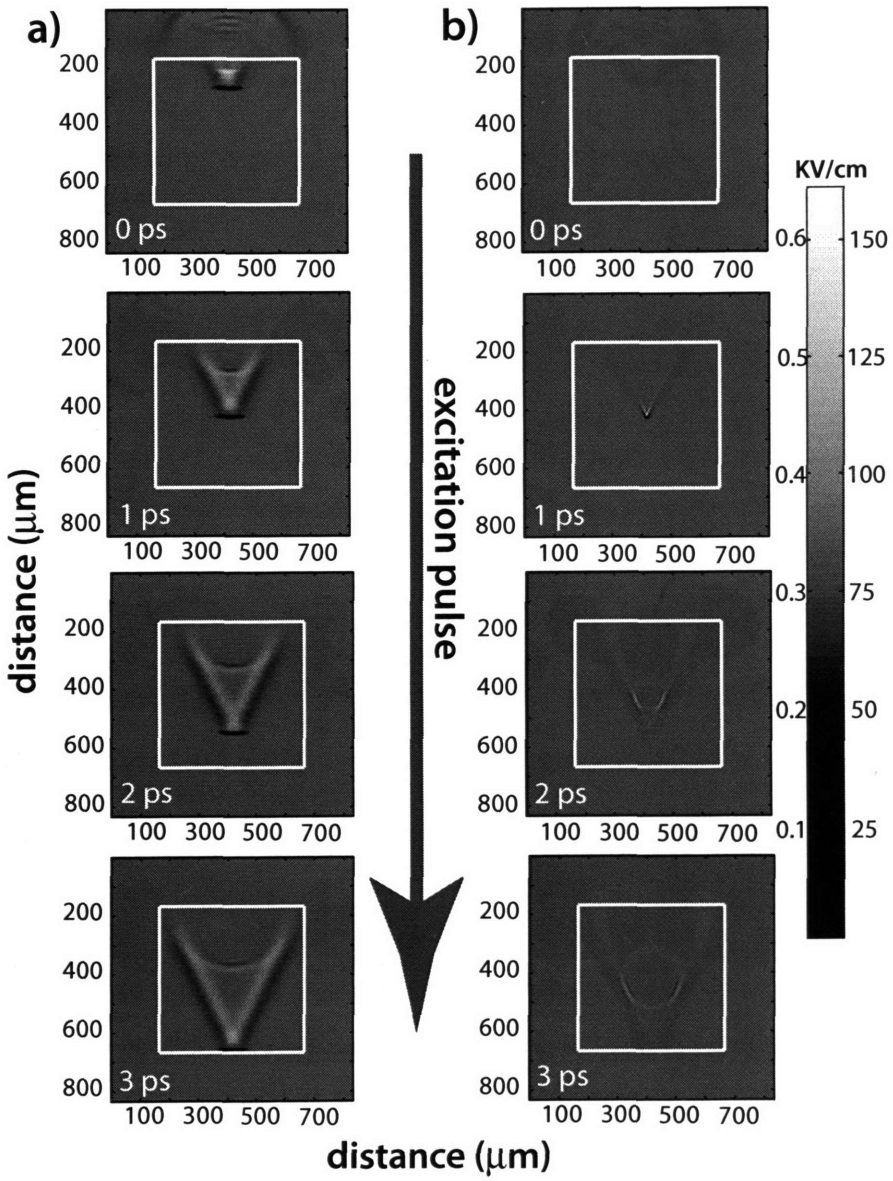

Figure 4-11: Two-dimensional plots of phonon-polariton generation by a 50 fs, 800 nm excitation pulse, and propagation at 1 ps intervals during the generation process for a Gaussian pulse. a) The confocal parameter is large, resulting in a low frequency excitation that is nearly identical to how it would be were the excitation pulse of uniform 50 μm beam waist through the crystal. Field strength legend is located to right. b) Phonon-polaritons resulting from tightly focused (5 μm spot-size at the focus) Gaussian excitation pulse. Appreciable phonon-polariton amplitude results only within the depth of focus. The focal point is set to the center of the crystal (edges indicated by white border) in both sets of images and the excitation pulse energy is 1 μJ. Additional values from these simulations are contained in Table 4.2 for a variety of confocal parameters.

plitude only in the phase matched direction, resulting in a tilted wavefront of approximately 26^o in Fig. 4-11(a) and 24^o in Fig. 4-11(b), which is in good agreement with calculations. Simulation results are also in good agreement with experimental observations reported elsewhere [91]. Further insight is gained by considering the simulated probe signal (see Fig. 4-12) obtained for the two excitations in Fig. 4-11 because it presents the entire phonon-polariton spatiotemporal evolution in a single two-dimensional plot. The two excitations are considered in detail below.

The first set of images (Fig. 4-11(a)) corresponds to an excitation pulse focused to a spot-size of 100 μm. Due to the extremely long Raleigh range, focusing of the beam can be neglected in a crystal of this size because the Cherenkov cone that results is approximately the same as it would be for an unfocused excitation pulse collimated to 100 μm. Also, it is evident from the simulated probe signal (see Fig. 4-12(a)) and its two-dimensional Fourier transform (see Fig. 4-12(c)) that there is virtually no dispersion, because the group and phase velocity are nearly the same and constant: $c = c_0/5.1$ for $LiNbO_3$ and $c = c_0/6.0$ for $LiTaO_3$ [22].

The second set of images (see Fig. 4-11(b)) is of a tightly focused beam with spot size 5 μm. The effect of focusing is non-negligible in this case as it is clear that the phonon-polaritons have appreciable amplitude only within the Raleigh range of the excitation pulse, which is considerably shorter than before. It is also apparent that considerable dispersion is present. Dispersion is more clearly evident in the two-dimensional Fourier transform (see Fig. 4-12(d)) of the simulated probe (see Fig. 4-12(b)). Though the waveform shape deviates from that predicted by Eq. (4.5), the center frequency as measured slightly beyond the excitation beam axis is still reasonably well described by Eq. (4.7).

Simulation results for a larger set of excitation pulse spot sizes are summarized in Tables 4.2 and 4.3 for $LiNbO_3$ and $LiTaO_3$, respectively. The field strength and ionic displacement for $LiNbO_3$ with a 130 μm excitation pulse spot size are 0.042 kV/cm and 0.001×10^{-3} Å, respectively, which is in reasonable agreement with the values of 0.010 ± 0.001 kV/cm and $3.0 \pm 0.1 \times 10^{-6}$ Å measured experimentally and reported in chapter 7. The observed center

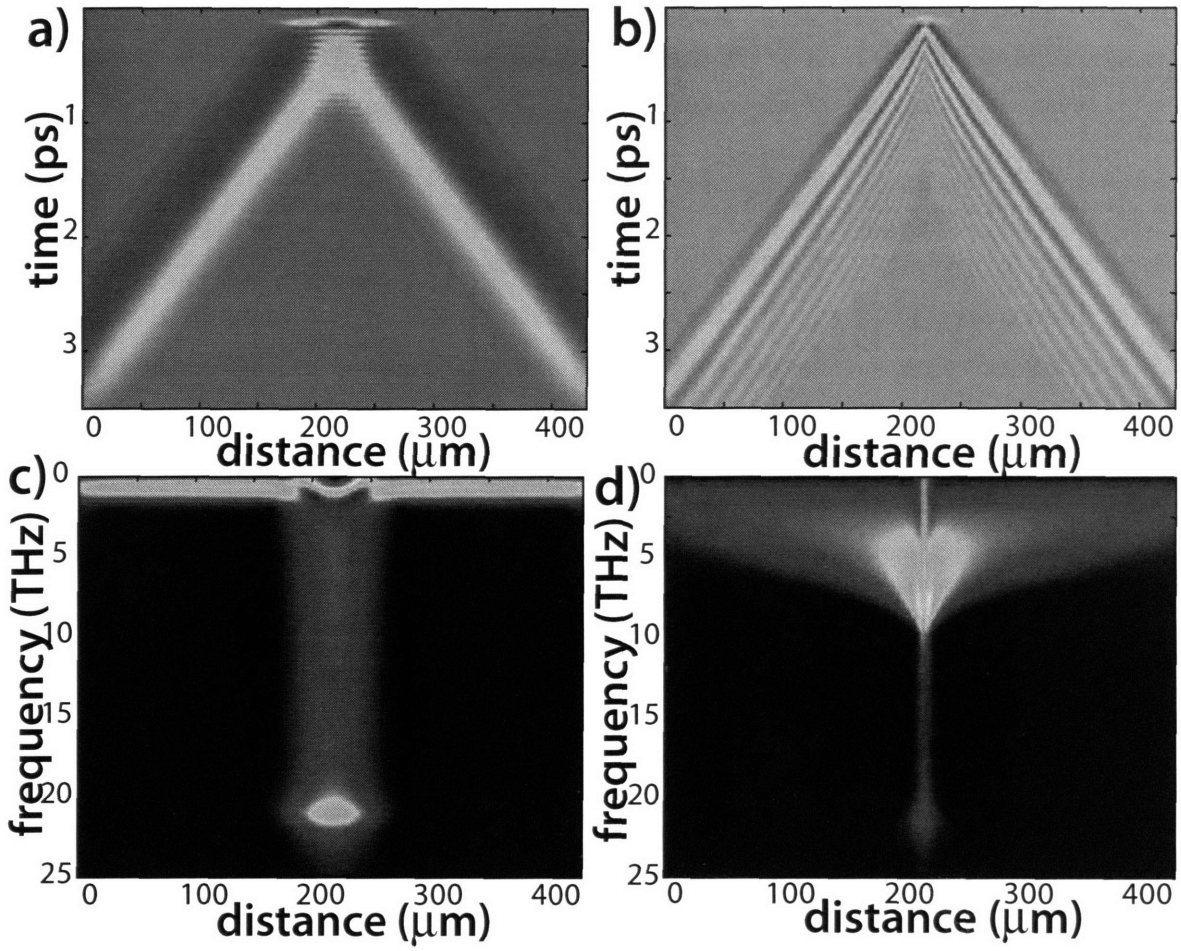

Figure 4-12: Simulated probe data for the two graphs in Fig. 4-11. Shown are space-time probe output images for a) low frequency excitation (500 GHz) in Fig. 4-11(a) and b) high frequency excitation (2.2 THz) in Fig. 4-11(b), c) Fourier transform of simulated probe in part a). d) Fourier transform of simulated probe in part b). Significant dispersion is present in the high frequency excitation, while it is negligible in the low frequency excitation. Evident in part c) and d) is the trend that at smaller excitation wavevectors, the upper branch enjoys significant coupling to the radiation field in the forward scattered direction, while at larger wavevectors the coupling is less.

frequencies from this larger data set are illustrated in Fig. 4-9(b), where all but the two shortest wavelength phonon-polariton waveforms in Table 4.2 are plotted. The observed lower branch frequencies plotted in Fig. 4-9(b) were fit to an equation of the form in Eq. (4.7), resulting in a relation for the simulated center frequencies given by (20.7 THz-μm)/ϱ, which is reasonably close to the theoretical value of (22.0 THz-μm)/ϱ for $LiNbO_3$.

$2w_0$(FWHM) (μm)	I_{pump} (TW/cm^2)	LB (THz)	Δw_{max} (10^{-3}Å)	E_{THz} (KV/cm)
132	0.02	0.29	0.001	0.042
100	0.04	0.30	0.002	0.097
80	0.06	0.34	0.004	0.187
60	0.11	0.40	0.010	0.435
50	0.15	0.50	0.034	0.750
40	0.24	0.60	0.067	1.453
30	0.43	0.80	0.079	3.401
20	0.97	1.15	0.263	11.013
15	1.72	1.45	0.574	23.561
10	3.81	1.86	1.384	55.891
5	15.48	2.20	3.370	135.870
2	97.05	2.40	3.804	152.775

Table 4.2: Broadband phonon-polariton generation results, for A_1 mode in $LiNbO_3$. $2w_0$ is the spot-size at the focus, I_{pump} is the maximum excitation pulse intensity at the focus, LB is the lower branch frequency, Δw_{max} is the maximum ionic displacement, and E_{THz} is the maximum lower branch field strength.

$2w_0$(FWHM) (μm)	I_{pump} (TW/cm^2)	LB (THz)	Δw_{max} (10^{-3}Å)	E_{THz} (KV/cm)
170	0.04	0.15	0.001	0.031
136	0.06	0.22	0.002	0.060
102	0.11	0.37	0.006	0.141
85	0.15	0.44	0.010	0.242
68	0.24	0.51	0.019	0.465
51	0.43	0.70	0.044	1.082
34	0.97	0.88	0.140	3.390
26	1.72	1.17	0.290	6.970
17	3.87	1.46	0.665	15.600
8.5	15.47	1.68	0.147	34.100

Table 4.3: Same as Table 4.2, except for $LiTaO_3$.

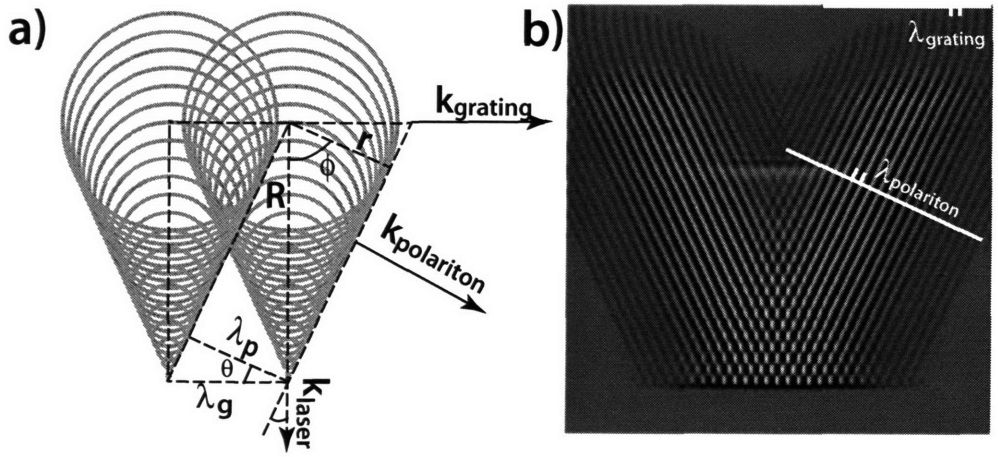

Figure 4-13: a)The phonon-polariton Cherenkov cones generated by two neighboring fringes in an excitation intensity grating used to generate narrowband phonon-polaritons. Shown are the grating wavelength ($\lambda_{grating}$) and the phonon-polariton wavelength $\lambda_{polariton}$, which corresponds to the excitation grating wavevector and phonon-polariton wavevector respectively. The forward phonon-polariton angle θ and Cherenkov angle ϕ are also shown. b) Terahertz field pattern resulting from an intensity grating incident from the top. Notice the difference between the phonon-polariton wavevector and the grating wavevector. The grating wavevector is directed along the surface near the back face of the crystal, while the phonon-polariton wavevector is directed into the crystal in the direction of power flow.

4.3.2 Narrowband Phonon-Polaritons

Narrowband, or multiple cycle, phonon-polaritons can be generated by shaping the optical excitation pulses in either space or time. In spatial shaping, a transverse intensity grating pattern imposes a wavelength (wavevector) across the crystal face, which generates a temporal response in accordance with the dispersion relation in Eq. (2.72). One phonon-polariton waveform with the lower branch frequency and another with the upper branch frequency result. Temporal shaping is achieved by shaping the optical excitation beam in the longitudinal direction of the pulse, i.e., a pulse train results and generates only one phonon-polariton waveform at the frequency of the pulse train. Simulations of these two regimes are presented below.

Spatial Shaping

An effective method of generating narrowband terahertz radiation experimentally has been described elsewhere [20], in which a phase mask grating pattern is employed to create an intensity grating pattern along the transverse profile of the optical excitation pulse. To simulate this intensity grating, a collimated Gaussian beam profile with a $\sin^2$ modulation was employed. The resulting waveforms and Cherenkov cones are in good agreement with the experiments. [20, 91]. Figure 4-13(a) illustrates how two Cherenkov cones can constructively interfere to form a grating excitation, as well as the phase matching condition responsible for the forward propagating phonon-polariton wavevector.

It is clear that there should also be a non-phase-matched grating wavevector parallel to the crystal face and present only at the surface of the crystal. This effect is confirmed in the simulated data shown in Fig. 4-13(b). Here, the Cherenkov grating results from an intensity grating with many fringes. Neglecting dispersion and damping, the bandwidth of the phonon-polaritons generated through spatial shaping of the excitation pulse does not change in time and is proportional to the number of fringes in the excitation grating.

Temporal Shaping

Though arbitrarily shaped optical pulses can be achieved with temporal pulse shaping, we focus here only on pulse trains with a constant repetition rate. In simulation, a series of pulses was directed into the crystal separated in time by the pulse train repetition rate period, resulting in narrowband phonon-polaritons with the same frequency as the pulse train repetition rate, as shown in Fig. 4-14.

Narrowband phonon-polaritons generated through temporal shaping are similar to those generated through spatial shaping, but substantial differences are evident in the simulated data. The bandwidth is proportional to the number of pulses in the pulse train, which is similar to the bandwidth dependence on the number of fringes in spatial shaping. However, in spatial shaping, all the fringes arrive at the crystal at the same time, whereas in temporal shaping, they do not, resulting in a time-dependent bandwidth for temporal shaped

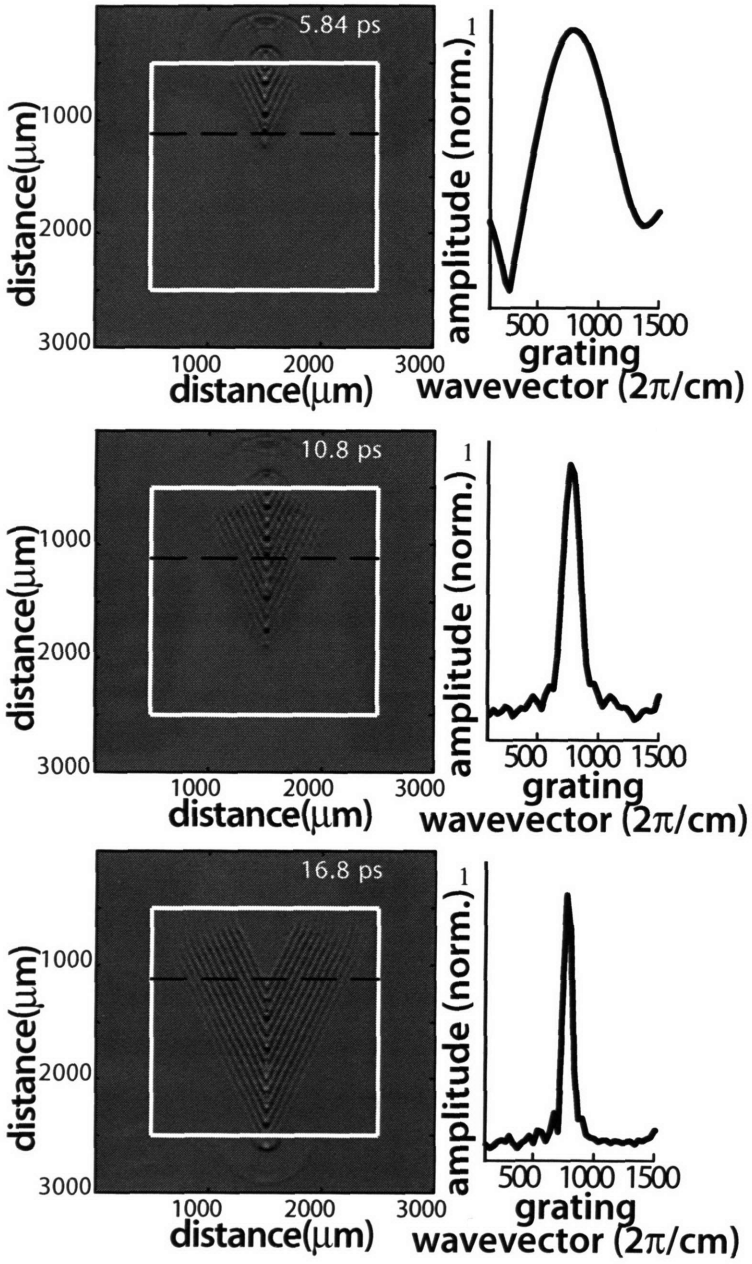

Figure 4-14: Time evolution of narrowband phonon-polaritons generated by optical pulse shaping of the excitation pulse. In comparison with Fig. 4-13(b), there is no overlap of the phonon-polariton Cherenkov cones, and the linewidth narrows as more pulses contribute to the phonon-polariton excitation. The black dotted line indicates the plane in which the Fourier transform on the right is taken. A white border frames the crystal border. Note that the spot-size of the incident pulse train is matched to the desired excitation frequency for maximum efficiency. Otherwise, a center frequency shift would accompany the line narrowing as subsequent excitation pulses arrive at the crystal.

excitations. That is, the bandwidth narrows as more pulses arrive at the crystal and does not reach the minimum attainable bandwidth until the full pulse train has arrived at the crystal. Also, to ensure that the spatial profile of the pulse train is narrow enough to support the pulse train repetition rate, the excitation spot size is chosen judiciously, guided by the measurements reported in section 4.3.1. If the excitation pulse spot size is too large, then phonon-polaritons will destructively interfere with phonon-polariton waveforms from previous pulses in the pulse train. Optimal narrowband phonon-polariton generation with temporal shaping is achieved by matching the spatial bandwidth to the temporal bandwidth.

4.3.3 Dispersion in Bulk Ferroelectric Crystals

As mentioned in chapter 2, phonon-polariton dispersion exhibits an avoided crossing between electromagnetic and vibrational degrees of freedom, resulting in two branches (upper and lower branch) in the dispersion relation separated by a bandgap (See Fig. 2-1). Just as electrons are not allowed in an electronic bandgap, phonon-polaritons are not allowed in a phonon-polariton bandgap, as the electric field is ninety degrees out of phase with the magnetic field in the bandgap, resulting in zero power flow. Each point in the dispersion relation corresponds to the phonon-polariton phase velocity for a particular wavevector k, while the slope at any point corresponds to the phonon-polariton group velocity for either the upper or lower branch. The lower branch (upper branch) displays light-like dispersion for small (large) wavevectors, and displays phonon-like dispersion for higher (lower) wavevectors.

Simulated, calculated, and experimental dispersion is illustrated in Figs. 4-15(a) and (b) for $LiNbO_3$ and $LiTaO_3$, respectively.

Narrowband phonon-polaritons were generated through ISRS with an initial phonon-polariton wavevector imposed by selecting phase gratings with the appropriate periodicity. Real-space imaging was used for monitoring and recording of the spatiotemporal evolution of the phonon-polaritons. Frames from the resulting phonon-polariton "movies" were used to construct space-time plots, like that in Fig. 4-7, which were Fourier transformed to obtain spectral information. This procedure was repeated with a range of phase gratings with 5-100

μm periodicity. The excitation pulses were polarized along the optic axis of a 500 μm thick crystal, so the dispersion reported here corresponds to the A_1 modes in $LiNbO_3$ and $LiTaO_3$.

Simulations were performed in a two-dimensional problem space with one component of the electric field normal to the problem space plane and two magnetic components in the plane, i.e., transverse magnetic (TM) simulations.

Lower Branch

As the excitation pulse traverses the crystal, phase matching of the excitation pulse group velocity to the lower branch phonon-polariton phase velocity results in a phonon-polariton wavevector with a slight forward component. The phonon-polariton wavevector can be calculated from the imposed grating wavevector, k_{grat}, and the forward propagation angle, Eq. (4.1), as follows,

$$k_{pol}^2 = k_{grat}^2 + \left(\frac{n_{pump}\,\omega}{c_0}\right)^2, \tag{4.8}$$

where k_{grat} is equal to $2\pi/\lambda_{grat}$, and λ_{grat} is the lateral periodicity in the excitation pulse intensity grating. As k_{pol} approaches zero, the maximum forward propagation angle is achieved, which is 21^0 and 26^o for $LiTaO_3$ and $LiNbO_3$, respectively. Near resonance, a minimum forward propagation angle of 11.5^o and 14^o in $LiTaO_3$ and $LiNbO_3$ respectively is obtained. Beyond this point, as resonance is approached, the forward propagation angle quickly becomes 90^o in both. Failure to account for the forward component can result in errors in the measured and simulated frequencies by as much as 10%.

Upper Branch

Corrections to the upper branch phonon-polariton wavevector are more involved than for the lower branch, and without these corrections more substantial errors are incurred than was the case for the lower branch. A key difference between upper and lower branch phonon-polaritons is that some portion of the upper branch lies to the left of the excitation pulse light-line ($c_{pump}\,k$ in Fig. 2-1(b)). In this region, the constructive interference required for the Cherenkov wavefront does not occur because the phonon-polariton phase velocity is greater

than the excitation pulse group velocity. The wavevector at which the excitation pulse light-line crosses the upper phonon-polariton branch corresponds to forward scattered light, i.e., θ=90^0. This crossing occurs at k_{pol}=7380 $(2\pi/cm^{-1})$ in $LiNbO_3$ and k_{pol}=9895 $(2\pi/cm^{-1})$ in $LiTaO_3$. Higher wavevectors have decreasing forward propagation angles, reaching a minimum of 44^0 and 54^0 for $\omega \gg \omega_{LO}$ in $LiTaO_3$ and $LiNbO_3$, respectively. Note that the 44^0 limit for the forward component in $LiNbO_3$ implies that nearly phase-matched terahertz excitations are possible at frequencies well above ω_{LO}, i.e., high frequency phonon-polaritons have nearly the same phase velocity as the excitation pulse group velocity.

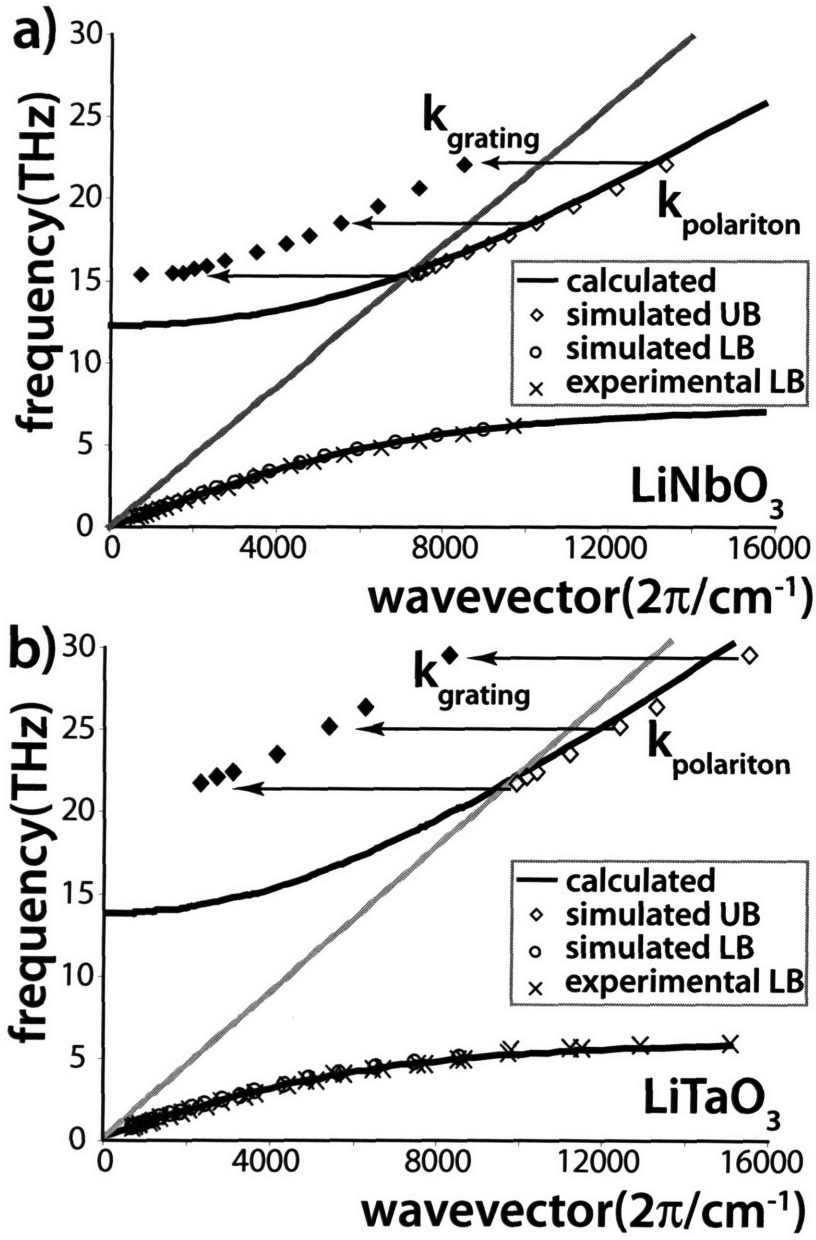

Figure 4-15: Experimental, simulated and calculated dispersion for a) $LiNbO_3$ and b) $LiTaO_3$. The lower branch dispersion requires a correction to the phonon-polariton wavevector due to the forward propagation angle. The upper branch also requires compensation for the forward propagation angle, but there is a minimum phonon-polariton wavevector below which no laterally propagating upper branch phonon-polaritons can be generated; they can only be generated to the right of where the excitation light-line (gray) intercepts the upper branch dispersion curve as pictured above. The simulated upper branch frequencies are plotted in the grating wavevector on left.

Chapter 5

Phonon-Polariton Propagation in Thin Ferroelectric Crystals

This work was done in collaboration with Eric Statz of the Massachusetts Institute of Technology, and Ryan Roth and Richard Osgood of Columbia University.

In this chapter, deviations from bulk phonon-polariton generation, propagation, and detection that occur when the crystal thickness is on the order of the phonon-polariton wavelength are considered. These deviations are accounted for by considering the slab waveguide modes intrinsic to the geometry of the film. Waveguide effects only for lower branch phonon-polaritons are considered because upper branch phonon-polaritons with forward propagation angles small enough for total internal reflection are of a sufficiently high frequency (~20 THz) that detection is not possible with our present experimental arrangement (See Fig. 4-8). Additionally, only confinement in the plane of an X- or Y-cut crystal is considered. Though the mathematical formalism and many of the results from this chapter are quite general to confinement in any dimension, the waveguides discussed here are different from the fabricated waveguides presented later in chapter 6, which are amenable to direct observation because the plane of confinement is visible to, and spatially resolved by, real-space imaging.

As the crystal thickness becomes sufficiently small, such that the phonon-polariton life-

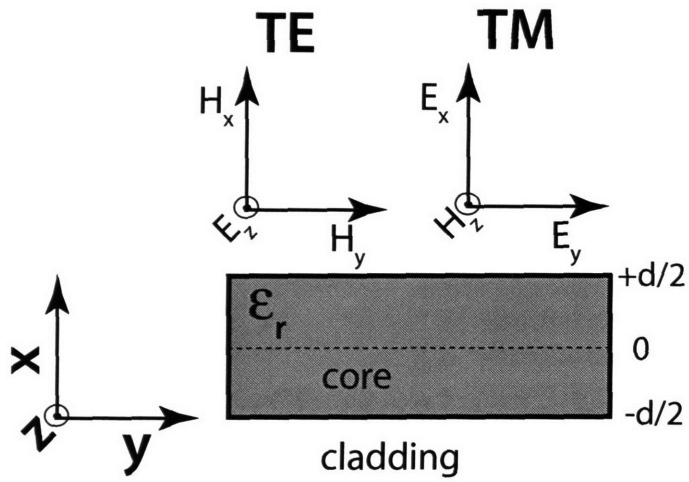

Figure 5-1: Transverse electric (TE) and transverse magnetic (TM) geometries employed for two-dimensional waveguide calculations.

time exceeds the time it takes for traversal through the crystal thickness, beating patterns emerge in real-space imaging. Though not directly related to waveguide phenomena, the beating is considered here as a precursor to the waveguide regime.

5.1 Theoretical Background on the Waveguide Regime

Slab waveguide modes originate from interference between reflections from the front and back faces of a crystal in which light is confined by total internal reflections. The modes form when the wavelength becomes on the order of the crystal thickness. In this section we explore the theoretical considerations necessary to understand polaritonic waveguides, which comprise the majority of the remainder of this chapter. We do so by considering the simple case of perfect magnetic conductor (PMC) boundary conditions, followed by a treatment of the more difficult dielectric boundary conditions. Detailed solutions to both problems can be found elsewhere [35, 73]; however, we describe them briefly below.

5.1.1 Perfect Magnetic Conductor Boundary Conditions

Consider the geometry in Fig. 5-1, which shows a waveguide composed of a dielectric material with relative permittivity ε_r, and an adjoining material that we assume to be a perfect magnetic conductor. In a PMC, the magnetic field on the surface and inside the PMC is zero, analogous to a perfect electric conductor, which models a perfect reflecting metal. PMC boundary conditions are useful because the phase of reflections from them is similar to that in a polaritonic material.

The electric field E_z is out of the plane and perpendicular to the wavevector along the waveguide, k_y, referred to as the propagation constant, and the wavevector in the direction of confinement, k_x. As a consequence of confinement in the x-direction, the magnetic field has a component in the direction of propagation as well as perpendicular to it. This configuration is referred to as the transverse electric (TE) geometry, and it is also illustrated in Fig. 5-1.

Waveguide Mode Solutions

The wave equation for TE geometry is

$$\left(\frac{\partial^2}{\partial x^2} - k_y^2 + \omega^2 \mu_0 \epsilon_0 \varepsilon_r\right) E_z(x) = 0, \tag{5.1}$$

where we have assumed plane wave solutions of the form

$$E_z(x,y,t) = E_z(x) e^{i(k_y y - \omega t)} \hat{k}, \tag{5.2}$$

$$H_x(x,y,t) = H_x(x) e^{i(k_y y - \omega t)} \hat{i}, \tag{5.3}$$

$$H_y(x,y,t) = H_y(x) e^{i(k_y y - \omega t)} \hat{j}. \tag{5.4}$$

All other field components are zero.

Solutions to Eq. (5.1) are dependent on the boundary conditions. Here we are considering

PMC boundary conditions, which are formally written as:

$$\hat{n} \cdot \left(\vec{E} - \vec{E}_{\text{PMC}}\right) = 0, \tag{5.5}$$

$$\hat{n} \times \left(\vec{H} - \vec{H}_{\text{PMC}}\right) = 0. \tag{5.6}$$

Eq. (5.5) is already satisfied since E_x=0, but Eq. (5.6) requires that $H_y(d/2) = H_y(-d/2) = 0$. Using Faraday's law (see Eq. (2.24)) we can write this as follows:

$$-\frac{\partial E_z(d/2)}{\partial x} = -\frac{\partial E_z(-d/2)}{\partial x} = 0. \tag{5.7}$$

We have only to solve for $E_z(x)$ in Eq. (5.2). It is simple to show that the solution is of the form

$$E_z = A_1 \cos(k_x x) + A_2 \sin(k_x x), \tag{5.8}$$

where A_1 and A_2 are constants. Applying Eq. (5.7) to Eq. (5.8) and exploiting the symmetry of the waveguide, odd solutions are found for the case A_1=0,

$$A_2 \cos(k_x \frac{d}{2}) = 0 \Rightarrow k_x = (2p+1)\frac{\pi}{d}, \tag{5.9}$$

and even solutions for A_2=0,

$$A_1 \sin(k_x \frac{d}{2}) = 0 \Rightarrow k_x = 2(p+1)\frac{\pi}{d}, \tag{5.10}$$

where $p = 0, 1, 2, \ldots$ and is identified with the waveguide modes, i.e., higher integers corresponding to higher order modes. The remaining fields, H_x and H_y, can be obtained by applying Ampere's law (see Eq. (2.25)) to Eq. (5.8).

The transverse magnetic (TM) geometry is similar to the TE geometry, and is also shown in Fig. 5-1. The TM geometry is obtained by a simple permutation of the fields in the TE geometry. Consequently, the TM solutions are just permutations of the TE solutions. Field solutions for both geometries are summarized in Table 5.1.

TE-even $k_x = 2(p+1)\frac{\pi}{d}$	$\lvert E_z(x,y,t)\rvert = E_0 \cos(k_x x)\cos(k_y y - \omega t)$ $\lvert H_x(x,y,t)\rvert = E_0\sqrt{\frac{\epsilon_0\epsilon_r}{\mu_0}}\cos(k_x x)\cos(k_y y - \omega t)$ $\lvert H_y(x,y,t)\rvert = E_0\sqrt{\frac{\epsilon_0\epsilon_r}{\mu_0}}\sin(k_x x)\sin(k_y y - \omega t)$
TE-odd $k_x = (2p+1)\frac{\pi}{d}$	$\lvert E_z(x,y,t)\rvert = E_0 \sin(k_x x)\cos(k_y y - \omega t)$ $\lvert H_x(x,y,t)\rvert = E_0\sqrt{\frac{\epsilon_0\epsilon_r}{\mu_0}}\sin(k_x x)\cos(k_y y - \omega t)$ $\lvert H_y(x,y,t)\rvert = E_0\sqrt{\frac{\epsilon_0\epsilon_r}{\mu_0}}\cos(k_x x)\sin(k_y y - \omega t)$
TM-even $k_x = (2p+1)\frac{\pi}{d}$	$\lvert H_z(x,y,t)\rvert = H_0 \cos(k_x x)\cos(k_y y - \omega t)$ $\lvert E_x(x,y,t)\rvert = -H_0\sqrt{\frac{\mu_0}{\epsilon_0\epsilon_r}}\cos(k_x x)\cos(k_y y - \omega t)$ $\lvert E_y(x,y,t)\rvert = -H_0\sqrt{\frac{\mu_0}{\epsilon_0\epsilon_r}}\sin(k_x x)\sin(k_y y - \omega t)$
TM-odd $k_x = 2(p+1)\frac{\pi}{d}$	$\lvert H_z(x,y,t)\rvert = H_0 \sin(k_x x)\cos(k_y y - \omega t)$ $\lvert E_x(x,y,t)\rvert = -H_0\sqrt{\frac{\mu_0}{\epsilon_0\epsilon_r}}\sin(k_x x)\cos(k_y y - \omega t)$ $\lvert E_y(x,y,t)\rvert = H_0\sqrt{\frac{\mu_0}{\epsilon_0\epsilon_r}}\cos(k_x x)\sin(k_y y - \omega t)$

Table 5.1: Field solutions for a waveguide with perfect magnetic conductor boundary conditions. $p = 0, 1, 2, \ldots$ for all, and higher integers indicate higher order modes.

Dispersion Relation

The dispersion relation is given by equating the total wavevector, $k = \sqrt{k_x^2 + k_y^2}$, with $\sqrt{\varepsilon_r}\omega/c_o$. Substituting in for k_x from the solutions in Table 5.1, we can write the dispersion relations as follows:

$$k_y(\omega) = \sqrt{\left(\frac{\varepsilon_r\omega}{c_0}\right)^2 - \left(\frac{2(p+1)\pi}{d}\right)^2}, \tag{5.11}$$

$$\omega(k_y) = \frac{c_0}{\sqrt{\varepsilon}}\sqrt{k_y^2 + \left(\frac{2(p+1)\pi}{d}\right)^2}, \tag{5.12}$$

for even TE modes or odd TM modes, and

$$k_y(\omega) = \sqrt{\left(\frac{\varepsilon_r\omega}{c_0}\right)^2 - \left(\frac{2(p+1)\pi}{d}\right)^2}, \tag{5.13}$$

$$\omega(k_y) = \frac{c_0}{\sqrt{\varepsilon}}\sqrt{k_y^2 + \left(\frac{(2p+1)\pi}{d}\right)^2}, \tag{5.14}$$

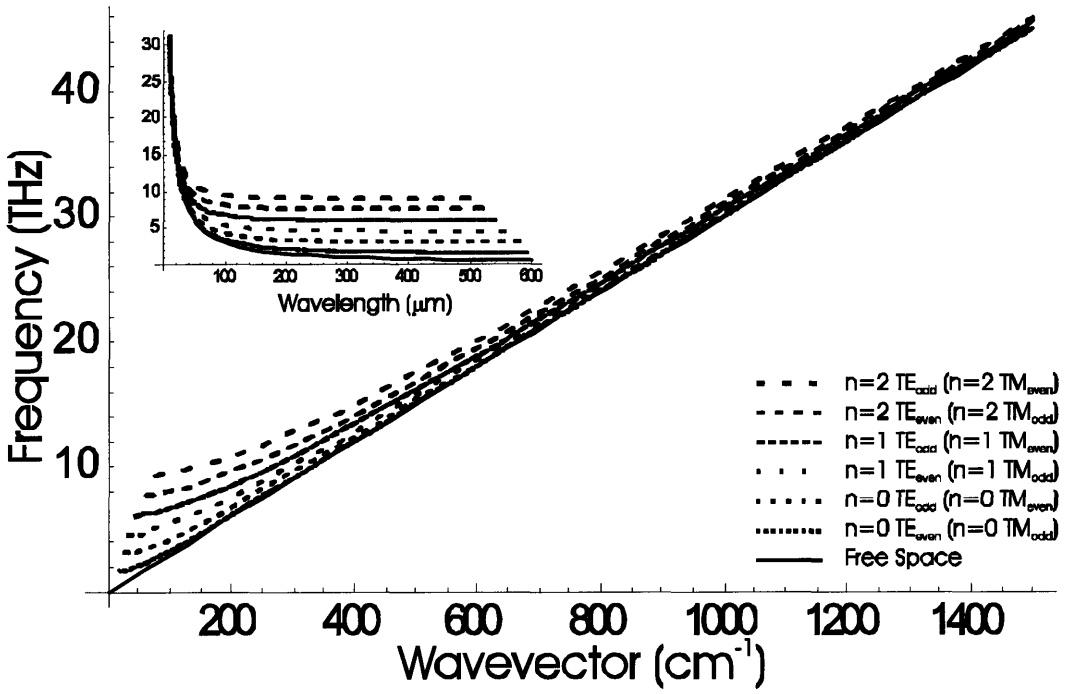

Figure 5-2: Dispersion relation for a 100 μm thick linear dielectric waveguide, $\varepsilon_r = 1$, with PMC boundary conditions. Shown are the first three even and odd modes. The inset shows the same graph plotted versus wavelength instead of wavevector.

for odd TE modes and even TM modes. The dispersion relation for a PMC waveguide in air is shown in Fig. 5-2, in which several waveguide modes are shown.

From inspection of Eq. (5.11) or (5.13), it is apparent that something unusual happens when the terms under the square root become less than zero. This phenomenon is referred to as cutoff, in which the field solutions are no longer propagating waves. The cutoff frequencies are given by

$$\omega_{co} = (2p+1)\frac{c_0\pi}{d\sqrt{\varepsilon_r}}, \tag{5.15}$$

for odd TE modes or even TM modes, and

$$\omega_{co} = 2(p+1)\frac{c_0\pi}{d\sqrt{\varepsilon_r}}, \tag{5.16}$$

for even TE modes or odd TM modes.

It immediately follows that the phase velocities, given by the relation,

$$v_p = \frac{c_0}{\sqrt{\varepsilon_r}} \sqrt{1 + \left(\frac{k_x}{k_y}\right)^2}, \tag{5.17}$$

are:

$$v_p = \frac{c_0}{\sqrt{\varepsilon_r}} \sqrt{1 + \left(\frac{(2p+1)\pi}{k_y d}\right)^2}, \tag{5.18}$$

for odd TE modes or even TM modes, and

$$v_p = \frac{c_0}{\sqrt{\varepsilon_r}} \sqrt{1 + \left(\frac{2(p+1)\pi}{k_y d}\right)^2}, \tag{5.19}$$

for even TE modes or odd TM modes.

Finally, the group velocities, which determine the curvature of the dispersion relations and are given by,

$$v_g = \frac{c_0}{\sqrt{\varepsilon_r}} \frac{1}{\sqrt{1 + \left(\frac{k_x}{k_y}\right)^2}}, \tag{5.20}$$

are:

$$v_g = \frac{c_0}{\sqrt{\varepsilon}} \frac{1}{\sqrt{1 + \left(\frac{(2p+1)\pi}{k_y d}\right)^2}}, \tag{5.21}$$

for odd TE modes or even TM modes, and

$$v_g = \frac{c_0}{\sqrt{\varepsilon_r}} \frac{1}{\sqrt{1 + \left(\frac{2(p+1)\pi}{k_y d}\right)^2}}, \tag{5.22}$$

for even TE modes or odd TM modes.

These metrics are employed in section 5.3.2 to explore limiting conditions in a polaritonic waveguide. Further, the PMC solutions are useful for describing polaritonic waveguides in which the wavepacket is confined mostly within the waveguide itself. As we shall see next, this high degree of confinement is not always the case.

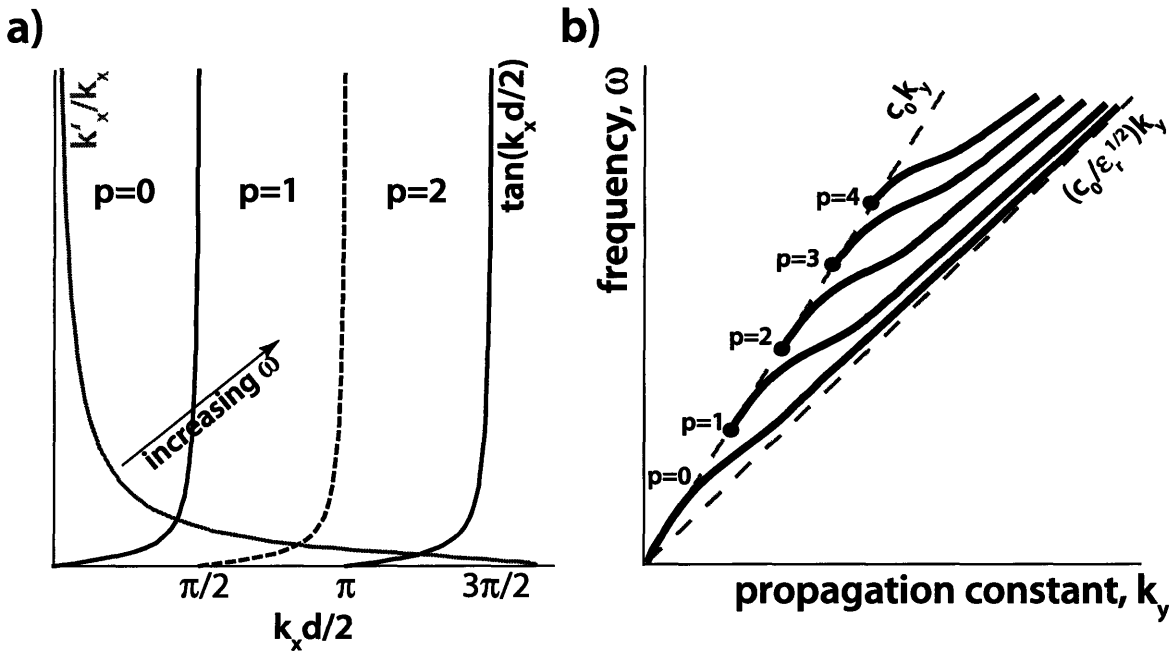

Figure 5-3: a) Transcendental solutions to Eqs. (5.30) and (5.32) obtained by locating their intersection points. b) The dispersion relation resulting from solutions from a) evaluated for every frequency.

5.1.2 Dielectric Slab Waveguide

In a dielectric slab waveguide, the inside of the waveguide is referred to as the core, and the exterior region is referred to as the cladding. The core is the same as it was for the PMC problem, but the cladding is now assumed to be just air, providing a dielectric contrast of ε_r-to-1 at the interface between the two. Waves inside the core that propagate with an angle greater than the critical angle, given by

$$\cos(\theta_c) = \frac{n_{\text{cladding}}}{n_{\text{core}}}, \tag{5.23}$$

where n_{cladding} is the index of refraction in air and is equal to 1, and $n_{\text{core}} = \sqrt{\varepsilon_r}$ is the index of refraction in the core, are confined by total internal reflection. The reflected waves at the interface undergo a phase shift that increases from 0 to π as grazing incidence is approached. Further, the reflection coefficient is unity and transmission is zero. Leaky modes, in which

the angle of incidence is less than the critical angle, are not considered here.

Solutions for a TE dielectric slab waveguide are determined in the same way as they were in the PMC problem, except instead of applying PMC boundary conditions, the general condition for reflection and transmission at a dielectric interface is required, which stipulates that tangential fields must be continuous across the interfaces.

Since fields can exist in core and cladding, this time we must consider solutions in both regions. Plane wave solutions in the core, $|x| < d/2$, take the form,

$$E_z(x,y,t) = E_0 \cos k_x^{\text{core}} x e^{i(-k_y y+\omega t)}\hat{k}, \tag{5.24}$$

$$H_x(x,y,t) = -E_0\sqrt{\frac{\epsilon_0\varepsilon_r}{\mu_0}} \cos k_x x e^{i(-k_y y+\omega t)}\hat{k}, \tag{5.25}$$

$$H_y(x,y,t) = -E_0\sqrt{\frac{\epsilon_0\varepsilon_r}{\mu_0}} \sin k_x x e^{i(-k_y y+\omega t)}\hat{k}, \tag{5.26}$$

where the magnetic field follows from Faraday's law (see Eq. (2.24)). Solutions in the cladding, $x > d/2$ and $x < -d/2$, take the form,

$$E_z(x,y,t) = E_0 e^{\pm k_x' x} e^{i(-k_y y+\omega t)}\hat{k}, \tag{5.27}$$

$$H_x(x,y,t) = -E_0\sqrt{\frac{\epsilon_0\varepsilon_r}{\mu_0}} e^{\pm k_x' x} e^{i(-k_y y+\omega t)}\hat{k}, \tag{5.28}$$

$$H_y(x,y,t) = \pm E_0\sqrt{\frac{\epsilon_0\varepsilon_r}{\mu_0}} e^{\pm k_x' x} e^{i(-k_y y+\omega t)}\hat{k}, \tag{5.29}$$

where the $\pm$ is + for $x < -d/2$ and - for $x > d/2$.

As before, we can exploit symmetry by matching the boundary conditions only at $x = d/2$. We then find that:

$$\tan(k_x \frac{d}{2}) = \frac{k_x'}{k_x}. \tag{5.30}$$

Further, from the wave equation, Eq. (5.1), it can be shown that,

$$k_y^2 - (k_x')^2 = \omega^2\mu_0\epsilon_0, k_y^2 - k_x^2 = \omega^2\mu_0\epsilon_0\varepsilon_r. \tag{5.31}$$

Combining these last two equations, we can write:

$$\frac{k_x'}{k_x} = \sqrt{\frac{\omega^2 \mu_0 \epsilon_0 (\varepsilon_r - 1)}{k_x^2} - 1}. \tag{5.32}$$

Solutions to the dielectric slab waveguide are manifest in the set of transcendental equations, Eqs. (5.30) and (5.32), which must be simultaneously satisfiedby constructing a graph, as shown in Fig. 5-3(a), to determine the intersection of these two curves. Notice that as ω decreases, k_x'/k_x moves toward the origin and no further intersections are possible, except with the first tangent function. This solution corresponds to the lowest order mode (p=0), which has no cutoff frequency; all the other modes do.

Figure 5-3(b) illustrates the dispersion relation given by Eq. (5.31), with the value of k_x evaluated for every frequency from Fig. 5-3(a). The phase velocity $v_p = \frac{\omega}{k_y}$ and the group velocity, $v_g = \frac{\partial \omega}{\partial k_y}$ may also be obtained from Eq. (5.31) in a similar fashion. Unfortunately, none of these useful metrics are amenable to closed-form solution, making the dielectric slab waveguide considerably less tractable than PMC waveguides.

5.2 100μm$\leq$Crystal Thickness$\leq$500μm

In this section, we consider effects that are not necessarily related to the waveguide regime, but instead are related to the frequent phonon-polariton reflections from the front and back faces of a thin crystal that are precursors to waveguide mode formation.

5.2.1 Signal Beating in Thin Crystals

As evident from table 4.1, the forward propagation angles for low frequency phonon-polaritons in $LiNbO_3$ and $LiTaO_3$ are already larger than the critical angles for total internal reflection; that is, phonon-polaritons are confined within the crystal by total internal reflections from the front and back crystal faces. As a result, the direction of the wavevector alternates between the two possible values shown in fig. 5-4, where the front face corresponds to the

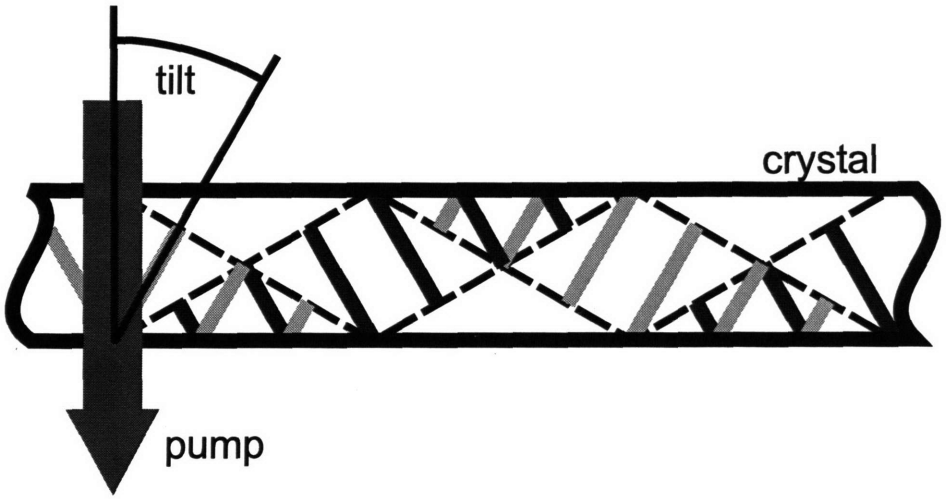

Figure 5-4: The phonon-polariton wavevector is tilted because the excitation at the back surface is delayed by the time the pump pulse takes to travel through the crystal. The vertical component of the wavevector alternates upon total internal reflection and the wavepacket remains confined in the host material.

bottom of the figure and the back face to the top. This effect is most pronounced in thin crystals, where the travel time from front to back is short compared to the phonon-polariton lifetime.

During excitation through ISRS, a phonon-polariton wavepacket travels with a component in the forward direction. Directly after the excitation pulse exits the crystal, the wavepacket begins to reflect, through total internal reflection, from the front face, which causes the signal detected through real-space imaging to slowly disappear. The reflected portion, which travels in the backward direction, is spatially displaced from the forward-propagating portion due to the lateral propagation component of the wavepacket. Just as the initial forward wavepacket is completely reflected, the reflected wavepacket traveling opposite to it begins to reflect from the back face of the crystal, and a forward-propagating wavepacket begins to emerge there, again appearing displaced in real-space imaging. Maxima in probe signal intensity appear when the wavepacket is either propagating entirely in the forward or backward direction; however, the maximum occurring for the backward traveling wavepacket is always less intense than that for the forward traveling wavepacket due

to phase-matching.

Real-space imaging with 400 nm tilted probe pulses, which was discussed in chapter 4, was performed in 500, 250, and 100 μm thick $LiNbO_3$ to measure and visualize this effect. Broadband phonon-polaritons (600 GHz central frequency) in the form of line excitations were generated in each crystal.

The recurrence times of reflections from front and back crystal faces, which appear in real-space imaging, are easily calculated as follows:

$$t_{\text{rec}} = \frac{n(\omega)d}{c_0 \sin(\theta)}, \tag{5.33}$$

where $n(\omega)$ is calculated with the aid of Eq. (2.47), and the forward propagation angle, θ is $\sim 26^o$. Using 600 GHz for the central frequency, we calculate recurrence times of approximately 20, 10, and 4 picoseconds in the 500, 250, and 100 μm thick crystals, respectively. These times correspond to the round trip time through a distance equal to the crystal thickness with the forward velocity obtained by projecting the phonon-polariton velocity along the x-axis.

Similarly, the observed signal displacements can also be calculated through a simple trigonometric relation,

$$l_{\text{rec}} = 2d \tan(\theta), \tag{5.34}$$

where θ is the forward propagation angle. Using 26^o for θ and again substituting the three sample thicknesses for d, we find displacements of 487, 243, and 97 μm, which is nearly equal to the sample thickness in each, due to the forward propagation angle.

The experimentally observed recurrence times and signal displacements are illustrated by the space-time plots in Fig. 5-5, and are in excellent agreement with the calculated values. Note that the discrepancy in the recurrence time for the 500 μm thick crystal arises because only two recurrences were recorded.

Though waveguide dispersion begins to appear in the thinnest sample (100 μm) considered here, in which the central phonon-polariton wavelength is just short of 100 μm, we

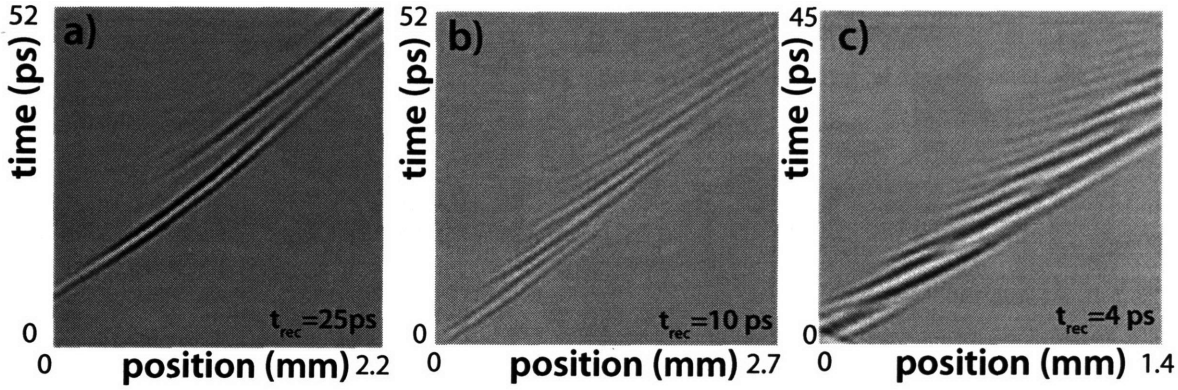

Figure 5-5: Measured signal for a) 500, b) 250, and c) 100 μm thick $LiNbO_3$ crystals. The signal disappears and reappears as the phonon-polariton bounces between the front and the back surface. Observed recurrence times are indicated in lower right hand corners of each frame.

defer discussion of this until section 5.4, where much thinner crystals are employed and the waveguide characteristics are much more dramatic. The three crystals considered here do, however, provide a useful illustration of the formation of waveguide modes from the front and back face reflections, which show the recurrence frequency approaching that of the phonon-polariton frequency as the waveguide regime is approached. This topic is explored in more detail through FDTD simulations in section 5.3. Finally, we note that a proper account of the beating apparent in thin crystals is important, as it has already been misidentified as lattice anharmonicity elsewhere [4].

5.2.2 Phonon-Polariton Tunneling

The frequent reflections encountered in thin crystals can be exploited to couple phonon-polaritons out of one crystal and into another through phonon-polariton tunneling.

Though there are no propagating waves exterior to the crystal in total internal reflection, there are evanescent fields that decay exponentially away from the interface and into the adjoining material. In most cases, the adjoining material is just air, but another ferroelectric crystal can be brought into close proximity such that phonon-polaritons in the first crystal may be coupled to lattice vibrations in the second, which in turn form phonon-polaritons.

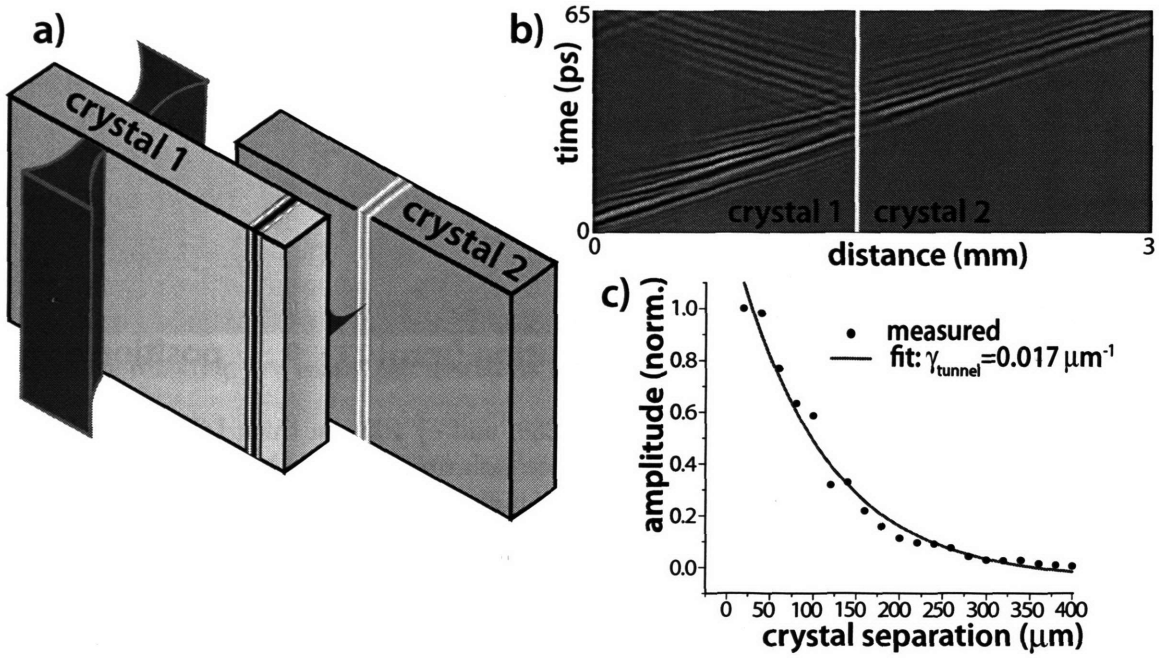

Figure 5-6: a) Phonon-polariton tunneling setup. Broadband phonon-polaritons are generated in crystal 1 through ISRS and after propagating into the crystal overlap region, they tunnel into crystal 2. Depending on the distance between the two crystals a substantial fraction of the amplitude may tunnel to the second crystal. b) Space-time plot of raw data for 50 μm separation. Phonon-polaritons impinging on the back face of crystal 1 reflect with some portion tunneling into crystal 2. c) Results from several measurements taken with increasing crystal separation. Amplitudes are normalized to the amplitude of the smallest separation. The decay constant resulting from a fit to the form in Eq. (5.35) is indicated in the figure.

A schematic illustration of this setup is shown in Fig. 5-6(a). As the second crystal approaches the first, tunneling between the two crystals becomes increasingly probable, and the amplitude observed in the second crystal E_2 increases according to

$$E_2 = E_1 e^{-\gamma_{\text{tunnel}} d_{\text{sep}}}, \tag{5.35}$$

where d_{sep} is the separation between the two crystals, and γ_{tunnel} the decay constant.

Tunneling experiments were performed by generating broadband phonon-polaritons in the first crystal, which was placed as shown in the figure, and observing coupling into the second

through real-space imaging. Both crystals were 250 μm thick. The excitation region was chosen such that the phonon-polariton wavepacket was propagating in the forward direction, which facilitates coupling into the second crystal as the incident wavepacket reflects from the front face. To ensure that no phonon-polaritons were generated in the second crystal, the excitation beam was placed sufficiently far away. Consequently, by the time the phonon-polariton wavepacket reached the coupling region, it had already reflected once from the front and back faces. A representative space-time plot from the experiment is shown in Fig. 5-6(b). Both the reflected wavepacket in the first crystal and the tunneled wavepacket in the second are clearly visible.

Figure 5-6(c) shows the normalized amplitude of the phonon-polariton wavepacket in the second crystal as a function of the distance between the two crystals. Performing a fit to the form in Eq. (5.35), a decay constant of $\beta = 0.017$ μm^{-1} was extracted. This value can be checked with theoretical considerations,

$$\beta = \frac{\omega}{n(\omega)c_0}\sqrt{\frac{n(\omega)^2 - 1}{1 - \sin^2\theta_{\text{inc}}}}, \tag{5.36}$$

where θ_{inc} is the incident angle of the phonon-polariton wavepacket. The wavepacket generated had approximately a 180 μm central wavelength and 390 GHz central frequency. Using these values, the index of refraction from Eq. (2.47), and an incident angle of 64^o determined by the forward propagation angle in Table 4.1, Eq. (5.36) gives a decay constant of 0.018 μm^{-1}, which the experimental decay constant is in close agreement with.

Potential applications of phonon-polariton tunneling include, but are not limited to, device integration and near field spectroscopy and microscopy. Tunneling in crystals sufficiently thin for the waveguide regime, discussed below, should display the characteristic sinusoidal coupling of power as a function of time [35], but experiments confirming this expectation have yet to be performed.

5.3 Transition to the Waveguide Regime

One effect on phonon-polariton generation in the waveguide regime is waveguide straightening, in which the phonon-polariton wavepacket straightens out after a propagation distance of only a few wavelengths. In bulk, the forward propagation angle of phonon-polaritons is the complement of the Cherenkov angle, which is dependent on the excitation pulse group velocity and the phonon-polariton phase velocity as discussed in chapter 4. When the crystal thickness is on the order of the phonon-polariton wavelength, the forward propagation angle generated deviates from that in bulk, separating into phonon-polariton excitations in one or more of the discrete slab waveguide modes. Though each mode has no forward component, the superposition of several modes results in a non-zero forward propagation angle that is less than that given by the Cherenkov cone. The larger the wavelength, with respect to crystal thickness, the fewer the modes that are excited, and the fewer modes excited, the smaller the forward propagation angle becomes. For single mode excitation, the forward angle is zero.

5.3.1 Waveguide Straightening

To illustrate waveguide straightening, we consider simulated broadband phonon-polariton generation and propagation of 300, 500 and 700 GHz single-cycle phonon-polaritons in a 250 μm thick $LiNbO_3$ crystal (See Fig. 5-7). Even at this thickness, the forward propagation angle is not given by its bulk value. In the figure, the optic axis is out of the page, and the excitation pulse traversed the thin dimension in the plane of the figure. The images are taken a short time after the excitation, such that the phonon-polaritons had time to travel distances equal to several times their wavelengths.

The 700 GHz phonon-polaritons have a wavelength, λ_{pol}, of approximately 80 μm, or relative to the crystal thickness, $\lambda_{pol}=3d$. The resulting Cherenkov cone forms after a propagation distance of a couple of wavelengths and was found to be $\sim$20 degrees, which is six degrees less than the bulk value. Very short wavelengths yield asymptotically the bulk forward propagation angle. The lowest frequency (300 GHz) phonon-polaritons shown have

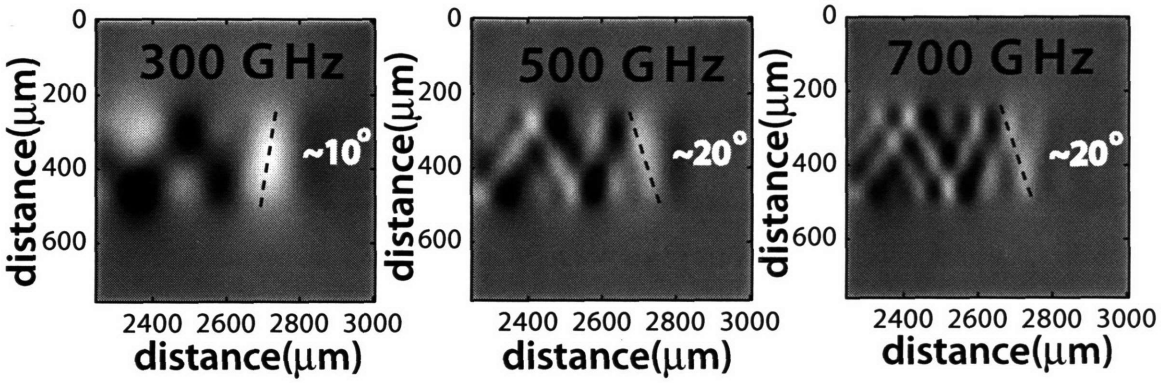

Figure 5-7: Phonon-polariton propagation becomes increasingly lateral, i.e., the forward propagation angle tends toward zero as the wavelength approaches the crystal thickness. Illustrated here is the waveguide straightening associated with the slab waveguide modes in 250 μm thick $LiNbO_3$ as the phonon-polariton wavelength approaches the crystal thickness. The mode-like behavior is most apparent in the longest wavelength excitation (left).

a wavelength of approximately 200 μm, or $\lambda_{\text{pol}} \sim d$. The forward propagation angle was determined to be $\sim$10 degrees.

The multi-mode nature of the excitation is evident in the figure as phonon-polaritons in higher modes have smaller phase velocities and lag behind those in the lowest order mode. As the number of available waveguide modes becomes small, the frequency separation between modes increases, as does the difference in phase velocity. Phonon-polaritons in different modes are then able to interfere to form the nodes evident in the figure. They correspond to through-plane phonon-polariton phase lags that exceed π radians, which occur when the excitation pulse propagation time through the crystal exceeds half the phonon-polariton oscillation period. Comparing the 300, 500 and 700 GHz excitations, we can see how the nodal patterns evident in the 300 GHz excitation develop as the wavelength approaches the crystal thickness.

5.3.2 Influence of Waveguide Dispersion

Waveguide straightening is not the only effect on phonon-polaritons in the waveguide regime. Unique spatial modes arise too, but because we are unable to image the electric field in the

modal plane we do not discuss them further in this work. As a final note, these modes are easily calculable and are illustrated elsewhere [35, 84].

Another effect, which we are easily able to measure, is waveguide dispersion, which is a direct consequence of the waveguide modes resulting from interference of confined waves. Polaritonic waveguide dispersion must be modified to account for the influence of phonon-polariton dispersion. To illustrate the influence of phonon-polariton dispersion on waveguide dispersion, or vice versa, we consider limiting behavior in the phase and group velocities of the waveguide modes, and later limiting behavior in the dispersion relation itself.

The high-index contrast and nearly in phase reflections that occur above, but near, the critical angle allow us to consider polaritonic waveguide dispersion through the use of perfect magnetic boundary conditions. In the limit that the frequency goes to infinity, the wavevector also goes to infinity. Imposing this requirement on the phase velocity,

$$\lim_{k_y \to \infty} v_p = \lim_{k_y \to \infty} \frac{c_0}{n(\omega)} \sqrt{1 + \left(\frac{k_x}{k_y}\right)^2} \propto \frac{c_0}{n(\omega)}, \tag{5.37}$$

and on the group velocity,

$$\lim_{k_y \to \infty} v_g = \lim_{k_y \to \infty} \frac{c_0}{n(\omega)} \frac{1}{\sqrt{1 + \left(\frac{k_x}{k_y}\right)^2}} \propto \frac{c_0}{n(\omega)}, \tag{5.38}$$

which shows that in the high frequency limit, phonon-polariton dispersion is dominant.

In considering the low frequency limit, it is useful to observe that the wavevector in the confined dimension is inversely proportional to the crystal thickness, $k_x \propto d^{-1}$, and in the unconfined direction, it is inversely proportional to the wavelength, $k_y \propto \lambda^{-1}$, due to waveguide straightening as discussed in section 5.3.1. Substituting these relations in for the wavevectors in Eqs. (5.37) and (5.38), and taking the limit as the wavelength approaches

infinity, which corresponds to the low frequency limit, we find that,

$$\lim_{\lambda\to\infty} v_p \propto \lim_{\lambda\to\infty} \frac{c_0}{n(\omega)}\sqrt{1+\frac{\lambda}{d}} \propto \lambda, \tag{5.39}$$

$$\lim_{\lambda\to\infty} v_g \propto \lim_{\lambda\to\infty} \frac{c_0}{n(\omega)}\frac{1}{\sqrt{1+\frac{\lambda}{d}}} \propto \frac{1}{\lambda}. \tag{5.40}$$

Furthermore, the frequency can be shown to be inversely proportional to the crystal thickness through the limit as k_y goes to zero,

$$\lim_{k_y\to 0} \omega = \lim_{k_y\to 0} \frac{c_0}{n(\omega)}\sqrt{k_y^2+k_x^2} \propto \frac{c_0}{\sqrt{\varepsilon_0}}k_x \propto \frac{c_0}{\sqrt{\varepsilon_0}d}. \tag{5.41}$$

There is a discrepancy with the previous analysis, which must be corrected for before proceeding. The discrepancy is in the failure to account for the fields extending into the cladding region (air) at low frequencies. The fields external to the waveguide core result in a decrease in the index of refraction due to effective index averaging of the power flow internal and external to the waveguide. In this case, the dielectric slab waveguide modes, discussed previously in this chapter, must be employed. Since the fields extend into the cladding only at the lowest frequencies, we have to amend only the low frequency limit from our earlier analysis.

When the wavelength is very long with respect to the slab thickness, we may make the approximation $\tan(k_x d/2) \approx k_x d/2$ for the lowest order mode (p=0). Using this in Eqs. (5.30) and (5.32) and replacing ε_r with ε_0, we find,

$$(\omega^2\mu_0\epsilon_0(\varepsilon_0-1)-k_x^2)\Big(\frac{d}{2}\Big)^2 \simeq \Big(\frac{k_x d}{2}\Big)^4. \tag{5.42}$$

Neglecting $\left(\frac{k_x d}{2}\right)^4$ compared to $\left(\frac{k_x d}{2}\right)^2$ we can write,

$$k_x^2 = \omega^2\mu_0\epsilon_0\Big(\varepsilon_0-1\Big). \tag{5.43}$$

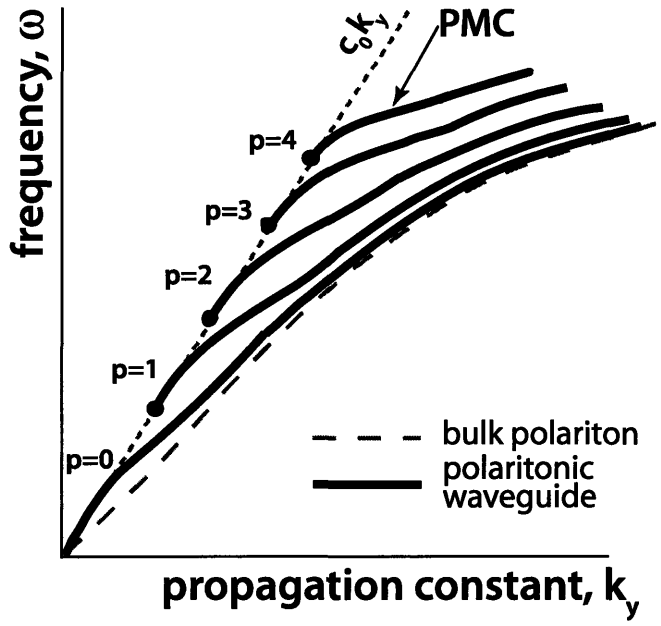

Figure 5-8: Illustrated polaritonic waveguide dispersion sketches constructed by analysis of limiting behavior in PMC waveguides (large values for the propagation constant starting in the flat regions) and dielectric slab waveguides (small values for the propagation constant). As the propagation constant decreases, dispersion approaches that of bulk phonon-polaritons.

Further, from Eq. (5.31), it is simple to show that,

$$k_y \simeq \frac{\omega}{c_0}, \tag{5.44}$$

which is just the dispersion relation in the cladding (air). Thus, the dispersive properties at long wavelengths are essentially due to the cladding layer of air surrounding the crystal, which may be explained by the fact that most of the field at extremely low frequencies resides outside of the core and in the cladding, a result later confirmed with FDTD simulations.

When ω approaches infinity, it can be shown that $k_x \frac{d}{2}$ approaches $\frac{\pi}{2}$, and we find from Eq. (5.31) that,

$$k_y \simeq \frac{\omega\sqrt{\varepsilon_\infty}}{c_0}, \tag{5.45}$$

which indicates that at high frequencies, propagation is confined to the waveguide core and material dispersion dominates, just as we found for the PMC case. Based on the low and

high frequency limits, we intuit that intermediate frequencies will be similar to those in bulk material with increasing deviation as the low frequency limit is approached. Polaritonic waveguide dispersion relations can be constructed from the limiting behavior graphically, by joining the regions for the two limiting cases smoothly, as was done in Fig. 5-8. In joining them, we assumed a flattening of the group velocity, corresponding to the low frequency PMC limit, prior to the low frequency limit for the dielectric slab. This region corresponds to wavelengths long enough for strong confinement effects, but short enough that the field is still predominantly within the waveguide core.

This analysis is convenient for understanding the limiting behavior of polaritonic waveguides, but the point at which the two limits are spliced is somewhat murky. We postulate, however, that it occurs where the phonon-polariton wavelength is near that of the crystal thickness—a hypothesis that is supported by our experimental findings.

5.4 Thin Films

There is currently intense interest in thin film electro-optic crystals, because of their potential uses in integrated photonic and optoelectronic circuits and devices. $LiNbO_3$ is particularly attractive given its large electro-optic and dielectric constants. However, $LiNbO_3$ films produced through rf sputtering, chemical vapor deposition, and sol-gel methods are polycrystalline and exhibit substantial reductions in the useful optical properties enjoyed in bulk single-crystalline $LiNbO_3$ [54]. Crystal ion slicing (CIS) utilizes high-energy ion implantation of bulk single crystals such as $LiNbO_3$ to allow the exfoliation of low-loss, thin (≤ 10 μm) layers of optical material. Since the films retain their favorable single-crystalline properties [67, 69], they have a wide range of potential applications. A unique possibility for $LiNbO_3$ and other ferroelectric films is extension of high-speed electro-optics, through which terahertz fields may be generated, to the thin film waveguide regime. In this section, we demonstrate that possibility and characterize the terahertz dispersion properties of a 10-μm thick $LiNbO_3$ film. This is a first step toward the extension of polaritonic devices to $LiNbO_3$ films of micron thickness. To distinguish thin film dispersion from that in bulk, we compare

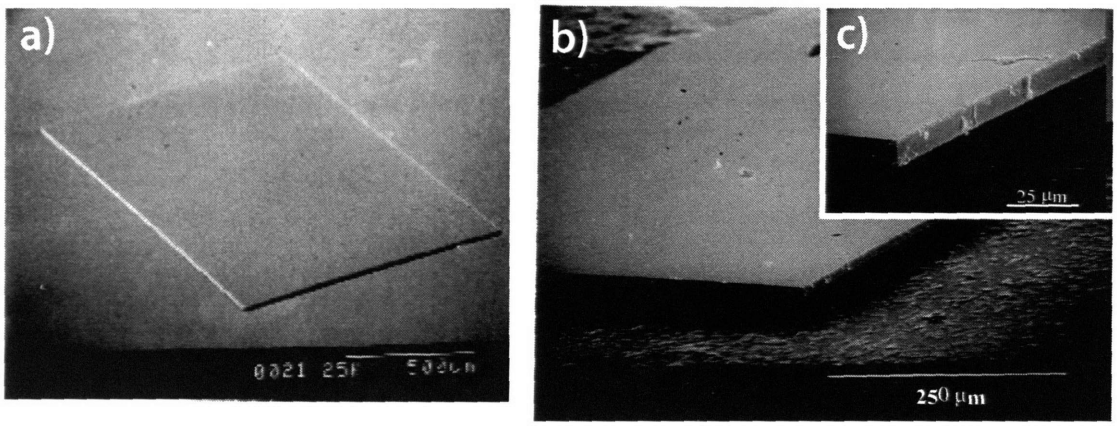

Figure 5-9: Electron micrograph of thin film fabricated by crystal ion slicing. a) 500 μm, b) 250 μm, and c) 25 μm scale. Electron micrographs provided by Richard Osgood of Columbia University.

measurements taken simultaneously in thin films and bulk.

5.4.1 Fabrication

Congruent X-cut optical grade wafers were implanted with He^+ ions at an energy of 3.8 MeV and an ion dosage of 2 x 10^{16} ions/cm^2. This implantation forms a buried damaged layer approximately 10 μm beneath the surface of the wafer. The samples were then cut into 4 mm x 4 mm rectangular pieces and cleaned thoroughly. To provide mechanical support during the rapid exfoliation procedure, the samples were temporarily bonded to a clean silicon wafer. This was done by placing the samples, implanted side down, on the silicon wafer and heating them to approximately 100 °C for more than 20 minutes. This heating generates a pyroelectric charge in the $LiNbO_3$, which then electrostatically holds the sample to the native SiO_2 layer present on the silicon wafer. Exfoliation was accomplished via thermal snapoff; the samples were rapidly annealed to 500 °C for 5 seconds. This annealing results in a dramatic separation of the top layer of the crystal as the helium ions present in the buried layer expands and builds enough pressure to separate the film from its parent crystal [67, 68]. After cooling, the temporary bond between the film and the silicon wafer was then removed with a drop of methanol, resulting in a freestanding, single-crystalline X-cut

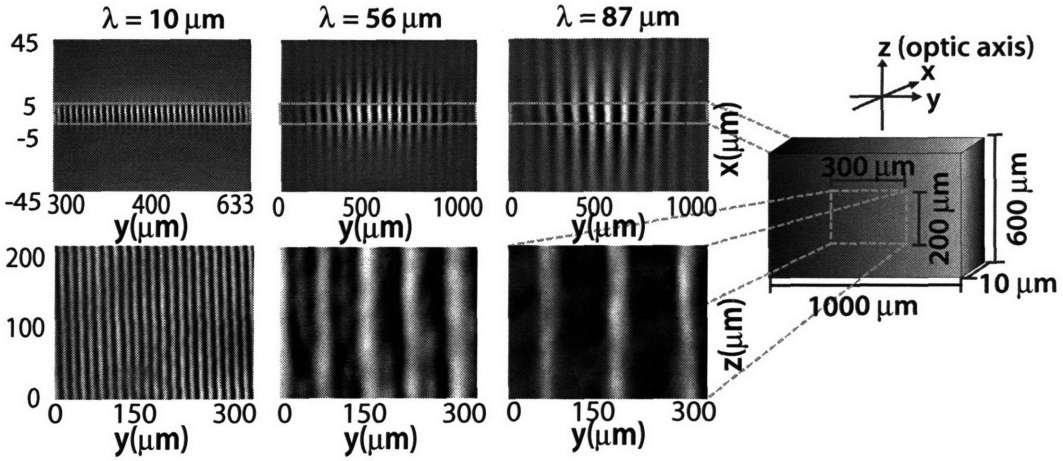

Figure 5-10: Real-space images (raw data) of phonon-polaritons with three different wavelengths in a 10-μm $LiNbO_3$ film (lower three images) and phonon-polariton electric field profiles extending through the film determined through FDTD simulations (upper three images). The electric field is polarized in the z-direction in both. The spatial periods in the phonon-polariton images give the phonon-polariton wavevector components k_y. The simulations illustrate that at wavelengths that exceed the film thickness, the field extends significantly into the cladding (air) above and below the film. Note that the vertical axes in the three pairs of images represent orthogonal sample dimensions. Orientations of the six images with respect to the film are indicated on right. The optic axis is along $\hat{z}$.

film of about 10 μm thickness. Previous work with X-cut $LiNbO_3$ CIS films has shown that the undercut roughness of such films is about 100 nm (peak-to-peak) and has demonstrated the utility of such films in real integrated optics applications [68].

The thin film samples were provided by Richard Osgood of Columbia University.

5.4.2 Dispersion

Narrowband phonon-polariton responses were generated through ISRS by crossed excitation pulses facilitated by a diffractive phase grating (see Fig. 4-1(b)) polarized parallel to the optic axis of the crystal (z-axis in Fig. 5-10), as was described in detail in chapter 4. The phonon-polariton wavevector magnitude k was varied from 600 to 10000 cm^{-1}, a range that corresponds to phonon-polariton wavelengths in the range of approximately 100 μm down to 6 μm. In terms of the crystal thickness, the wavelength was varied over a range of

$\lambda_{pol} \approx 1 - 10\ x\ d$. The total excitation pulse energy was typically about 100 μJ, and the spot size at the sample was typically about 1 mm in the grating dimension and 600 μm in the perpendicular direction.

Phonon-polaritons were probed using real-space imaging. Raw CCD camera images from phonon-polaritons with three different wavevectors are shown in Fig. 5-10. The phonon-polariton wavelength projections in the film plane were measured directly from the spatial periods in the images, using a calibration reference image. These measurements yielded the phonon-polariton wavevector components in the film plane.

As we recall from chapter 4, the phonon-polariton wavevector in bulk crystals has a significant component k_x in the forward (through-plane) direction as well as the larger component k_y (propagation constant) in the grating direction within the film plane, resulting in phase fronts that are tilted in the forward direction. The forward wavevector must be accounted for in bulk crystals in order to obtain the phonon-polariton wavevector, which is different than the grating wavevector imposed during the experiments. Meanwhile, in films whose thickness d is much less than the phonon-polariton wavelength, i.e., $kd << 1$, the phonon-polaritons are guided within the film plane with a wavevector equal to the waveguide propagation constant. Propagation predominantly in the lowest order mode of the film occurs for all wavevectors considered here. In both the film and bulk crystals, the wavelength is determined from a calibrated CCD image, but only the bulk data receives a correction to the wavevector, which is determined by the observed frequency.

In order to account for the wavevector direction and magnitude accurately, two-dimensional TM FDTD simulations that included the ISRS excitation process as well as subsequent phonon-polariton propagation were conducted, as described in chapter 3. In the simulations, just as in the experiments, the excitation pulses and the phonon-polaritons were polarized along the optic axis, and phonon data for the A_1 normal mode were used in the auxiliary equation in the algorithm in Eq. (3.14) [6]. Typical simulation results for the phonon-polariton electric fields are shown in Fig. 5-10. The results illustrate that at long wavelengths, in the $kd << 1$ limit, the phonon-polariton field extends far outside the $LiNbO_3$

crystal and into the cladding (air) above and below the film layer.

Simulations show that confinement occurs in the cross-section perpendicular to the optic axis and results in a TE waveguide mode. For the phonon-polariton wavelengths explored, which are comparable to or larger than the film thickness d, the phonon-polariton response was dominated by the lowest-order TE mode, which has no nodes in the plane of the crystal. This mode does not have a cutoff wavelength, as discussed previously, and propagation can occur for any wavelength. Simulations of short wavelengths demonstrate that the phonon-polaritons are confined well within the crystal volume and have nearly the same dispersion as in bulk. As the phonon-polariton wavelength was increased well beyond the film thickness, much of the radiation field was found to reside in the cladding, i.e., in air (See Fig. 5-10). This results in an increase in phonon-polariton phase velocity that is responsible for the deviations in dispersion from that of bulk. The forward wavevector component was also seen to change in magnitude, diminishing as the wavelength became long compared to the film thickness In this limit, the time delay and corresponding phase lag between phonon-polariton responses that originate at the front and back of the crystal are negligible compared to the oscillation period.

Experimental measurements of phonon-polariton dispersion in a thin film are shown and compared to bulk and simulations in Fig. 5-11. It is clear that deviations from bulk dispersion become more pronounced as the wavelength is increased and the limiting condition $kd << 1$ is approached, which supports our earlier hypothesis that the dispersive properties at long wavelengths are essentially due to the cladding layer of air. This finding is consistent with the simulated field profiles in the upper half of Fig. 5-10, where the field at long wavelengths can be seen to extend well outside the film boundary. The experimental and simulated dispersion are in good agreement with theoretical calculations at the beginning of this chapter.

5.4.3 Multi-Mode Behavior

To illustrate multi-mode behavior, we have made measurements in thicker films, which were not fabricated through the CIS procedure, but were instead ground and polished from bulk

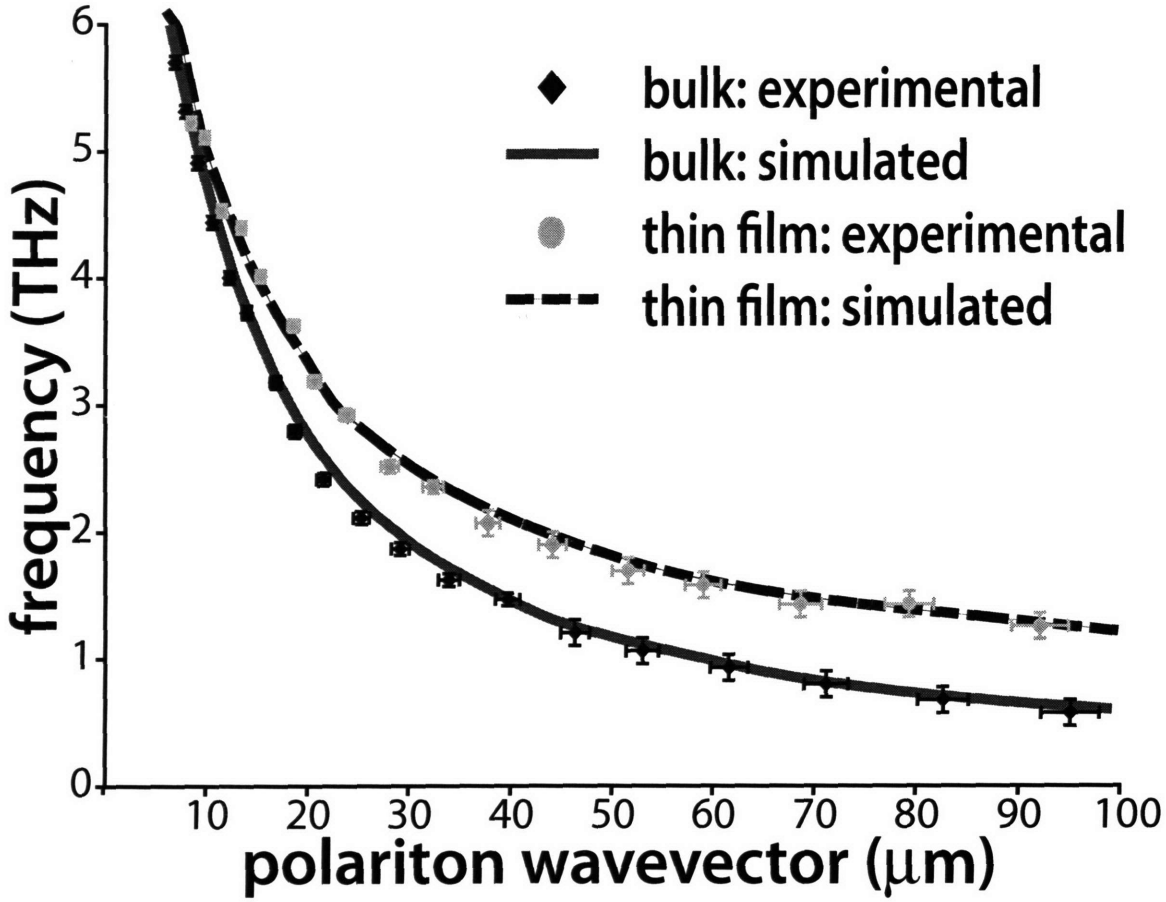

Figure 5-11: Dispersion relations for thin film (10-μm thick) and bulk (500-μm thick) $LiNbO_3$ crystals, determined from experiment (points) and simulations (curves). The increasing deviation between bulk and thin film results as the phonon-polariton wavelength increases is due to slab waveguide effects in the film.

crystals. Films as slim as 30 μm can be made in this way and are commercially available.

Broadband phonon-polaritons were generated in 34 and 50 μm thick films, and using real-space imaging, the spatiotemporal evolution of the phonon-polariton wavepacket was recorded. Because a broadband wavepacket only consists of a couple of cycles, propagation in different modes will become apparent as wavepackets in each mode separate after having propagated a sufficient distance due to the difference in group velocities for each mode.

The dispersion relations resulting from Fourier transforming the space-time plots for both films are shown in Fig. 5-12 alongside the space-time plots from which they came. Note that the wavevector in the figure is the inverse propagation constant, which is measured directly with real-space imaging. The space-time plot for the 50 μm film shows three modes, which are outlined with a white line in the figure, and show propagation at three different group and phase velocities.

Several trends apparent in the data are worth discussing in some detail. First, inspection of the space-time plots for both films indicate beating at times soon after generation, similar to that in thin crystals, discussed earlier. The beating disappears first in the thinnest film after 10-15 ps of propagation, and after 20-25 ps in the thicker film. This corresponds to interference between the different waveguide modes prior to their separation, and results in a phenomenon similar to the alternating wavevector observed in thin crystals. After they separate, it is evident that each mode propagates in the plane with no apparent alternating wavevector.

Second, comparison of the experimental dispersion relations for each film indicates that the frequency gap between modes decreases with an increase in film thickness. Intuitively this finding makes sense, since in the limit of a bulk crystal, we expect a dense manifold of modes spaced closely enough that their discreteness may be neglected and a continuum model used instead.

Third, the number of modes accessible to the wavevector range considered experimentally appears to increase with crystal thickness. Calculations confirm that only three modes are accessible for the range of wavevectors measured in the 50 μm thick film. Similarly,

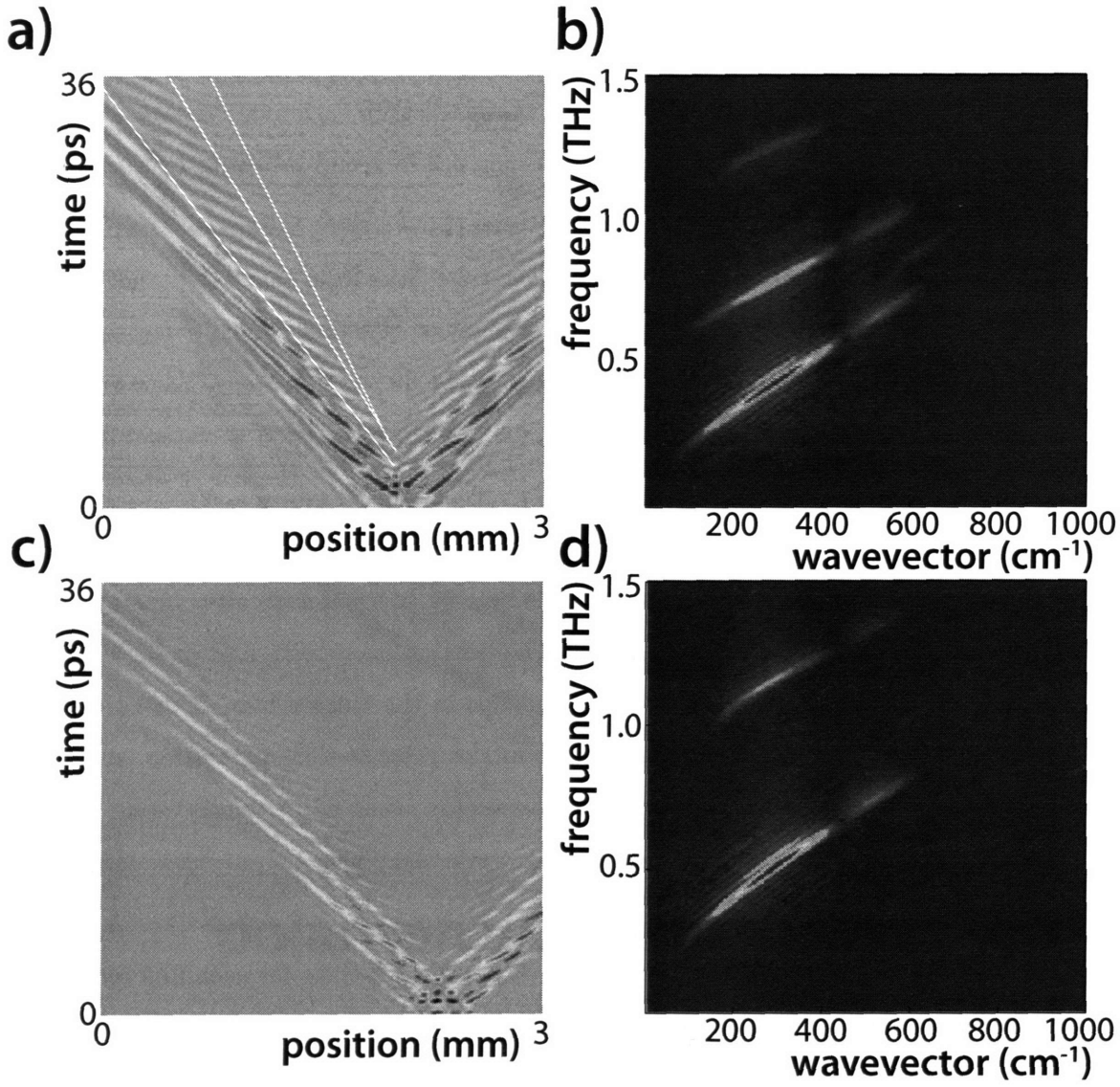

Figure 5-12: Broadband phonon-polaritons in thin films. Shown are the space-time plots for a) a 50 μm thick film and c) a 34 μm thick film, as well as the dispersion relations resulting from Fourier transforming the space-time plots for a) the 50 μm thick film and c) the 34 μm thick film.

calculations for a 34 μm thick film, indicate that only two modes should be present. This is confirmed experimentally in Fig. 5-12(c)-(d).

Fourth, the modes illustrated in Fig. 5-12(c)-(d), indicate that the group velocity is less in higher order modes, a trend that is consistent with waveguide theory. Waveguide modes can be expressed in terms of the bounce angles, measured with from the y-axis in Fig. 5-1, for the reflections responsible for interference and waveguide mode formation [73]. Higher order modes have more oblique bounce angles, which lead to longer propagation times than lower order modes for the same distance along y. That the fields extend into the cladding is a competing effect, but it appears to lose as penetration into the cladding decreases with wavelength, which in order to stay below cutoff, gets smaller for higher order modes.

Finally, just as was the case for narrowband measurements reported earlier, we see that the effective index of refraction for the low frequency excitations is smaller than that in bulk. In the 34 μm thick film, the effective indices of refraction observed were $\sim$3.0 for the lowest order mode (p=0) and $\sim$1.5 for the second mode (p=1). In the 50 μm thick film, they were $\sim$4.0 for the lowest order mode (p=0), $\sim$2.0 for the second mode (p=1), and $\sim$1.2 for the third mode (p=3).

Chapter 6

Fabrication of Patterned Materials with Femtosecond Laser Machining

This work was done in collaboration with Nikolay Stoyanov of the Massachusetts Institute of Technology.

The technique employed in this thesis for fabrication of patterned materials in $LiNbO_3$ and $LiTaO_3$ is femtosecond laser machining. Using 800 nm, 50 femtosecond (FWHM) ultrafast laser pulses with energies ranging from 10 μJ up to 350 μJ, we have fabricated polaritonic devices such as waveguides, resonators, focusing reflectors, diffractive and dispersive elements, and photonic bandgap materials. The damage feature sizes for these devices range from 10-100 μm. Furthermore, we demonstrate ablation depths as deep as 500 μm, which is five times the ablation depth achieved by other fabrication technologies [7]. Functional polaritonic structures fabricated with the techniques discussed in this chapter are demonstrated in chapter 7.

6.1 Introduction

6.1.1 Damage in $LiNbO_3$ and $LiTaO_3$

$LiNbO_3$ and $LiTaO_3$ are of considerable interest academically and industrially due to their electrooptic and acoustooptic, piezoelectric, non-linear optical, and far infrared properties. Performing controlled damage, i.e., patterning, in them has been a topic of investigation for over twenty years. In $LiNbO_3$, traditional patterning methods employed in semiconductors, like the use of photoresists with wet etching, are very slow and difficult to control [109]. These methods are most effective in z-cut crystals, whereas we are concerned mainly with X- or Y-cut crystals. Synchrotron plasma etching has been shown to produce accurate, controllable damage, though problems related to chemical deterioration and chipping of the etched surface have been observed [62]. Ultraviolet and sub-bandgap CW and pulsed laser ablation have been used for surface patterning of waveguides in $LiNbO_3$ with some success. However, the fluences required to generate even modest ablation depths cause considerable surface damage and chemical alteration deleterious to waveguide performance [15, 59]. With long pulse and CW sub-bandgap laser ablation, absorption is mediated by defects in the crystal, e.g., lithium and oxygen vacancies, and produces damage with a low repeatability due to the stochastic distribution of defects within the crystal [17]. Consequently, this method is less useful for stoichiometric $LiNbO_3$, which enjoys higher electrooptic coefficients than the congruent crystal.

Photonic devices fabricated in transparent glasses using femtosecond laser machining have been previously demonstrated [61]. In this chapter we extend the capabilities of femtosecond laser machining to include $LiNbO_3$ and $LiTaO_3$, which historically have been difficult to pattern. The photonic devices fabricated are for guidance and control of phonon-polariton waveforms. The requirements for this, as well as the machining characteristics, differ greatly from those elsewhere. To facilitate polariton guidance and manipulation within a crystal, damage that extends all the way through the thickness of the crystal is required. In many cases, thicker crystals are desirable because they offer more distance over which a signal may

be generated, increasing the phonon-polariton intensity and signal strength.

Aside from our results here, the largest ablation depth reported for $LiNbO_3$ is 150 μm [7]. The technique employed a patterned photoresist on periodically poled z-cut $LiNbO_3$. The preferential etching of the -Z face was exploited to produce the $\sim$150 μm deep grooves, but only after 20 hours in a heated hydrofluoric and nitric acid solution. This should not, however, be possible in X- or Y-cut $LiNbO_3$ and $LiTaO_3$. Ablation depths available to X- or Y-cut crystals through technologies other than that demonstrated in this chapter are on the order of a few microns. Such depths would not be acceptable for our needs, even in the thinnest crystals and films considered in this thesis.

6.1.2 Fabrication Requirements for Polaritonic Devices

Polaritonic devices, which guide and control phonon-polaritons with wavelengths ranging from 5-200 μm, require damage feature sizes on roughly the same scale as the wavelength. Since phonon-polariton propagation takes place not only in the plane, but throughout the full depth of the crystal as well (see chapter 4), patterning in the plane of the crystal face that extends throughout the depth of the crystal is required. Furthermore, it is important that regions outside of that intended for damage remain chemically unaltered and of pristine optical quality to ensure that phonon-polariton generation and detection are comparable to those achieved in unpatterned crystals. Photonic bandgap materials, which are fabricated by machining a periodic array of "air" holes in the crystal face, require a high degree of precision in the imposed periodicity for operation. This requirement places an addition constraint on fabrication, in that it requires damage with a high degree of repeatability.

Specifically, feature size requirements for patterning structures on the face of a ferroelectric crystal for polaritonic device fabrication are in the range of 1-50 μm. Additionally, the patterned features must extend uniformly throughout the thickness of the crystals, which are typically 10-500 μm thick.

These are the goals that that we have strived to achieve in the work presented in this chapter. We show that femtosecond laser machining, using the techniques presented here, is

suitable for meeting these requirements.

6.2 Femtosecond and Picosecond Laser Machining

Laser ablation is divided into two regimes: long pulse and short pulse ablation. Long pulse laser ablation involves Q-switched pulses of duration >10 ps, while short pulse ablation pulse durations are typically on the order of 50-100 femtoseconds. Common to both is that energy from the laser field is transferred to the material, resulting in damage that completely removes the material in the laser focus region. The two regimes differ in the mechanism by which energy is deposited and material is ejected, as illustrated below.

6.2.1 Picosecond Laser Machining

Long pulse lasers typically transfer energy to the lattice through heating. Since absorption cross-sections are particularly low for transparent materials, large laser fluences are typically required to initiate the ablation process. Within the working region, which corresponds to the laser spot focal volume, the temperature is raised sufficiently to generate a pressure wave that removes material as the wave travels toward the surface. In brief, the mechanism for long pulse ablation is as follows:

- Free electrons within the laser spot are heated via a Coulomb interaction with the electric field of the laser pulse. If the wavelength is within the bandgap of the crystal, then carrier electrons may be promoted from the valence band directly. Defect sites within the lattice can facilitate absorption by providing loosely bound electrons.

- Some of the energy from the hot electrons goes into heating the lattice via electron-phonon coupling, and some goes into generating more free electrons.

- Within the working region, the lattice temperature grows until the lattice is sufficiently destabilized as to initiate ejection of the lattice atoms/ions. As the local lattice temperature elevates, some heat diffuses into the surrounding area, creating what is known

as a heat-affected zone.

- When many lattice sites are destabilized, the ejected atoms/ions initiate a pressure wave, which can either form a voxel (a small rarefied region beneath the crystal surface and within the bulk) or cause complete ablation, resulting in complete removal of the material in the heated region. Ejection takes the path of least resistance (usually toward the nearest surface), resulting in a material void that starts at the surface and penetrates into the crystal along the laser beam path.

Because picosecond pulse durations are comparable to or greater than typical heat diffusion times away from the laser spot size, extensive collateral damage from heating usually results. In transparent crystals, damage repeatability is poor because of the inhomogeneous and sparse distribution of free electrons and defect sites available to initiate the ablation process [17]. In some cases, surface shock waves, associated with heat diffusion, can cause catastrophic surface delamination [1]. Further, micro-cracks and recast layers, or slag, can form in the heat-affected zone [1].

Features like those listed above are detrimental to the fabrication of optical grade components. Even if the lattice chemical composition is unchanged, melting can destroy the single crystalline nature of the material in the machined region, altering its optical and electrical properties. Alterations such as these can destroy the vibrational normal modes responsible for phonon-polariton generation and propagation [59]. The cumulative effects of these processes, related to heat diffusion, make picosecond laser machining unsuitable for polaritonic device fabrication.

6.2.2 Femtosecond Laser Machining

The mechanism for femtosecond laser ablation is not lattice heating. Instead a plasma that destabilizes the crystal lattice, eventually resulting in ejection of the remaining ions, is generated by the intense electric fields characteristic of femtosecond laser pulses. Briefly, this mechanism is as follows:

- Valence electrons are promoted to the conduction band through multiphoton or tunneling ionization. Ionization takes place uniformly throughout the portion of the working region containing sufficient intensity to initiate either of these processes [74].
- The heated electrons form a plasma on the surface of the material.
- Electron-electron collisions, electron-phonon collisions, and overwhelming electrostatic forces facilitate local destabilization of the lattice and avalanche ionization [1].

Damage through femtosecond laser machining is highly repeatable because ablation takes place exclusively in the portion of the working region with sufficient intensity for either multiphoton or tunneling ionization. The distinction between multiphoton and tunneling ionization is that the former is related to the simultaneous absorption of sufficient photon energy to promote a valence band electron into the conduction band, and the latter is related to a reduced tunneling barrier facilitated by the extreme instantaneous intensity of the femtosecond pulse [74]. Heat diffusion is minimized as the laser pulse duration is much shorter than the characteristic time scales for thermal transport away from the irradiated region.

The damage thresholds in most materials are low enough that even a Ti:Sapphire oscillator is sufficient to induce damage. However, the work in this chapter utilizes amplified pulses, and the fluences employed here greatly exceed the material damage threshold for $LiNbO_3$ and $LiTaO_3$. Such high fluences are necessary to achieve uniform damage that extends throughout the crystal thickness.

A detailed comparison of long versus short laser pulse machining is available online [1]. The physics behind femtosecond pulse ablation and optical breakdown is described in detail elsewhere [33, 74, 92].

6.2.3 Confocal Optics

In this chapter, we consider the effect of focusing a Gaussian beam into a crystal using a microscope objective. A thorough exposition of confocal optics is available elsewhere [73],

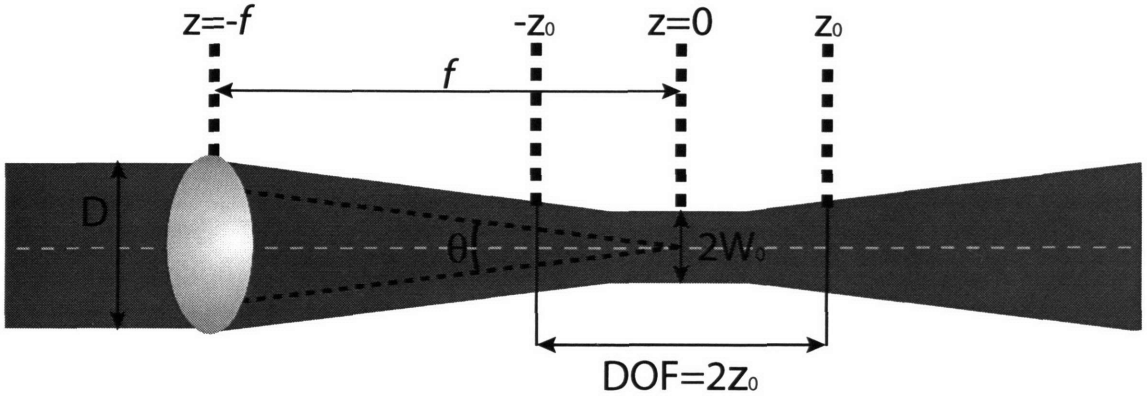

Figure 6-1: Collimated Gaussian pulse focusing after passing through a microscope objective of arbitrary numerical aperture. The beam waist, $2W_0$; Rayleigh range, z_0; depth of focus, $2z_0$; beam divergence, θ; beam diameter, D; and microscope objective focal length, f are indicated.

but a summary of useful formulas is given below.

Microscope objectives are usually specified by the numerical aperture of the objective, instead of focal length, where numerical aperture (NA) is defined as,

$$NA = n\sin(\theta/2), \tag{6.1}$$

where θ is the angle subtended by beamlets from the top and bottom of the objective as they bend inwards to focus, and n is the index of refraction in the material outside of the objective, most often air. Focusing is illustrated in Fig. (6-1). The beam waist, $2W_0$, and depth of focus, DOF=$2z_0$ (where z_0 is the Rayleigh range), can then be expressed in terms of the numerical aperture, assuming that the incident beam is nearly collimated ($\text{DOF}_{inc} \gg f$, where f is the focal length). This assumption is valid for every confocal parameter considered in this chapter.

In the lab, rules of thumb and more "rough and ready" formulas are of considerable benefit. The beam waist and depth of focus for 800 nm light can be simplified by noticing that $4\lambda/\pi \approx 1$, where wavelength is in units of microns. Additional simplifications are obtained if the beam divergence is sufficiently small such that $\cos\theta/2 \approx 1$. The beam waist

and depth of focus may then be written in simpler form, as follows:

$$2W_0 = \frac{2\lambda}{\pi}[\tan(\sin^{-1}(NA/n))]^{-1}, \quad (6.2)$$

$$\approx \frac{1}{2NA}\ \{\mu m\}, \quad (6.3)$$

$$DOF = 2z_0 = \frac{8\lambda}{\pi}[\tan(\sin^{-1}(NA/n))]^{-2}, \quad (6.4)$$

$$\approx 2\frac{1}{NA^2}\ \{\mu m\}, \quad (6.5)$$

$$(6.6)$$

where focussing in air ($n = 1$) has been assumed in the approximation.

The rate at which a focused beam ablates material is proportional to the optical power flow. It would then follow that ablation at the center of the beam occurs faster than at the periphery. This non-uniform ablation profile results in milled edges with a slight bevel, rather than entirely uniform damage throughout the sample thickness.

6.3 Femtosecond Laser Machining Setup

In this section, femtosecond laser machining with an amplified Ti:sapphire laser is described. The experimental setup used for fabrication is illustrated in Fig. 6-2. Briefly, it consists of a mechanical shutter to control the number of pulses to which the crystal is exposed; polarization selective optics to control the beam intensity; a microscope focusing objective (NA 0.1); a spatial filter; a phase-locked chopper to control repetition rate; and a computer actuated, three-axis translation stage to move the crystal through the focus of the beam. A user specified pattern encoded in HPGL is loaded into a Labview program that interfaces with the translation stage and beam shutter. Upon execution, the program directs the crystal position and exposure time such that the input pattern is reproduced in the crystal with damage extending throughout the crystal thickness. The femtosecond laser machining system is discussed in more detail below.

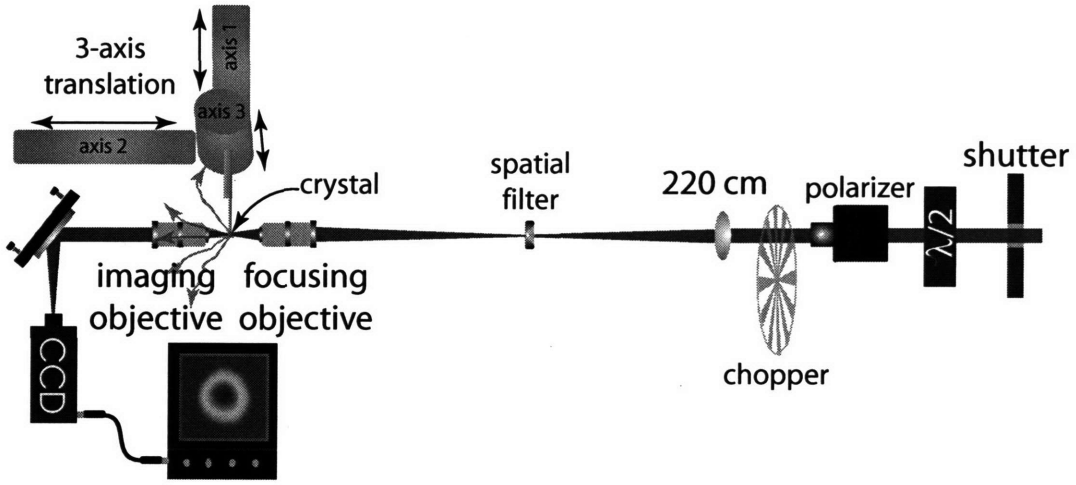

Figure 6-2: Femtosecond laser machining setup. A computer-actuated mechanical shutter controls the number of pulses. A half-wave plate/polarizer combination controls the pulse energy. The spatial mode of the beam is improved by focusing the beam through a 600 μm teflon spatial filter with a 220 cm focal length lens. The beam is focused into the working crystal with a microscope objective. The position of the crystal is controlled by a computer-actuated 3-axis translation stage. To facilitate alignment of the crystal focus and lateral position, an imaging objective is used to project the beam focal plane onto a CCD camera with a magnification of ~500. The imaging objective may also be used to measure the beam profile, shown in the bottom left of the figure, and also in Fig. 6-3.

6.3.1 Light Source

The laser system consists of a KM labs Ti:sapphite oscillator and a home-built Ti:sapphire multipass amplifier.

KM Labs Ti:sapphire Oscillator

The oscillator delivers 780-810 nm center wavelength pulses of 20 fs (FWHM) duration. At a 88 MHz repetition rate, the oscillator pulse energy is typically on the order of 3 nJ/pulse. A practical threshold for damage in $LiNbO_3$ or $LiTaO_3$ is on the order of ~1 J/cm^2. A 3 nJ pulse would then require a numerical aperture of at least 1.65, which is only possible using oil immersion objectives. Thus, machining is not easily implemented with the oscillator alone. Femtosecond laser machining in glass using an oscillator is discussed elsewhere [33], though the oscillator employed there is of a slightly higher pulse energy and the damage it induces

takes the form of submicron-sized voxels located beneath the surface of the glass.

Multi-Pass Ti:sapphire Amplifier

The multi-pass amplifier is employed to achieve the necessary fluence for damage feature sizes and ablation depths required for fabrication of polaritonic devices, which were given in section 6.1.2. The amplifier is similar in design to that described in the thesis of Greg Wakeham [92], which contains many of the details of the laser. The multi-pass amplifier used here is also described in an unpublished paper by Jianping Zhou, which is contained in the appendix of Ciaran Brennan's thesis [13]. The multi-pass amplifier is capable of producing 50 fs (FWHM) pulses at a 1 KHz repetition rate with pulse energies in the neighborhood of 800 μJ. The central wavelength of the output pulses is around 800 nm, but may vary with operating conditions. After having passed through the optics in the machining setup, the pulse energy is usually no more than 350 μJ due to losses intrinsic to the optical elements encountered along the beam path. Reflections from the plasma generated in the machined crystal, which retroreflect back through the amplifier, can destabilize the oscillator. To avoid this complication a broadband optical isolator (Optics For Research, model #IO5-BB-800-hp) is placed directly after the Pockels cell in the amplifier.

6.3.2 Machining Setup Components

Sample Exposure Time

A mechanical shutter (JML, model #SES 16505) with a 6 mm aperture is placed in the beam path to control the number of pulses incident on the crystal during fabrication. The number of pulses is specified by controlling the time for which the shutter is open. If the shutter is open for one second, then this is equivalent to sending 1000 pulses into the crystal at the 1 KHz laser repetition rate. The fastest rated switching time for the shutter is 1 ms, which means that it is theoretically possible to open the shutter only long enough to transmit a single pulse. Realistically, however, single pulses are more dependably obtained by chopping the 1 KHz output at 500 Hz and opening the shutter for 2 ms, as the shutter

becomes slightly erratic when switched at the maximum speed. The shutter is synchronized with the laser amplifier via an external trigger from the amplifier. Communication between the machining control computer and the shutter is established using the *visa* serial port protocol, implemented with a Labview VI. It is also possible to control the shutter with a TTL pulse from a Stanford delay box, which in turn may be communicated with via the GPIB or GPIB2 protocol.

Pulse Energy

The pulse energy is tunable via three components in the setup. The first, and most robust, is a combination half-wave plate and polarizer placed in the beam path prior to focusing into the sample. This component provides tunability of 1-5% of the maximum transmitted intensity. The range of values is dependent on the polarization purity of the amplifier output, i.e., the ratio of amplified spontaneous emission, which is randomly polarized, to the amplified seed, which is only s polarized. The polarizer also allows for continuous tunability. If care is taken in aligning the polarizer, and to a lesser degree, the half waveplate, then negligible beam walk-off from the optical path through the machining setup is possible.

The second technique is achieved through the use of optical density (OD) filters. Employing these filters can effect large, order of magnitude, changes in the pulse energy. If the OD filter is placed before the telescope and spatial filter in the machining setup, then the beam will need to be realigned to accommodate the OD filter; however, minimal beam walk-off from the optical path through the machining setup can be achieved by placing the OD filter directly in front of the microscope objective entrance aperture.

Third, the spatial filter diameter may be chosen to transmit more or less light by varying the diameter of the filter. The standard configuration, which is set to spatially filter at the beam waist, $2W_0$, of the milling beam, transmits 86% of the incident power.

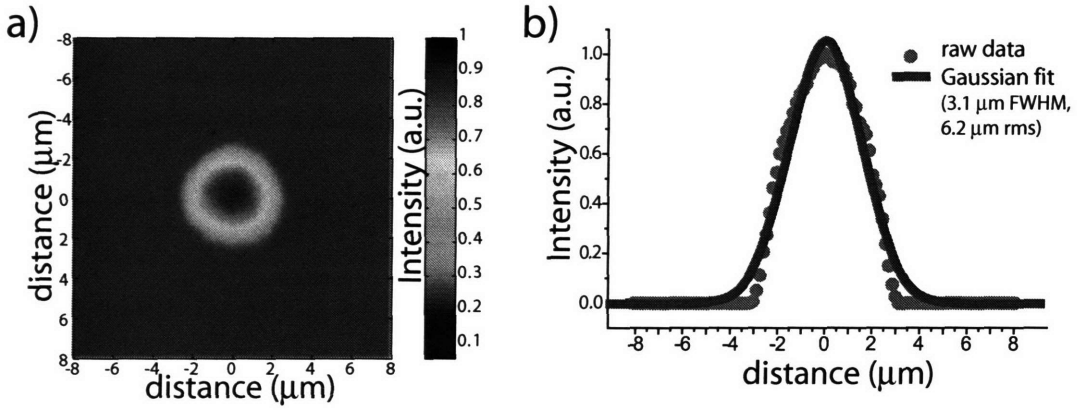

Figure 6-3: a) The beam profile is measured by imaging the focus of the machining objective onto a CCD with a magnification of 500. b) Spot size profile along the widest point in a).

Spatial Beam Profile

The spatial mode out of the amplifier is typically too poor for femtosecond laser machining, i.e., not of a single transverse mode. Imperfections in the beam profile will result in non-uniform damage in the machined crystal. A spatial filter, placed in the Fourier plane of a 220 cm focal length lens telescope, is employed to improve the spatial profile of the beam prior to focusing in the sample. By the time the pulses reach the spatial filter, loss sustained along the way has typically reduced the laser pulse energy to 400-500 μJ. If focused too tightly, white light will be generated, and the spatial filter may become damaged. This is dependent on the aperture size relative to the beam waist, and the damage threshold of the spatial filter material.

In practice, metallic spatial filters smaller than 500 μm will sustain considerable damage over time, rendering them unsuitable for use. Presently, the beam is focused to a spot size of 670 μm (rms), and to avoid long-term damage, a teflon spatial filter with a $\sim$600 μm aperture is placed at the focus instead of a metal one. The teflon spatial filter passes $\sim$80% of the incident power. Teflon has a very low absorption cross-section around 800 nm, and it does not appear to be damaged easily by the beam. For practical reasons, the filter thickness is $\sim$5 mm. The spatial filter was manufactured by using a drill press with a 24 thousandths drill bit. The longitudinal mode after the spatial filter and focusing microscope objective is

NA	$2W_0(\lambda)$ (Eq. (6.2))	$DOF(\lambda)$ (Eq. (6.4))
0.1	5.1 μm	202 μm
0.25	2.0 μm	31 μm
0.45	1.0 μm	8 μm
	$2W_0^{800\ nm}$ (Eqn. 6.3)	$DOF^{800\ nm}$ (Eqn. 6.5)
0.1	5.0 μm	200 μm
0.25	2.0 μm	32 μm
0.45	1.1 μm	10 μm

Table 6.1: Useful confocal parameters derived from exact calculation and through the more "rough and ready" rules of thumb.

shown in Fig. 6-3.

Focusing Optics

A microscope objective is used to focus the laser beam into the sample to be machined. The microscope objective is placed $\sim$ 30 cm beyond the spatial filter telescope. The numerical aperture of the objective is chosen based on the desired confocal parameter for machining, which is determined by the damage feature size desired. Table 6.1 lists the confocal parameters, beam waist, and focal lengths for the variety of microscope objectives currently on hand.

A convenient way to ensure that the objective is aligned properly with the incident beam is to focus at high power with a business card, or appropriate substitute, placed several centimeters past the focus. White light formation in air takes place at the focus, resulting in a circular color spectrum visible on the card. When the color spectrum appears uniform and symmetrical, the microscope objective is usually fairly well aligned. Rough alignment can be obtained by adjusting position for maximal transmitted power, and by ensuring that retroreflections from the back side of the microscope objective closely retrace the incident optical path.

Another microscope objective is placed directly behind the focusing objective to image the plane in which machining is to take place. By translating the imaging objective forward,

nearer to the focus of the focusing objective, the beam focus may be imaged with a magnification given by the ratio of the focusing objective focal length and the distance from the imaging objective to the image plane. Typically, a magnification of 500 is used. Magnified imaging may be used to construct a beam profile like that shown in Fig 6-3.

Initial Sample Alignment

It is important that the sample be placed precisely in the beam focus, and that the orientation of the sample attached to the translation stage be aligned so that motion along either axis 1 or axis 2 corresponds to the desired translation in the sample plane.

Alignment of the sample position in the beam focus is accomplished by imaging the sample with the imaging objective as follows. If the laser beam is substituted with an intense incoherent light source (Halogen lights work well) placed in the optical path and directed toward the sample through the focusing objective, then the sample machining plane can be safely imaged onto a CCD and visualized at a magnified scale. Doing so facilitates crystal alignment with the beam focus, since the focus for the incoherent light source will not be much different than the focus for the 800 nm laser beam.

The incoherent light source can also be used to ensure that the crystal edges are aligned to coincide with motion along either axis 1 or axis 2 (x or y). To do so, a reference mark on the CCD monitor is made, which corresponds to the beam location. Translation of the crystal along axis 1 and 2 is then checked against this reference point to ensure proper crystal orientation.

Automated Sample Position Control

To effect user-specified milling of the sample, a computer-actuated 3-axis translation stage is used to position the sample in the beam focus. Patterns to be machined onto the sample are drawn in CorelDraw, exported to the Hewlett-Packard graphics language (HPGL) syntax, and loaded into a Labview program that reads this file and directs the translation stage that positions the sample in the beam focus.

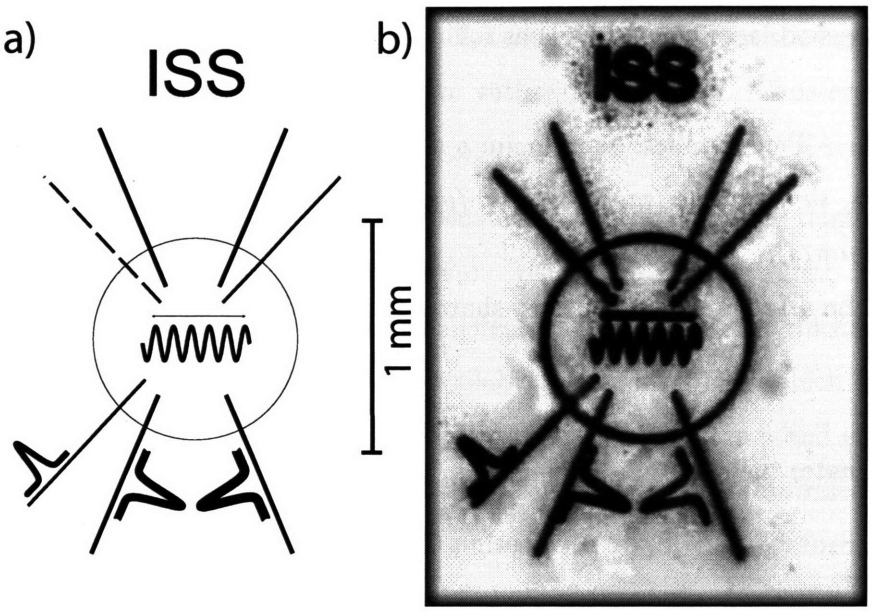

Figure 6-4: Any structure that can be drawn in Coreldraw and expressed in HPGL can be milled into a crystal with the femtosecond laser machining setup. The vector graphics line art drawing is shown in a), and the corresponding structure from the femtosecond machining setup is shown in (b).

The HPGL syntax is relatively simple, and is designed to control the motion of a multipen plotter. It utilizes essentially only two commands. It can instruct the stage to move from point A to point B in a plane, with either the PU (pen up) command, which indicates that the shutter in the beam line should be closed, or PD (pen down), which indicates the converse. The axis translation speed, number of shots/position, and spatial step size are encoded with the PN (pen number) command. Any of these preset variables can be accessed by changing the pen number with the SP (select pen) command. For most applications, the crystal is moved to a new point with the shutter closed, and then the shutter is opened for a specified time period, during which the translation stage is stationary.

This procedure allows for the milling of complex structures like that shown in Fig. 6-4. Motion is, however, confined to a plane. Three-dimensional motion may be encoded through the pen color specification, i.e., pen 1 (blue) corresponds to axes 1 and 2 (x and y), pen 2 (red) corresponds to axes 2 and 3 (y and z), etc. The syntax for HPGL files in the context

of femtosecond laser machining is as follows:

PN Pen Number

PNpen #, shutter time (ms), step size (μm), axis 1 speed (μm/s), axis 2 speed (μm/s), axis 3 speed (μm/s);

Sets the axis translation speeds, shutter time, and step size.

LT Line Type

LT;

Designates the start of a new line.

SP Select Pen

SPpen #;

Changes the settings (speed, shutter time, step size) based on the preset values from PN command.

PU Pen Up

PUaxis 1 axis 2;

Moves the crystal from its present location to that in the argument of the command with the shutter closed.

PD Pen Down

PDaxis 1 axis 2;

Moves the crystal from its present location to that in the argument of the command with the shutter open.

Note that there is no space between the command name and its first argument.

6.4 Femtosecond Laser Machining of $LiNbO_3$ and $LiTaO_3$

The machining parameters are largely dependent on the desired structure, but mainly on the crystal thickness. A good metric for deciding on the appropriate microscope objective for a given crystal thickness is the depth of focus (DOF) listed in Table 6.1. The DOF indicates the distance over which the beam radius changes by a factor of $\sqrt{2}$. As a practical metric we

have observed that relatively uniform damage that extends throughout the crystal thickness d can be obtained with a microscope objective with a DOF of $d/2$. Thus crystals thinner than 500 μm can be machined effectively with a microscope objective of NA=0.1.

A larger numerical aperture is desirable because it affords a smaller damage spot size, which is proportional to the beam waist ($2W_0$). Using the rule of thumb for the DOF, a microscope objective NA=0.25 can be used effectively in crystals of thickness less than 60 μm. The thinnest ferroelectric crystals available to us are 10 μm thick $LiNbO_3$ films produced by crystal ion slicing, which is discussed further in chapter 5 and elsewhere [54]. In this case, a microscope objective with NA=0.45 can be used. We confirmed the reduced feature size by exposing a 10 μm film to 1000 pulses with 20 μJ/pulse, which resulted in a damage spot of 5 μm. Reducing the number of shots reduced the damage spot size below what we are able to detect optically, but by patterning a small rectangle from ten 20 μJ pulses, we discerned that the damage must have extended throughout the film thickness, as the rectangle separated from the film after patterning was complete. This structure is shown in Fig. 6-5(b). Feature sizes down to about 1 μm are detectable with our microscope, so we expect the damage spot size for ten 20μJ pulses must be submicron. Further, using higher pulse energies, 100 μJ, 20 μm damage spot sizes that extended throughout the film thickness were obtained with a single pulse.

Thicker crystals require multiple pulses in order to achieve penetration throughout the depth. Femtosecond laser-induced damage from 100 μJ pulses for a variety of exposure times in 500 μm thick $LiNbO_3$ is illustrated in Fig. 6-6. Damage resulting from 1000 pulses of variable pulse energy is illustrated in Fig. 6-7. Both the damage radius and penetration depth were observed to increase monotonically with exposure time toward asymptotic values. Variation in hole radius is observed between 2-500 pulses and is limited by the beam waist at the focus, while penetration depth depends on the pulse energy (see Fig. 6-8) and is ultimately limited by the Rayleigh range.

The pulse fluences employed here greatly exceed the damage threshold in $LiNbO_3$ and $LiTaO_3$ in order to achieve damage that extends throughout the thickness of the crystal.

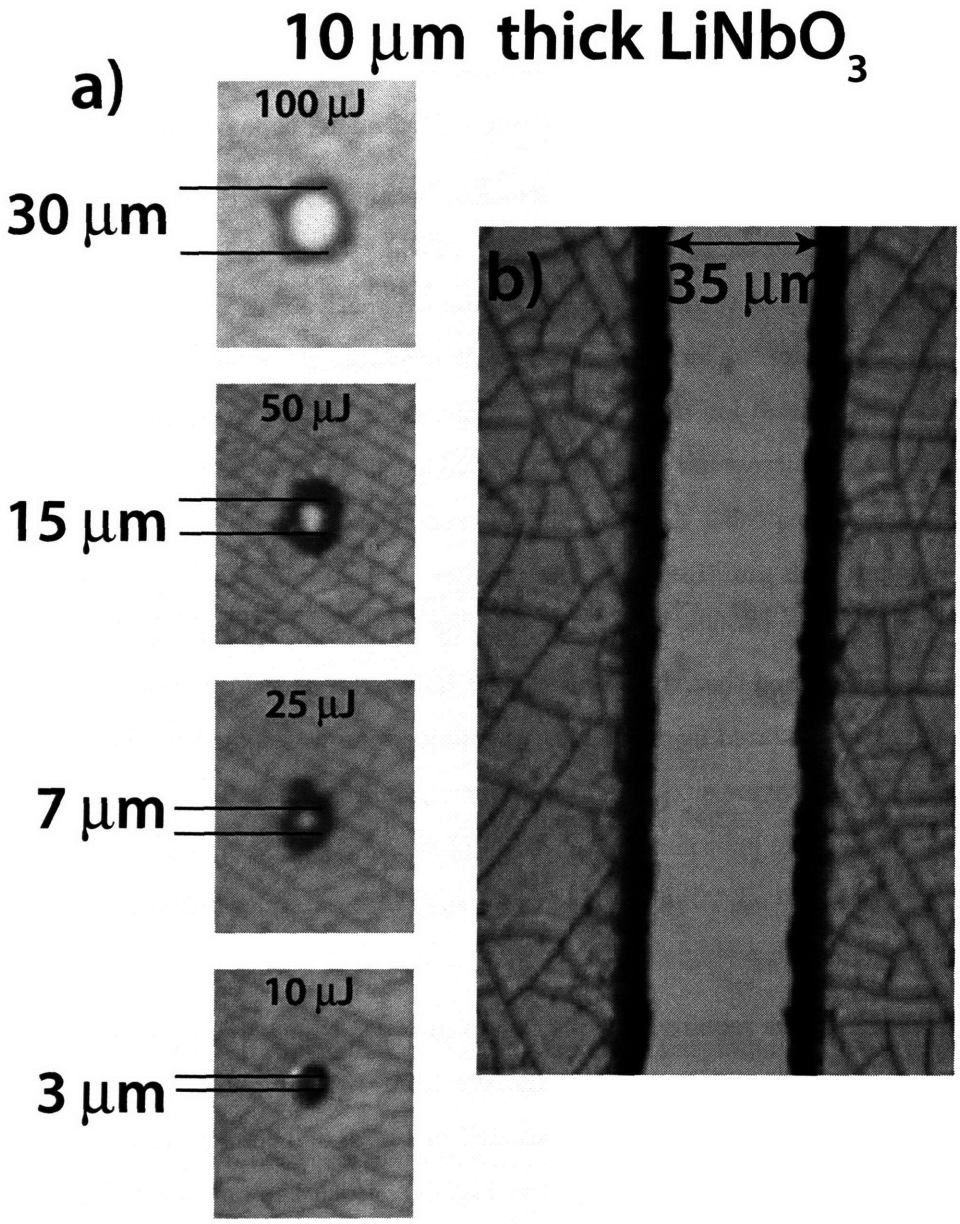

Figure 6-5: a) Optical micrograph of single-shot femtosecond laser induced damage in 10 μm thick $LiNbO_3$ for a variety of pulse energies (indicated in figure) and focused with a NA 0.1 microscope objective. Hole diameters are indicated on left. b) Optical micrograph of a rectangular trench carved from an array of sub-micron holes. Each hole was created by focusing 20 μJ pulses with an NA 0.45 microscope objective. The crystal was exposed to a single pulse and then translated by 1 μm. This was repeated until the rectangle in the figure was traced once. Note that the patterns of thin lines in the images are normal for films that are fabricated through crystal ion slicing, and are not caused by the laser machining process.

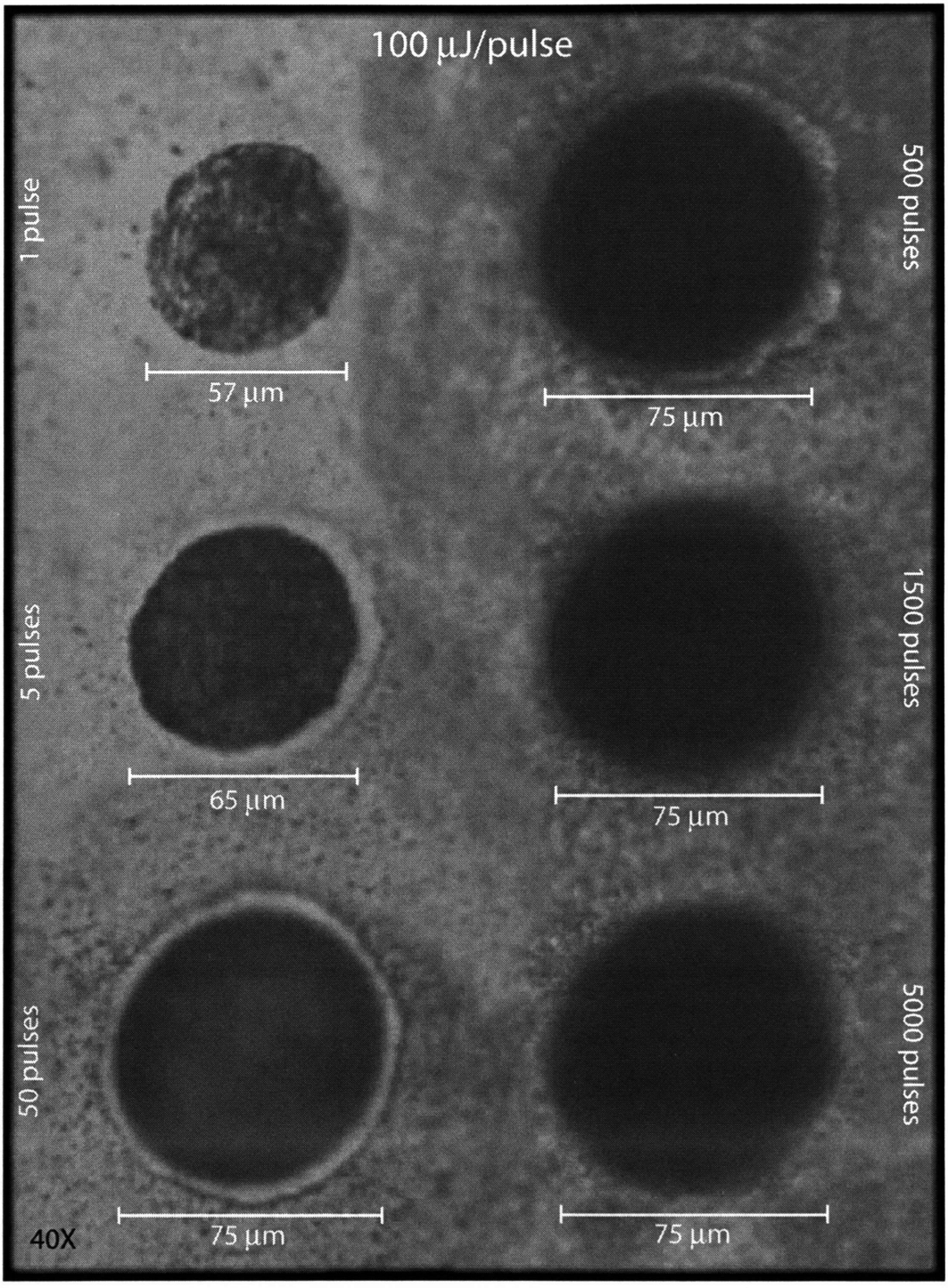

Figure 6-6: Optical micrograph of femtosecond laser induced damage in 500 μm thick $LiNbO_3$ with 100 μJ pulses.

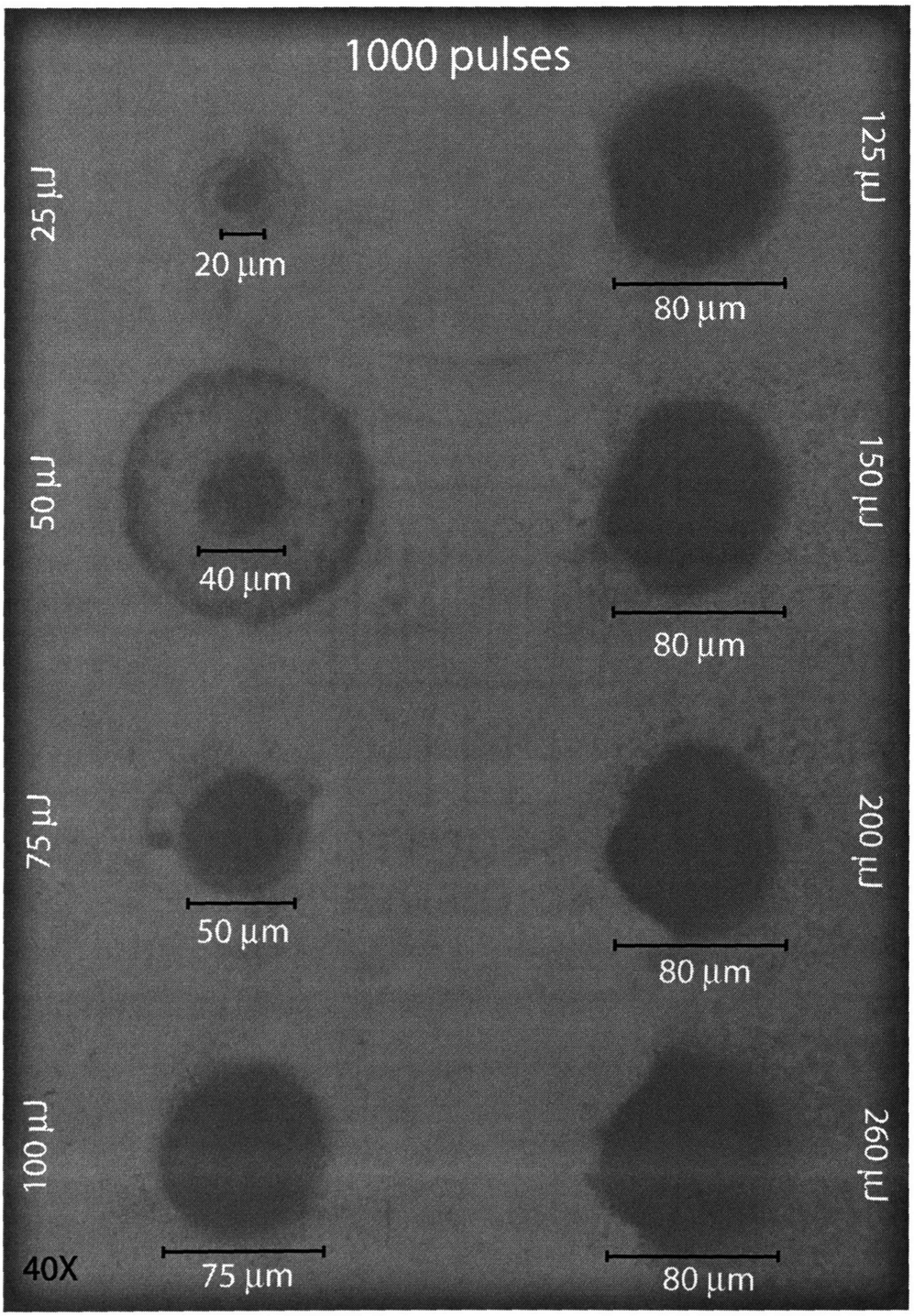

Figure 6-7: Optical micrograph of femtosecond laser induced damage in 500 μm thick $LiNbO_3$ with 1000 pulses of variable pulse energy.

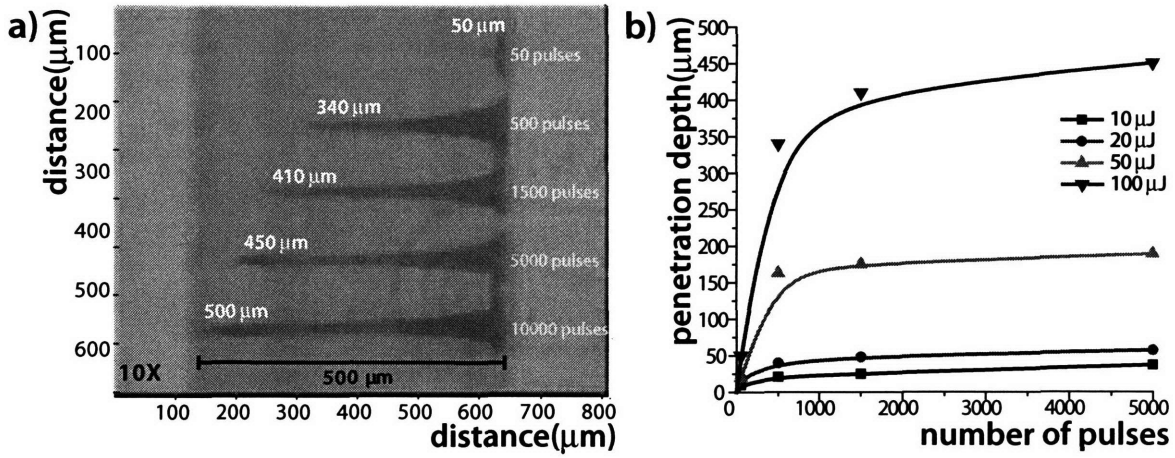

Figure 6-8: Laser-induced damage assays. In order to fabricate arbitrary structures in $LiNbO_3$ and $LiTaO_3$, details of the laser induced damage were discerned by collecting data on the extent of damage with pulse energy and exposure time. a) Optical micrograph (10X) of a cross-section through the crystal thickness showing laser damage penetration depth with 100 μJ pulses. b) Representation of several data sets showing variation in penetration depth with pulse energy and exposure time (number of pulses) and a fit to form $a(1-\exp(-b\cdot x))$, where a is the asymptote.

The rate at which a focused beam ablates material is proportional to the optical power flow. It would then follow that ablation at the center of the beam occurs faster than at the periphery. This non-uniform ablation profile results in milled edges with a slight bevel, rather than entirely uniform damage throughout the sample thickness. Through-plane damage is observed to have this bevel, but it tapers off to a constant diameter in the first 300 microns from the crystal surface, as evident in Fig. 6-8(a). The eventual straightening of the channels is likely due to wave guiding from a combination of the previously machined channel's dielectric contrast and self-focusing. A sacrificial layer of material placed in front of the crystal to be machined may be employed to obtain uniform through-plane damage. Two 25 μm diameter holes that were drilled in a 250 μm thick $LiNbO_3$ crystal using this technique are shown in Fig. 6-9. In the figure, there is no evidence of a bevel. There is some debris on the crystal surface that was covered by the sacrificial layer. This may be avoided through the use of a thin liquid layer (e.g. ethylene glycol or water) between the two solids.

In some cases incomplete damage may be remedied by exposing the crystal to hydrofluoric

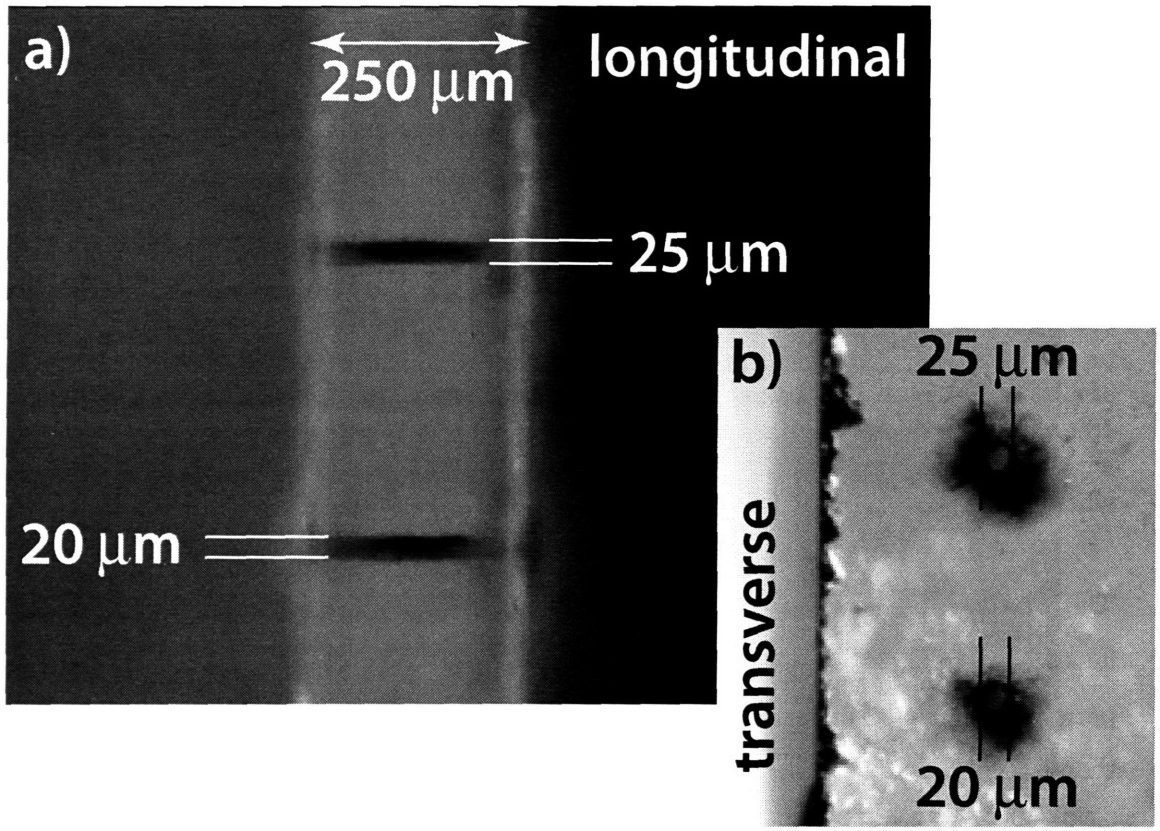

Figure 6-9: Optical micrograph of the a) longitudinal and b) transverse profile of two holes machined in 250 μm thick $LiNbO_3$ in which a glass microscope cover slip (100 μm thick) was placed on the surface of the $LiNbO_3$ crystal to function as a sacrificial layer. The hole diameter is 20 and 25 μm for 5000 and 10000 pulses, respectively, of energy 340 μJ per pulse. There is no apparent bevel in the longitudinal profile. Some debris is evident at the interface that separated the sacrificial layer from the machined crystal, but this is easily removed with ethanol and some scraping. The edge of the bulk crystal is visible on the left in part (b).

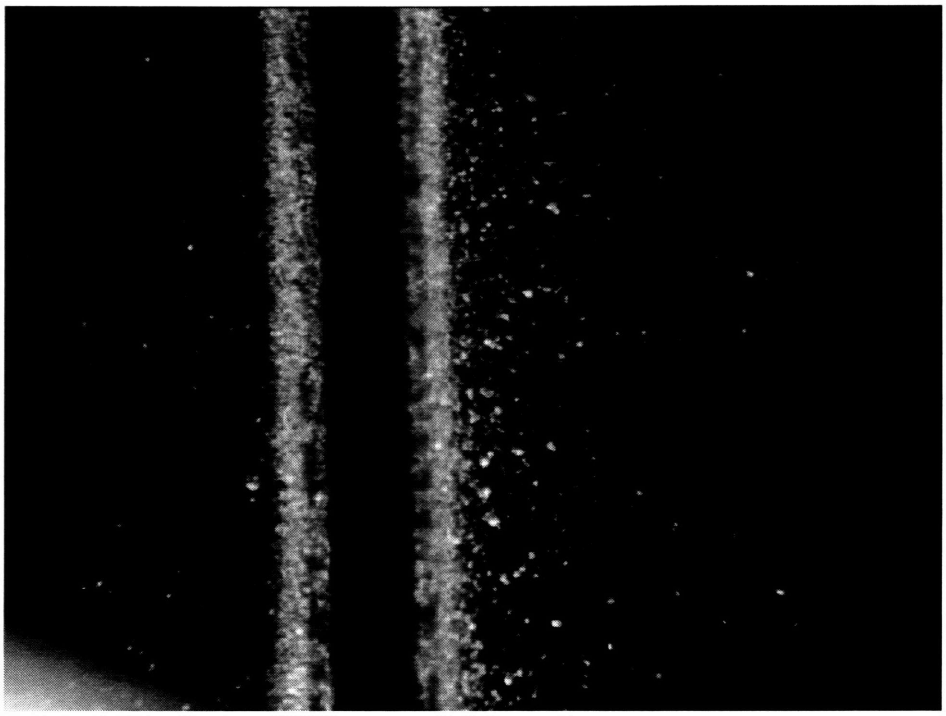

Figure 6-10: Front-lit optical micrograph of a 50 μm wide trench milled in 500 μm thick $LiNbO_3$ with 200 μJ per pulse showing debris accumulation on the surface. This can usually be removed by applying ethanol and scraping with a razor blade.

acid (50%, 70 °C, 10-15 minutes), but this often results in surface damage that reduces the optical quality of the resulting structures; however, the surface damage should have no effect on terahertz radiation, which is confined beneath the surface.

As larger amounts of material are removed, debris from the ablation process begins to accumulate on the surface (see Fig. 6-10). This debris can be dealt with in several ways. One way is to uniformly coat the front and back surface with clear enamel. This technique is usually effective, though some surface charring may still be observed, and is probably due to scorching of carbon compounds in the enamel. It is possible that an inorganic enamel may be used instead. An alternative solution is to clean the surface with ethanol, and then scrape away the debris with a razor blade. It is also possible to reduce debris accumulation by maintaining a continuous flow of an inert gas, like N_2, across the front face of the crystal; however, this technique is not an option with the present crystal mounting scheme, as the

sample is then susceptible to random motion, which decreases the precision of the milling.

6.4.1 Machined Structures

Photonic bandgap materials and other structures consisting of periodic 'air' holes, in which a cylindrical column of material is removed throughout the crystal thickness, are produced by exposing the crystal to the laser beam for a sufficient interval to achieve the desired hole radius and penetration depth, translating by the period of the structure with the shutter closed, and repeating at the new position in the crystal.

Figure 6-11 illustrates a periodic array of holes machined as described above. In the figure, the periodicity is 100 μm and the filling fractions are 9%, 15%, and 25% in part (a),(b), and (c), respectively, which was accomplished by exposing the sample, for each hole, to 50, 200, and 500 20 μJ pulses, also respectively. As evident in the figure, the damage features become more obscured, i.e., less round and pristine, as the number of pulses to which the sample is exposed increases. The charring around the hole diameter is confined to the surface.

Several functional devices composed of a periodic array of holes are illustrated in Fig. 6-13(a)-(c). Part (a) of the figure shows crossed waveguides that eliminate crosstalk between the two waveguide "channels" by introducing a one-dimensional photonic bandgap material, of periodicity 60 μm, at the intersection, as described elsewhere [47]. A photonic bandgap waveguide bend is shown in part (b). Simulations performed elsewhere indicate that transmission around the bend is nearly 100 % [46]. Photonic bandgap crystals, of period 100 μm, like those in Fig. 6-11 with variations in filling fraction from 10-50% are shown in part (c). Photonic crystals are described in more detail in chapter 7.

Waveguide structures that consist of continuous damage across the crystal surface are achieved in the same way as periodic structures, except the translation distance between shots is selected to be less than the damage feature size—usually by a factor of five or ten. Quasi-continuous damage made with this technique results in smooth lines that are continuous on the micron scale as shown in Fig. 6-12.

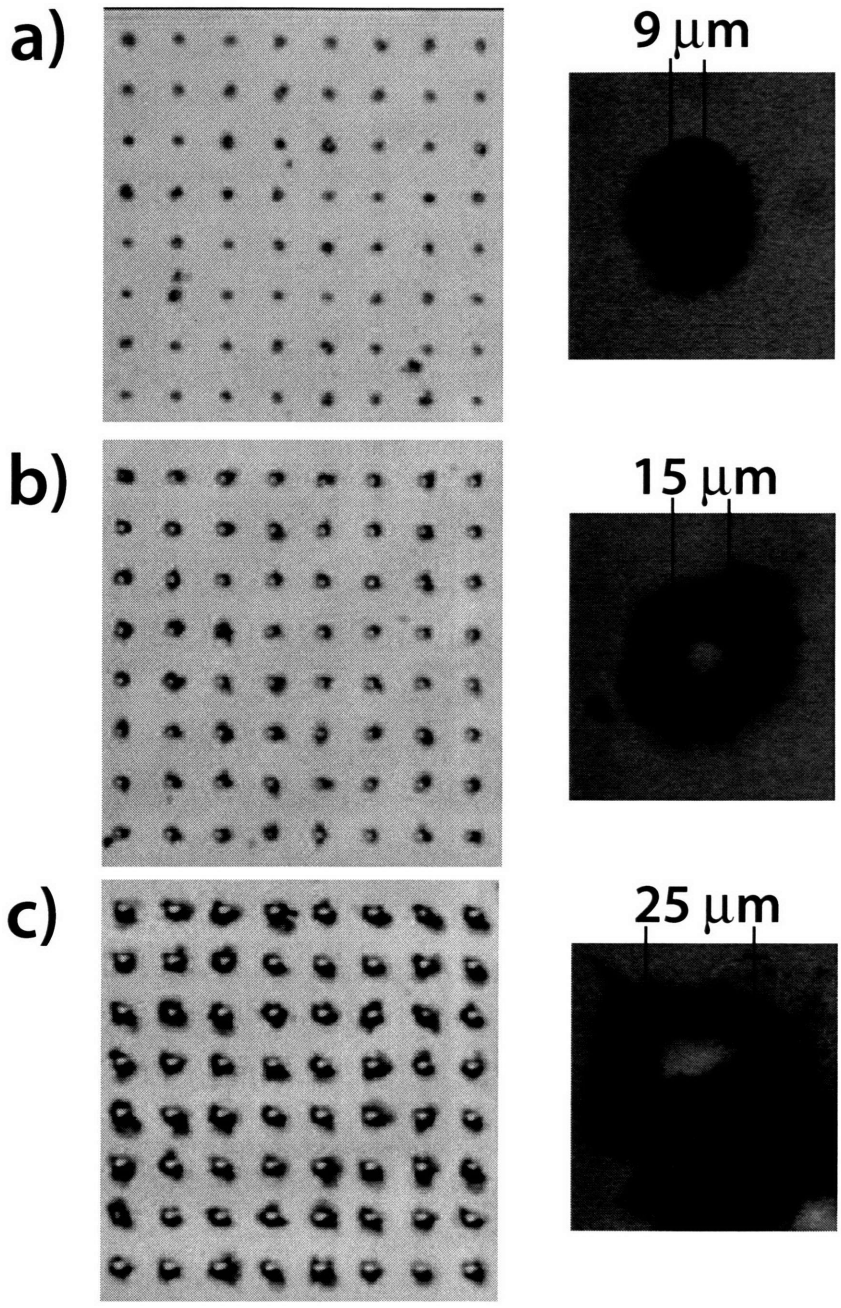

Figure 6-11: Two-dimensional photonic bandgap materials of period 100 μm machined in 34 μm thick MgO:$LiNbO_3$. The pulse energy is 20 μJ/pulse in each. 50, 200, and 500 pulses per hole were used to create different filling fractions.

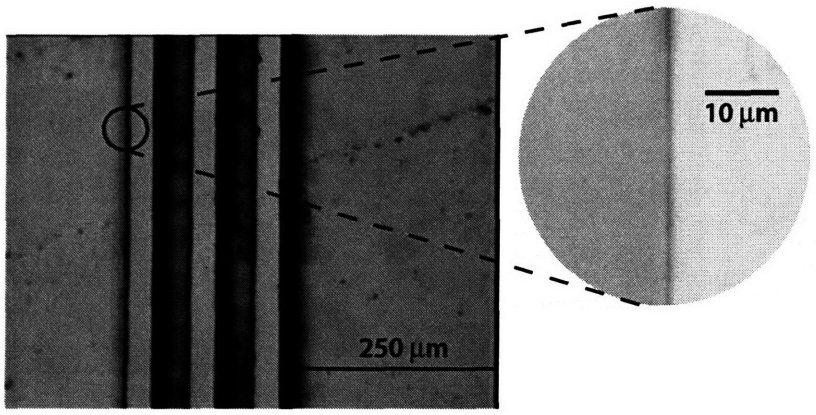

Figure 6-12: Three ~40 μm lines milled into 250 μm thick $LiNbO_3$, leaving two 50 μm wide crystal channels. The pulse energy was 150 μJ per pulse. Quasi-continuous damage was effected by irradiating a region with 100 pulses, translating by 5 μm, and repeating. The inset shows a machined edge at a higher magnification.

Several guided wave and photonic bandgap material structures are shown in Fig. 6-13(d)-(f). The oddly shaped waveguide in part (d) exploits cavity resonances in the "arms" that extend out from the waveguide axis (vertical centered) to exhibit frequency dependent transverse modes. Optimum performance is dependent on the smaller features in each arm, which is on the scale of about five microns. The length of the waveguide is 3 mm and the overall width including the "arms" is ~5 mm. A resonant cavity (center section) with one-dimensional photonic bandgap walls to increase reflectivity is shown in part (e). The center cavity is 224 μm wide. The air cavities of the photonic crystal are 250 μm wide, and the $LiNbO_3$ cavities are 60 μm wide. In addition to straight lines, curved lines are easily fabricated as well using the same procedure. A series of progressively smaller curved surface resonators is shown in part (f). The center $LiNbO_3$ sections remain intact in the bulk crystal because the two curved walls are not joined at the center of the cavities.

Phonon-polariton generation, propagation, and detection in structures similar to those illustrated here are demonstrated in chapter 7.

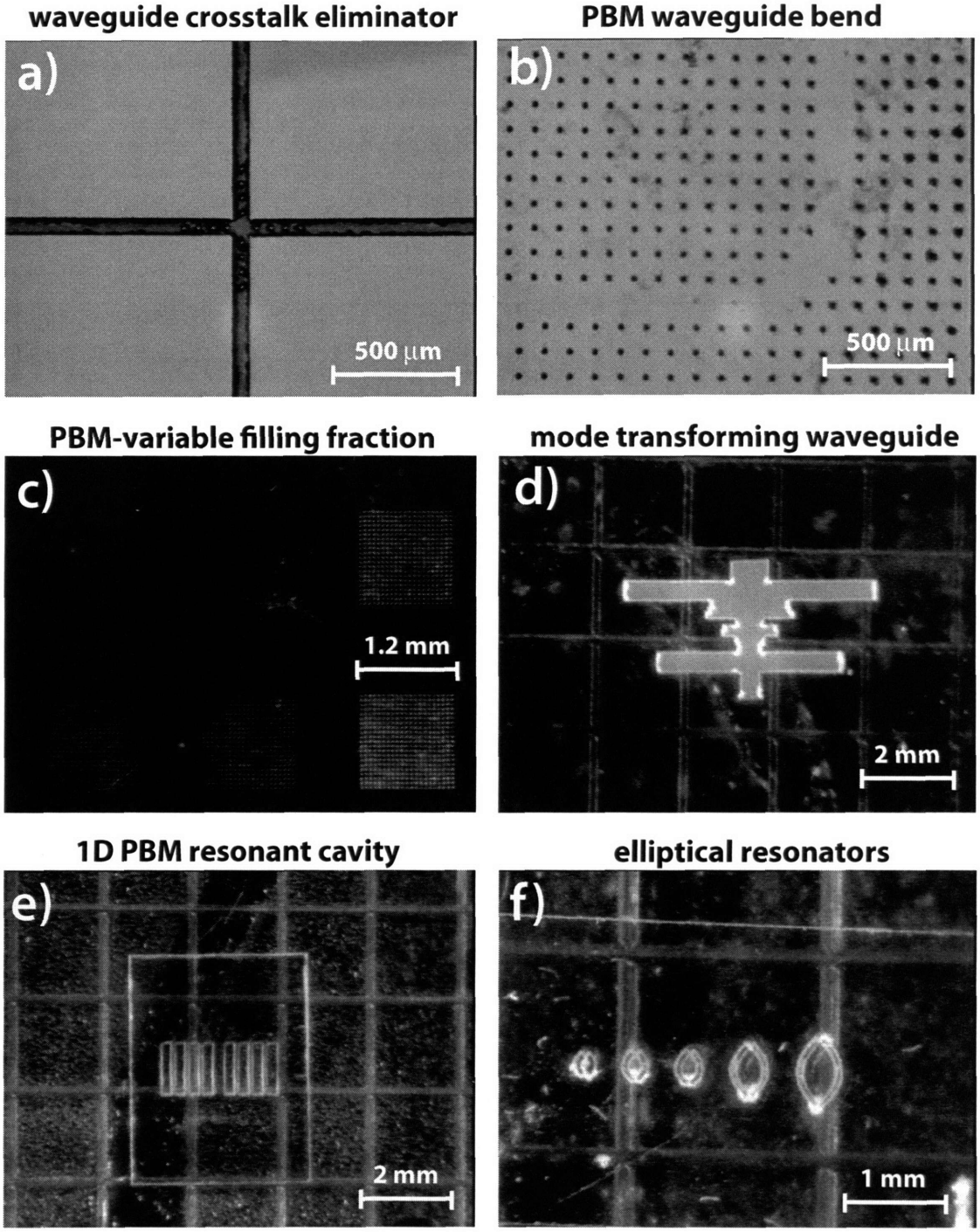

Figure 6-13: a)-c) Several photonic bandgap material (PBM) and d)-f)guided wave structures fabricated through femtosecond laser machining. The two-dimensional photonic bandgap materials are in 34 μm thick MgO:$LiNbO_3$, while all the rest are in 250 μm thick $LiNbO_3$.

Chapter 7

Guidance and Control of Phonon-Polaritons in Patterned Materials

This work was done in collaboration with Thomas Fuerer, Eric Statz, Jaime Choi, and Nikolay Stoyanov of the Massachusetts Institute of Technology.

In recent years, considerable progress has been made in the development of pulsed sources of THz radiation, methods for their characterization, and their applications in THz spectroscopy [27]. Biased semiconductor surfaces or nonlinear crystals may be irradiated with femtosecond optical pulses to generate broadband (roughly single-cycle) THz wavepackets, and a variety of methods including the use of femtosecond pulse sequences or periodically poled nonlinear crystals, have been introduced to produce multiple-cycle THz waves with narrower bandwidths. These methods result in THz radiation that is projected into the free space adjacent to the THz source. The radiation then may be directed toward a sample of interest, and again through free space toward a detector at which the field is analyzed.

For many applications, a fully integrated platform that supports THz generation, manipulation, propagation into a sample of interest, and spectroscopic analysis would be more versatile and convenient. Generation of THz phonon-polariton waves (admixtures of lattice

vibrational and electromagnetic modes that propagate coherently at light-like speeds) in nonlinear crystals including $LiTaO_3$ and $LiNbO_3$ through impulsive stimulated Raman scattering (ISRS) [3, 23] offers strong prospects for such a system, since the THz responses remain within the solid-state hosts, where their spatial and temporal evolution can be fully characterized through spatiotemporal imaging. [51] Generation of single-cycle, broadband THz wavepackets or multiple-cycle, frequency-tunable narrowband waves, or, in fact, nearly arbitrary THz waveforms, can be conducted with such a platform through the use of spatial, temporal, and spatiotemporal femtosecond pulse shaping methods. [29] In addition, THz functional elements, including waveguides, interferometers, and diffraction gratings, have recently been fabricated in these materials through femtosecond laser machining. [83, 81, 98, 99, 85, 93, 101, 100, 102] Thus, THz generation, delivery to and from a sample, detection, and spectroscopic analysis may all be integrated into a single solid-state platform. Information processing in which coherent THz signals are used to modulate photonic signals or as the information carriers themselves, or in which incoming THz radiation is detected and analyzed, may also be facilitated through the use of an integrated platform.

Among the elements needed for a fully functional integrated THz signal processing or spectroscopy system, structures that are resonant at selected frequencies will play important roles. Frequency-selective filters and resonators will be used for spectral analysis, photonic or optical signal modulation, and a wide range of other purposes, just as resonant structures are widely used in integrated MHz (ultrasonic) and GHz (microwave) signal processing, photonics, and some forms of optical spectroscopy. In this chapter we demonstrate integrated polaritonic devices fabricated by femtosecond laser machining. These integrated devices provide guidance and control over the phonon-polariton waveforms that are generated in and propagate through them.

7.1 Reflective and Refractive Devices

What happens when phonon-polaritons reach the end of their host crystal? When the angle of incidence is greater than the critical angle, total internal reflection results, which has already

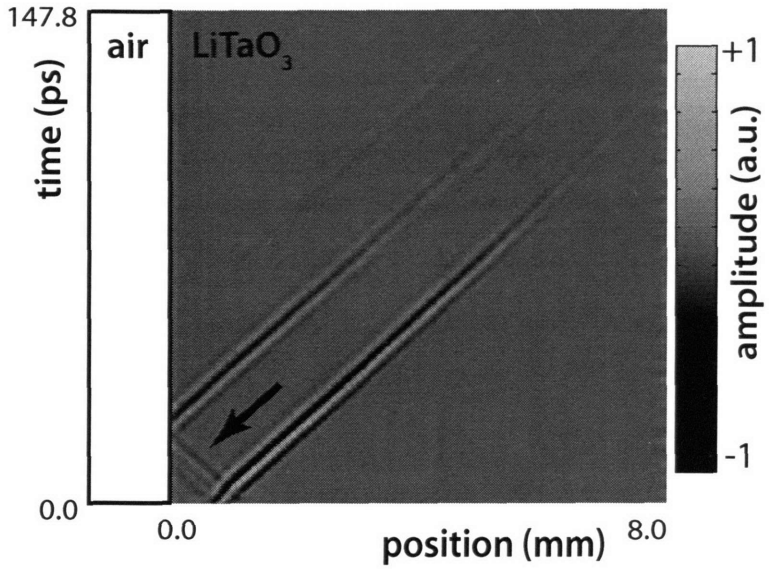

Figure 7-1: Phonon-polariton amplitude as a function of space and time. Line excitations like that in Fig. 4-4 were generated through cylindrical lens focusing. Whereas the phonon-polariton wave travelling from the excitation region to the right leads to a strong signal, the left-going counterpart is barely visible (arrows). Only after reflection at the crystal edge does it cause a strong signal. The asymmetry is an artifact of 400 nm tilted pulse imaging. The signal recurrence and displacement, as described in detail in chapter 5, evident in the figure are consistent with a 2 mm thick crystal.

been discussed and exploited in chapter 5, to achieve waveguide confinement and guidance. When the angle of incidence is less than the critical angle (See Table 4.1), and when the secondary material of the interface does not form phonon-polaritons, then the transmitted power is manifest in terahertz radiation derived from the electromagnetic component of incident phonon-polaritons. In this case, the usual description of optical interfaces, including Snell's law of refraction and incident angle dependent transmission/reflection coefficients, applies, with the frequency dependent refractive index derived from Eq. (2.47). [10, 35].

Reflection, refraction, and transmission can provide functionality for a host of polaritonic devices. In this section, we first demonstrate total internal reflection of phonon-polaritons at an interface. Next, we show that micromachining of curved interfaces can be used to make large amplitude phonon-polaritons and terahertz pulse trains; the latter is the first demonstration of an all-terahertz pulse shaper.

7.1.1 Reflections at a Crystal Interface

Figure 7-1 shows the spatiotemporal amplitude distribution of a line excitation generated close to the edge of a 2 mm thick $LiTaO_3$ crystal. Phonon-polaritons moving to the right are clearly visible, whereas those travelling to the left are barely detectable. The disparity between phonon-polaritons traveling in opposite directions was explained in chapter 4, where it was related to the imaging geometry (tilted 400 nm imaging). However, after being reflected at the left side of the crystal the phonon-polaritons reverse direction and a strong signal is recovered. Comparing the amplitudes indicates that the reflectivity is about 100%. Recall that phonon-polaritons are generated with a slight forward propagation angle ($\sim 20^o$ here), causing them to arrive at the interface at an angle greater than the total internal reflection angle for the crystal, which explains why we observed 100% reflection. Therefore, by choosing the angle of incidence larger than the critical angle of total internal reflection, the crystal-air interface behaves as a perfect plane mirror.

7.1.2 Terahertz Focusing Reflectors

Polaritons with high amplitudes offer the possibility of probing nonlinear lattice dynamics and can serve as a strong source of terahertz radiation, which can be used for nonlinear terahertz spectroscopy. Due to white light generation, which places an upper limit on the intensity of the pump, generation of polaritons with high amplitude is not trivial. Polariton focusing is a straightforward way to achieve enhanced amplitudes. Optical beam shaping to achieve polariton focusing has been demonstrated previously [84], but anisotropic materials prevent uniform focusing by this method because polariton polarization components along the ordinary and extraordinary axes travel toward a common focus at different speeds. Focusing via the axicon optic described in chapter 4 is illustrated in Fig. 7-2. To overcome this problem, a surface with curvature designed to correct for anisotropy is milled into $LiNbO_3$ using the femtosecond laser machining described in chapter 6.

We first consider a single focusing element in $LiNbO_3$ that focuses an incident broadband polariton waveform despite the material anisotropy. By accounting for the material

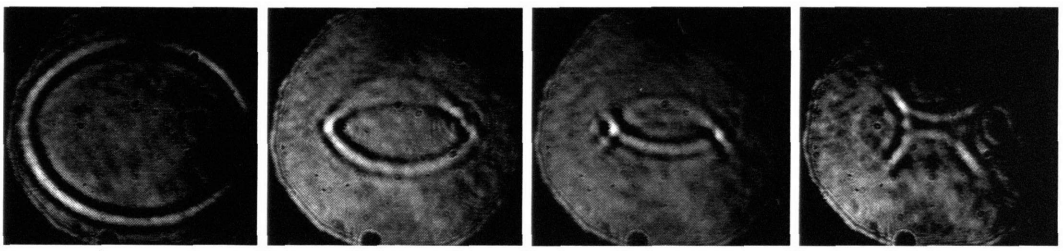

Figure 7-2: Full ring excitation in $LiNbO_3$ from an axicon. The results reveal strong anisotropy in the dielectric function. The optic axis lies along the horizontal dimension in the figure. The image dimensions are 0.77X0.71 mm^2.

anisotropy in the curvature of the focusing element this can be overcome. The focusing element illustrated in Fig. 7-3 is elliptical with main axes of 1.2 mm and 1.8 mm, where the axis ratio is the reciprocal of the refractive index ratio. To avoid evanescent coupling of the reflected polaritons, the unnecessary crystalline material on the back face of the reflector is removed. Figure 7-3 shows a broadband polariton ripple generated by focusing the pump onto the crystal with a 10 cm cylindrical lens. The polaritons propagating to the right reflect from the elliptical mirror. The elliptical mirror with the correct choice of axis ratio leads to sharp focusing of the polaritons in this strongly anisotropic medium. The amplitude enhancement factor is approximately a factor of three. Greater amplification could be achieved by focusing in the through-plane dimension as well, but phase matching in the present experimental geometry will not allow for detection of the focusing in this dimension.

In some instances, it may be beneficial to generate a broadband polariton waveform and transform it to narrowband using a patterned material, producing an all-terahertz pulse shaper. This can be achieved with multiple reflecting surfaces, i.e., a series of spatially staggered focusing elements. A terahertz reflective pulse shaper is composed of i individual reflecting surfaces, which are staggered spatially by a distance dx. Each facet of the pulse shaper has a slightly different curvature than the next, given by, $f_i = f_0 + idx$, where f_0 is the curvature of the center reflector. The number of reflecting/focusing elements determines the number of cycles in the reflected waveform, given that the incident waveform is single cycle. The output frequency, $1/dt$, is determined by the pulse delay, which is related to the

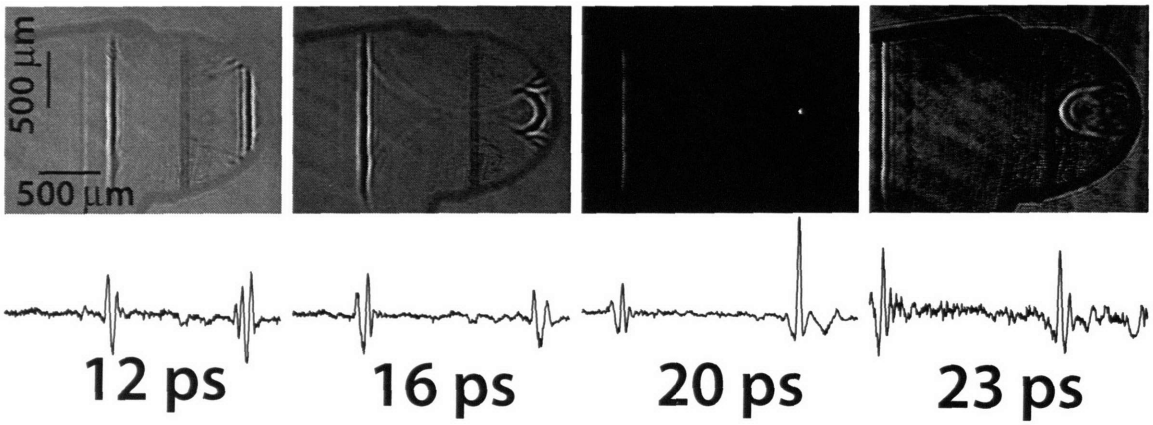

Figure 7-3: THz focusing element with broadband polaritons. The machined crystal edges are visible in the real-space imaging frames. The polaritons propagate away from the excitation region in both directions. The right-going wave impinges upon the femtosecond laser machined reflective surface, the curvature of which is designed to account for anisotropy in $LiNbO_3$ that would otherwise prevent uniform focusing. c) Same as part (b) except the crystal behind the focusing elements has been removed.

spatial staggering through $dt = dx/(c/2n)$.

Figure 7-4 illustrates two three-element reflective pulse shapers, which converts a single-cycle broadband polariton wavepacket, of ~300 GHz central frequency, into a three cycle plane wavepacket at the focus. The material patterning is outlined in the figure. The incident polariton waveform is obtained by focusing an 800 nm, 70 fs pulse to a spot size of ~110 μm to the right of the probing area at the focus of the reflectors.

The first reflector, part (b), consists of a set of 100μm wide troughs milled as an arc into the surface of a 200 μm thick $LiNbO_3$ crystal. Due to evanescent coupling across the troughs, only 10% of the initial polariton amplitude is obtained at the focus. Beyond the focus, the waveform begins to diverge, but a waveguide machined into the $LiNbO_3$ crystal at the focus can be used to collimate the narrowband pulse over an arbitrary distance (See section 7.3).

Reflection amplitude can be improved by removal of the material behind the reflectors, as shown in Fig. 7-4 (c). Removal of the material behind the reflectors resulted in amplitude enhancement similar to that in a single reflector (approximately a factor of two). However,

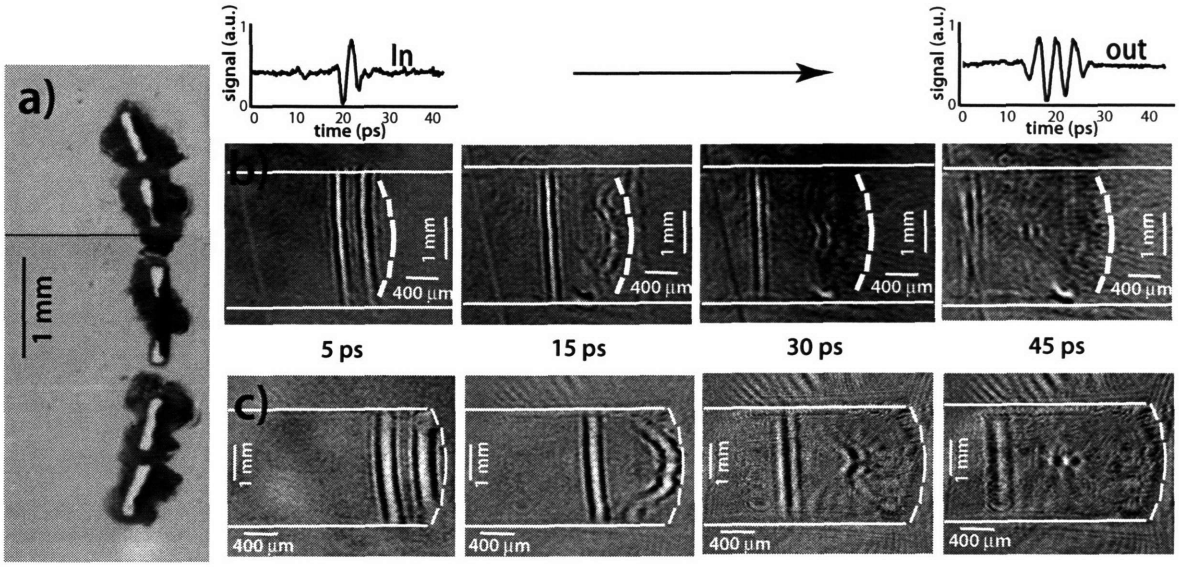

Figure 7-4: All terahertz-pulse-shaping implemented with multiple reflecting surfaces. a) Optical micrograph of THz pulse shaper focusing elements. The curvature of each reflecting/focusing element is slightly different and staggered spatially so that an incident broadband pulse is transformed into a three-cycle narrowband plane wavepacket. The radii of curvature of the focusing elements are (from center to periphery) 1 mm, 1.025 mm, and 1.05 mm. b) Structure milled into crystal without removal of material behind the reflectors, and c) with removal of the material behind the reflectors. Temporal cross-sections taken at the focus in the structure in part (b) are shown at top. Both signals are normalized to unity.

by removing a limited amount of material, the functionality of the device can be maintained while making it easier to integrate into a larger network of THz elements machined into a single crystal.

7.2 Diffractive Devices

We first demonstrate two diffraction effects, namely diffraction at a single slit and diffraction at an edge, and then we demonstrate interference effects related to diffraction. Whenever two or more waves are present simultaneously at a specific spatial location, the total amplitude is determined by the sum of the individual amplitudes which gives rise to interference phenomena. Due to the linearity of the wave equation, the superposition principle is also ap-

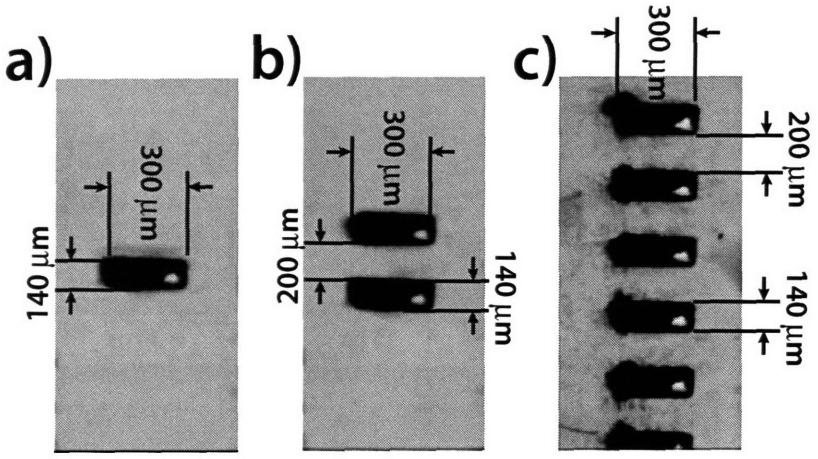

Figure 7-5: Microscope image of the laser-machined a) single-slit structure, b) two-slit structure, c) grating structure.

plicable to phonon-polariton modes. We demonstrate two different interference phenomena: first, a classic double slit experiment, and second, diffraction of a grating.

7.2.1 Single slit

The single slit is realized by laser-machining a rectangular structure into a 0.5 mm thick $LiNbO_3$ crystal. The single slit is an opaque obstacle in the path of the plane phonon-polariton wavepacket with highly reflective walls. Therefore, we would expect to see the diffraction pattern of a single slit in the backward direction and its counterpart, diffraction at a 'wire', in the forward direction. The single-slit structure fabricated through femtosecond laser machining is shown in Fig. 7-5(a). The width of the rectangular structure is about 0.14 mm.

Figure 7-6(a) shows a sequence of snapshots as the plane wavepacket intercepts and passes the single slit obstacle. As expected, the diffraction pattern of a single slit, which is almost a perfectly spherical wave, is observed in the backward direction. In the forward direction, however, the diffraction pattern of an obstacle is observed.

Similar to the single slit experiment, diffraction off an edge was observed in the backward direction off an obstacle that was many wavelengths wide. Figure 7-6(b) shows the spatial

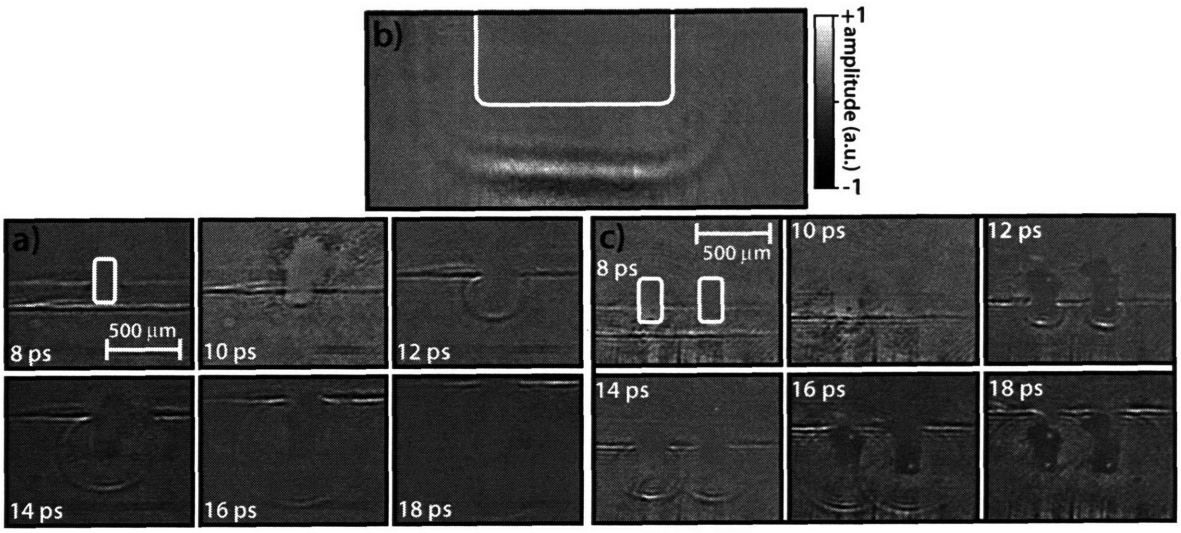

Figure 7-6: a) Phonon-polariton amplitude for different pump-probe delays. The plane wavepacket travels from the bottom to the top and the circular wavepacket is reflected back toward the sides and bottom. The images show the diffraction pattern from a single slit. b) Phonon-polariton amplitude for a fixed pump-probe delay of 10 ps. The reflected part of the wavepacket travels towards the bottom of the image. The image shows the diffraction pattern in the presence of two edges. c) Phonon-polariton amplitude for different pump-probe delays. The plane wavepacket travels from the bottom to the top and the circular wavepackets are reflected toward the sides and bottom. The images show the diffraction pattern from a double slit.

phonon-polariton amplitude distribution at a given pump-probe delay. The wavepacket has already been reflected at the broad laser-machined structure, which is indicated by the white area, and is propagating towards the bottom of the image. The circular structure, which develops at the ends of the reflected phonon-polariton wavepacket, is caused by diffraction at the two edges of the laser-machined structure.

7.2.2 Double slit

The double slit was fabricated by laser-machining two rectangular structures into a 0.5 mm thick $LiNbO_3$ crystal, and is shown in Fig. 7-5(b). The two single slits are opaque obstacles in the path of the plane wavepacket with highly reflective side surfaces. As in the case of the single slit, one would expect to see the diffraction pattern of a double slit in the backward

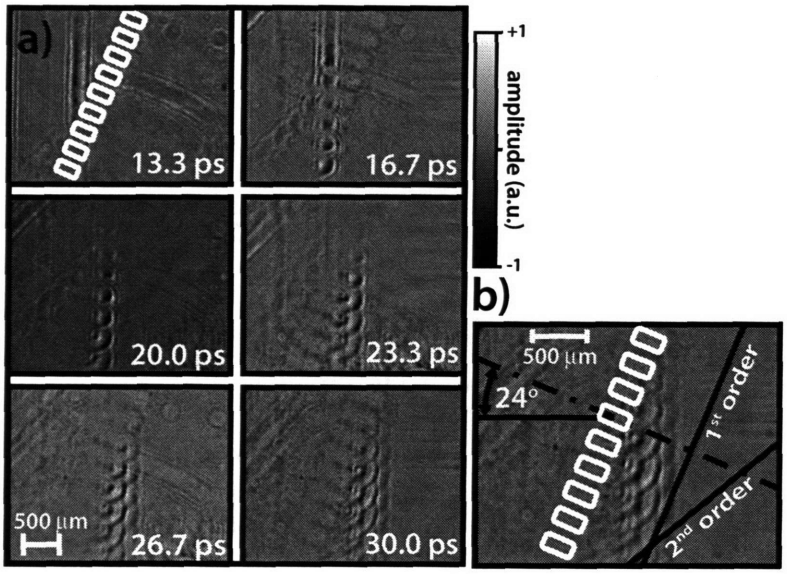

Figure 7-7: a) Phonon-polariton amplitude for different pump-probe delays. The wavepacket travels from the left to the right and impinges on the grating at an angle. The images show the diffraction pattern of the grating in reflection and transmission. b) Phonon-polariton amplitude at 30 ps.

direction and its counterpart, diffraction of two 'wires,' in the forward direction. The width of the rectangular structures is 0.14 mm and their separation is 0.2 mm. Almost perfectly circular wavefronts originate at both structures and start to interfere when their amplitudes spatially overlap. The double slit interference pattern is clearly observed at the bottom of the Fig. 7-6(c) in the backward direction.

7.2.3 Grating

Fabrication of a periodic sequence of 'single slit' structures eventually leads to a grating. Again, due to the unique characteristics of the laser-machined structures, we expect to see the amplitude pattern of a transmission and a reflection grating at the same time. A micrograph of the laser-machined grating is shown in Fig. 7-5(c). The single features in a 0.5 mm thick $LiNbO_3$ crystal are about 0.14 mm wide and the distance between two neighboring structures is 0.2 mm.

Figure 7-7(a) shows a sequence of snapshots of the phonon-polariton amplitude for a

geometry where the generated line-like phonon-polariton response moves from left and right and intercepts the grating at a non-zero angle. Due to the imaging geometry and the polarization of the imaging beam, the transmitted signal is much more pronounced. At a delay of about 30 ps, almost all of the incident plane wavepacket passed the grating structure and the far-field diffraction pattern is clearly visible.

The center wavelength of the generated phonon-polariton wavepacket is about 0.15 mm. The angle of incidence in fig. 7-7(b) is 25 deg. For a grating constant of 0.34 mm, one would expect the first order diffraction to appear around the grating normal and the second order diffraction around an angle of 27 deg. In fig. 7-7(c) the phonon-polariton amplitude is shown for a pump-probe delay of 30 ps. Indicated by two straight lines are the expected wavefronts for first order and second order diffraction of the grating.

Within the observed diffracted wavefronts, two distinct features that almost perfectly coincide with the indicated wavefronts for first and second order diffraction may be identified. In principle, with a grating/lens or grating/curved mirror combination, it should be possible to realize an all-integrated phonon-polariton spectrometer.

7.3 Waveguides

Slab waveguide effects, which arise when the excitation wavelength is comparable to the crystal thickness, were discussed in the chapter 5. Confinement is also possible when polaritons are confined to restricted regions within the plane of propagation, and may be accomplished by milling "trenches" that extend throughout the (30-300 μm) crystal thickness. Guidance is then facilitated by the dielectric contrast between the host crystal and air that occupies the void within the "trench". Polariton rectangular waveguides have been fabricated within $LiNbO_3$ and $LiTaO_3$ crystals using femtosecond laser machining to mill the "trenches" into the crystal [83]. Due to the high index contrast provided by $LiNbO_3$ and $LiTaO_3$, results can be compared to theoretical predictions based on the simple "perfect magnetic conductor" waveguide equations for rectangular waveguide TE and TM modes, which were presented in chapter 5 and elsewhere [84].

7.3.1 Coherent Control Using Spatial Beam Shaping

Coherent control can be exerted over phonon-polariton propagation through shaping of the spatial profile of the excitation beam to generate waveforms well suited for coupling into a waveguide. This control was accomplished here with an axicon optic, as described in chapter 4, in which a portion of the excitation ring was blocked to create an "arc" excitation. By judiciously choosing which portion of the full ring to block, we can specify arcs of light that generate phonon-polaritons which propagate in the desired direction and focus to the desired spot size. We illustrate this process by focusing into a waveguide, shown in Fig. 7-8(b), from two different locations in the sample. Automation of this procedure using two-dimensional pulse shaping could be used to selectively enter one waveguide or another [29].

In addition to demonstrating a simple control technique, these data also offer compelling evidence that the fabricated waveguides do in fact guide phonon-polaritons. The same excitation employed in the figure would in bulk show phonon-polaritons spreading outward after the focus in an arc identical to that prior to the focus. The presence of the waveguides prevent this problem, as the phonon-polaritons are instead forced into the lowest order mode of the waveguide, directed through the waveguide without diverging, and allowed to exit at the end of the waveguide. Note that upon exiting the waveguide, the phonon-polaritons diverge as expected for transmission through a small aperture.

7.3.2 Waveguide Bend

Waveguides can also be made to steer phonon-polaritons in a different direction from which they came. The structure in Fig. 7-9(a) was fabricated to steer phonon-polaritons around a ninety degree bend. Figure 7-9(b) shows the results of excitation directly within the waveguide structure in $LiTaO_3$. The excitation region is a nearly vertical line of light, which gives rise to two counterpropagating, single-cycle wavepacket "ripples". Each ripple propagates without enlargement of its transverse spot size, again demonstrating waveguide behavior. The wavepacket propagating toward the left is reflected by the 45 degree edge, and is then observed propagating upward within the vertically oriented waveguide. Total

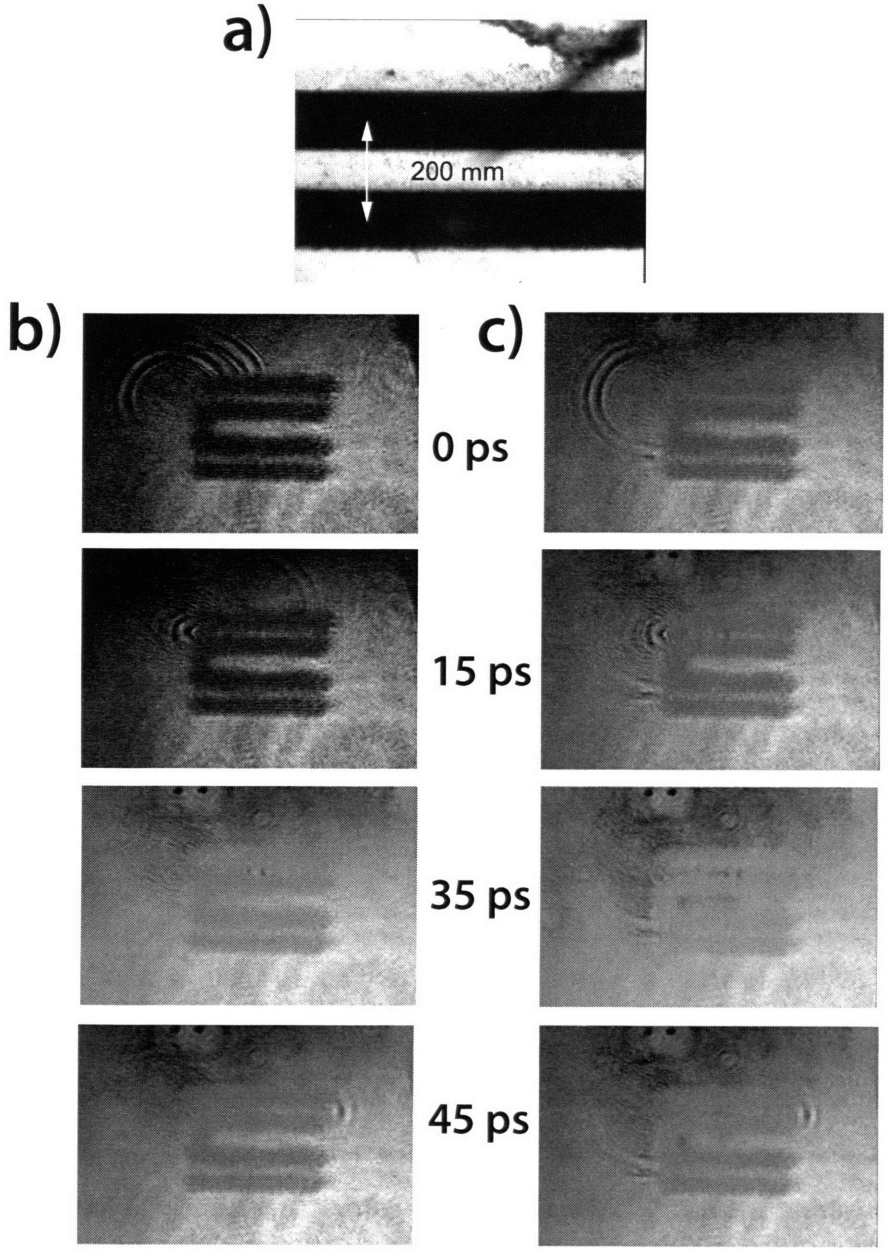

Figure 7-8: Two semicircular polariton wavepackets are generated and focused from different locations into a 200 μm wide, 1.7 mm long $LiNbO_3$ wavegude. Phonon-polaritons could be directed into either the top or bottom waveguide shown. Once the polaritons are in the waveguide, they remain confined until the end of the channel. The semicircle that persists at the excitation region is due to photorefractive damage from the excitation pulses. This does not appear to influence polariton generation. Images at the top correspond to oblique incidence focusing and images on the bottom correspond to normal incidence focusing.

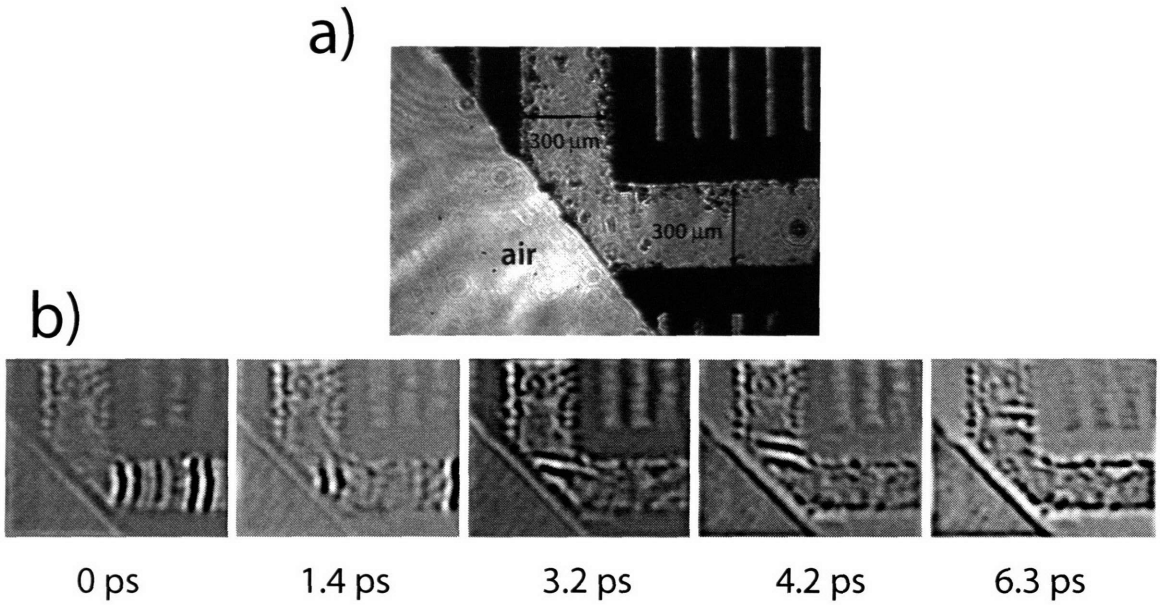

Figure 7-9: Two counterpropagating polariton ripples are generated inside a waveguide (horizontally oriented in the figure) at a nearly linear excitation region. The ripple propagating to the left reflects off the crystal wall at the end of the first waveguide and then passes into the second waveguide, thus making a 90 degree turn. The images are Fourier filtered.

internal reflection allows polaritons to turn extremely sharp corners with high efficiency, as is observed.

7.3.3 Waveguide Interferometers

To illustrate transverse rectangular waveguide effects, we demonstrate a polariton Y-coupler, which couples radiation into a selected subset of the waveguide modes [83]. Figure 7-10 shows a Y-coupler fabricated in 250 μm thick $LiNbO_3$. A 100 μm grating excitation pattern is used to generate a several-cycle polariton response, parts of which propagate into the two entry waveguides of the Y-coupler (See Figs. (7-11) and (7-12)). Depending on the orientation of the excitation grating wavevector, the polaritons in the two waveguides meet either in phase or out of phase and are coupled into either symmetric or antisymmetric rectangular waveguide modes, predominantly of lowest order (i.e. TM_{10} or TM_{20} modes), respectively.

Results of experiments are shown in Figs. 7-11(a) and 7-12(a), and two-dimensional TM

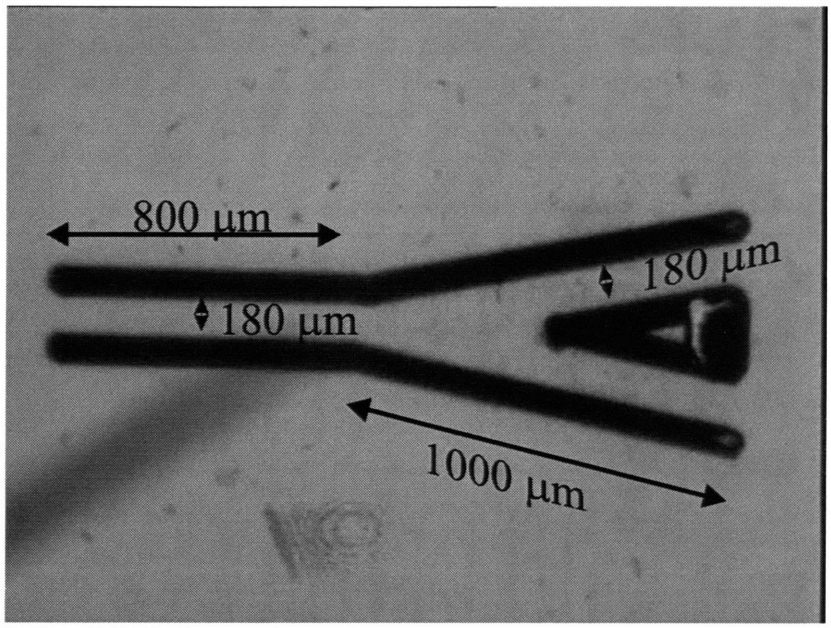

Figure 7-10: Optical micrograph of a Y-coupler machined in 250 μm thick $LiNbO_3$. The center-to-center separation of the walls in all of the three waveguide segments is 180 μm. The angle between the two merging guides is 20^o.

FDTD simulations are shown in Figs. 7-11(b) and 7-12(b), for the even and odd mode coupling respectively. The crystal portion of the problem space is 500 micron thick $LiNbO_3$, the thickness of each of the waveguide walls is 30 μm, and the width of the waveguides is 150 μm. Figures 7-11(b) and 7-12(b) show the spatial distribution of the component of the vibrational coordinate polarized along the optic axis (perpendicular to the output waveguide of the structure). This component is observed by probe light with polarization parallel to the optic axis. Not shown is the vibrational component along the propagation direction. The spatial distribution of the simulated polariton waveform in the output waveguide confirms that the polariton response couples predominantly into the TM_{10} mode in the case of in-phase coupling. The simulation shows that a small portion of the response couples into the TM_{30} mode. In the case of the tilted excitation wavefront, the simulated polariton wave couples mostly into the antisymmetric TM_{20} mode, in good agreement with the experimental observations.

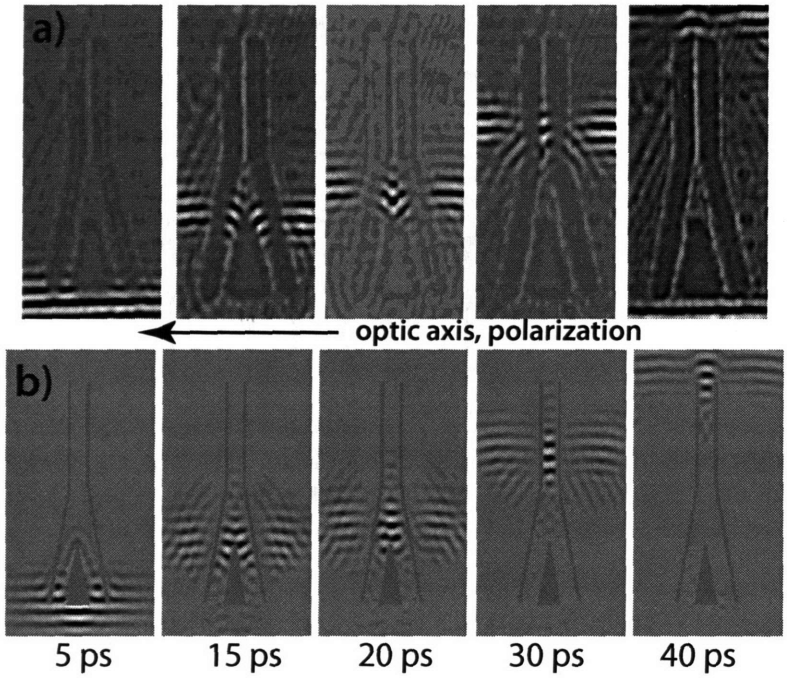

Figure 7-11: In-phase coupling. a) Experimental: A portion of the narrowband phonon-polaritons enters the two waveguides. The two wavefronts are in phase, and when they meet, they make an interference pattern which favors coupling into the low order TM modes with symmetric transverse electric field component and uniform distribution along the crystal depth—predominantly the TM_{10} mode. The fourth image shows the wave inside the coupling waveguide, and the fifth image shows the exiting phonon-polaritons. Note: the wave at the very bottom of the fifth image is a reflection from a crystal wall at the bottom of the structure (out of the field of view). b) Simulation: FDTD polariton simulation of the configuration in a), where the excitation grating wavevector is parallel to the waveguide output channel at the top of the figures. The displacement component Q along the optic axis is shown.

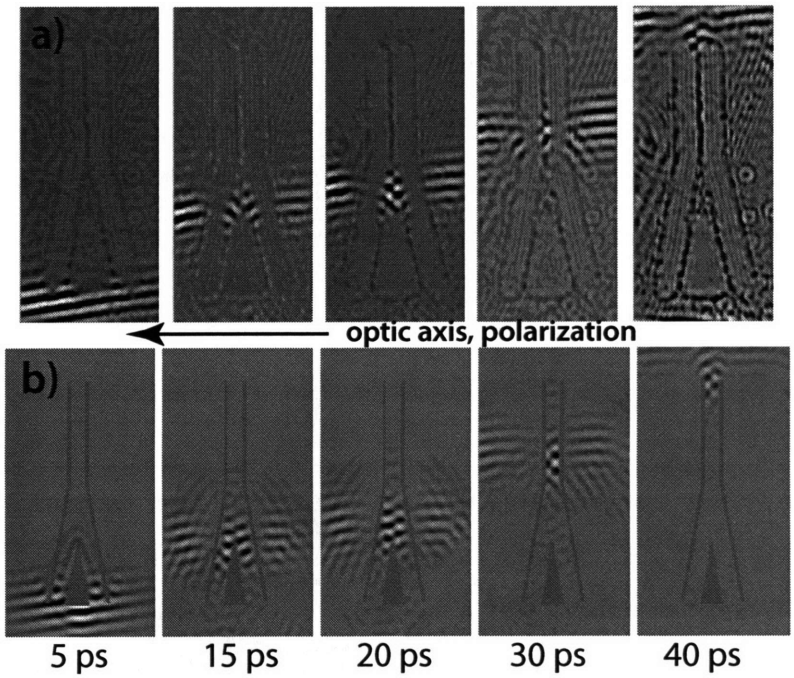

Figure 7-12: Out-of-phase coupling. a) Experimental: The wavefront of the phonon-polaritons has been tilted with respect to the Y-coupler so that the two waves that enter the two leading waveguides with a phase difference of π. Upon interference, as the second image shows, the pattern is antisymmetric with respect to the merging waveguide. This favors coupling into the modes with antisymmetric transverse electric field component—predominantly the TM_{20} mode. The fourth image shows the anti-symmetric mode well inside the merging waveguide, and the fifth image clearly shows the antisymmetric nature of the diverging wave emanating from the waveguide. b) Simulation: FDTD polariton simulations of the configuration in a), where the excitation grating wavevector forms an 8^o angle with the bisector of the angle of the merging waveguides. The displacement component Q along the optic axis is shown.

7.4 Resonators

Waveguides and resonators both rely on confinement, but in a resonator, waves are trapped rather than guided. A resonator's primary mission is confinement of waves. However, the spectral properties of resonators can also be exploited to enable spectral filtering since only certain frequencies have significant lifetimes within the cavity, characterized by a frequency dependent cavity Q. In this section we demonstrate confinement of phonon-polaritons in a resonant cavity, visualize the modes of the cavity through real-space imaging, and exert coherent control over those modes using temporal pulse shaping.

7.4.1 Fabrication

The resonant cavity was fabricated through femtosecond laser machining (see chapter 6), in which 10-20 μm features that fully extend through the thickness of an x-cut $LiNbO_3$ crystal (5 x 4 x 0.25 mm) were formed by a series of femtosecond laser pulses (100-200 μJ, 50 fs) that were focused onto the crystal to a beam waist of approximately 10 μm (microscope objective: NA $\sim$ 0.1). The procedure is described briefly below.

The same region of the 250 μm thick $LiNbO_3$ sample was left in the beam path for 3 seconds, during which time a hole was drilled through the depth of the crystal. Damage throughout the thickness of the crystal was facilitated by the long Rayleigh range of the focused beam. The sample was then translated laterally by a distance of 10 μm, irradiated for 3 seconds, and the process was repeated until a trench of specified length had been carved. The resonator structure was machined in this manner by carving out two 0.5 mm $\times$ 0.6 mm rectangular pieces separated by 300 μm. After machining all four sides, each rectangle was removed by applying minimal pressure. An optical micrograph of the fabricated polariton resonator is shown in Fig. 7-13(a). The front side of the $LiNbO_3$ resonator is (290 ± 5) μm wide and the width of the back side is (220 ± 5) μm, that is, the side surfaces are tilted by about 7 degrees (see part (b) of the figure).

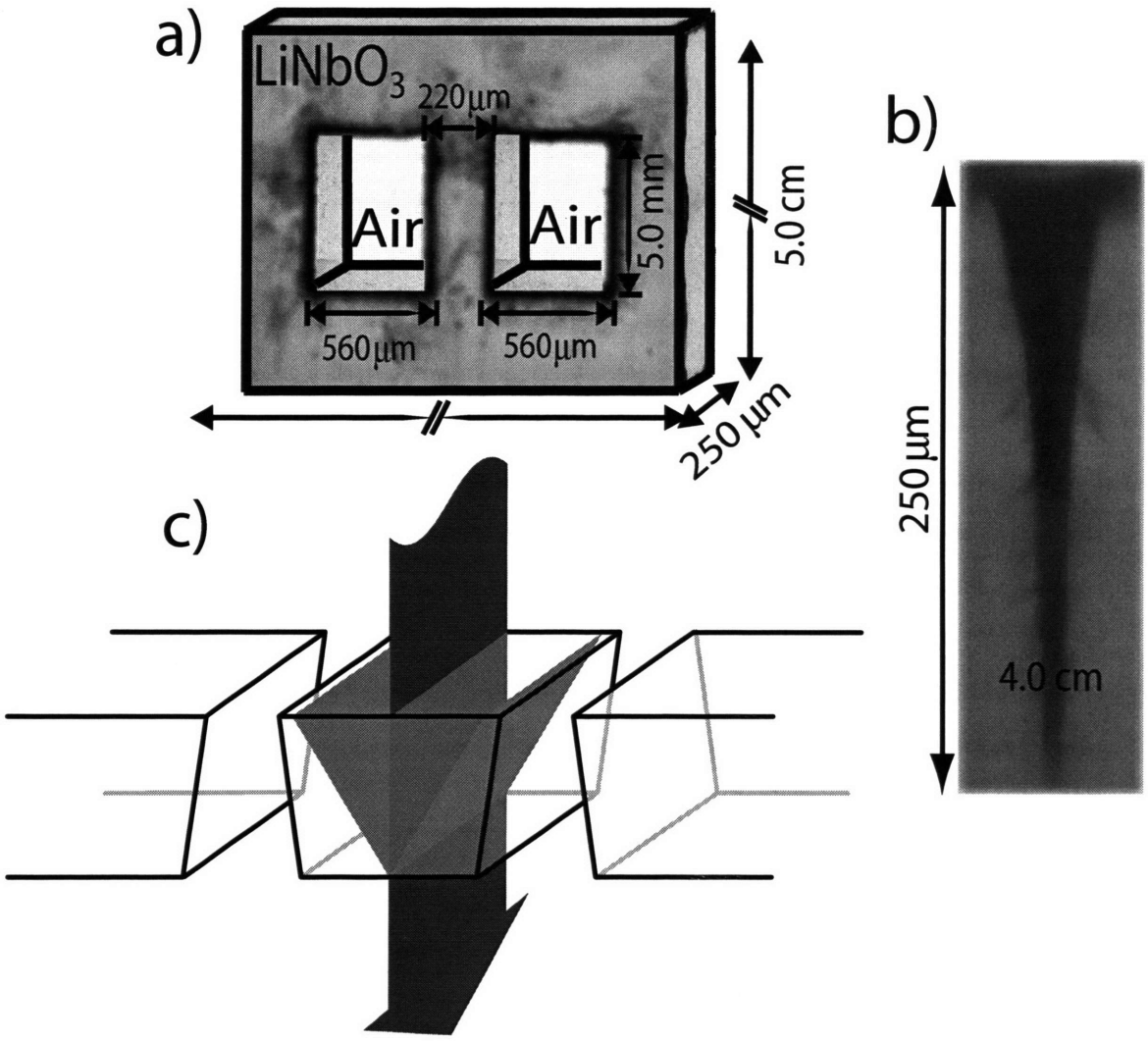

Figure 7-13: a) Polariton resonator fabricated with femtosecond laser machining. The front face of the illustration is an optical micrograph of the structure. b) Profile of a hole milled in $LiNbO_3$ indicates the presence of a bevel of approximately 7^o. c) Schematic illustration of the coupled system of resonators with tilted side surfaces. The excitation pulse (in red) passes through the center of the $LiNbO_3$ resonator and generates two polariton waveforms (in green) propagating in opposite lateral directions with a forward component.

7.4.2 Experimental

Two sets of experiments were performed on the same polariton resonator: direct visualization of waveguide modes using real-space imaging, and coherent control over polariton resonator modes. Polariton excitation is illustrated schematically in Fig. 7-13(c).

Coherent Control

For polariton measurements, the excitation light was focused (to spot size $2w_0$=130 μm) into the center of the resonator. To exert coherent control over the response, a 1 μJ excitation pulse was split into a train of seven evenly spaced pulses with a nearly Gaussian profile and with tunable temporal spacing using a recirculating reflection based pulseshaper described in chapter 4. The temporal evolution of polaritons inside the cavity was monitored through grating-based interferometry, which was also described in chapter 4, wherein a beam is split by a phase grating into ± 1 orders of diffraction, which serve as probe and reference arms. The beams are focused ($2w_0$=25 μm) and transmitted through the resonator and a reference crystal of the same thickness, respectively, and recombined interferometrically at a second phase mask. [34] The probe arm, which is overlapped spatially with the pump, undergoes a time-dependent phase shift due to the polaritons.

Visualization

Phonon-polaritons were generated with single or crossed excitation pulses and monitored with real-space imaging, using an expanded probe beam that illuminated the entire crystal and was projected onto a CCD camera as shown in Fig. 4-1(c). Binary phase masks with various fringe spacings were inserted into the excitation beam path (along with a 1:1 cylindrical 2-lens telescope) to project 2-5 interference fringes within the resonator. Alternatively, a third cylindrical lens was used to project a single line of excitation light, roughly 40 μm wide, onto the structure, as shown in Fig. 4-1(a).

The pump energy was typically on the order of 20 μJ. The probe pulse (2 μJ) was frequency-doubled with a 100 μm thick β-barium borate crystal, illuminating the whole

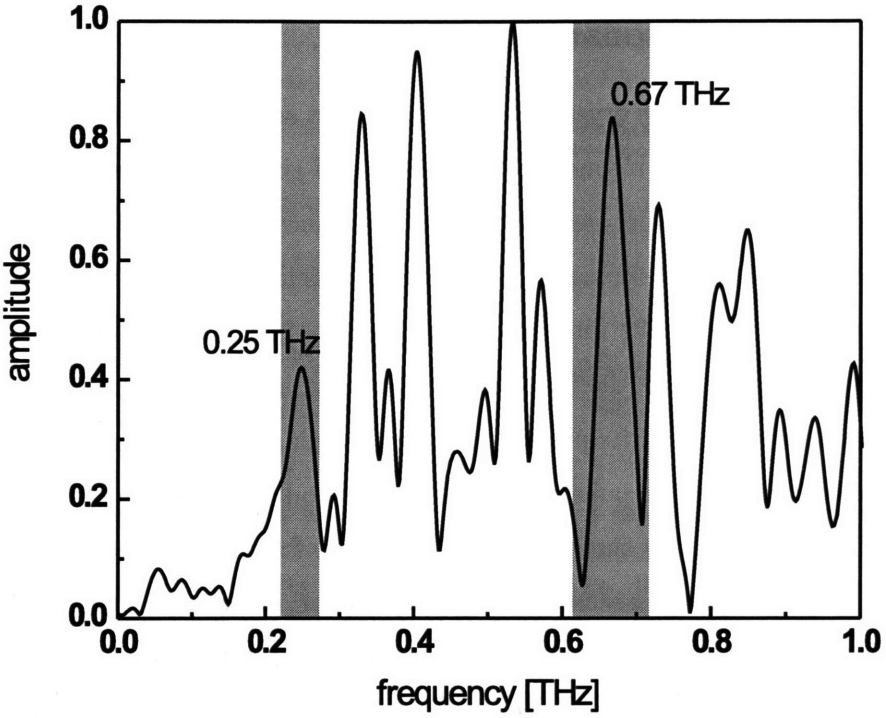

Figure 7-14: Calculated frequency response. The two modes observed in the experiments are indicated by two gray bars, where the width corresponds to the uncertainty in the measured frequency.

crystal including the resonator structure with an angle of incidence of 10-degrees to partially compensate for group velocity mismatch with the 800 nm excitation pulse(s), and projected onto a CCD camera with a 0.55 numerical aperture microscope objective. The CCD camera had 640 $\times$ 480 pixels, a frame rate of 30 Hz, and an integration time that was typically 200 ms.

An undesired feature of Talbot imaging is some loss of resolution, which leads to blurring of the resonator structure. In order to illustrate the signal recurrences within the resonator with optimal clarity, all images were rescaled as they were recorded so that weaker signals recorded after several recurrences could still be observed clearly. This procedure sacrifices quantitative information about the resonator loss from polariton damping and partial transmission.

7.4.3 System Resonances

The air gaps, as well as the crystalline region, can act as THz resonators, so the whole system consists of three coupled resonators. The degree of coupling depends on the reflectivity at the crystal-air interfaces between them. The resonance frequencies of the system of coupled resonators were obtained through FDTD simulations incorporating the excitation process as well as probing. The probe intensity at the center of the $LiNbO_3$ resonator was extracted as a function of time, and the frequency response was obtained by Fourier transformation. In order to cover a broad frequency range with a single simulation, the full width at half maximum of the excitation pulse was chosen to be about 1/5 (50 μm) of the $LiNbO_3$ resonator width. Therefore, what is shown in Fig. 7-14 is the frequency response convolved with the spectrum of polaritons generated. Additional simulations with just the $LiNbO_3$ bridge show that only the resonances below approximately 0.28 THz, which corresponds to a wavelength of about 200 μm, are visibly affected by the air gap resonators. Even then, however, the effect of coupling is minor. While the line widths of resonances for frequencies below 0.6 THz are dominated by reflection losses, for higher frequencies absorption starts to play a major role.

7.4.4 Coherent Control Using Temporal Pulse Shaping

In this section, we demonstrate polariton confinement and amplification through a combination of temporal pulse shaping and patterned materials. The finite damage threshold for optical pumping and the propagation of polaritons away from the excitation region constitute the chief impediments to polariton amplification through which nonlinear wave propagation and lattice dynamics might be explored. Temporal pulse shaping alone is sufficient to alleviate the damage threshold burden, as it allows for the redistribution of the optical pump energy from a single pulse into a sequence of less intense pulses. However, unlike spatiotemporal pulse shaping [51], temporal pulse shaping does not address the fact that the polaritons move out of the beam path before subsequent pulses can arrive. Here we employ temporal pulse shaping and a polariton resonator which spatially confines the polaritons by reflection

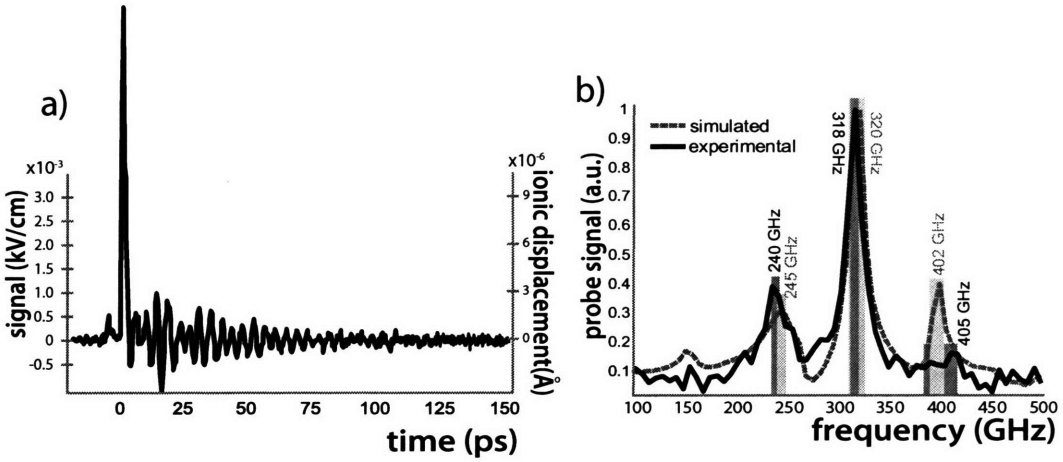

Figure 7-15: a) Time-dependent polaritonic response of the $LiNbO_3$ resonator shown in Fig. 7-13(a) to a single excitation pulse. b) Fourier transform of part (a) and of finite difference time domain simulation of the response. The dark vertical bars indicate the uncertainties in the experimentally measured frequencies. The light vertical bars indicate the ranges of frequencies determined by reasonable variation of the simulation parameters. The discrepancy in the strength of the 400 GHz resonance is likely due to inaccuracy in the excitation spot size, which limits the polariton bandwidth.

between two $LiNbO_3$-air interfaces, thereby preventing propagation out of the pumping region. This allows subsequent pulses in the pulsetrain to amplify the polaritons each time they pass through the center of the cavity.

The time-dependent polariton response of the resonator to a single optical pulse is illustrated in Fig. 7-15(a). In a bulk sample, the single pulse would generate a single-cycle polariton wavepacket centered at about 300 GHz, with approximately 400 GHz of bandwidth. Repeated reflections in the cavity give rise to multiple-cycle responses whose resonant frequencies are revealed in the Fourier transform shown in Fig. 7-15(b).

Responses of the cavity to multiple-pulse excitation with several repetition rates are shown in Fig. 7-16. The polariton responses overlap temporally with the initial electronic signal contributions and continue thereafter, with the strongest and most persistent polariton contributions occurring when the excitation repetition rate matches one of the cavity resonances. The results illustrate the ability to drive either of the accessible resonance frequencies independently. Comparison of the 320 GHz resonance frequency in the Fourier transform of

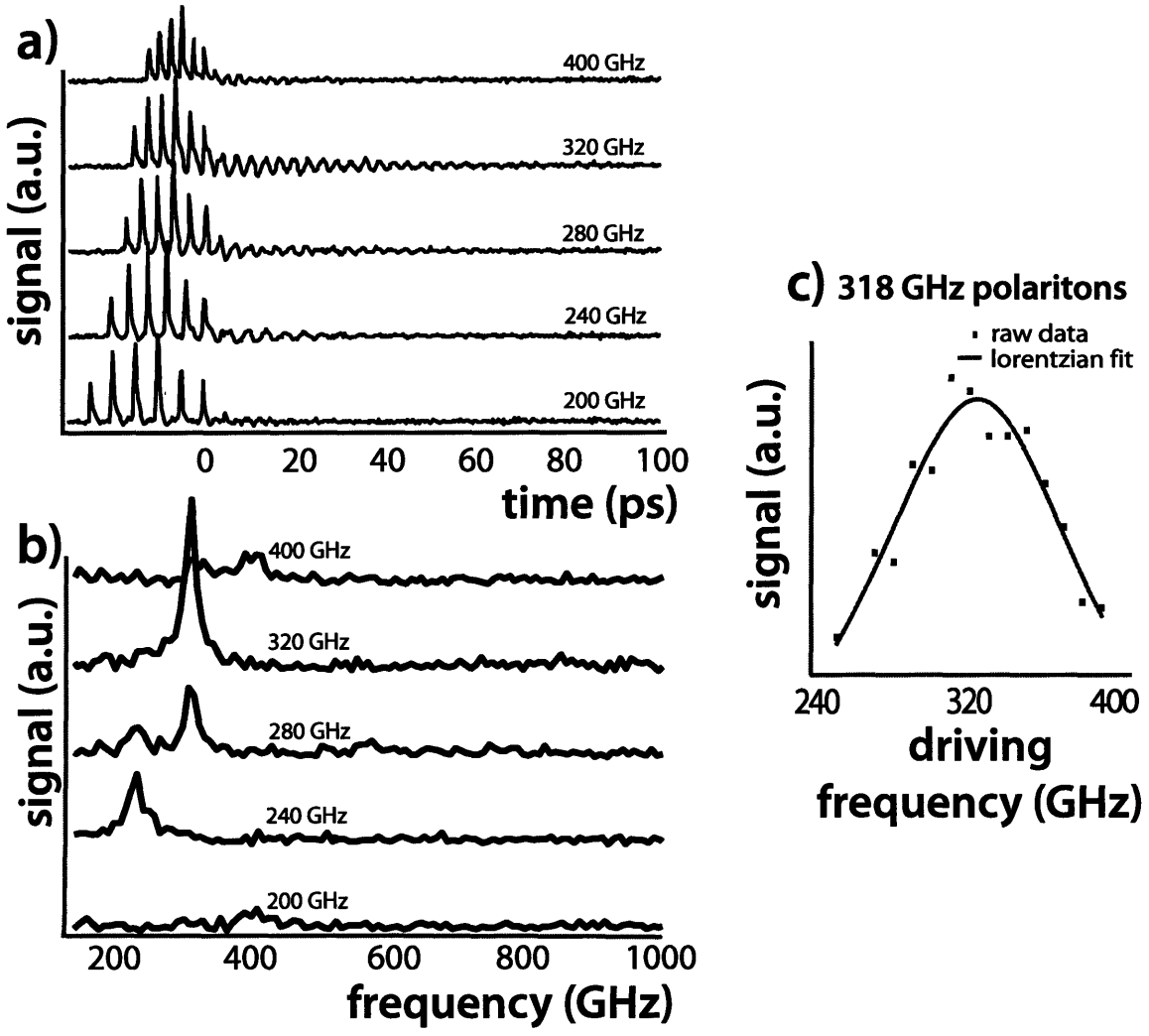

Figure 7-16: Time-dependent responses (a) of the polariton resonator to excitation pulsetrains with the repetition rates shown. The initial signal contributions ($t < 0$) are due largely to non-resonant electronic responses to the excitation pulses. The stronger and more persistent polariton responses observed when the resonator is driven at its cavity resonance frequencies are illustrated in the time-dependent data (a) and the Fourier transforms (b). Driving frequency is indicated alongside each plot. (c) Relative amplitude of the 320 GHz Fourier component as a function of pump pulsetrain repetition rate.

a single broadband pulse in the resonator (Fig. 7-15(a)) with the same frequency component when excited with a 300 GHz pulsetrain—which approximates the center frequency of the broadband pulse were it in bulk $LiNbO_3$—indicates nearly an order of magnitude increase in polariton energy with the latter.

The experimental results were compared with finite difference time domain (FDTD) simulations that take into account the polariton generation process as well as polariton propagation (see chapter 3). Two-dimensional simulations (neglecting the vertical dimension of Fig. 7-15(a) were performed to discern the origin of the two resonance frequencies observed experimentally. The simulation results shown in Fig. 7-15(b) clearly reveal these frequencies.

Several nontrivial features complicate interpretation of the experimental results. First, the bevel at the sample edges leads to modifications in the resonator eigenmodes and their frequencies. Second, the sample actually presents a set of three coupled resonators arising from the central $LiNbO_3$ cavity and the two adjacent air cavities [85]. Third, since the excitation pulses travel at a finite speed through the crystal, the polaritons are generated with a small but significant forward wavevector component in addition to the transverse wavevector components. If the back face of the crystal is parallel to the front face, then, depending on the crystal thickness, the polaritons may undergo repeated total internal reflections off the front and back faces as they propagate mainly in the transverse directions. If the side faces of the crystal are perpendicular to the front and back faces, then the polaritons undergo total internal reflection at the sides as well. If the sides are beveled, as in the present case, then the angle of incidence needs to be considered to determine whether it exceeds the total internal reflection angle of 11^o. Fourth, if the sample is thin relative to the polariton wavelength, then it may act as a planar waveguide and the forward polariton wavevector component may be reduced or eliminated as propagation occurs. Fifth, since the probe pulses travel at a finite speed through the crystal, probing of the polaritons is phase-matched optimally when they retain their forward wavevector component. Loss of this component due to planar waveguide effects or reversal of this component due to reflection off the back face of the sample leads to reduced signal levels.

The influence of the aforementioned five effects was considered with the aid of two-dimensional FDTD simulations. Including the bevel in the simulations, the first effect, reveals the cavity mode frequencies shown in Fig. 7-15(b). Consideration of the second, third, and fourth effects, shown in Fig. 7-17(a), indicates that the multiple resonances are primarily due to the bevel, and not due to coupling between the air cavity and $LiNbO_3$ cavity. In particular, 318 GHz polaritons, whose wavelength is 180 μm, do not experience substantial planar waveguide effects in the 250 μm thick crystal. They therefore reach the edges with forward or back propagation angles exceeding the total internal reflection angle. Polaritons at the lower resonance frequency experience partial loss of the forward wavevector components by the time they reach the edges, and these can undergo weak transmission at the edges. This phenomenon contributes to loss, but not to observable coupled cavity effects.

Finally, consideration of the fifth effect through incorporation of the probing process into the FDTD simulations accounts for reduced signal levels in the data from polaritons at both resonant frequencies. The presence of the bevel causes the polariton trajectory inside the cavity to walk off from the phase matched direction. Probe signal reductions were observed in the 240, 318, and 400 GHz modes, but the strongest effects were seen in the two higher frequency modes.

Simulations show that the 400 GHz resonance has nodes that are periodic in the forward direction, indicating the resonance is primarily due to the crystal thickness and not the resonator width. When the simulated resonator width was varied in the lateral direction, the 400 GHz resonance frequency stayed nearly the same. By varying the resonator crystal thickness, however, substantial shifts in the 400 GHz mode resonance frequency were observed. This indicates that the mode is primarily related to forward/backward polariton propagation and should be poorly resolved due to a lack of phase matching with the probe pulses. Probing simulations shown in Fig. 7-17(b) confirm this.

A similar trend was observed with the 318 GHz peak for probing in cavities with increasing bevel angles, but this peak was still observed as the dominant peak at all bevel angles considered. Further, increasing bevel angle caused a strong rise in the amplitude of this

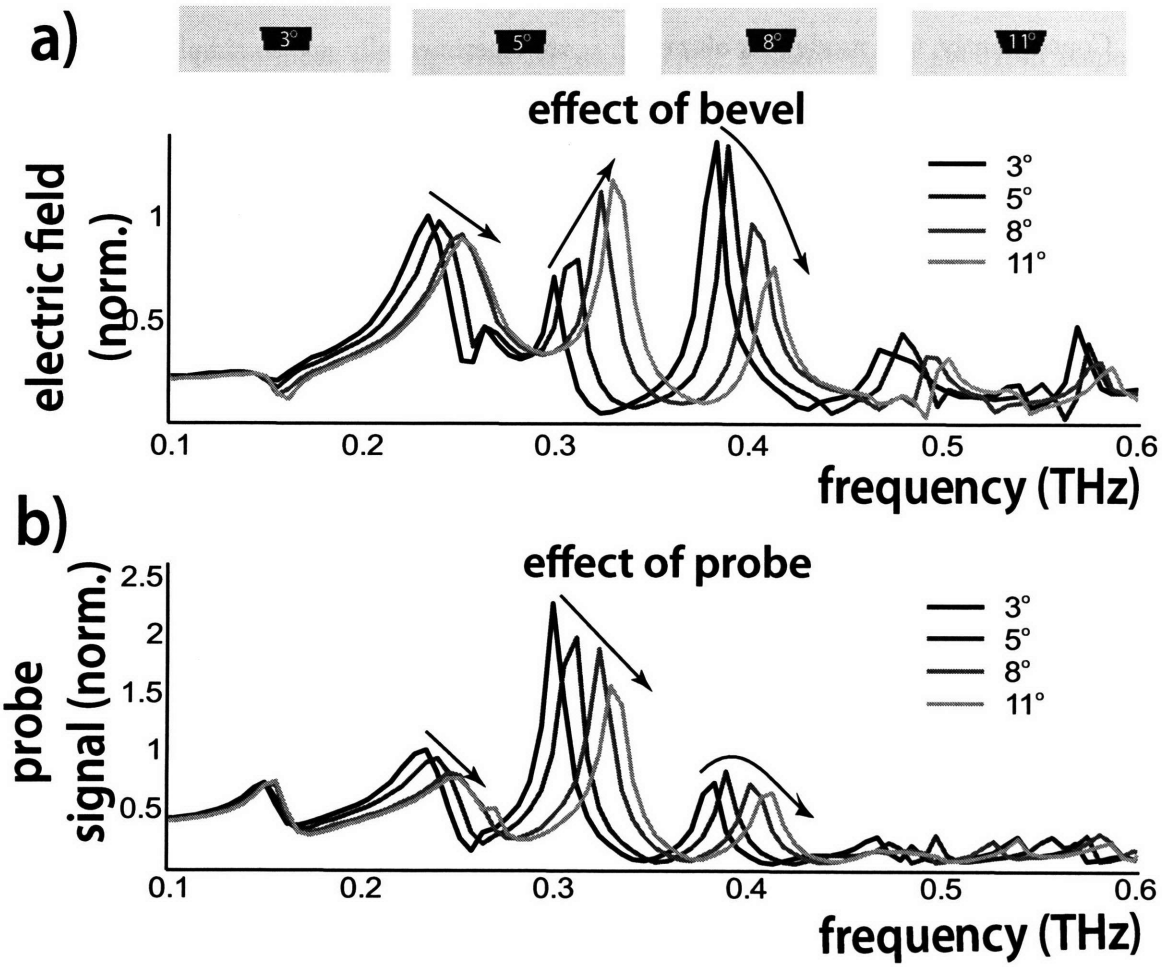

Figure 7-17: FDTD analysis of the effect of the bevel and probing. a) Simulations of the observed cavity resonance frequencies in resonant cavities with progressively larger bevel angles. b) Simulations showing the reduction in signal levels through real-space imaging due to phase matching issues that arise due to the bevel angle.

peak and caused the largest shifts in resonance frequency of the three modes investigated.

The 240 GHz peak appears to be due to predominantly lateral motion as variation in the sample thickness had little effect on its resonance frequency. It was the only mode that exhibited non-zero transmission through the resonator walls at all bevel angles considered. Consequently, this mode was observed, both experimentally and in simulations, to have the lowest cavity Q, which is due to loss upon each reflection at the resonator wall.

The high cavity Q of the 318 GHz mode is caused by total internal reflection, which was observed in simulation for cavities with bevel angles greater than 3^o. Smaller bevel angles resulted in lower amplitudes for this mode, and coupling effects were observed. The small peak between the 240 and 318 GHz mode in simulations with a 3^o bevel angle is present only when both the $LiNbO_3$ and air cavities are included in the simulations. The reason coupling can exist for small bevel angles is that as the bevel is reduced, the 318 GHz mode resonance frequency becomes low enough that waveguide straightening facilitates transmission through the resonator walls, thus enabling interaction with the adjoining air cavity.

Including these five effects in the FDTD simulations ensures the data at all excitation pulsetrain repetition rates can be fit well with 1/e decay times for polariton amplitudes in the 318 GHz and 240 GHz modes of 33 ps and 20 ps, respectively, corresponding to cavity Q values of 33 and 15 respectively (energy not amplitude). These Q values could likely be improved somewhat through improvements in the flatness of the machined faces, the use of reflective coatings of those faces or of dielectric quarter-wave stacks, and cooling of the crystal or selection of a different crystalline material to reduce polariton damping (a minor but non-negligible contribution to the observed losses).

7.4.5 Real-Space Imaging of Resonator Modes

In this section, we illustrate direct visualization of phonon-polaritons in the resonator shown in Fig. 7-13(a). This allows us to not only track the temporal evolution of these modes, but the spatial evolution as well. The resonator modes of interest are illustrated in Fig. 7-14.

We first present results of almost single-mode excitation, i.e., the spatial excitation pat-

tern almost perfectly matches that of a longitudinal resonator mode. We then show results of a single line excitation where the width of the line is about a fifth of the resonator width and the phonon-polariton response bounces back and forth between the two resonator walls, producing periodic recurrences of the original spatial pattern.

By using a phase mask grating with 80 μm spacing, a narrowband polariton response is generated inside the resonator, and its evolution is monitored for over 25 ps. By careful positioning of the excitation grating, we excite a response that is very close to one of the eigenmodes of the resonator corresponding to a standing wave with a wavelength which is a third of the central resonator width (see Fig. 7-14). The intensity of the mode reaches a maximum at the two resonator walls. When electromagnetic radiation is reflected from an interface transitioning from a high to low dielectric medium, the reflected wave undergoes no phase shift, and the polariton waveform generated sets up a standing wave within the resonator.

The recurrent behavior of the standing wave is summarized in Fig. 7-18. The two terminal quarter wavelengths at the walls of the resonator are not as clearly imaged due to scattering of the 400 nm probe pulse at the walls of the resonator and the out-of-focus Talbot imaging. Figure 7-19 is constructed by averaging the signal in the uniform direction along the length of the resonator for each image. Note that Fig. 7-19 makes it seem that the waveform persists uniformly for some time and then abruptly switches sign. This artifact is a result of the bitmap recalibration done at every image for maximum contrast.

Figure 7-19 reveals that between approximately 5 ps and 8 ps, the signal intensity seems to pass through a local minimum. As mentioned above, phonon-polaritons propagate with a slight forward component and the length of phasematched overlap with the probe pulse is large when they propagate toward the back side but very small when travelling toward the front side. Therefore, the signal intensity will decrease or increase depending on whether the phonon-polariton is propagating in the forward or backward direction. Due to the bitmap recalibration, this effect becomes visible only if the noise level exceeds the signal level, in which case the oscillations seem to disappear for a number of delay steps.

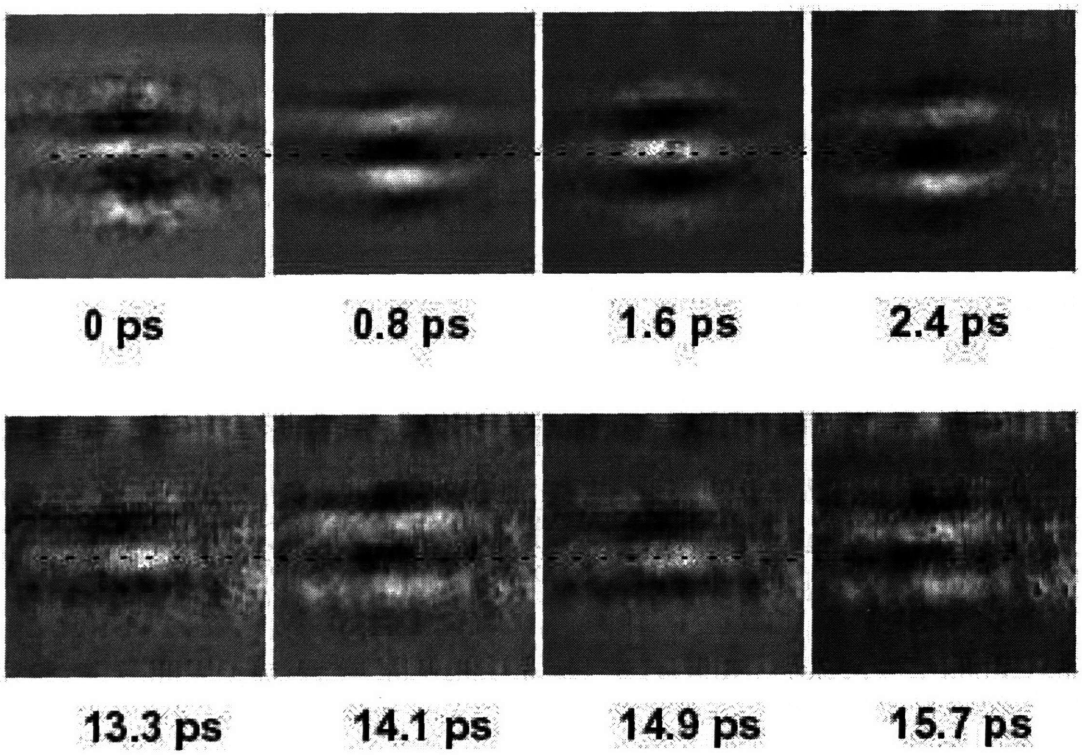

Figure 7-18: A phonon-polariton response with approximately 80 μm wavelength has been generated inside the resonator. A well-defined standing wave and its confined oscillations at a frequency of (0.67 ± 0.02) THz ((1.50 ± 0.05) ps period) are clearly observed.

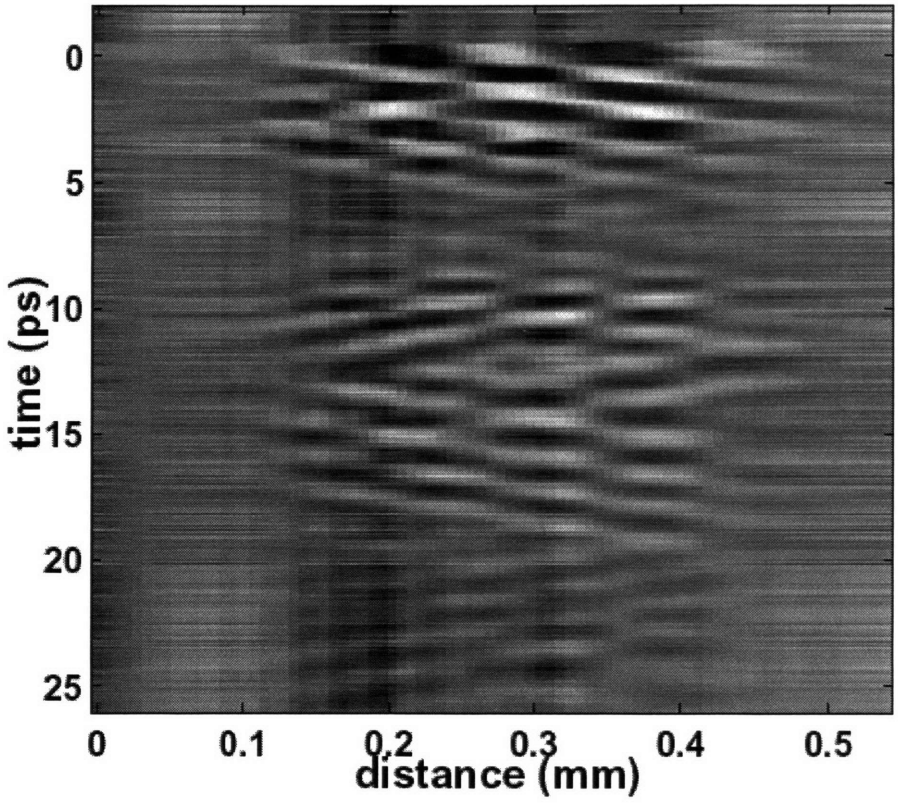

Figure 7-19: Each horizontal line is constructed from an image at a different time steps such as those in Fig. 7-18, by averaging the signal along the resonator length where the signal extends.

The standing-wave response has a period of (1.50 ± 0.05) ps, which corresponds to a frequency of (0.67 ± 0.05) THz. This is in good agreement with the system resonance at 0.67 THz, as seen in Fig. 7-14.

The response to a single line of excitation light, incident at the middle of the resonator, is shown in Fig. 7-20. The selected images come from a series of snapshots recorded at different probe delays. They show the recurrences typical of resonator behavior. The excitation light extends through the 600 μm tall resonator and into the surrounding (bulk) material. The first frame (0 ps) shows the single-cycle 'ripple'-like polariton response which similarly extends through and outside of the resonator structure. Selected frames from a polariton movie,

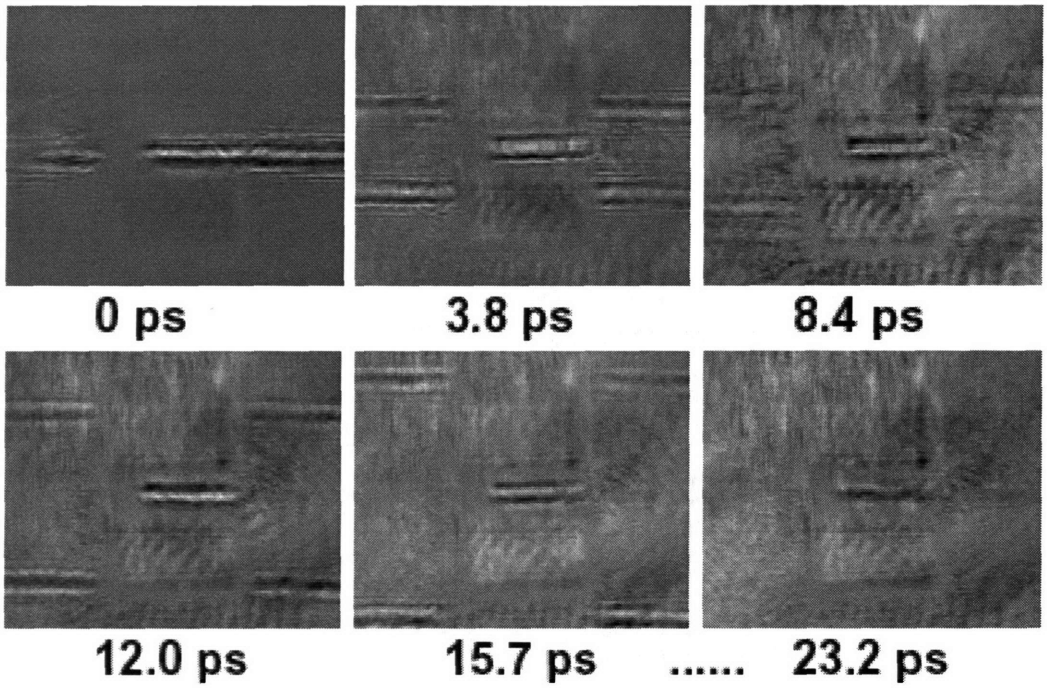

Figure 7-20: Line excitation inside the resonator and subsequent recurrences. As evident from the figure, recurrences occur on average every (4.1 ± 0.4) ps. The dotted line between the last two images indicates that they are separated by two recurrence periods.

which are given in Fig. 7-20, show that within the resonator, the response reflects back and forth between the side walls and yields recurrences which are seen to occur with a period of approximately (4.1 ± 0.4) ps. The corresponding frequency is (0.24 ± 0.03) THz, which, within the error bars, corresponds to the system resonance at 0.24 THz.

Figure 7-21 is constructed by selecting a region within the resonator from each of the images like those in Fig. 7-20. Each region is essentially a horizontal line segment, contained within the resonator region, defined by its vertical position between the top and bottom of the resonator. The signal along such a line is essentially uniform, so it is averaged and reduced to a point, which represents the signal level at that vertical position inside the resonator at a particular time. The process is repeated for the image recorded at the next time step, and so on, and all of the resulting points are placed in time order to produce a horizontal line

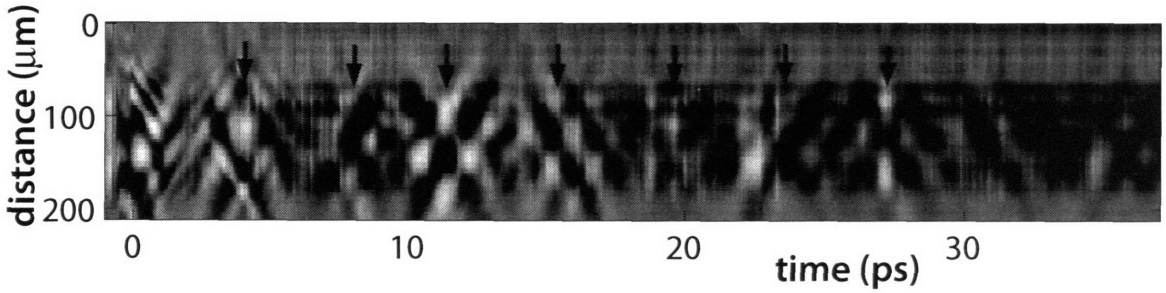

Figure 7-21: Each vertical line is constructed from images at different time steps, such as those in Fig. 7-20, by averaging the signal along the resonator length where the signal extends.

in Fig. 7-21. This line displays the time-dependent signal at the selected vertical position in the resonator averaged across the horizontal extent of the resonator. This entire process is repeated for the different vertical positions in the resonator, and the resulting times are placed above each other to generate Fig. 7-21. The figure shows that up to 6-7 recurrences can be clearly observed. The slight differences in the details of the recurrence patterns result from the fact that the initial line excitation is not perfectly centered in the resonator.

The decay of the signal is mostly due to partial transmission through and scattering at the resonator boundaries which, due to limitations of the laser machining process, are not perfectly smooth, uniform, or perpendicular to the front and back crystal surfaces.

The polariton responses outside the resonator structure propagate away from their regions of origin without constraints. In the low wave vector range included within the bandwidth of the single-cycle polariton response, the group velocity shows very little dispersion. The images clearly show that the single-cycle pulse does not spread significantly over millimeter distances.

7.4.6 Measurements of the Differential Polarizability, Terahertz Electric Field Strengths, and Ionic Displacements for Phonon-Polaritons in $LiNbO_3$

$LiNbO_3$ is well known as an electrooptic crystal, but it is also becoming increasingly important as a terahertz radiation source due to its far infrared (FIR) properties [3, 20, 91]. As we have seen in this chapter, structures like waveguides, resonators, and diffractive elements can be machined directly into $LiNbO_3$, which can be integrated into a single solid-state platform that can include terahertz generation, manipulation, readout, and other functionalities [29, 83, 81, 93]. This is not the case for other coherent terahertz radiation sources that generate phase matched (forward scattered) radiation that co-propagates with the optical excitation pulse [27]. Phonon-polaritons generated through ISRS propagate laterally within the crystal with a slight forward component, which was discussed in chapter 4. The differential polarizability, related to the second-order nonlinear susceptibility, is the constant of proportionality that relates the optical excitation pulse intensity to the terahertz electric field strength that results from ISRS.

In this section, we describe ISRS experiments conducted to measure the terahertz field strengths of an off-resonance phonon-polariton excitation in a resonant cavity, as well as the differential polarizability and maximum ionic displacement associated with phonon-polariton generation through the A_1 symmetry phonon mode in $LiNbO_3$. These measurements were done in the resonator, rather than bulk, because the phonon-polariton amplitude is localized in the cavity, which makes the analysis of the radiation field generated through ISRS less complicated due to the absence of electronic signals in the recirculating phonon-polariton waveform.

Phonon-polariton generation was achieved as described in the experimental section on coherent control. The interferometric probe arm experiences a time-dependent phase shift due to the phonon-polariton amplitude in the resonator, where the phonon-polariton induced index of refraction, Δn in $n(t) = n_0 + \Delta n$, is related to the magnitude of the ionic

displacement for the A_1 normal mode by,

$$\Delta n(t) \approx N\left(\frac{\partial \alpha}{\partial \mathrm{w}}\right)_0 \mathrm{w}(t), \tag{7.1}$$

where $(\frac{\partial \alpha}{\partial \mathrm{w}})$ is the differential polarizability in terms of the ionic displacement w along the optic axis, and N is the oscillator density. This phonon-polariton induced index of refraction change is the source of the relative phase shift in the probe arm of the interferometer. The two orders are recombined interferometrically at a second phase grating. The phase shift corresponding to the maximum ionic displacement, as discussed below, was taken from the maximum signal in the phonon-polariton cavity, which actually occurs after a couple of round trips in the cavity due to phase matching [93]. The resulting signal is shown in Fig. 7-13(a) as a function of probe delay in terms of electric field and ionic displacement.

Observed Terahertz Field Strength

We first consider the phonon-polariton electric field strengths using the interferometric measurement technique described above. The interferometer was calibrated by measuring the photodiode voltages V_{max} and V_{min} that correspond to the interferometric maximum and minimum [34]. The sensitivity of the interferometer, i.e. the change in intensity (or photodiode voltage) with probe displacement ζ, relative to the phonon-polariton excitation is described by,

$$\frac{dV}{d\zeta} = -(V_{\mathrm{max}} - V_{\mathrm{min}})\frac{\pi}{\lambda_{\mathrm{probe}}} \sin\frac{2\pi\zeta}{\lambda_{\mathrm{probe}}}. \tag{7.2}$$

For this experiment λ_{probe} was 400 nm. The maximum sensitivity at which the experiment is performed is found when $\zeta = \lambda_{\mathrm{probe}}/4,\ 3\lambda_{\mathrm{probe}}/4$, etc. In this case, the expression for the sensitivity simplifies such that $\sin(2\pi\zeta/\lambda_{\mathrm{probe}}) \approx 1$ on the right hand side of Eq. (7.2). The sensitivity in the experiment was 0.192 nV/nm and the relative phase shift for the first phase matched phonon-polariton peak was measured to be $(V_{\mathrm{max}}^{\mathrm{pol}} - V_{\mathrm{min}}^{\mathrm{pol}}) \approx 0.1$ nV, which results in a $\pi/4000$ relative phase shift. These values can be further translated into phonon-polariton electric field strength with the aid of the known electrooptic coefficient (r_{33}) for the A_1 mode

in $LiNbO_3$ and the measured phase shifts through the relation:

$$E = \frac{\Delta\phi\lambda_{\text{probe}}}{\pi d n_{\text{probe}}^3 r_{33}}, \tag{7.3}$$

where $\Delta\phi$ is the observed phonon-polariton-induced phase shift, n_{probe} is the index of refraction for the probe beam in $LiNbO_3$, d is the $LiNbO_3$ crystal thickness, and r_{33} is the electrooptic coefficient for probing along the extraordinary axis of $LiNbO_3$ with parallel polarized probe light. Using the measured phase shift, $n_{\text{probe}} = 2.33$ [22], and $r_{33} = 30.9$ x 10^{-7} cm/kV [48], the observed terahertz field strength was measured to be 0.010 $\pm$ 0.001 kV/cm.

Observed Differential Polarizability

The differential polarizability can be extracted from the excitation pump and probe parameters and the measured relative phase shift for maximum ionic displacement. We consider first the action of the excitation pulse. The stimulated Raman force imparted to the ions by an optical excitation pulse is given by

$$F_{SR} = \frac{\epsilon_0 Z}{2}\left(\frac{\partial\alpha}{\partial \mathrm{w}}\right)_0 \xi S(t), \tag{7.4}$$

where ϵ_0 is the permittivity of free space, Z is the wave impedance in $LiNbO_3$, $S(t)$ is the power flow of the optical field, and ξ is the ISRS conversion efficiency, which is discussed in detail elsewhere [23]. The Raman force can be related to the ionic momentum through the time integral of the force,

$$P_{\text{ionic}} = \int F_{SR}\cdot dt = \frac{\epsilon_0 Z}{2}\left(\frac{\partial\alpha}{\partial \mathrm{w}}\right)_0 \frac{\Delta U}{\pi w_0^2}, \tag{7.5}$$

$$\Delta U = \pi \mathrm{w}_0^2 \xi e^{\frac{-\omega^2\tau^2}{4}} \int_{-\infty}^{\infty} S(t)\cdot dt, \tag{7.6}$$

where ΔU is the energy imparted to the ions, $2\mathrm{w}_0$ is the excitation spot-size, ω is the phonon-polariton frequency, and τ is the FWHM pulse duration. Note, the convolution factor in Eq. (7.6) accounts for the fact that the impulsive force is a Gaussian envelope and not a delta

function. The excitation pulse energy, ΔU, is computed by dividing the measured average power by the repetition rate and multiplying by the convolution factor and the conversion efficiency. Initially, the impulsive force imparts a velocity to the ions and all the energy is kinetic. The kinetic energy becomes zero at the maximum ionic displacement. However, not all of the kinetic energy is transferred to the lattice; the kinetic energy imparted to the lattice is $(U_{\text{mech}}P_{\text{ionic}}^2)/(2MU_{\text{total}})$, where M is the reduced mass for the A_1 normal mode in $LiNbO_3$. The ratio of mechanical to total energy, neglecting damping, is approximately 0.437 for 300 GHz phonon-polaritons [13]. Equating the initial kinetic energy with the lattice potential energy and solving for the maximum ionic displacement, w_{max}, we find,

$$\text{w}_{\text{max}} = \left(\frac{\partial\alpha}{\partial \text{w}}\right)_0 \frac{\epsilon_0 Z}{2M\omega_{\text{TO}}} \sqrt{\frac{U_{\text{mech}}}{U_{\text{total}}}} \frac{\Delta U}{\pi \text{w}_0{}^2}. \tag{7.7}$$

Next, we consider the details of the probe beam. The detected signal intensity resulting from the interference of the probe arm and the reference arm is $I_{\text{det}} = |E_{\text{prober}} + E_{\text{ref}}|^2 = I_{\text{probe}} + I_{\text{ref}} + 2\sqrt{I_{\text{ref}}I_{\text{probe}}}\cos\phi$ where $\phi = \phi_{\text{probe}} - \phi_{\text{ref}}$ is the relative phase between probe and reference arms, and I is the measured intensity. If the probe and reference arms are of the same intensity, this reduces to, $I_{\text{det}} = 2I_0(1 + \cos\phi)$, where I_0 is the intensity of either the probe or reference arms. If the probe arm alone encounters an additional contribution to the index of refraction, $n = n_{\text{probe}} + \Delta n$, then the relative phase between probe and reference arms is $2\pi d\nu_{\text{probe}}\Delta n/c_0$. Inserting this into I_{det} and solving for Δn we find $\Delta n = (c_0/(2\pi\nu_{\text{probe}}d))\cos^{-1}((I_{\text{det}}/2I_0) - 1)$. This can be related to Eq. (7.1), and we can again solve for the ionic displacement, obtaining a relation for the maximum ionic displacement in terms of the differential polarizability and measured probe pulse parameters,

$$\text{w}_{\text{max}} = \left(\frac{\partial\alpha}{\partial \text{w}}\right)_0^{-1} \frac{c_0^2}{N(\omega_{\text{probe}}d)^2} \left(\cos^{-1}\left(\frac{I_{\text{det}}}{2I_0} - 1\right)\right)^2. \tag{7.8}$$

The maximum ionic displacements calculated in Eqs. (7.7) and (7.8) are equal and can be related to each other directly, resulting in an expression for the differential polarizability

n_{probe}	index of refraction for probe	2.33
n_{pump}	index of refraction for pump	2.18
M	A_1 mode reduced mass	11.40 amu
ω_{TO}	A_1 phonon frequency	2π·7.6 THz
λ_{probe}	probe wavelength	400 nm
$\frac{U_{\text{mech}}}{U_{\text{total}}}$	mechanical coupling ratio	0.431
$4I_0$	value for a $\pi/2$ phase shift	1.380 a.u.
I_{det}	signal at first vibrational peak	0.7117 a.u.
d	crystal thickness	250 μm
N	oscillator density	6.285 x 10^{27} m^{-3}
$2w_0$	spot size	130.0 μm
ΔU	energy imparted to normal mode	0.00135 μJ
ξ	ISRS conversion efficiency	0.2%

Table 7.1: Values used in Eq. (7.9) to arrive at the measured value 1.2 ± 0.1 x $10^{-18}m^2$ for the differential polarizability and 3.0 ± 0.1 x 10^{-6}Å for the maximum ionic displacement.

in terms of the known or measured excitation and probe beam parameters,

$$\left(\frac{\partial\alpha}{\partial w}\right)_0 = \sqrt{\frac{n_{\text{probe}} n_{\text{pump}} c_0 M \lambda_{\text{probe}}^2 \omega_{\text{TO}} w_0^2}{2\pi N d^2 \Delta U}} \sqrt{\frac{U_{\text{mech}}}{U_{\text{total}}}} \cdot \cos^{-1}\left(\frac{I_{\text{det}}}{2I_0} - 1\right). \tag{7.9}$$

Using the measured relative phase from the first phase matched cycle in Fig. 8-15(a), accounting for the $\sim$ 60% reflection at the crystal interfaces and the 200 fs pulse duration, and using 0.2% conversion efficiency for ξ, the measured differential polarizability was found to be 1.2 ± 0.1 x $10^{-18}m^2$. Note, all values used in Eq. (7.9) and the results are contained in Table 7.1. The measured differential polarizability can be compared to the calculated differential polarizability by using the value for the second-order nonlinear susceptibility from the literature: $(\frac{\partial\alpha}{\partial w})_0 = 4\omega_{\text{TO}} d_{33}(M/(\epsilon_0(\varepsilon_0 - \varepsilon_\infty)N))^{1/2}$ where ε_0 and ε_∞ are the below and above resonance dielectric constants respectively and is taken from Raman and IR spectroscopy data [6, 5]. This was calculated to be 1.14 x 10^{-18} m^2, which is in close agreement with our measured value. With the aid of the differential polarizability, the maximum ionic displacement can be expressed through either Eqs. (7.7) or (7.8). The value obtained using the result from Eq. (7.9) is 3.0 ± 0.1 x 10^{-6}Å.

The measurements performed here provide a convenient metric for the terahertz field strengths available from ISRS phonon-polariton generation in ferroelectric $LiNbO_3$. Accounting for resonance enhancement, frequencies closer to resonance can produce fields on the order of hundreds of kV/cm [104]. Higher field strengths are possible very near resonance, though there will be substantially more damping at these higher frequencies. Since the differential polarizability is proportional to the second-order nonlinear susceptibility, which can be related to the electrooptic coefficient [3], higher terahertz field strengths should be accessible in doped crystals like $MgO:LiNbO_3$. Radiation fields on the order of hundreds of kV/cm will be useful in femtosecond nonlinear terahertz experiments, which have yet to be demonstrated in the field of terahertz spectroscopy.

7.5 Photonic Crystals

When the crystal is patterned with periodic 'air' holes, the dispersive properties are modified such that in addition to the polariton bandgap, a photonic bandgap related to the dielectric periodicity is introduced. Recently the interplay between the intrinsic LO-TO bandgap and a photonic bandgap in an overlapping frequency range that is produced through fabrication of a periodic structure in the crystalline host has been discussed [40, 41]. Here we demonstrate polaritonic bandgap structures fabricated by machining 'air' holes into an $MgO:LiNbO_3$ crystal, generating coherent THz phonon-polaritons in the material through ISRS [23], and monitoring phonon-polariton wave propagation through the photonic bandgap materials (PBMs) with real-space imaging [51].

7.5.1 Introduction to Photonic Bandgap Crystals

A bandgap is a region of frequencies in which no propagation is allowed. Radiation with frequencies in the bandgap of a material will be completely reflected at the material interface. $LiNbO_3$ has a natural bandgap, which is a consequence of the polariton mode associated with either the A_1 or E symmetry transverse optic phonon mode. The bandgap starts at phonon

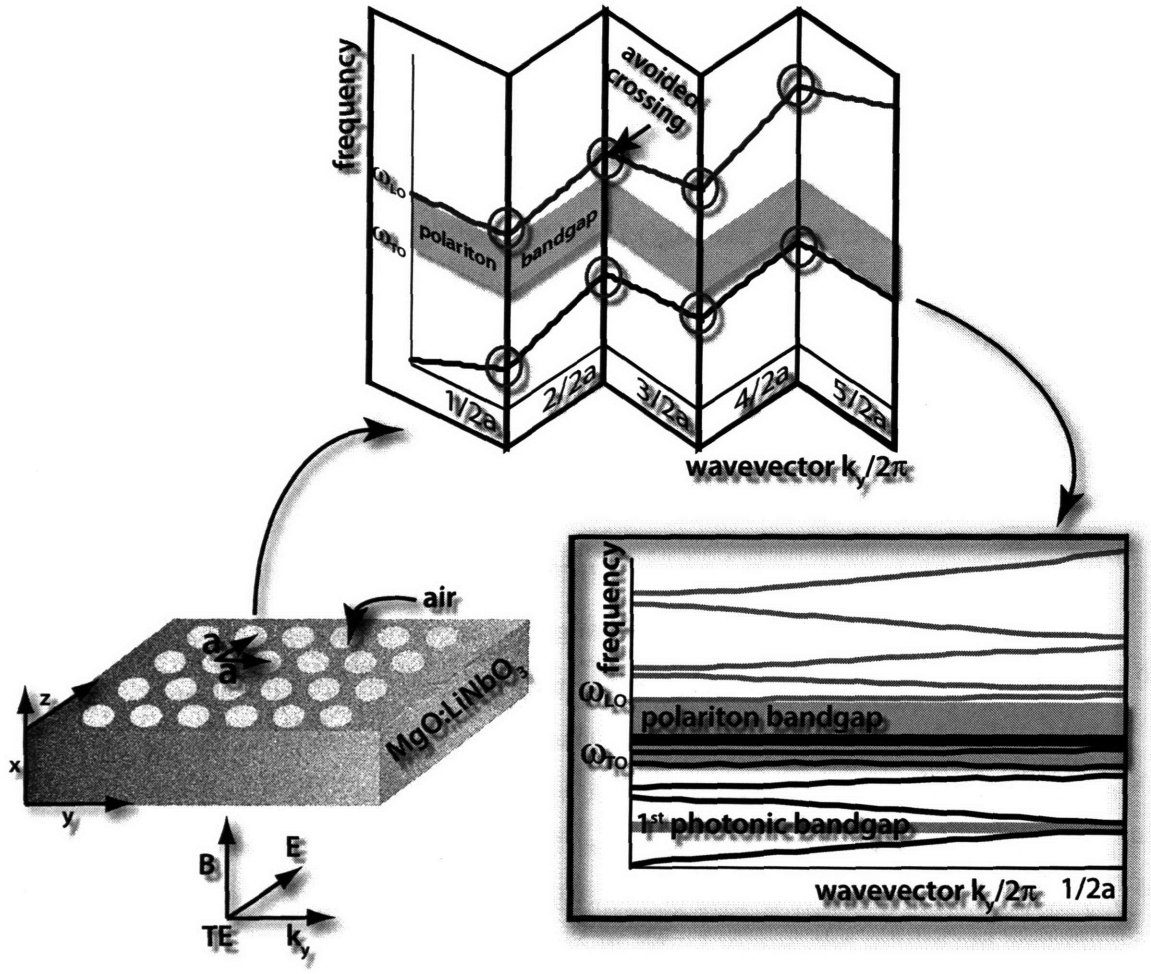

Figure 7-22: Illustration of the effect of introducing periodicity into a crystal. This can be accomplished, as is the case in this thesis, by drilling a periodic array of holes in a dielectric material. Bandgaps result at the fold points due to avoided crossing in the dispersion (red). Evident in the figure is the dense manifold of states that arises from the presence of a polariton bandgap (gray) and photonic bandgap, the combination resulting in a polaritonic bandgap.

resonance frequency and the ends at the longitudinal optic phonon frequency. Tuning of the polariton bandgap would require changing the chemical constituents of the crystal, which, for obvious reasons, is not viable.

Photonic bandgaps, which result from the presence of a periodic dielectric, can be tailored by choosing the periodicity and filling fraction (volumetric ratio of the two materials comprising the array) appropriately [46]. Figure 7-22 illustrates how the effect of periodicity is implemented into the dispersion relation. The introduction of periodicity in the crystal dielectric by milling air holes in a regular pattern with lattice constant a, results in folding of the bulk dispersion relation with a periodicity of $2a$. At the fold points, marked in red in Fig. 7-22, an avoided crossing is present that is the source of a photonic bandgap in frequency, the first of which is marked in blue. The photonic bandgap is proportional to the filling fraction, which is determined by the diameter of the air holes.

Consider the simple one-dimensional photonic bandgap material composed of a linear dielectric material and air shown in Fig. 7-23. A simple rule of thumb for discerning the bandgap frequency for air holes in a dielectric is to use the frequency associated with the wavelength in the material equal to twice the periodicity, i.e., $\omega_{BG} \approx c_0/2a$. By considering the electric field modes directly above and below the bandgap frequency, we can show the physical origin of the bandgap. Both of these modes have a wavelength of $2a$. There are two ways to position a standing wave of wavelength $2a$ in the periodic array in the figure. The higher frequency mode (black) has most of its electric field in the air portion of the array; hence, it will experience a lower index of refraction in proportion to the volume fraction averaged index of refraction. The other possible configuration of the standing wave is the lower frequency mode, which has electric field amplitude predominantly in the dielectric, and has a larger index of refraction for the same reason as before. Recognizing that interference prevents standing waves other than these two configurations, it is then clear why there is a bandgap. Further, by considering a larger filling fraction, as shown in part (b) of the figure, and reconstructing the previous argument, the relationship between filling fraction and bandgap is evident if one thinks of the small amount of dielectric as a perturbation

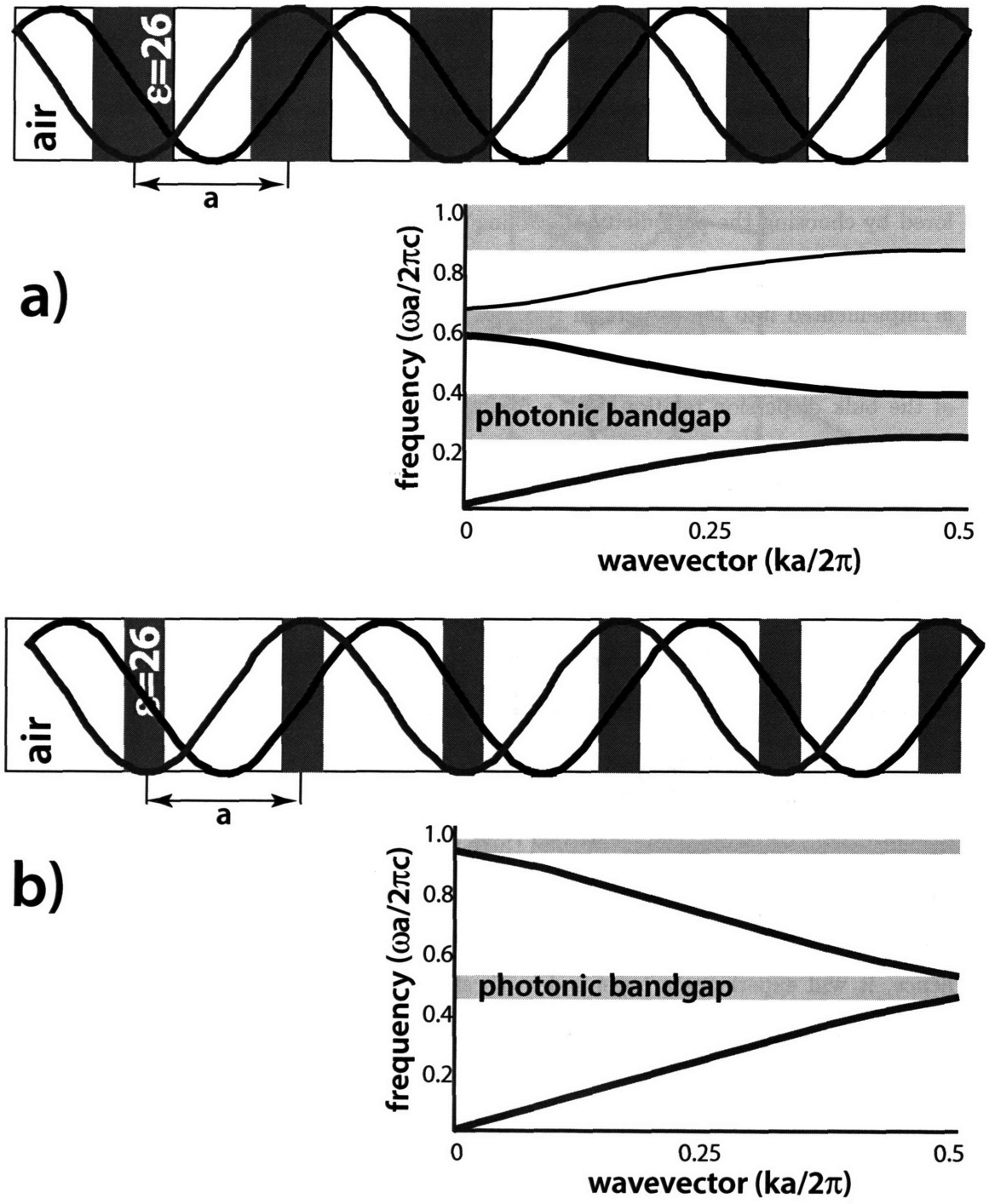

Figure 7-23: The origin of a photonic bandgap is illustrated by considering the electric field mode above (black) and below (red) the gap. Also shown is the a) larger bandgap that results when the air filling fraction is reduced, and b) the smaller bandgap from a larger air filling fraction.

to the cavity. That is, the volumetric averaged index of refraction for the small amount of dielectric in part (b) is very near that in air, whereas in part (a) the average index would be higher, resulting in a larger difference between upper and lower band frequencies.

Notice that there is a difference between the dispersion in Fig. 7-23 and 7-22. The dense manifold of states present in the later is not present in the former. The manifold arises because as the dispersion relation is folded, the slope of the lower branch dispersion curve approaches zero as the frequency asymptotically approaches ω_{TO}, causing an infinite number of avoided crossings at the fold points. This has several interesting consequences that are described elsewhere [40, 41]: mode selective behavior and a high degree of energy confinement results when polariton and photonic bandgaps overlap.

Photonic bandgap slabs are technically different than photonic crystals in that photonic crystals are infinite in the dimension orthogonal to the periodicity, whereas photonic bandgap slabs are of finite thickness and more accurately describe the structures presented here. We point out that in photonic bandgap slabs, the bandgap near the zone center (k=0) is due to symmetry breaking in the slab waveguide modes presented in chapter 5 and results in transmission out of the slab and the continuum radiation modes of the crystal. On the other hand, at the zone edge (k=$2\pi/2a$), the bandgap is the same as in a photonic crystal--destructive wave interference inside the photonic bandgap material. Radiation incident upon a photonic bandgap slab with a wavevector at the zone center should result in no transmission into the photonic bandgap slab and no reflections in the plane of slab, whereas wavevectors at the zone edge should reflect in the plane of the slab. Finally, optimal bandgaps in a photonic bandgap slab are achieved by choosing the slab thickness to be on the order of half the wavelength in the dielectric [47].

7.5.2 Preliminary Results

Though we have succeeded in overcoming the obstacles involved in the fabrication of photonic bandgap materials, limitations related to real-space imaging prevent demonstration of many of the devices presented in chapter 6. Specifically, since real-space imaging using the Talbot

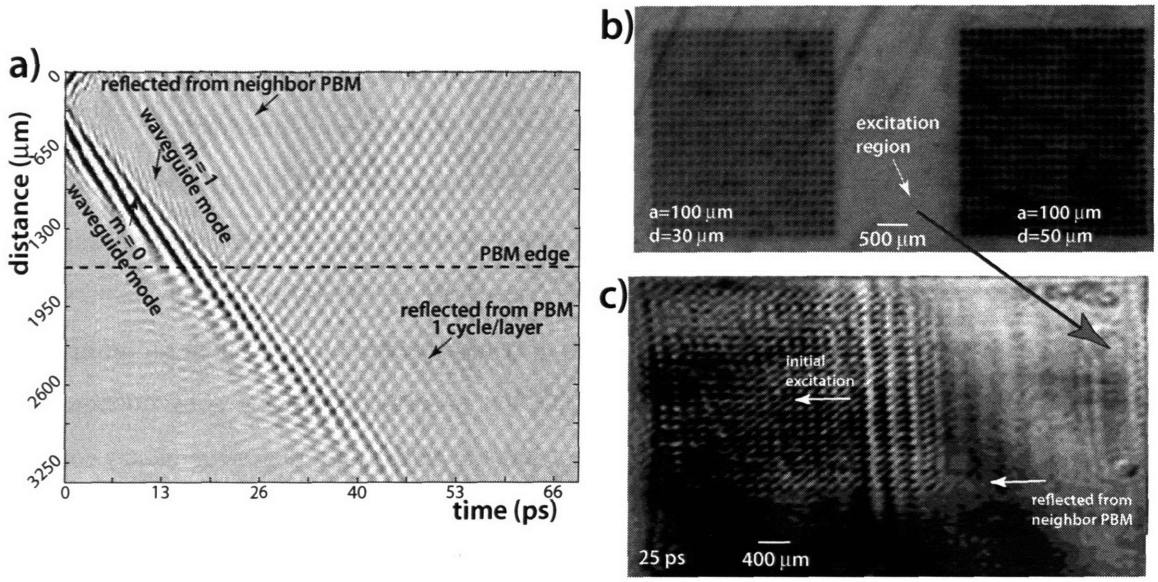

Figure 7-24: Square lattice photonic bandgap material. A broadband terahertz line excitation is generated in the region indicated in b). An image of the THz fields 25 ps after excitation is shown in c). The initial left-going waveform is shown propagating through the left most structure in b). Also shown is the reflected radiation from the right-going THz waveform, which corresponds to frequency components in the bandgap of the right most structure. a) Space-time plot constructed by integrating along the vertical axis in c) for each frame recorded at different probe-delays. Reflections from both photonic bandgap material structures are evident as are the two slab waveguide modes of the crystal slab (indicated in figure). These waveguide modes are due to confinement in the dimension of the crystal thickness. The periodicity, a, and hole diameter, d, are indicated in b).

effect, which is preferred in most cases due to the high throughput, involves out-of-focus imaging, seeing the phonon-polaritons in the photonic bandgap materials fabricated has been challenging. Schlieren imaging, which relies on blocking of diffracted orders, is an obvious alternative, but in its present implementation with real-space imaging, signal levels after blocking the zero order light are too low to be effective. We have, however, managed to obtain encouraging preliminary results, some of which are presented below and elsewhere [85, 101, 100, 102].

For a two-dimensional array of holes with periodicity a, like that in the structure shown in Fig. 7-24(b), we expect the bandgap to be centered at wavelengths in the vicinity of $2a$. Radiation with frequencies in this bandgap incident upon the photonic bandgap material

will undergo reflection, with little to no propagation within the photonic bandgap material. The lower end of the bandgap corresponds to the mode predominantly in the crystal since the crystal has a higher index of refraction, and the upper end of the bandgap corresponds to the mode predominantly in the "air" holes. Since polariton imaging relies on the ferroelectric host material for the signal, it is not possible to image the electric fields in the "air" holes; however, the full bandgap will be evident in the linewidth of reflection measurements. The slab dispersive properties will differ from those in bulk since some fraction of the in-plane electromagnetic radiation is in air, giving rise to a slightly lower effective index of refraction. The presence of a photonic bandgap material in a dielectric slab introduces an additional deviation from bulk dispersion because the "air" holes further reduce the effective index of refraction.

Figure 7-24 illustrates the visualization of terahertz waveform propagation in a square lattice photonic bandgap material. Broadband, nearly single cycle polaritons were generated in between two photonic bandgap structures (Fig. 7-24(b) and (c)) by a line of light, cylindrically focused to a width of approximately 130 μm, whose length exceeded the extent of the photonic bandgap materials in the vertical dimension of Fig. 7-24(b). Their spatiotemporal evolution was recorded through images like that shown in Fig. 7-24(c). Since the polariton responses within the photonic bandgap materials showed no systematic variation in the vertical dimension, a space-time plot (Fig. 7-24(a)) was constructed by compression of the images in this dimension. The compressed images display only one spatial dimension (horizontal in Fig. 7-24(b), vertical in Fig. 7-24(a)) vs. probe pulse delay time. The reflected light in the bandgap from both photonic bandgap materials is clearly visible. This reflected wave is exactly as we expect for a wavevector at the zone boundary.

It is also apparent that the reflected light has a much narrower linewidth than the incident. The incident broadband waveform has a center frequency of approximately 290 GHz with 400 GHz bandwidth FWHM. The reflected waveform has a frequency of 250 GHz with less than 10 GHz of bandwidth FWHM and a wavelength of approximately 200 microns, which corresponds to $2a$. Also shown (Fig. 7-24(c)) is a single frame, 25 ps after polariton excitation,

which illustrates propagation through the photonic bandgap material. Visualization inside the photonic bandgap material may not be possible for larger filling fractions, as real-space imaging is only possible in the ferroelectric portion of the photonic bandgap material.

We have also generated phonon-polaritons directly in the photonic bandgap material by focusing the optical excitation beam, to the same spot size as before, directly in the photonic bandgap material. In doing so, we expect to excite the natural modes of the photonic bandgap material and recover the impulsive response of the modes. Phonon-polariton movies constructed from real-space imaging in the photonic bandgap material show a standing wave formed after the broadband wavepacket excited in the structure exits the excitation region. A frame from a movie showing the standing wave in the structure is shown in Fig. 7-25. A space-time plot was constructed from many frames to illustrate the spatiotemporal evolution of polaritons in the photonic bandgap material and is shown in Fig. 7-25(b). It is also interesting to note that three of the slab waveguide modes in the vicinity of the broadband wavepacket are visible in the space-time plot as well. Results and calculations from chapter 5 indicate that only two modes should be present with this excitation. Perhaps the additional mode is a result of the influence of the periodicity on the slab waveguide modes, which is plausible since we are already aware that wavevectors near the zone center couple to the continuum slab radiation modes.

A spatial cross-section was taken from the space-time plot, which shows the temporal evolution at a point inside the photonic bandgap material. This is shown in Fig. 7-25(c). Inspection of the Fourier transform of this cross-section shows the broadband wavepacket with a hole that is presumably due to the bandgap in the photonic bandgap material. The spectral width of the hole is about what we expect for the filling fraction of the photonic bandgap material. To the left of this hole is a narrowband peak (<10 nm bandwidth) that corresponds to the standing wave excited in the photonic bandgap material. The standing wave is one of the two possible modes of the photonic bandgap material, as was discussed at the beginning of this section. That it is lower in frequency than the observed bandgap makes sense since we excited directly in the structure and thereby were unable to excite

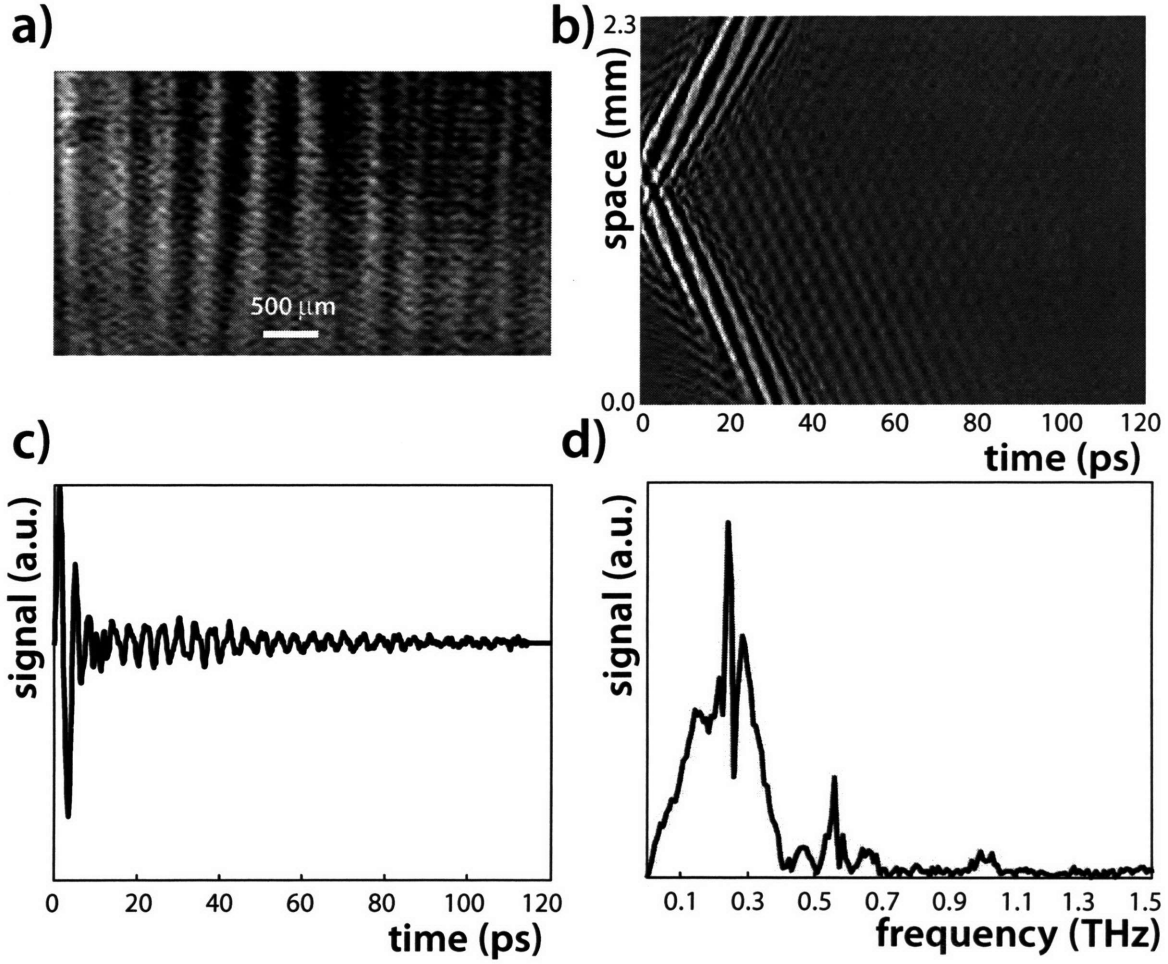

Figure 7-25: Standing wave resulting from direct ISRS excitation in the photonic bandgap material shown in Fig. 7-24(b). Shown are a) a single frame from a phonon-polariton movie taken inside the structure, b) a space-time plot constructed from many frames like that in part (a), c) a spatial cross-section of the space-time plot, which results in the temporal evolution of phonon-polaritons at a single point in the photonic bandgap material, and d) the Fourier transform of this cross-section showing the presence of the bandgap (hole at center of spectrum) and the lower frequency mode, discussed in Fig. 7-23, of the photonic bandgap material that was excited (to left of hole).

the higher frequency mode that corresponds to the majority of the electric field amplitude residing in the "air" holes. The three slab waveguide modes evident in the space-time plot are also evident in the Fourier transform and are at slightly higher frequencies than were observed in unpatterned 34 μm films.

7.5.3 Conclusions

We have demonstrated the femtosecond laser fabrication and testing of polaritonic bandgap structures in ferroelectric crystals. Photonic bandgap materials in this frequency range may find a wide range of applications in integrated terahertz structures. Because of the capability for direct visualization of the electric fields that are propagated through and reflected from polaritonic bandgap structures, these techniques –ferroelectric photonic bandgap materials and polariton imaging – constitute a novel testbed for design and implementation of photonic bandgap materials at any wavelength due to the scalable properties of Maxwell's equations. Further, the propagation time of radiation through the structures, which is analogous to the computation time in a simulation or calculation, makes this procedure highly competitive with existing computer techniques for photonic bandgap material design. We note that improvements in real-space image quality are possible with higher spatial resolution and with the use of phase-to-amplitude conversion methods that preserve optimal focusing of the polaritons and the fabricated structures.

Chapter 8

Advanced Polaritonic Materials

This work was done in collaboration with Eric Statz of the Massachusetts Institute of Technology, and Ming-Chuan Yang and Kevin Webb of Purdue University.

In order to achieve terahertz computing elements comparable to their electronic analogs, like AND and NOT gates, etc., it is necessary first to realize simple bistable devices. Bistability, however, normally requires nonlinearities [73]. $LiNbO_3$, $LiTaO_3$ and other poled ferroelectric crystals are intrinsically nonlinear due to the presence of a bistable potential energy surface; however, the requisite field strength for domain switching exceeds that presently available in terahertz fields [104, 94, 95]. This limitation can likely be overcome, but it is not desirable to rely on extremely large field strengths for device operation. Instead, other alternative sources of nonlinearity should be pursued. Likely candidates to achieve these field strengths are isolated ferroelectric nanocrystals, semiconductor quantum wells, and laser-activated semiconductor reflective switches.

The field strengths required for switching become much smaller as the ferroelectric crystal is reduced in size. It is now possible to produce ferroelectric crystals with dimensions of tens of nanometers [63]. It may be possible to isolate nanocrystals in a polaritonic device to provide the necessary bistability. For example, nonlinear switching between two coupled waveguides may be achieved by introducing a ferroelectric nanocrystal in between them.

Alternatively, the use of semiconductor quantum wells as the source of nonlinearity requires large field strengths (~10 KV/cm), but it has the advantage that the nonlinearity is tunable. Quantum wells are manufactured through photolithography and can be made with arbitrary well shape. For example, a square well closely approximates a two-level system, which, under high field irradiation, will undergo Rabi oscillations [18]. Quantum wells could be used in a similar fashion as the nanocrystals to enable bistable polaritonic devices.

A simple approach to switching is the exploitation of a semiconductor bandgap in photonic crystals. The "air" holes in the photonic bandgap materials presented in chapter 7 could be replaced with semiconductor rods. By activating the rods with femtosecond laser pulses with frequencies in the electronic bandgap, electrons are promoted from the valence band to the conduction band, making the rods metallic in character. The lifetime of this metallic state is on the order of picoseconds [36]. In the 'on' state, the photonic bandgap is dictated by the dielectric contrast between the ferroelectric host and the semiconductor and is relatively broad compared with the metallic photonic crystal present in the 'off' state. By employing pulse shaping of the optical switching pulse, a pulse sequence can be generated to selectively turn the photonic bandgap switch on or off.

Also of interest is negative refraction, which may enable novel polaritonic device functionalities. Some possible functionalities are explored in this chapter. Negative refraction is exhibited when a material has a negative permittivity and permeability that overlap in frequency [90, 96]. Light incident upon such a material will refract to the opposite side of the normal as given by Snell's law for a positive refractive material. Additionally, the phase velocity will propagate in the opposite direction as the group velocity, giving the appearance of backwards wave propagation. Other effects like reverse Cherenkov cones and perfect lenses, in which imaging below the diffraction limit is possible, have been proposed [90, 105, 65, 106, 97]. Presently, negative refraction has only been demonstrated in metamaterials with X-band microwaves [75], but there is considerable interest in extending negative refraction to the THz regime [66, 96].

There are no intrinsically negative refractive materials known at present, but recently it

has been suggested that photonic bandgap materials may be able to realize negative refraction [42, 71, 57, 56]. Using the techniques of chapter 6, negative refractive photonic crystals could be fabricated with femtosecond laser machining, and electromagnetic wave propagation within the structures could be observed with real-space imaging. If successful, it would be the most dramatic demonstration of negative refraction to date. Further, polaritonics provides a natural proving ground for devices based on negative refraction, such as perfect lenses and negative refractive waveguides.

The remainder of this chapter addresses anharmonic lattice dynamics and nonlinear terahertz in $LiNbO_3$ and $LiTaO_3$ necessary for bistable devices and the possibility of hybrid ferroelectric/ferromagnetic systems capable of negative refractive phenomena. The results presented here are all theoretical with support from numerical experiments performed with the FDTD method of chapter 3. Though device fabrication is not the topic of the sections to follow, it is the motivation.

8.1 Lattice Anharmonicity and Nonlinear Terahertz

Time-resolved light scattering experiments on perovskites, including ferroelectric crystals like $LiNbO_3$ and $LiTaO_3$, are motivated by the need for sufficient data to characterize the ionic potential energy surfaces that dictate lattice dynamics. These data would be paramount in understanding structural phase transitions and the role of long range order in lattice dynamics [25, 24]. So far, only studies in the linear regime have been performed, but intense sources of terahertz radiation, like those discussed in this chapter, present new opportunities to probe nonlinear lattice dynamics.

In this section we contrast lattice anharmonicity manifest in the b-coefficients of Eq. (2.104) with the second-order nonlinear susceptibilities d_{il} manifest in $\bar{\bar{\alpha}}'$. The former is discerned from the potential energy surface of $LiTaO_3$ taken from ab-intio frozen phonon mode computations [43], while the latter come from measurements in the infrared.

We first explore nonlinear polariton generation through higher-order terms in the potential energy surface for the A_1 mode. Finally, we use $\bar{\bar{\alpha}}$ to explore phase matched second har-

	r(Å)	ΔU(meV)	ν_{TO}(THz)	$\alpha(s^{-2})$	$\beta(m\ Kg^{-1}\ s^{-2})$
$LiTaO_3$(A_1 mode)	0.774	235	8.09	$-7.10\ x\ 10^{26}$	$9.68\ x\ 10^{44}$
$LiNbO_3$(A_1 mode)	0.866	249	7.43	$-1.14\ x\ 10^{27}$	$1.28\ x\ 10^{45}$

Table 8.1: Quartic potentials for $LiNbO_3$ and $LiTaO_3$ [43]. The symbols r, ΔU, and ν_{TO} respectively correspond to the equilibrium displacement, which is related to the permanent dipole moment; the barrier height, which is related to the coercive field; and the transverse optical phonon frequency for small displacements about the center of either well. α and β are illustrated in Fig. 8-1.

monic terahertz generation polarized along the A_1 mode from fundamental polarized along an E mode by way of the experimentally measured second-order nonlinear susceptibilities.

8.1.1 Lattice Anharmonicity

In this section we describe anharmonicity as expressed through a Taylor series expansion in b_{311}, which is related to the potential energy surface for the ions.

Ferroelectric crystals below the Curie temperature have a permanent dipole moment due to a distortion of the unit cell along the optic axis (see Fig. 8-1(a)). We consider only the harmonic restoring force for displacements along the ordinary axes, but because the potential energy is bistable along the extraordinary axis, we include anharmonicity up to fourth order [43]. A general form of the potential energy along the extraordinary axis of a poled ferroelectric crystal is:

$$U(Q) = \frac{\alpha}{2}Q^2 + \frac{\beta}{4}Q^4. \tag{8.1}$$

Note that the meanings of symbols α and β used in this section are distinct from those used in previous sections and chapters. The permanent dipole moment is equal to $\sqrt{-\alpha/\beta}$, which can be discerned from either capacitance measurements or from a combination of far infrared (FIR) spectra and neutron or x-ray scattering data. The curvature in each well, α, is taken from Raman scattering data and related to the transverse optic phonon frequency through $\omega_{\mathrm{TO}}^2 = -2\alpha$. The barrier height is equal to $-\alpha^2/4\beta N$. The parameters used here for the quartic potential are contained in Table 8.1 and illustrated in Fig. 8-1.

The phonon mode information enters into Eq. (2.104), from chapter 2, through the b-

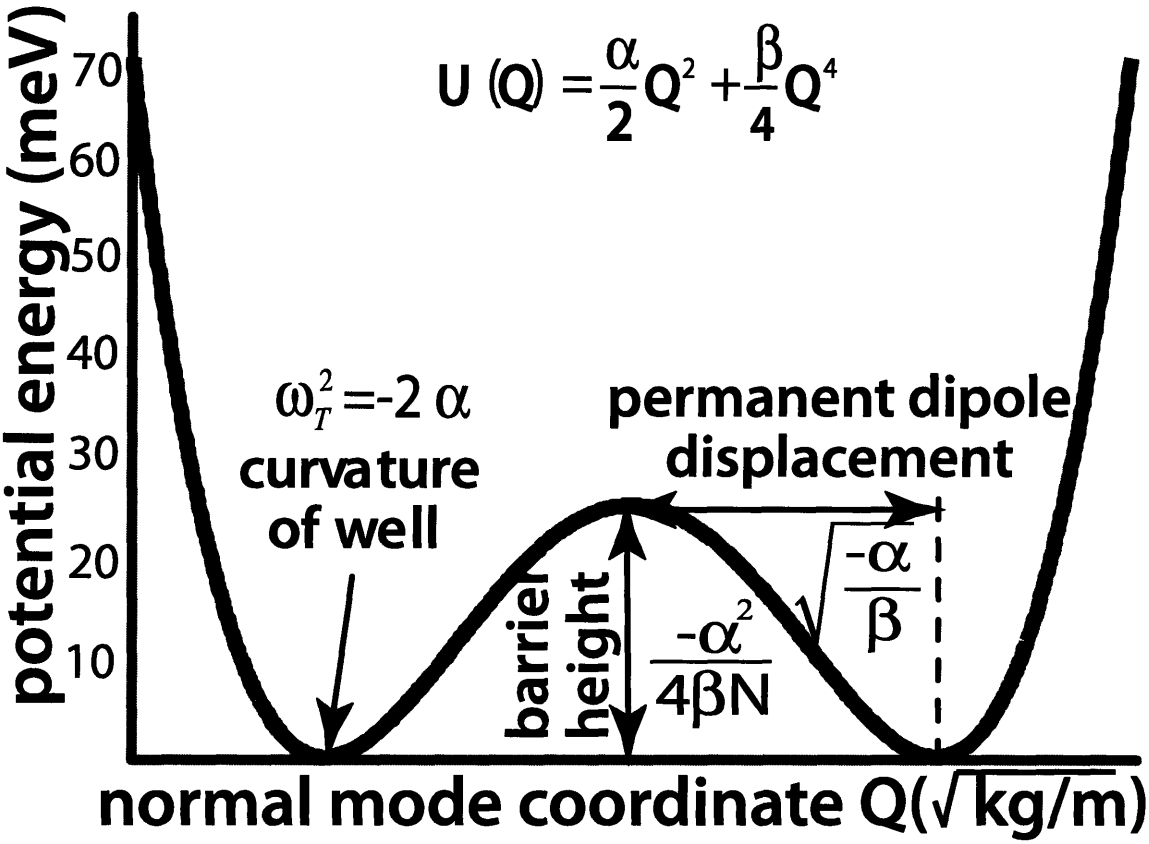

Figure 8-1: Fourth order model of the potential energy surface along the normal mode coordinate corresponding to the extraordinary (optic) axis of either $LiNbO_3$ or $LiTaO_3$. The parameters α and β are determined using the transverse optic phonon frequency and either the barrier height, which corresponds to the measured coercive field, or the permanent dipole displacement, which corresponds to either static capacitance or X-ray diffraction measurements. Alternatively, all these parameters may be estimated with frozen phonon-mode calculations [43].

coefficients. The anharmonicity in Eq. (8.1) is realized by performing a Taylor series expansion on b_{311} in Q about the equilibrium displacement, as follows,

$$b_{311}(Q_3) = b_{311}(Q_{3,\text{eq.}}) + \Big(\frac{\partial b_{311}}{\partial Q_3}\Big)Q_3 + \frac{1}{2}\Big(\frac{\partial^2 b_{311}}{\partial Q_3^2}\Big)Q_3 \cdot Q_3 + ... \tag{8.2}$$

The expansion coefficients in Eq. (8.2) for an anharmonic potential of the form in Eq. (8.1) centered about either minimum are,

$$\begin{aligned}
b_{311}(Q_{3,\text{eq.}}) &= -\omega_{TO}^2, && (8.3)\\
\Big(\frac{\partial b_{311}}{\partial Q}\Big) &= \frac{3\omega_{TO}^2}{2\delta \mathrm{w}\sqrt{MN}}, && (8.4)\\
&= \frac{3\omega_{TO}^3}{4\sqrt{2\delta \mathrm{U} MN}}, && (8.5)\\
\Big(\frac{\partial^2 b_{311}}{\partial Q^2}\Big) &= \frac{\omega_{TO}^2}{\delta \mathrm{w}^2 MN}, && (8.6)\\
&= \frac{\omega_{TO}^4}{16N\delta \mathrm{U}^2}, && (8.7)
\end{aligned}$$

where the coefficients are given in terms of the permanent dipole displacement δw (Eqs. (8.4) and (8.6)) and the barrier height δU (Eqs. (8.5) and (8.7)) in Fig. 8-1. All higher order terms are identically zero for the quartic potential.

Broadband ISRS generation simulations were performed on a 1 mm thick $LiTaO_3$ crystal using the values in Table 8.1. The excitation pulses were focused to a spot size of 50 μm. Figure 8-2(a) shows the Cherenkov cones that resulted from excitation pulses with energies of 100 μJ, 1 mJ, and 10 mJ. Few to no nonlinear signals were detected for the lowest energy excitation pulses. However, distortions in the Cherenkov cone related to lattice anharmonicity in the crystal are present for the 1 mJ and 10 mJ excitation pulses. Space-time plots for these excitations are shown in Fig. 8-2(b). Upon inspection, we see that the distortions in the Cherenkov cone related to lattice anharmonicity should be detectable using real-space imaging.

These results are preliminary and will require further analysis before any definitive conclusions can be drawn on how close nonlinear terahertz experiments are to being achieved

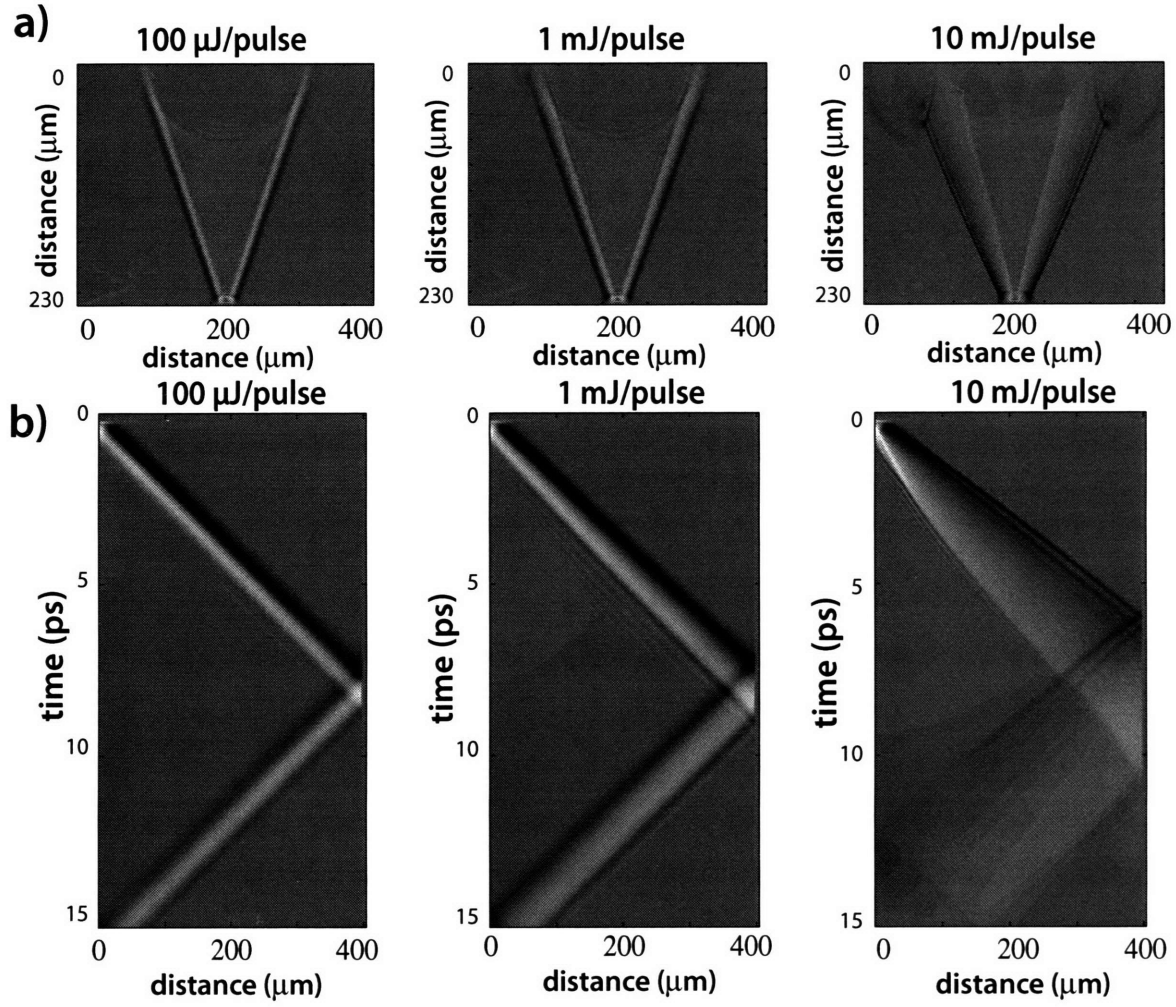

Figure 8-2: Simulations of lattice anharmonicity in $LiTaO_3$ using the values from Table 8.1. a) The Cherenkov cones resulting from broadband excitations with increasing pulse energy. b) Space-time plots from probe data for the excitation pulses in part (a). Distortions in the Cherenkov cone are evident at large pulse energies. These distortions should be detectable by real-space imaging since they show up in the simulated probe data.

experimentally. The data do show, however, that lattice anharmonicity can be detected using the techniques discussed in this thesis.

8.1.2 Second Harmonic Susceptibilities

When sufficient information about the potential energy surface for the ions is unavailable, we can make predictions about $\chi^{(2)}$ terahertz wave generation through $\overline{\overline{\alpha}}'$. This approach is particularly useful when the fundamental is polarized orthogonal to the induced second-order polarization—type I phase matching. Here we consider terahertz second harmonic generation through type I phase matching.

Figure 8-3 shows plots for phase-matching in *oe*, *eo*, *oo*, and *ee* second harmonic generation, where *o* denotes polarization along the ordinary axis, and *e* the extraordinary axis of the crystal. The notation refers to the polarization of the fundamental and second harmonic. For example, in *eo* second harmonic generation, two photons at the fundamental frequency and polarized along the ordinary axis of the crystal combine to generate a single photon at the second harmonic of the fundamental and polarized along the extraordinary (optic) axis.

In the figure, regions in which the two curves cross correspond to phase matched excitations. For example, *oe* second harmonic generation in $LiTaO_3$ is phase matched to the fundamental at 1.25, 2.95, 4.33, and 6.60 THz producing second harmonic radiation at 2.5, 5.90, 8.66, and 13.2 THz respectively. In the event that the fundamental propagates faster than the second-harmonic, Cherenkov radiation, like that considered previously for an optical excitation pulse, is possible. For example, consider a single cycle terahertz wavepacket polarized along the ordinary axis of $LiTaO_3$. Through the right hand side of Eq. (2.104), the square of this wavepacket exerts a force on the ions. The Cherenkov angle, the complement of the forward propagation angle, is the phase-matched direction of propagation. The forward propagation angle for second-harmonic generation is based on a variation of Eq. (4.1) expressed in terms of the fundamental and second-harmonic relative permittivities,

$$\theta_{ij} = \arcsin \sqrt{\frac{\varepsilon_i(\omega)}{\varepsilon_j(2\omega)}}, \tag{8.8}$$

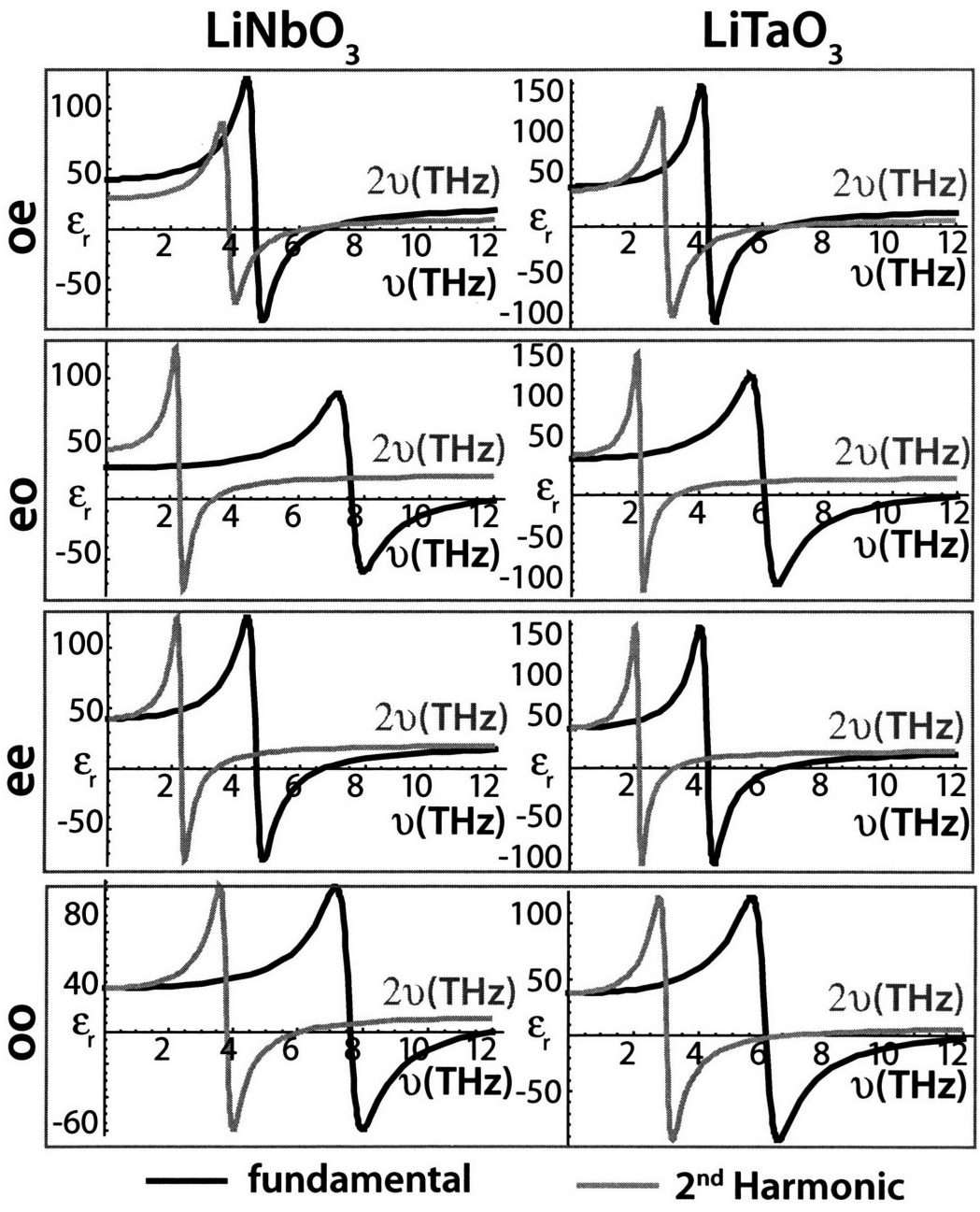

Figure 8-3: Considerations for Type-I phase matched second-harmonic generation in $LiNbO_3$ and $LiTaO_3$. Cherenkov cone radiation is possible in regions where the second harmonic phase velocity exceeds the fundamental phase velocity, though spot size limits the generation efficiency. Where the second-harmonic and fundamental have the same values for the permittivity, forward scattered phase matched second-harmonic occurs.

where i, j corresponds to the polarization of the fundamental and second-harmonic, respectively.

For *eo* generation in $LiTaO_3$, the frequency range $[0, 1.25]$ THz has no Cherenkov cone because the second-harmonic propagates faster than the fundamental. However, Cherenkov radiation exists in the range $[1.25, 2.95]$ THz with propagation angles of 90^o at the end-points and reaching almost 45^o in between, as confirmed by simulation. The second-harmonic propagation velocity again exceeds the fundamental in the range $(2.95, 4.33)$. Higher frequencies are either in the bandgap of the fundamental or the second harmonic, so no propagation is allowed. Thus the only useful range of frequencies is $[1.25, 2.95]$ THz. The extreme end near 2.95 THz is very near resonance for the A_1 mode and experiences substantial damping. However, the opposite extreme seems very promising for experimental investigation, and has been previously investigated in the FIR using a CW terahertz source [60].

Two-dimensional FDTD simulations of type-1 phase matching terahertz second harmonic confirmed that Cherenkov radiation is possible in the regions identified in Fig. 8-3. However, the field strengths in the Cherenkov cone were found to be weaker than the forward scattered second harmonic, even at frequencies where there is no forward scattered phase-matching, as illustrated in Fig. 8-4.

In the figure, narrowband phonon-polaritons of frequency 2 THz and collimated to their diffraction limited spot size, generate both forward scattered second harmonic and a second harmonic Cherenkov cone. The Cherenkov cone, though visible, is less intense than was expected. Second harmonic Cherenkov cone generation is limited by the fundamental excitation pulse spot size, which cannot be made smaller due to the diffraction limit.

8.2 Negative Refractive Materials

In 1968, Veselago suggested that a material with a negative index of refraction would enjoy certain peculiar properties. Foremost among these was negative refraction, where a ray incident on the interface of such a material would refract on the same side of the normal rather than away from it [90]. The subject lay dormant until 1999, when Pendry proposed

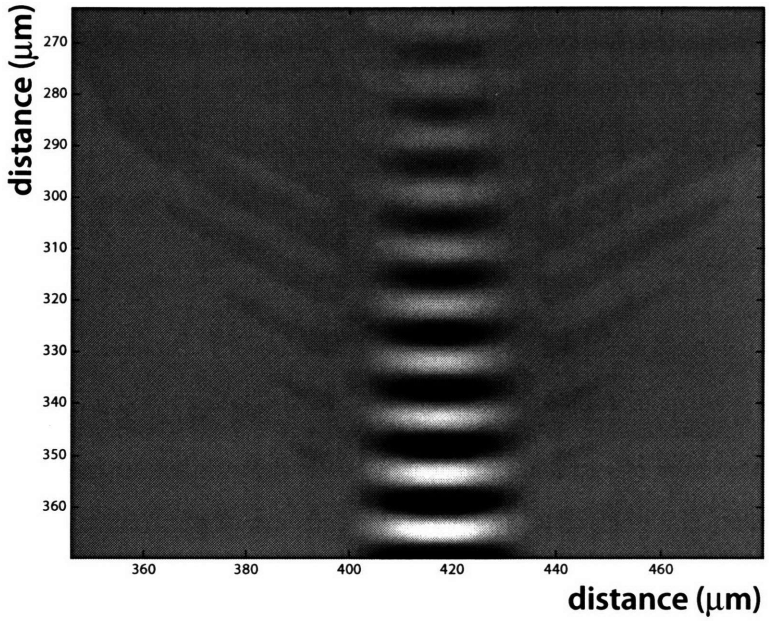

Figure 8-4: Type 1 phase matching in $LiTaO_3$. The efficiency of the second harmonic Cherenkov cone is limited by the spatial bandwidth of the fundamental terahertz excitation pulse.

designs for magnetic metamaterials [66] that were subsequently implemented by Shelby *et al.*, along with a dispersed electric metamaterial, to demonstrate negative refraction in 2001 [75]. Despite the fact that no naturally occurring negative index material is available, there has been a surge in interest, particularly with regard to the prospect of creating a perfect lens [65].

8.2.1 The Physical Origins of the Negative Index of Refraction

In this section, we explore the physical origins of the negative index of refraction. The formalism developed here differs from previous macroscopic descriptions of negative refraction in that it is developed from a microscopic model consisting of an array of electric dipoles and magnetic dipoles undergoing precession due to an external static magnetic field. By considering the extension of the microscopic model to a macroscopic electromagnetic description, a physical basis for why the propagation phase velocity of light, v_p, should appear

negative when the permittivity and permeability are simultaneously negative is established. This extends the macroscopic arguments originally formulated by Veselago [90], and, for example, applied under the context of a Drude model [114], to include a physical, microscopic basis. Finally, we use the microscopic model to suggest some possibilities for the use of ferromagnetic and ferroelectric materials to enhance the capabilities of negative index metamaterials.

To illustrate how negative refraction might arise, we apply Fermat's principle of least time [10] to the case of negative refractive index materials and interpret it in terms of least action. Consider the path of least action for a stream of photons in vacuum ($n_1 = 1$) incident on a homogeneous, isotropic material with an index of refraction n_2. The most probable path is determined by the path of stationary phase, which corresponds to an extremum in the spatial derivative of the total travel time through all possible paths. This is well established for the case of positive refraction. From the diagram in Figure 8-5(a), the optical path length in vacuum from source **A** to the interface point **O** is $c_1 t_1 = \mathbf{AO} = \sqrt{a^2 + y^2}$, and in the semi-infinite material from **O** to **B** it is $c_2 t_2 = \mathbf{OB} = \sqrt{b^2 + (l-y)^2}$. To find the extremum in the time of travel from **A** to **B**, we form $d(t_1 + t_2)/dy = 0$, with a and b fixed at arbitrary values, which upon substituting for the optical path lengths gives $n_1 y/c_0\sqrt{a^2 + y^2} = n_2(l-y)/c_0\sqrt{b^2 + (l-y)^2}$, with $l - y \geq 0$. Recognizing the trigonometric relations $\sin(\theta_1) = y/\sqrt{a^2 + y^2}$ and $\sin(\theta_2) = (l-y)/\sqrt{b^2 + (l-y)^2}$, this can be rewritten in the familiar form of Snell's law: $n_1 \sin(\theta_1) = n_2 \sin(\theta_2)$. If we postulate that the photons refract to the other side of the normal, as depicted in Figure 8-5(b), then $l - y \leq 0$, which implies that the angle of refraction becomes $-\theta_2$. The extremum for this optical path gives $n_1 y/c_0\sqrt{a^2 + y^2} = -n_2|l-y|/c_0\sqrt{b^2 + (l-y)^2}$, which can only be satisfied if $n_2 < 0$. Since $n_1 \sin(\theta_1) > 0$ and $\sin(-\theta_2) = -\sin(\theta_2)$, Snell's law is found to be valid for both positive and negative refraction, provided we allow for the possibility of a negative index of refraction. The curvature becomes $d^2(t_1+t_2)/dy^2 = n_1 a^2/[c_0(a^2+y^2)^{3/2}] + n_2 b^2/[c_0(b^2+(l-y)^2)^{3/2}]$. For $n_2 > 0$, the curvature is positive, indicating that Fermat's result indeed gives the minimum time (and distance). Interestingly, for $n_2 < 0$, the curvature is negative, indicating a maximum.

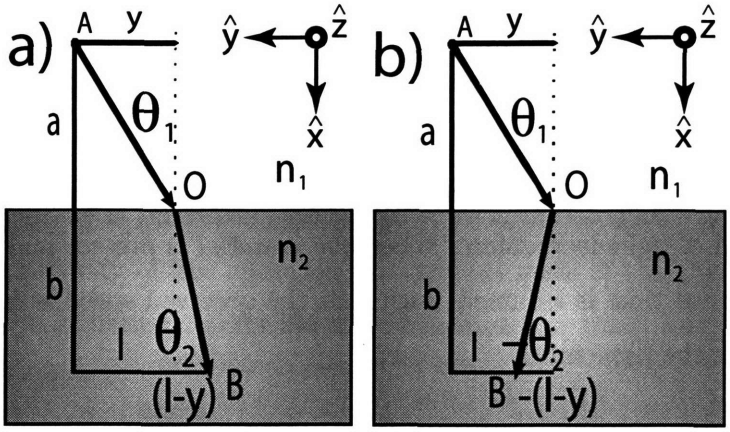

Figure 8-5: Illustration for a) positive and b) negative refraction for a light ray incident on a material with $|n_2| > |n_1|$. In a) $0 < n_1 < n_2$ and in b) $0 < n_1 < |n_2|$ and $n_2 < 0$.

In terms of least time this result does not make much sense, since the path for negative refraction corresponds a maximum. The principle of least action, based on Feynman's path integral approach to quantum mechanics, supplanted the principle of least time [30]. The negative curvature from before is then properly interpreted as the path of stationary phase, which in the framework of the least action principle determines the proper path for refraction, thereby removing any ambiguity as to whether negative refraction is physical.

The disparity between the frequency dependent speed of light in a material and the constant speed of photons in a vacuum is resolved by recognizing that photons impinging on a medium can drive resonances in that medium, which may radiate and contribute to the total scattered field. When there is a difference in phase between the source and radiated field, the wavefronts at the detector will appear to be advanced or retarded with respect to the source, and it is on this basis that the concept of negative velocity is explained.

To relate our microscopic model to the index of refraction, which is a macroscopic phenomenon, we employ an approach developed by Feynman, thereby extending the physical origins of the index of refraction to include negative index materials [30]. Our system con-

sists of a monochromatic plane wave source of radial frequency ω travelling at the speed of light in vacuum, c_0, in the $\hat{x}$-direction, incident on a slab of material of thickness d, and a detector on the other side of the slab, sufficiently far away. If the slab were removed, then the observed travel time to the detector, a distance x from the source, would be commensurate with the speed of light in vacuum. When the material is present and an observed delay or advance in arrival time is assumed, such that the observed speed is c_0/n, consider that the electric field at the detector is

$$E_z^d = E_0 e^{i\frac{\omega}{c_0}d(n-1)} e^{-i\omega(t-\frac{x}{c_0})}, \tag{8.9}$$

which is the source field of initial strength E_0 (neglecting amplitude scatter in the dilute limit) multiplied by a phase term. Feynman showed that for dilute media in which the phase term is small, (8.9) can be written in a more suggestive manner as [30]

$$E_z^d \simeq E_0 e^{i\omega(t-\frac{x}{c_0})} - i\frac{\omega}{c_0} E_0 d(n-1) e^{i\omega(t-\frac{x}{c_0})}. \tag{8.10}$$

Written this way, it is clear in (8.10) that the plane wave at the detector is the sum of the source term (the incident field without the material) and a material response term (the scattered field). This representation is thus consistent with the Born approximation for scattered photons.

To provide a mechanism for the apparent augmentation of the arrival time of the photons, we employ a microscopic model that replaces the slab with a thin sheet of electric and magnetic dipoles, find the fields due to each source, and then apply superposition. We assume a Lorentz electric dipole resonance and a Bloch magnetic resonance.

The field radiated in the $x-$direction by a thin sheet of microscopic electric dipoles is

$$E_z^{se} = -\frac{d}{2c_0}[i\omega\chi_e E_0 e^{-i\omega(t-\frac{x}{c_0})}], \tag{8.11}$$

with the relative electric susceptibility given by [9]

$$\chi_\varepsilon = \frac{\chi_{\varepsilon_0}\omega_0^2}{(\omega_0^2-\omega^2)^2+\Gamma^2\omega^2}((\omega_0^2-\omega^2)+i\Gamma\omega), \tag{8.12}$$

where $\chi_{\varepsilon_0} = Nq^2/m\epsilon_o\omega_0^2$ is the static susceptibility, N is the oscillator density, q the dipole charge, ϵ_o the permittivity of free space, m the reduced mass of the charges in the normal mode that results in radiation, ω_0 the electric resonance frequency, and Γ is a phenomenological damping constant.

Also within our slab is a sheet of magnetic dipoles with a static external field H_0 applied in the $\hat{x}$-direction. Equivalently, we could assume a slab of ordered spins, where the static magnetic field is provided by dipolar coupling, as in the case of a ferromagnetic material. The equation for the field radiated by a magnetic dipole sheet, E_z^{sm}, can be shown to be of the same form as (8.11) with the replacement of χ_ε with χ_μ, the relative magnetic susceptibility for a Bloch resonance, which is given by [77]

$$\chi_\mu = \frac{\frac{\chi_{\mu_0}}{2}\Omega_0 T_2}{1+(\omega-\Omega_0)^2T_2^2}((\Omega_0-\omega)T_2+i), \tag{8.13}$$

where χ_{μ_0} is the ratio of the magnetization and the static magnetic field H_0 that induced it, Ω_0 is the magnetic resonance frequency, and T_2 is the spin dephasing time.

The field due to both the radiating electric and magnetic dipoles, using (8.11) and its magnetic analog, is then

$$E_z^s = -\frac{i\omega d}{2c_0}(\chi_\varepsilon+\chi_\mu)E_0 e^{i\omega(t-\frac{x}{c_0})}. \tag{8.14}$$

Comparing the microscopic equation of (8.14) with our previous macroscopic expression in (8.10), the index of refraction can be expressed in terms of the microscopic susceptibilities as

$$n = 1+\frac{1}{2}(\chi_\varepsilon+\chi_\mu). \tag{8.15}$$

We will employ some foresight and recognize that (8.15) is the same as the index of refraction derived from the macroscopic Maxwell's equations for dense media of arbitrary thickness in

the limit of small susceptibilities. Accordingly, we assume the usual form for the index of refraction, $n = \sqrt{\varepsilon_r \mu_r}$, where the relative permittivity is $\varepsilon_r = 1 + \chi_\varepsilon$ and the relative permeability is $\mu_r = 1 + \chi_\mu$, so as to not limit our discussion to dilute materials with weak susceptibilities. What we gain by doing so is that a layer of dipoles can augment the source field for subsequent layers of dipoles.

To describe the effect of the microscopic susceptibility on wave propagation, we introduce the permittivity, $\varepsilon_r = |\varepsilon_r| \exp(i\phi_\varepsilon)$, and permeability, $\mu_r = |\mu_r| \exp(i\phi_\mu)$, in polar form into the index of refraction ($n = |n|e^{i\phi_n} = (|\varepsilon_r||\mu_r|)^{1/2} e^{i(\phi_\varepsilon + \phi_\mu)/2}$), and wave admittance ($Y = |Y|e^{i\phi_Y} = Y_0(|\varepsilon_r|/|\mu_r|)^{1/2} e^{i(\phi_\varepsilon - \phi_\mu)/2}$). $Y_0 = (\epsilon_0/\mu_0)^{1/2}$ is the free space admittance, the inverse of the wave impedance. The domain for the index of refraction and the wave impedance come from the range of the permittivity and the permeability. Accordingly, with the loss implied by the damping in (8.12) and (8.13), the permittivity and permeability are restricted to the upper-half of the complex plane, in order for a propagating wave to lose energy (under the assumed $e^{-i\omega t}$ convention). Thus, $\phi_{\varepsilon,\mu}$ is in the interval $[0, \pi]$, and the index of refraction shares the same interval, since $0 \leq (\phi_\varepsilon + \phi_\mu)/2 \leq \pi$. However, the domain of the wave impedance phase is $[-\pi/2, \pi/2]$, since $-\pi/2 \leq (\phi_\mu - \phi_\varepsilon)/2 \leq \pi/2$. Note that loss becomes more significant in the neighborhood of the resonances. However, even perturbational loss poses limitations on the potential amplification of evanescent fields in a negative index slab [105].

The effect of the index of refraction on the source field as it propagates through the slab is seen by introducing the polar form of the index of refraction into (8.9) and replacing the thickness d with the independent coordinate system in Figure 8-5. From (8.9), ignoring the time dependence, and assuming $d = x$, we get $E_z^d(x) = E_0 e^{(-\omega x|n|/c_0)\sin\phi_n} e^{i(\omega x|n|)/c_0)\cos\phi_n}$. By use of either the right hand rule or Faraday's law, we find that the magnetic field associated with propagation in the x-direction is $H_y^d(x) = -|Y|e^{i\phi_Y} E_z^d(x)$. Thus, the wave admittance introduces a relative phase shift in the electric and magnetic field, which has consequences on power flow (See Fig. 8-6).

In the case of a material with only electric dipole coupling, the value of ϕ_ε is restricted

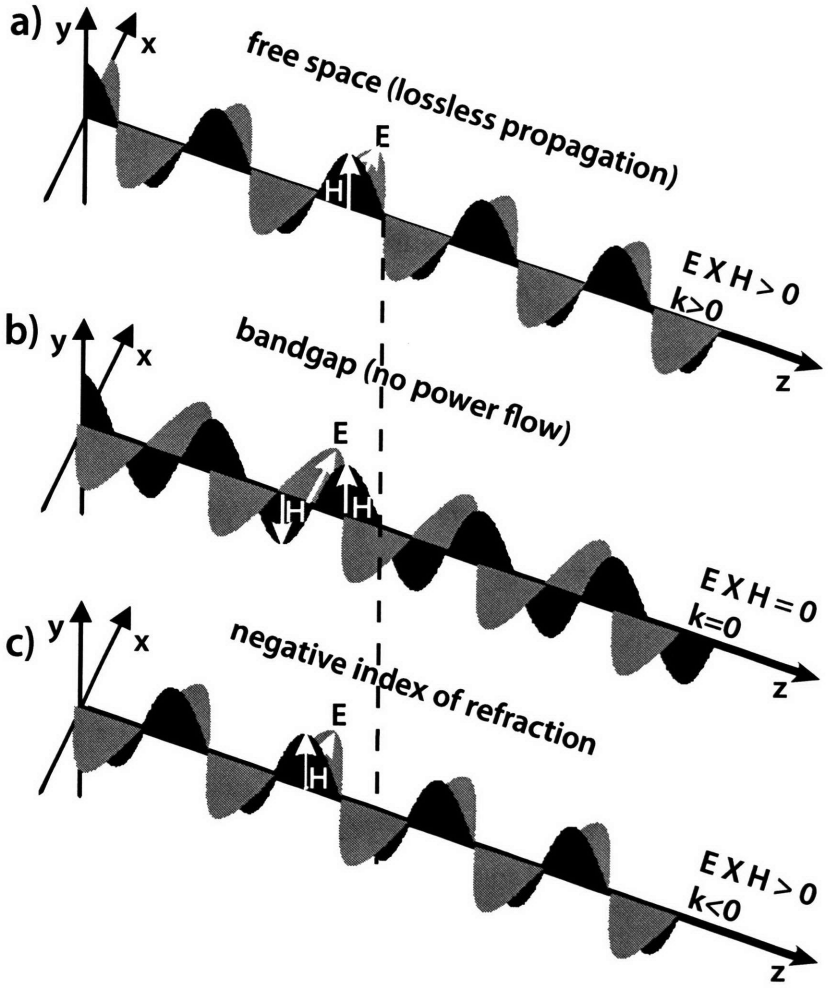

Figure 8-6: (a) In free space or in a lossless medium, bound charges are driven at a frequency well below or well above any resonance frequencies in the material. The resulting polarization is in phase with the driving field and there is no phase shift in $\vec{E}$ with respect to $\vec{H}$. In a lossy medium with an electric dipole resonance, the phase of $\vec{E}$ is shifted slightly with respect to $\vec{H}$ resulting in attenuated power flow given by the right-hand rule. The same would be true for a magnetic dipole resonance except the phase of $\vec{H}$ would be shifted instead. As the resonance frequency is approached the relative phase approaches that in (b), in which the polarization is ninety degrees out of phase with the driving field resulting in destructive interference between the polarization and driving field. Thus no power flow or propagation is allowed within the bandgap of a material. (c) If simultaneous electric and magnetic dipole resonances with overlapping resonance frequencies are present, then both the phase of $\vec{E}$ and $\vec{H}$ are shifted by nearly the same amount due to the resonances, thus nearly restoring a zero relative phase between $\vec{E}$ and $\vec{H}$. As a consequence the phase velocity becomes negative and negative refraction results. The vertical dotted line is a point of reference for the absolute phase.

to the interval $[0, \pi]$ and $\phi_\mu = 0$. This limits the range of ϕ_n and ϕ_Y to the interval $[0, \pi/2]$. However, if we allow for the simultaneous existence of magnetic and electric dipole coupling, we find that the interval for the phase of the index of refraction becomes $[0, \pi]$ and the interval for the wave admittance becomes $[-\pi/2, \pi/2]$. The most interesting result of this additional phase contribution comes from consideration of a material that without the magnetic dipole resonance would exhibit a bandgap for the frequency under consideration, assuming negligible loss, resulting in an evanescent wave. If we introduce a small magnetic phase contribution, then we find a return to a propagating wave solution. In the lossless electric dipole only case, the field does not propagate and does not carry real power because the electric and magnetic fields are $\pi/2$ radians out of phase. However, when both electric and magnetic dipole coupling is present, the phase contribution from the magnetic dipole can 'undo' the deleterious effects of the electric dipole by partially restoring the relative phase of the electric and magnetic fields such that power can flow. In the remarkable case that ϕ_ε and ϕ_μ are both equal to π (or 0), it follows that $\phi_n = \pi$ (or 0) and $\phi_Y = 0$, and we find that propagation results with no attenuation, giving a time average Poynting vector $\mathbf{S} = \hat{x}\frac{1}{2}|E_0|^2 Y_0 \sqrt{|\varepsilon_r|/|\mu_r|}$. If the magnitudes of the relative permittivity and permeability are chosen to be identical, then unimpeded propagation takes place, i.e., there is no back-scattered wave. The range of values for the index of refraction and wave impedance as a function of the electric and magnetic dipole phase is illustrated in Fig. (8-7).

The negative refractive index range, ϕ_n in $[\pi/2, \pi]$, corresponds to the frequency range where $(\chi'_\epsilon + \chi'_\mu)/2 < -1$, with $\chi_q = \chi'_q + i\chi''_q$. These overlapping frequency bands for the resonances in (8.12) and (8.13) define the frequencies where propagation can occur. Within this band, a negative phase velocity occurs, i.e., $v_p = c_0/n' < 0$, where $n = n' + in''$. This means that with advancing time, the wave crests move in the $-x$-direction. However, in this same frequency range, the group velocity (v_g), which describes the power flow of a wave packet, is positive. This can be established from $v_g = c/(n' + \omega \mathrm{d}n'/\mathrm{d}\omega)$ with use of (8.15), (8.12), and (8.13). As a consequence, $(\omega/2)(\mathrm{d}\chi'_\epsilon/\mathrm{d}\omega + \mathrm{d}\chi'_\mu/\mathrm{d}\omega) > |1 + (\chi'_\epsilon + \chi'_\mu)/2|$ in the frequency range of negative refractive index. Therefore, conservation of power holds, i.e.,

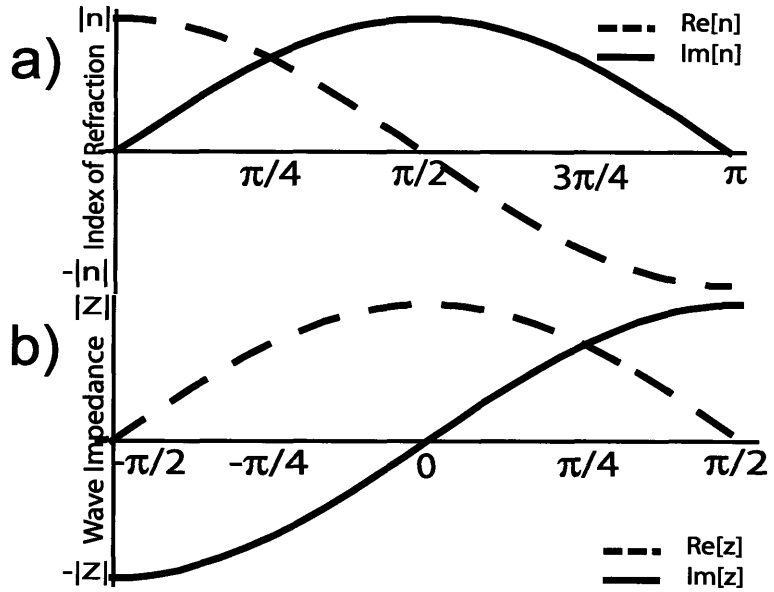

Figure 8-7: Polar representation for the a) index of refraction and b) wave impedance. The domain $[0, \frac{\pi}{2}]$ in a) represents the well known phenomenon of attenuation, while $(\frac{\pi}{2}, \pi]$ corresponds to a negative index of refraction.

with incident power in the x-direction, there is power flow in the x-direction in the negative refractive index medium. Furthermore, causality can be established based on power flow, equivalent to the procedure used in developing the Kramers-Kronig relations for permittivity [45]. Note that conservation of energy is thus the basic metric for causality, and others such as least time based on phase (velocity), for example, Fermat's least time argument, require a revised interpretation from the standard view for positive index materials.

To summarize, by determining the path of stationary phase for a an electromagnetic wave incident on an arbitrary dispersive medium, we found that negative refraction occurs when the index of refraction is negative, indicating that the wave traverses this path with what seems to be a negative phase velocity. While Fermat's least time principle correctly predicts Snell's law for refraction at an interface with a negative refractive index material, it does not produce a least time solution, a consequence of the negative phase velocity. The microscopic model we have used for electric and magnetic dipole interactions provides a basis for the collective oscillator phase shift that results in negative phase velocity in the case of negative

refractive index. We found that when the electric and magnetic dipoles in this model have nearly the same resonant frequency, the augmentation of the electric component by the Lorentz dipoles is partially compensated for by the Bloch dipoles acting on the magnetic component, where the phase shifts in the electric and magnetic components of the field are directly related to the phases of the microscopic electric and magnetic dipoles. While any simultaneous resonance in the electric and magnetic constitutive parameters can provide a model for negative refraction, the dilute microscopic interaction model presented, and its generalization to the dense limit, provide a foundation for macroscopic interpretations. As a consequence, it is clear that dispersion and loss cannot be circumvented.

Finally, the dipole resonance models presented have a finite bandgap that is representative of physical systems such as ferroelectrics which can, with a concomitant magnetic resonance bandgap, provide negative refractive index over a finite frequency range. While there are ferroelectric and ferromagnetic materials that may be candidates for negative refractive index applications, achieving simultaneous bandgaps in an appropriate frequency range and having other satisfactory properties, such as low loss in the composite system, appears challenging. On the other hand, use of one or the other physical resonance, i.e., ferroelectric or ferromagnetic materials, in combination with a metamaterial implementation for the other resonance, is tractable and may yield practical functionalities.

8.2.2 Negative Refraction in the Polariton Regime

Here we describe numerical experiments performed with the FDTD simulations of chapter 3, which are modified to include a magnetic resonance to model hybrid ferrolectric/ferromagnetic materials.

The formalism developed in section 8.2.1 has direct application to ferroelectric and ferromagnetic resonances as either the electric dipole or the magnetic dipole source in a negative index material. A good metric for the resonance frequency of ferromagnetics is the Bohr magneton divided by Planck's constant, which can conveniently be written as $\simeq$ 14 GHz/Tesla [77]. This metric places the possible range of resonance frequencies somewhere between 1

and 100 GHz. Ferroelectrics do not have such a convenient metric, but the resonant frequencies tend to be on the order of ten terahertz [9]. Antiferromagnets can sometimes have resonance frequencies near a THz, but they have relative susceptibilities similar to paramagnetic materials, which are only slightly greater than unity. It may, however, still be possible to observe a negative index with an antiferromagnetic-ferroelectric composite. Within their respective frequency ranges, ferroelectrics and ferromagnets offer very strong resonances, with susceptibilities approaching up to 10,000 in both. The frequency range over which the material may have a negative index is given by the extent of the bandgap in the limiting material, i.e., the one with the smallest bandgap, where the bandgap is the region between the resonance frequency (ω_0) and its conjugate frequency (ω'). In ferroelectrics, the latter is given by the Lyddane-Sachs-Teller relation, $\omega'^2/\omega_0^2 = \varepsilon_0/\varepsilon_\infty$, where ω_0 is the resonance frequency usually associated with a transverse optical phonon in a ferroelectric crystal, ε_0 is the static dielectric constant and ε_∞ is the high frequency permittivity usually associated with electronic resonances [9]. In ferromagnetics, the bandgap is equal to $\Omega_0(\mu_\infty - 1)$, where μ_∞ is the relative permeability above resonance [49]. These materials offer an alternative to providing both electric and magnetic resonances with a metamaterial. Furthermore, ferromagnetic materials can be employed now with existing metamaterials that operate normally around 10 GHz. One advantage in doing so is to exploit the modest tunability of the ferromagnetic resonance and the associated bandgap to provide a tunable negative index that could possibly be used in a device, e.g., a switch that refracts light one way or the other, based on the static magnetic field applied. Ferroelectrics also offer benefits for application to existing THz frequency split ring resonators [111], in that the electric field of an electromagnetic wave can be imaged directly as it propagates through the ferroelectric material [51].

Methods

In the case of ferroelectricity, resonance was established and a polar transverse optic phonon mode in a crystal lattice contributed to the electric field through a time dependent polar-

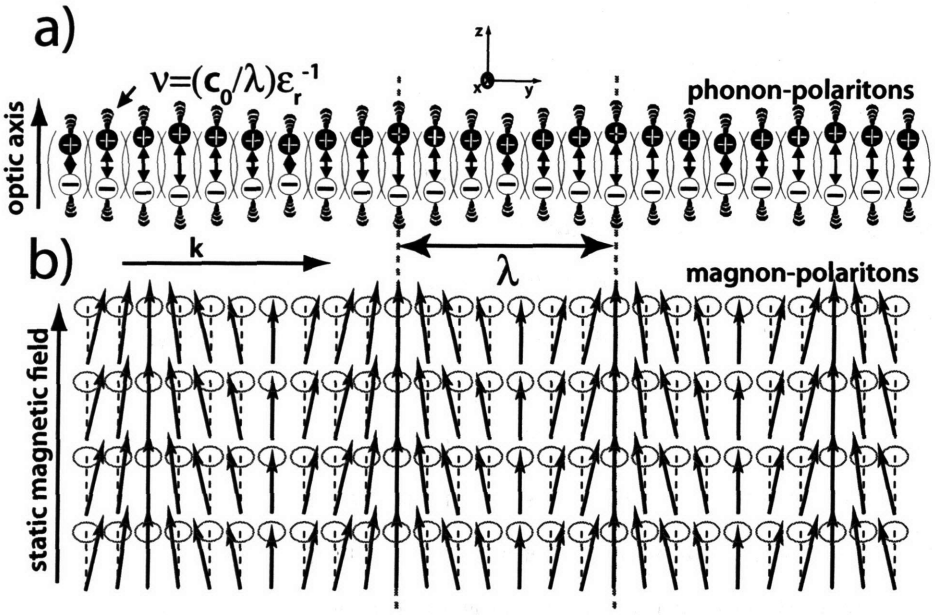

Figure 8-8: Illustration of coupled phonon-polaritons and magnon-polaritons. The former consist of vibrational waves in which polar normal modes are coupled through the radiation field, and the latter consists of magnetic dipoles associated with unpaired electrons that are coupled through the radiation field.

ization, as was discussed in detail in chapters 2 and 4. In this section we consider magnetic effects, which manifest themselves through a time dependent magnetization, $\vec{M}(t) = -g(q_{eff}/2\mathbf{m})\vec{J}(t)$, where g is the Lande' g-factor, $\mathbf{m}$ is the magnetic dipole moment, and $\vec{J}(t)$ is the angular momentum [77]. The last can be expressed classically as $\vec{J}(t) = m\vec{v}(t)r$, where m is the mass, $\vec{v}(t)$ is the velocity, and r is the lever arm length, or it can be expressed quantum mechanically as $\vec{J}(t) = 2S + L$, where S is the spin angular momentum quantum number, and L is the orbital angular momentum quantum number. In either case, the equation of motion for the magnetization, which is related to the magnetic field by $\vec{M}(t) = \chi_\mu \vec{H}(t)$ (where χ_μ is the magnetic susceptibility which is related to the permeability through the relation $\mu_r = 1 + \chi_\mu$), is $\dot{\vec{M}} = g\vec{M} \times \vec{H}(t)$.

In the case of a ferromagnetic or anti-ferromagnetic crystal with either an applied static field or simply the static field from the permanent magnetization, it can be shown that at sufficiently low wavevectors neighboring spins can couple through the radiation field,

giving rise to spin wave propagation in the form of magnon-polaritons. Magnon-polaritons are the ferromagnetic analog to phonon-polaritons [49]. A graphical depiction of magnon-polaritons is shown in Fig. 8-8, where they are contrasted with phonon-polaritons. The relative magnetic susceptibility takes the form in Eq. (8.13).

We ignore the fact that ferromagnetic resonance frequencies are typically on the order of tens of gigahertz and assume that it is possible to establish magnetic resonances on the order of a terahertz. The dispersion relation is derived in a similar fashion, as was done for phonon-polariton dispersion in chapter 2, which resulted in Eq. (2.72). The dispersion relation for magnon-polaritons can be obtained by equating the permeability with the free space dispersion relation as follows,

$$\frac{c_0^2 k^2}{\omega^2} = 1 + \frac{\frac{\chi_{\mu_0}}{2}\Omega_0 T_2}{1 + (\omega - \Omega_0)^2 T_2^2}((\Omega_0 - \omega)T_2 + i), \tag{8.16}$$

and solving for ω in terms of the wavevector k, which results in plot analogous to that for phonon-polaritons shown in Fig. 2-1(a). As in the case of phonon-polaritons, there are two branches to the dispersion relation. The upper branch terminates at $\omega = g\vec{B}$ for $k = 0$, and the lower branch approaches the asymptote $\omega = g\vec{H}$. The splitting is due to displacement currents and not de-magnetization, as explained elsewhere [49]. This relation is analogous to the Lyddane-Sachs-Teller relation for phonon-polaritons. A bandgap exists between these two frequencies, $g\vec{H}$ and $g\vec{B}$.

To implement magnetic resonance of the form in Eq. (8.13) into the FDTD method presented in chapter 3 we introduce another auxiliary parameter I, similar to Q, that accounts for spin precession in the harmonic limit as follows:

$$\ddot{I} = a_{211} I - \gamma_M \dot{I} + a_{212} H. \tag{8.17}$$

I is then introduced into Maxwell's equations, Eqs. (2.24) and (2.25), through the magnetization,

$$M = a_{221} I + a_{222} H, \tag{8.18}$$

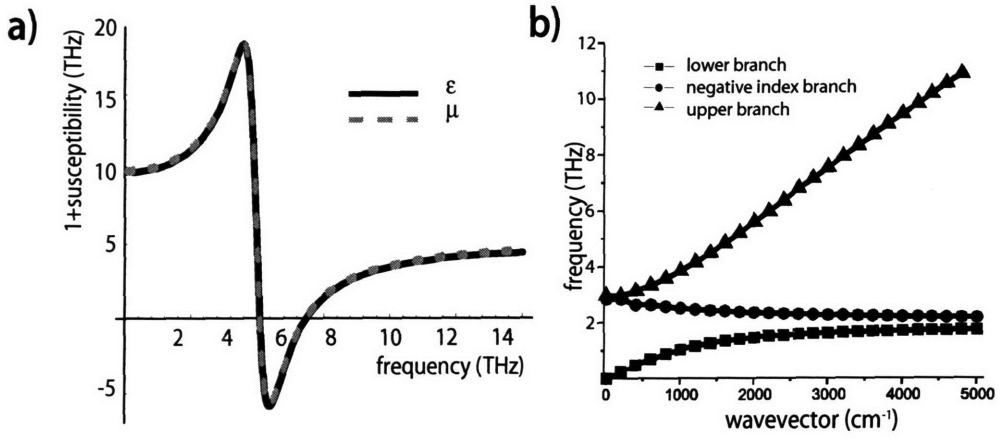

Figure 8-9: a) Overlapping electric and magnetic susceptibilities. b) Dispersion relation for composite phonon/magnon-polariton material determined through FDTD simulation indicates that a new branch of dispersion emerges. The negative index branch is located in between the upper and lower branches. The curvature indicates that the group and phase velocities are of different sign.

which, after substitution into Eq. (2.24) yields,

$$\dot{\vec{H}} = -\frac{1}{\mu_0(1+a_{222})}\left(\nabla \times \vec{E} + \mu_0 a_{222}\dot{I}_2\right), \tag{8.19}$$

where a_{imn} is the same form as the b-coefficients from chapter 2. The magnitudes of the a-coefficients are made the same as the b-coefficients to achieve overlap in the same frequency range of the electric and magnetic resonances that have the same oscillator strengths.

The equivalence of the form used here for the new auxiliary parameter I, which is identical to the polariton resonance in Eq. (2.68), and that of $1+\chi_{\mu_0}$ in Eq. (8.13) can be established through Siegman's on-resonance approximation [76].

Transmission, Reflection, and Refraction at an Interface

In the simulations that follow, we assumed a hypothetical material with overlapping electric and magnetic susceptibilities, as shown in Fig. 8-9(a). The magnetic and electric susceptibilities were given resonance frequencies of 5 THz. They were also given the same oscillator strengths, as seen in the figure.

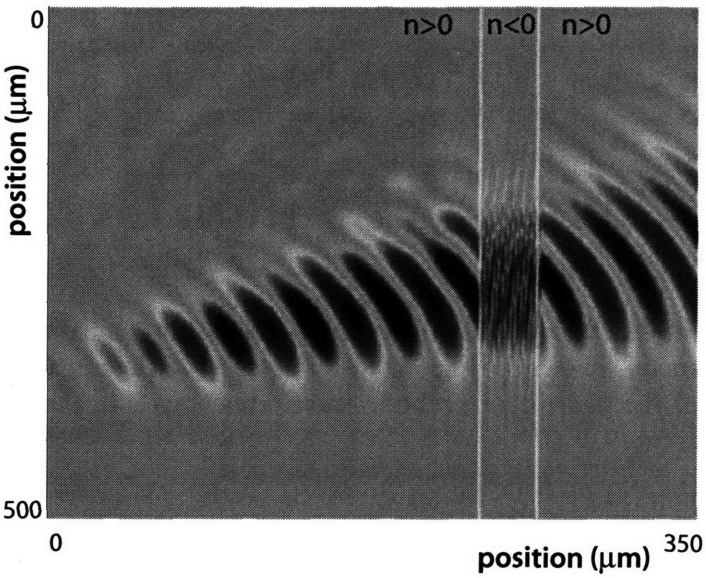

Figure 8-10: Negative refraction occurring at the interface of a positive and negative index material interface. Also observed, though not evident in a single frame, was backward wave propagation in which the phase velocity has the opposite sign of the group velocity. This is consistent with the negative index branch of dispersion in Fig. 8-9.

One-dimensional simulations similar to those in section 3.7.1, in which terahertz radiation was directed from air into the crystal, were performed in the composite system. As expected, transmission of electromagnetic waves into the material was observed for frequencies between 1 and 10 THz. Nothing remarkable is expected outside of this frequency range. If only a single resonance, electric-dipole or magnetic-dipole, was included in the simulated material, then we would expect a bandgap above the resonance frequency as was observed before in chapter 3.

We also performed two-dimensional TE simulations with the composite material in which CW terahertz radiation was directed toward the material interface at an angle. In a positive index material, the incident ray should bend towards the normal in accordance with Snell's law. Veselago speculated that in a negative index material, with overlapping electric and magnetic resonances, the ray should bend to the opposite side of the normal, as that in positive, or normal, refraction [90]. This was observed in our simulations, as shown in

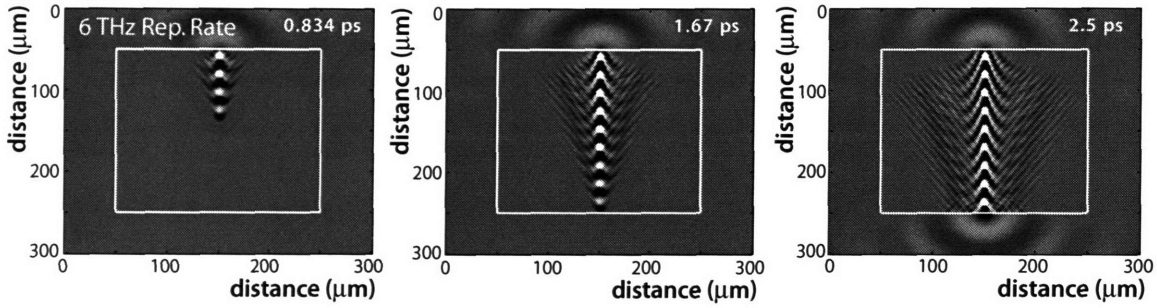

Figure 8-11: ISRS excitation pulse train of repetition rate coinciding with the negative index branch of dispersion, shown in Fig. 8-9(b), results in backward Cherenkov radiation. The phase velocity of the generated terahertz waveforms travels in the opposite direction as the incident pulse train.

Fig. 8-10. Additionally, movies constructed from frames like that in the figure and viewed in order of consecutive time steps indicate that the phase velocity is in the opposite direction of power flow. That is, after the leading edge of the incident radiation traversed the crystal width, the phase fronts traveled toward the incident radiation, giving the appearance of a non-causal wave in which the incident forward-traveling phase fronts meet at the interface with the backward-traveling phase fronts in the material.

Nonlinear Generation

Phonon/magnon-polariton generation through ISRS was also performed on the composite material with a one-dimensional simulation. The coupling mechanism of the incident optical field is the same as it is for phonon-polariton generation, i.e., the stimulated Raman force on the polar TO phonons as described in chapter 2. Optical excitation pulses with amplitude gratings corresponding to excitation wavelengths ranging from 5 μm-100 μm were simulated, and the resulting electric fields inside the material were monitored at a single point in the excitation region, giving a mapping of the temporal response of the composite material. Spectral data were extracted from the temporal responses for each simulation. The observed frequencies for each excitation wavevector are plotted in the dispersion relation in Fig. 8-9(b).

We observed that, in addition to an upper and lower branch for the dispersion relation, there is a new third branch, which we term the negative index branch. It is located between

the lower branch $k \rightarrow \infty$ asymptote at ω_{TO} and $g\vec{B}$, and the upper branch $k \rightarrow 0$ asymptote at ω_{LO} and Ω_0. Apparent in the figure is that the phase and group velocities for the negative index branch are of opposite sign for all wavevectors. This observation is consistent with the theory from section 8.2.1.

Two-dimensional TE FDTD simulations of ISRS generation using optical pulse train excitations indicate that Cherenkov radiation, comparable to that observed in chapter 4 for phonon-polaritons, results for repetition rates that coincide with upper and lower branch frequencies. However, repetition rates of frequency corresponding to the negative index branch result in backward Cherenkov cones, as shown in Fig. 8-11. What is not apparent in the figure, and can only be seen by movies of the generation process, is that the phase fronts travel toward the incident pulse train, giving the appearance of backward traveling waves like that observed in the simulations of negative refraction. Veselago speculated on a similar phenomenon for true Cherenkov radiation resulting from charged particles traversing a negative index material.

Waveguides

Patterned composite material simulations were also performed. We present results from a negative index waveguide, in which the cladding is composed of the hybrid phonon/magnon-polariton material, and the core has a relative permittivity and permeability of one. A CW terahertz wave of frequency corresponding to the negative index dispersion branch was directed into the waveguide. In addition to monitoring the electric field strength in the core and cladding, we constructed the Poynting vector, which indicates the direction of power flow, at each point in the simulation mesh from the electric and magnetic fields at those points. A graph of power flow and electric field is shown in Fig. 8-12.

We observed that power flow in the core is in the opposite direction from that in the cladding. This is a consequence of the negative index material and the requirement from Maxwell's equations that tangential fields must be continuous at the boundary of the core/cladding interface. Since the wavevector for the phase fronts inside the core determines

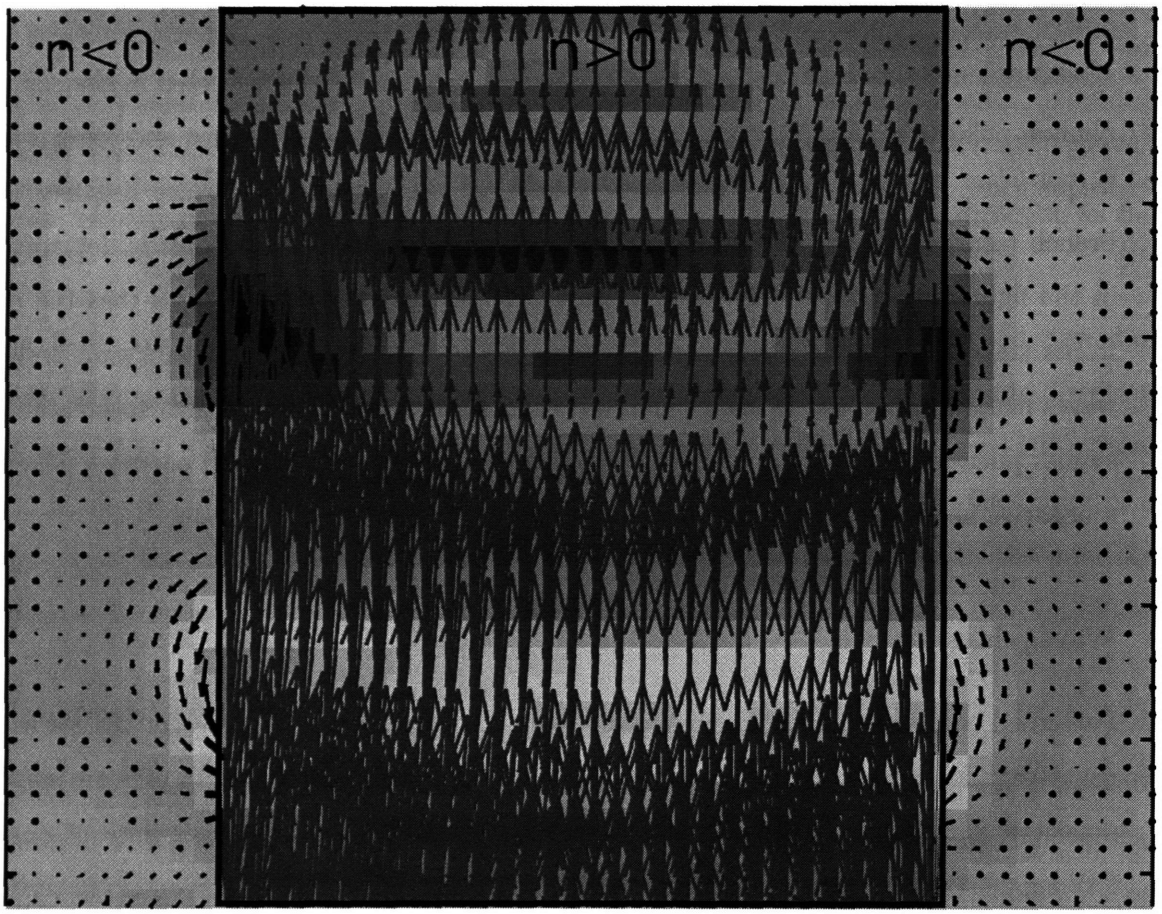

Figure 8-12: Illustration of a negative refractive material waveguide, which shows power flow in opposite directions at the waveguide boundary. The arrows are the Poynting vectors at each position in the problem space, and they indicate the direction of power flow at each position inside and outside of the waveguide. The Poynting vectors are constructed from the electric and magnetic fields at each point in the problem space.

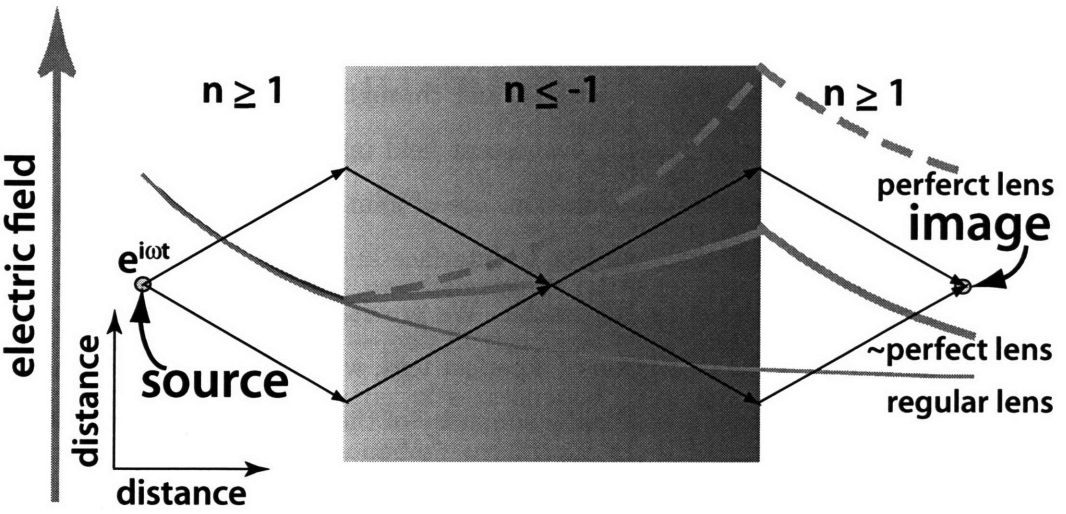

Figure 8-13: A negative refractive index slab, which has the potential to provide a more accurate image than could be achieved with a positive refractive index system. The electromagnetic fields from the source or object can be decomposed into propagating and decaying plane wave components. The propagating waves undergo negative refraction, converging at the image point, as shown by the solid black lines. Evanescent fields decay away from the source. In a perfect lens, this decay would be compensated by growth in the lens, as shown by the dashed blue line. To some degree, loss will diminish the decaying field growth, producing the solid blue curve result.

the evanescent field phase fronts in the cladding, the phase velocity is the same inside and outside of the waveguide. However, in the core, power flow and phase velocity are in the same direction due to the positive index of refraction, but they are in opposing directions in the negative index cladding, which results in the observed power flow disparity across the core/cladding interface.

8.2.3 Nearly Perfect Lenses: A Perturbational Loss Approach

In the case of LH media, we associate the phenomenon with one of simultaneous resonances in both the ensemble electric and magnetic field dipole moments, and this implies concomitant absorptive losses [90]. Equivalently, LH media are dispersive, with real and imaginary components of the magnetization (permeability) and polarization (permittivity) being related by the Kramers-Kronig relations [45]. Therefore, any meaningful model of a LH medium must

be dispersive and must be lossy. The need to incorporate loss into the field solution in a LH medium slab problem has been identified, and through an example it has been suggested that the loss may change a growing evanescent field into a decaying field [32]. To counter the deleterious impact of loss on operation, use of gain media has been proposed [70]. Remaining was the prospect that, subject to interface scattering, fields may be able to grow in a LH medium surrounded by RH media. We provide constraints on this prospect here, which ultimately limit the resolution of a perfect lens, which would then be more accurately called a nearly perfect lens. A schematic summary of the effect of loss on imaging resolution is shown in Fig. 8-13.

Consider a current sheet in the geometry of Fig. 8-14(a) with

$$\mathbf{J}_s = \hat{x} J_0 e^{-ik_{x0}x} \tag{8.20}$$

on the $z = 0$ plane. We assume throughout that the time dependence is $e^{i\omega t}$. A unique field solution can be obtained using the boundary conditions for the tangential fields at $z = 0$, together with radiation conditions for each region, whereby waves having k_z associated with an outward Poynting vector $\mathbf{S} = \mathbf{E} \times \mathbf{H}^*$ are selected, where $\mathbf{E}$ is the electric field and $\mathbf{H}$ the magnetic field. The general solution for $\mathbf{H}$ with arbitrary μ_i and ϵ_i is

$$\begin{aligned} H_{y1} &= -J_0 \frac{\frac{Z_2}{Z_1}}{\frac{Z_2}{Z_1}+1} e^{-i(k_{x0}x + k_{z1}z)} \\ H_{y2} &= J_0 \frac{1}{\frac{Z_2}{Z_1}+1} e^{-i(k_{x0}x + k_{z2}z)}, \end{aligned} \tag{8.21}$$

where $k_{z_2^1} = \sqrt{k^2 - k_{x0}^2}$ and $Z_{\frac{1}{2}} = k_{z_2^1}/(\omega \epsilon_{\frac{1}{2}})$. Given Eq. (8.21),

$$E_{x_2^1} = \frac{k_{z_2^1}}{\omega \epsilon_{\frac{1}{2}}} H_{y_2^1}. \tag{8.22}$$

Consider the lossy case with $\epsilon_1 = -\epsilon' - i\epsilon''$ and $\epsilon_2 = \epsilon' - i\epsilon''$, where all quantities are positive. The corresponding propagation constants are $k_{z1} = -\beta - i\alpha$ and $k_{z2} = -\beta + i\alpha$,

both representing decaying fields away from the source when $\alpha > 0$. With $\epsilon'' \neq 0$, the boundary condition $\hat{n}_{21} \times (\mathbf{H}_1 - \mathbf{H}_2) = \mathbf{J}_s$ implies that

$$H_{y2}|_{\substack{x=0 \\ z=0}} = -H_{y1}^*|_{\substack{x=0 \\ z=0}}. \tag{8.23}$$

The fields in Eq. (8.21) are thus well behaved as $|z| \to \infty$, i.e., they decay. As $\epsilon'' \to 0$ and $\beta \to 0$, $Z_2/Z_1 \to -1$, and $H_{y_2^1} \to \infty$. In this limit of evanescent fields, $Z_1 + Z_2 = 0$, and the field solution has the character of a resonance. The introduction of loss thus damps this resonance. To satisfy all boundary conditions when Regions 1 and 2 are lossless, the evanescent field must grow in one domain, which is non-physical. The fields in the semi-infinite domains must decay away from the source and they must carry power away from the source.

To address the potential for field growth in a LH material, consider the field solution due to a current source within a LH slab of thickness $2d$, as in Fig. 8-14(b). The geometry is symmetric, with $0 < z < d$ being Region 1 and $z > d$ Region 3. The solution for $\mathbf{H}_1 = H_{y1}\hat{y}$ is

$$H_{y1} = Ae^{-ik_{x0}x}\left(e^{-ik_{z1}z} + \Gamma_h e^{-i2k_{z1}d}e^{ik_{z1}z}\right), \tag{8.24}$$

where Γ_h is the magnetic field reflection coefficient, given by $\Gamma_h = (Z_1 - Z_3)/(Z_1 + Z_3)$, and $A = -J_0\left[2\left(1 + \Gamma_h e^{-i2k_{z1}d}\right)\right]^{-1}$. Field growth requires $|H_{y1}(d)| > |H_{y1}(0)|$. From Eq. (8.24), we define the field growth function

$$f = \frac{|(1+\Gamma_h)e^{-ik_{z1}d}|^2}{|1+\Gamma_h e^{-i2k_{z1}d}|^2}. \tag{8.25}$$

Field growth therefore occurs for $f > 1$, and the field decays for $f < 1$.

Consider the case of some degree of loss, resulting in real power flow in Region 1 and complex wave impedance $Z_1 = Z_{1r} + iZ_{1i}$. If the loss were small, the solution is perturbed from what would otherwise have purely evanescent fields. With the complex reflection coefficient $\Gamma_h = |\Gamma_h|\exp(i\phi)$, and using Eq. (8.24) and the corresponding $\mathbf{E}_1$, the Poynting vector

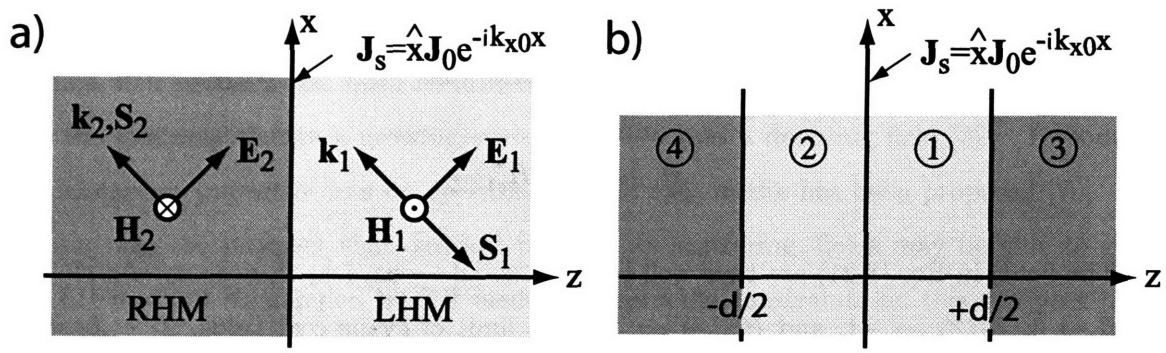

Figure 8-14: a) Current source at the interface between a right-hand (RH) and left-hand (LH) material system. b) Current source centrally located in a slab of thickness $2d$.

expressions evaluated at $z = d$ ($S(d)$) and at $z = 0$ ($S(0)$) are

$$S(d) = \frac{|A|^2}{2} e^{-2\alpha d}[Z_{1r}(1 - |\Gamma_h|^2) + 2Z_{1i}|\Gamma_h|\sin(\phi)] \tag{8.26}$$

$$\begin{aligned} S(0) = \frac{|A|^2}{2}[&Z_{1r}(1 - |\Gamma_h|^2 e^{-4\alpha d}) \\ &+2Z_{1i}e^{-2\alpha d}|\Gamma_h|\sin(\phi + 2\beta d)], \end{aligned} \tag{8.27}$$

where $k_{z1} = -\beta - i\alpha$. The conditions $S(d) \leq S(0)$, and $S(d) \geq 0$ and $S(0) \geq 0$ must hold. We consider a normalized Poynting vector of the form

$$S_n(0) = \frac{S(0)}{S(0)|_{k_{x0}=0}}, \tag{8.28}$$

i.e., $S(0)$ in Eq. (8.28) is normalized to the power density in the normal propagating wave.

Let the constitutive parameters for Regions 1 and 3 be: $\epsilon_1 = -\epsilon_1' - i\epsilon_1''$, $\epsilon_3 = \epsilon'$, $\mu_1 = -\mu'$, and $\mu_3 = \mu'$. In this case, $S(d) = 0$. For convenience, we assume that $\mu_1'' = 0$. To facilitate

generality, we define the normalized variables

$$a = \frac{k_3}{\alpha_3} \tag{8.29}$$

$$\delta = \frac{(\epsilon_1' - \epsilon') + i\epsilon_1''}{\epsilon'}$$

$$= \delta_r + i\delta_i \tag{8.30}$$

$$D = \alpha_3 d \tag{8.31}$$

$$p = k_3 d, \tag{8.32}$$

where $k_3 = \omega\sqrt{\mu'\epsilon'}$ is the wave number in Region 3 and, for $k_{x0} > k_3$, $\alpha_3 = |\sqrt{k_3^2 - k_{xo}^2}|$ is the attenuation coefficient for the evanescent field in Region 3. Given k_3, p becomes a normalized slab thickness parameter. Also, from Eqs. (8.29), (8.31), and (8.32), $p = aD$. For a given k_3 and ϵ', all field characteristics can be described by the four variables a, δ_r, δ_i, and p or D.

Figure 8-15 shows f and $S_n(0)$ for low loss ($\delta_i = 10^{-3}$ in Fig. 8-15(a) and (b)) and high loss ($\delta_i = 10^{-1}$ in Fig. 8-15(c)) as a function of the normalized length parameter p. Figure 8-15(a) shows the case $a = 1$, where $\alpha_3 = k_3$, and Fig. 8-15(b) and (c) gives the result for $a = 0.1$. Decreasing a values correspond to evanescent plane waves in Region 3 having larger attenuation coefficients, and $a \to \infty$ when a particular plane wave goes through cut-off. Resonant features occur for both $f(p)$ and $S_n(0,p)$. The peak $S_n(0)$ is significantly higher for $a = 0.1$, and occurs for smaller values of p. The maximum f occurs for larger p than that for $S_n(0)$. For effective field growth, we require large f and small $S_n(0)$. For a given a there is a range of $f(p)$ where field growth and moderate dissipation can occur. However, comparing the results for $a = 1$ and $a = 0.1$, it becomes clear that this lower-loss growth regime cannot apply to all evanescent plane waves in Region 3.

To understand the impact of the power dissipation in Fig. 8-15, and to place a measure on $|f|$, we relate the problem of Fig. 8-14(b) to the LH lens application. The sheet current source $\mathbf{J}_s(k_x)$ in Fig. 8-14(b) is an equivalent source for the fields in the half-space comprised of a lens of thickness d (Region 1) and the free space image region (Region 3). With planar

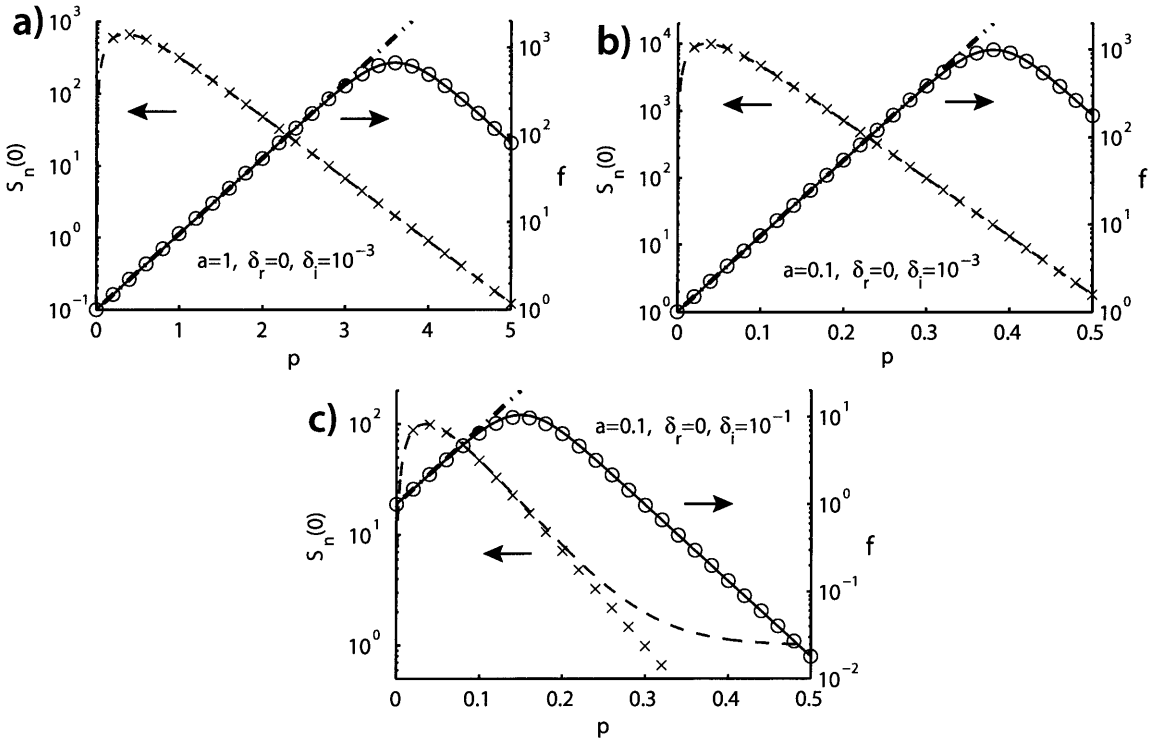

Figure 8-15: Normalized Poynting vector $S_n(0)$ (defined in Eq. (8.28)) and field growth f (from Eq. (8.25)) as a function of normalized slab thickness p (defined in Eq. (8.32)) for (a) low loss and a low-order decaying field, (b) low loss and a high-order decaying field, (c) high loss and a high-order decaying field. Dashed: $S_n(0)$. Crosses: perturbational result in Eq. (8.36). Solid: f. Dot-dashed: required field growth r. Circles: perturbational result in Eq. (8.39).

surfaces, the plane wave spectrum is decoupled, i.e., the scattering problem can be separated into a superposition of solutions for each incident propagating or evanescent plane wave from the object. The finite power from the object can thus be written as the superposition of powers in each plane wave field expansion term. Therefore, the normalized Poynting vector for the true object total field at $z = 0$ can be written as

$$S_{on}(0) = \zeta S_n(0), \tag{8.33}$$

where ζ correctly scales each plane wave solution according to the physical object power density, and $S_n(0)$ is given by Eq. (8.28). The object field is thus

$$H_{oy1} = \zeta^{1/2} H_{y1}, \tag{8.34}$$

where H_{y1} is given by Eq. (8.24) and $\zeta^{1/2} = [S_{on}(0)/S_n(0)]^{1/2}$. Consequently, in the solution of the complete scattering problem for each plane wave, those with high $S_n(0)$ in Fig. 8-15 would have small field amplitudes in the image half-space. Therefore, increasing $S_n(0)$ for fields that do not propagate in Region 3 places more of the spectrum below a given detector noise floor.

For a perfect lens, the field growth in the LH lens must compensate for the decay of the evanescent field in the object and image regions. For a lens of thickness d, the sum of the distances from the lens to the object and image planes is also d, and the required field growth can be described by

$$r = e^{2\alpha_3 d}, \tag{8.35}$$

so that $r = f$ is necessary for each evanescent plane wave to achieve perfect lensing. Figure 8-15 shows $r(p)$ for each case. In Fig. 8-15(a), for low loss and a low-order field closer to cut-off, there is a small p-window where $f \approx r$ and $S_n(0)$ is not extremely large. However, perfect lensing is precluded under all circumstances when there is any degree of loss.

Figure 8-16 further explores the impact of loss on the normalized f/r spectrum. Figure 8-16(a) shows f/r as a function of k_{x0}/k_3, under the assumption of a uniform current spectrum

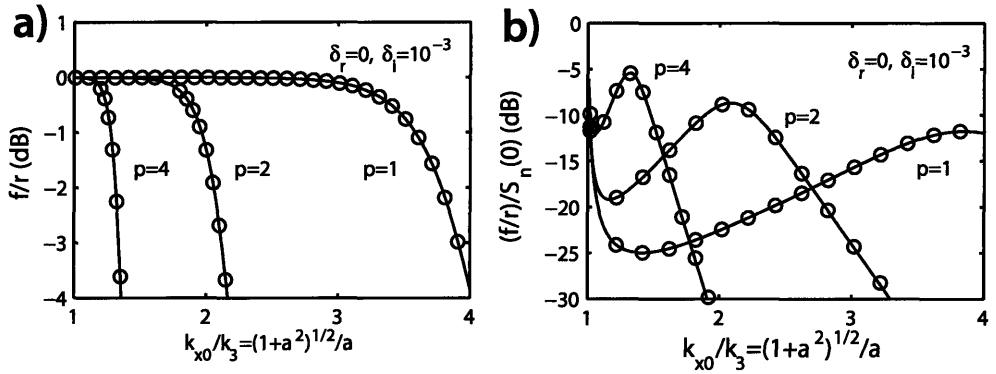

Figure 8-16: Spectrum of the decaying field (f from Eq. (8.25) and r from Eq. (8.35)) at $z = d$ under two different assumptions with various p, with $\delta_r = 0$ and $\delta_i = 10^{-3}$, as defined in Eqs. (8.29)-(8.32). (a) A uniform current spectrum is assumed at $z = 0$. (b) A uniform normalized power spectrum is assumed at $z = 0$. Solid lines: numerical simulation. Circles: perturbational result from Eqs. (8.36) and (8.39).

at $z = 0$. Increasing p reduces the plane wave spectrum over which $f/r \sim 0$ dB (we could, for example, define a 3 dB bandwidth). To illustrate the impact of the loss further, Fig. 8-16(b) shows the field spectrum normalized to $S_n(0)$ for each k_{x0} component, i.e., assuming a uniform power spectrum and using the power dissipated in the decaying wave normalized to the power in the normally incident field at $z = 0$. Therefore, in this case, $\zeta = S_n^{-1}(0)$. This power normalization more clearly demonstrates the adverse impact of perturbational loss on the potential field growth.

Equation (8.28), under the assumption that $\delta_r = 0$, $a^2\delta_i << 1$ (perturbational loss and the plane wave not near cut-off), and $Da^2\delta_i << 1$ (sufficiently small thickness), can be approximated as

$$S_n(0) = \frac{8e^{-2D}(1 - e^{-2D})}{a(2 + a^2)\delta_i}. \tag{8.36}$$

Using Eq. (8.36), the maximum of $S_n(0)$ occurs when

$$D_{S_n(0)_{\max}} = \frac{1}{2}\ln 2 \tag{8.37}$$

or $p = \frac{a}{2}\ln 2$, and the value at the maximum is

$$S_n(0)_{\max} = \frac{2}{a(2+a^2)\delta_i}. \tag{8.38}$$

Use of Eq. (8.36) predicts the location and value of $S_n(0)_{\max}$ for the parameters used in Fig. 8-15 nicely. We find it remarkable that the value of $D_{S_n(0)_{\max}}$ is a constant. Under the same assumptions ($\delta_r = 0$, $a^2\delta_i \ll 1$ and $Da^2\delta_i \ll 1$), the field growth function in Eq. (8.25) becomes

$$f = \left[\frac{16}{(2+a^2)^2\delta_i^2}e^{-2D}\right]\left[1 + \frac{16}{(2+a^2)^2\delta_i^2}e^{-4D}\right]^{-1}. \tag{8.39}$$

Using Eq. (8.39), the maximum of f occurs at

$$D_{f_{\max}} = \frac{1}{2}\ln\frac{4}{(2+a^2)\delta_i}, \tag{8.40}$$

and the value at the maximum is

$$f_{\max} = \frac{2}{(2+a^2)\delta_i}. \tag{8.41}$$

From Eqs. (8.38) and (8.41), $f_{\max} = aS_n(0)_{\max}$. From $D_{S_n(0)_{\max}}$ and $D_{f_{\max}}$, the $p(= aD)$ window for field growth while keeping low energy dissipation is a function of both the evanescent field attenuation constant (through k_{x0}) and the material loss. The results using the approximations in Eqs. (8.36) and (8.39) are shown as circles and crosses in Fig. 8-15. Figure 8-16(a) and (b) also show the good agreement between the perturbational treatment of Eqs. (8.36) and (8.39) (circles) and the numerical simulation (solid lines).

Field growth with propagating fields can occur in either RH or LH materials when standing waves occur. In the case of decaying fields in LH media, field growth in finite domains is not excluded based on conservation of energy through the Poynting vector. One must therefore conclude that it is plausible that field decay in RH media can be compensated to some degree by LH media with appropriate parameters. The degree to which this can be accomplished is a function of the lens material and geometry, and this can be evaluated

using power and field growth metrics. Our understanding of LH material implies that there must be some loss. Unfortunately, any amount of loss in the LH material will preclude the possibility of a perfect lens. It may, however, be possible to build a better lens using LH material. In the case of a curved surface to achieve magnification, by assuming a locally planar geometry, i.e., a large radius of curvature, the conclusions regarding field growth in the planar geometry apply.

Bibliography

[1] http://www.cmxr.com/Industrial/Handbook/Index.htm.

[2] N. W. Ashcroft and N. D. Mermin. *Solid State Physics.* Harcourt College Publishers, New York, 1976.

[3] D. H. Auston and M. C. Nuss. Electrooptic Generation and Detection of Femtosecond Electrical Transients. *IEEE Journal of Quantum Electronics*, 24(2):184–196, 1988.

[4] H. J. Bakker, S. Hunsche, and H. Kurz. Investigation of Anharmonic Lattice Vibrations with Coherent Phonon Polaritons. *Phys. Rev. B*, 50(2):914–920, 1994.

[5] A. S. Barker, A. A. Ballman, and J. A. Ditzenberger. Infrared Study of the Lattice Vibrations In $LiTaO_3$. *Phys. Rev. B*, 2(10):4233–4239, 1970.

[6] A. S. Barker and R. Louden. Dielectric Properties of Optical Phonons in $LiNbO_3$. *Phys. Rev.*, 158(2):433–445, 1967.

[7] I. E. Barry, G. W. Ross, P. G. R. Smith, R. W. Eason, and G. Cook. Microstructuring of Lithium Niobate Using Differential Etch-Rate Between Inverted and Non-Inverted Ferroelectric Domains. *Mat. Lett.*, 37:246–254, 1998.

[8] M. C. Beard and C. A. Schmuttenmaer. Using the Finite-Difference Time-Domain Pulse Propagation Method to Simulate Time-Resolved THz Experiments. *J. Chem. Phys.*, 114(7):2903–2909, 2001.

[9] M. Born and K. Huang. *Dynamical Theory of Crystal Lattices.* Oxford University Press, Oxford, 1954.

[10] M. Born and E. Wolf. *Principles of Optics : Electromagnetic Theory of Propagation, Interference and Diffraction of Light.* Cambridge University Press, Cambridge, 6 edition, 1997.

[11] R. W. Boyd. *Nonlinear Optics.* Academic Press, San Diego, 1992.

[12] H. Boysen and F. Altorfer. A Neutron Powder Investigation of The High-Temperature Structure and Phase Transition in $LiNbO_3$. *Acta. Cryst.*, 50(4):405–414, 1994.

[13] C. Brennan. *Femtosecond Wavevector Overtone Spectroscopy of Anharmonic Lattice Dynamics in Ferroelectric Crystals.* PhD thesis, Massachusetts Institute of Technology, 1997.

[14] L. Brillouin. Wave Propagation and Group Velocity. In *Congres International d'Electricite*, Gauthier-Villar, Paris, 1932.

[15] P. T. Brown, S. Mailis, I. Zergioti, and R. W. Eason. Microstructuring of Lithium Niobate Single Crystals using Pulsed UV Laser Modification of Etching Characteristics. *Opt. Mat.*, 20:125–134, 2002.

[16] J. D. Choi. *Generation of Ultrahigh Frequency Acoustic Waves for the Characterization of Complex Materials.* PhD thesis, Massachusetts Institute of Technology, 2005.

[17] F. K. Christensen and M. Mullerborn. Sub-Band-Gap Laser Micromachining of Lithium Niobate. 66:2772–2773, 1995.

[18] B.E. Cole, J.B. Williams, B.T. King, M.S. Sherwin, and C.R. Stanley. Coherent Manipulation of Semiconductor Quantum Bits with Terahertz Radiation. 410:60–63, 2001.

[19] D. J. Cook, J. X. Chen, E. A. Morlino, and R. M. Hochstrasser. Terahertz-Field-Induced Second-Harmonic Generation Measurements of Liquid Dynamics. *Chem. Phys. Lett.*, 309(3-4):221–228, 1999.

[20] T. F. Crimmins, N. S. Stoyanov, and K. A. Nelson. Heterodyned Impulsive Stimulated Raman Scattering of Phonon-Polaritons in $LiTaO_3$ and $LiNbO_3$. *J. Chem. Phys.*, 117(6):2882–2896, 2002.

[21] T.F. Crimmins, M. J. Gleason, D.W. Ward, and K.A. Nelson. A Simple Terahertz Spectrometer. In T. Elsaesser, S. Mukamel, M.M. Murnane, and N. F. Scherer, editors, *Ultrafast Phenomena XII*, volume 66 of *Chem. Phys.*, pages 221–223, Charleston, SC, 2000. Springer-Verlag.

[22] V. G. Dmitriev, G. G. Gurzadyan, and D. N. Nikogosyan. *Handbook of Nonlinear Optical Crystals*, volume 64 of *Springer series in optical sciences.* Springer-Verlag, New York, 3^{rd} edition, 1999.

[23] T. P. Dougherty, G. P. Wiederecht, and K. A. Nelson. Impulsive Stimulated Raman Scattering Experiments in the Polariton Regime. *J. Opt. Soc. Am. B*, 9(12):2179–2189, 1992.

[24] T. P. Dougherty, G. P. Wiederecht, K. A. Nelson, M. H. Garrett, H. P. Jenssen, and C. Warde. Femtosecond Resolution of Soft Mode Dynamics in Structural Phase Transistions. *Science*, 258(5083):770–774, 1992.

[25] T. P. Dougherty, G. P. Wiederecht, K. A. Nelson, M. H. Garrett, H. P. Jenssen, and C. Warde. Femtosecond Time-Resolved Spectroscopy of Soft Modes in Structural Phase Transistions of Perovskites. *Phys. Rev. B*, 50(13):8996–9019, 1994.

[26] U. Fano. Atomic Theory of Electromagnetic Interactions in Dense Materials. *Phys. Rev.*, 103(5):1202–1218, 1956.

[27] B. Ferguson and X. C. Zhang. Materials for Terahertz Science and Technology. *Nat. Mat.*, 1(1):26–33, 2002.

[28] T. Feurer, S. Stoyanov, D. W. Ward, and K. A. Nelson. Direct Visualization of the Gouy Phase by Focusing Phonon-Polaritons. *Phys. Rev. Lett.*, 88(25), 2002.

[29] T. Feurer, J. C. Vaughan, and K. A. Nelson. Spatiotemporal Coherent Control of Lattice Vibrational Waves. *Science*, 299:374–377, 2003.

[30] R. P. Feynman, R. B. Leighton, and M. Sands. *The Feynman Lectures on Physics, Volume I.* Addison-Wesley, New York, 1965.

[31] G. Gallot, S. P. Jamison, R. W. McGowan, and D. Grischkowsky. Terahertz Waveguides. *J. Opt. Soc. Am. B*, 17:851–863, 2000.

[32] N. Garcia and M. Nieto-Vesperinas. Left-Handed Materials Do Not Make a Perfect Lens. *Phys. Rev. Lett.*, 88(20):207403, 2002.

[33] E. N. Glezer and E. Mazur. Ultrafast-Laser Driven Micro-Explosions in Transparent Materials. 71:862–864, 2001.

[34] C. Glorieux, K. Van de Rostyne, J. D. Beers, W. Gao, S. Petillion, N. Van Riet, K. A. Nelson, J. F. Allard, V. E. Gusev, and W. Lauriks. Acoustic Waves at Interfaces Studied by Laser Ultrasonics. *Rev. Sci. Inst.*, 74:465–469, 2003.

[35] H. A. Haus. *Waves and Fields in Optoelectronics.* Prentice Hall, New York, 1983.

[36] F.A. Hegmann and M.S. Sherwin. Generation of Picosecond Far-Infrared Pulses Using Laser-Activated Semiconductor Reflection Switches. In *Proceedings of the SPIE, international conference on millimeter and submillimeter waves and applications III*, Boston, MA, 1996.

[37] J. J. Hopfield. Theory of the Contribution of Excitons to the Complex Dielectric Constant of Crystals. *Phys. Rev.*, 112(5):1555–156, 1958.

[38] R. Hsu, E. N. Maslen, D. du Boulay, and N. Ishizawa. Synchrotron X-ray Studies of $LiNbO_3$ and $LiTaO_3$. *Acta. Cryst.*, 53(3):420–428, 1997.

[39] K. Huang. On the Interactions Between the Radiation Field and Ionic Crystals. *Proc. Roy. Soc. A*, 208(1094):352–365, 1951.

[40] Kerwyn Casey Huang, Peter Bienstman, J.D. Joannopoulos, Keith A. Nelson, and Shanhui Fan. Field Expulsion and Reconfiguration in Polaritonic Photonic Crystals. *Phys. Rev. Lett.*, 90:196402, 2003.

[41] Kerwyn Casey Huang, Peter Bienstman, J.D. Joannopoulos, Keith A. Nelson, and Shanhui Fan. Phonon-Polariton Excitations in Photonic Crystals. *Phys. Rev. B*, 68:075209, 2003.

[42] Kerwyn Casey Huang, M.L. Povinelli, and J.D. Joannopoulos. Negative Effective Permeability in Polaritonic Photonic Crystals. 85(4):543–545, 2004.

[43] I. Inbar and R. E. Cohen. Comparison of the Electronic Structures and Energetics of Ferroelectric $LiNbO_3$ and $LiTaO_3$. *Phys. Rev. B*, 53(3):1193–1204, 1996.

[44] E. P. Ippen. 6.634 Nonlinear Optics Course Notes Booklet. Technical report, Massachusetts Institute of Technology, 2001.

[45] J. D. Jackson. *Classical Electrodynamics.* John Wiley & Sons, New York, 3 edition, 1999.

[46] J.D. Joannopoulos, R.D. Mead, and J.N. Winn. *Photonic Crystals: Molding the Flow of Light.* Princeton, New York, 1995.

[47] S.G. Johnson and J.D. Joannopoulos. *Photonic Crystals: The Road from Theory to Practice.* Kluwer, Boston, 2002.

[48] I. P. Kaminow and J. W. D. Johnston. Quantitative Determination of the Sources of the Electro-Optic Effect in $LiNbO_3$ and $LiTaO_3$. *Phys. Rev.*, 160(3):519–522, 1967.

[49] C. Kittel. *Quantum Theory of Solids.* John Wiley and Sons, New York, second edition, 1987.

[50] R. M. Koehl. *Spatial and Temporal Ultrafast Imaging and Control of Terahertz Wavepackets.* PhD thesis, Massachusetts Institute of Technology, 2000.

[51] R. M. Koehl, S. Adachi, and K. A. Nelson. Real-Space Polariton Wave Packet Imaging. *J. Chem. Phys.*, 110(3):1317–1320, 1999.

[52] R. M. Koehl and K. A. Nelson. Terahertz Polaritonics: Automated Spatiotemporal Control over Propagating Lattice Waves. *Chem. Phys.*, 267:151–159, 2001.

[53] R. J. Leubbers and F. Hunsberger. FDTD for N^{th}-Order Dispersive Media. *IEEE Trans. Antennas and Propagation*, 40(11):1297–1301, 1992.

[54] M. Levy, Jr. R. M. Osgood, R. Liu, L. E. Cross, III G. S. Cargill, A. Kumar, and H. Bakhru. Fabrication of Single-Crystal Lithium Niobate Films by Crystal Ion Slicing. 73:2293–2295, 1998.

[55] R. Louden. Theory of Stimulated Raman Scattering from Lattice Vibrations. *Proc. Phys. Soc.*, 82:393–400, 1963.

[56] C. Luo, S.G. Johnson, J.D. Joannopoulos, and J.B. Pendry. Negative Refraction Without Negative Index in Metallic Photonic Crystals. *Phys. Rev. Lett.*, 90:196402, 2003.

[57] Chiyan Luo, Steven G. Johnson, and J.D. Joannopoulos. Subwavelength Imaging in Photonic Crystals. *Phys. Rev. B*, 68:145115, 2003.

[58] R. H. Lyddane, R. G. Sachs, and E. Teller. On the Polar Vibrations of Alkali Halides. *Phys. Rev.*, 59(8):673–676, 1941.

[59] S. Mailis, C. Riziotis, P. G. R. Smith, J. G. Scott, and R. W. Eason. Continuous Wave Ultraviolet Radiation Induced Frustration of Etching in Lithium Niobate Single Crystals. *App. Surf. Sci.*, 206:46–52, 2003.

[60] A. Mayer and F. Keilmann. Far-Infrared Nonlinear Optics. $\chi^{(2)}$ Near Ionic Resonance. *Phys. Rev. B*, 33(10):6954–6961, 1986.

[61] K. Minoshima, A. M. Kowalevicz, I. Hartl, E. P. Ippen, and J. G. Fujimoto. Photonic Device Fabrication in Glass by Use of Nonlinear Materials Processing with a Femtosecond Laser Oscillator. *Opt. Lett.*, 26:1516–1518, 2001.

[62] N. Mitsugi and H. Nagata. Challenges in Electron Cyclotron Resonance Plasma Etching of $LiNbO_3$ Surface for Fabrication of Ridge Optical Waveguides. *J. Vac. Sci. Technol. A*, 16:2245–2251, 1998.

[63] F.D. Morrison, J.F. Scott, M. Alexe, T.J. Leedham, T. Tatsuta, and O. Tsuji. Use of the 'Mist' (Liquid-Source) Deposition System to Produce New High-Dielectric Devices: Ferroelectric-Filled Photonic Crystals and HF-Oxide and Related Buffer Layers for Ferroelectric-Gate FETs. *Microelectronic Eng.*, 66:591–599, 2003.

[64] W. P. Oaka, A. Taflove, M. J. Piket, and R. M. Joseph. Parallel Finite Difference Time Domain Calculations. *IEEE Trans. Antennas and Propagation*, 30(3):83–85, Jan. 1991.

[65] J. B. Pendry. Negative Refraction Makes a Perfect Lens. *Phys. Rev. Lett.*, 85(18):3966–3969, 2000.

[66] J. B. Pendry, A. J. Holden, D. J. Robbins, and W. J. Stewart. Magnetism from Conductors and Enhanced Nonlinear Phenomena. *IEEE Trans. Microwave Theory Tech.*, 47(11):2075–2084, 1999.

[67] A. M. Radojevic, M. Levy, Jr. R. M. Osgood, A. Kumar, H. Bakhru, C. Tian, and C. Evans. Large Etch-Selectivity Enhancement in the Epitaxial Lift-Off of Single-Crystal $LiNbO_3$ Films. 74:3197–3199, 1999.

[68] A. M. Radojevic, Jr. R. M. Osgood, M. Levy, A. Kumar, and H. Bakhru. Zeroth-Order Half-Wave Plates of $LiNbO_3$ for Integrated Optics Applications at 1.55 μm. *IEEE Photonics Tech. Lett.*, 12:1653–1655, 2000.

[69] T. A. Ramadan, M. Levy, and Jr. R. M. Osgood. Electro-Optic Modulation in Crystal-Ion-Sliced Z-cut $LiNbO_3$ Films. 76:1407–1409, 2000.

[70] S. A. Ramakrishna and J. B. Pendry. Removal of Absorption and Increase in Resolution in a Near-Field Lens Via Optical Gain. *Phys. Rev. B*, 67:201101, 2003.

[71] Evan J. Reed, Marin Soljacic, and J.D. Joannopoulos. Reversed Doppler Effect in Photonic Crystals. *Phys. Rev. Lett.*, 91:133901, 2003.

[72] D. P. Rodohan and S. R. Saunders. Rapid Solution of the Finite Difference Time Domain Method Using Parallel AssociativeTechniques. *IEEE Trans. Antennas and Propagation*, 31(2):596–599, Jan. 1993.

[73] B.E.A Saleh and M.C. Teich. *Fundamentals of Photonics.* John Wiley and Sons, New York, 1991.

[74] Chris B. Schaffer, Andre Brodeur, and E. Mazur. Laser-Induced Breakdown and Damage in Bulk Transparent Materials Induced by Tightly-Focused Femtosecond Laser Pulses. *Meas. Sci. Technol.*, 12:1784–1794, 2001.

[75] R. A. Shelby, D. R. Smith, and S. Schultz. Experimental Verification of a Negative Index of Refraction. *Science*, 292:77–79, 2001.

[76] A. E. Siegman. *Lasers.* University Science Books, New York, 1986.

[77] C. P. Slichter. *Principles of Magnetic Resonance.* Springer-Verlag, New York, 1980.

[78] Marin Soljacic and J.D. Joannopoulos. Enhancement of Nonlinear Effects Using Photonic Crystals. *Nat. Mat.*, 3(4):211–219, 2004.

[79] A. Sommerfeld. About the Propagation of Light in Dispersive Media. *Ann. Phys.*, 4(44):177–202, 1914.

[80] D. E. Spence, P. N. Kean, and W. Sibbett. 60-fsec Pulse Generation from a Self-Mode-Locked Ti:sapphire Laser. *Opt. Lett.*, 16(1):42–44, 1991.

[81] N. S. Stoyanov, T. Feurer, D. W. Ward, and K. A. Nelson. Integrated Diffractive Terahertz Elements. 82(5):674, 2003.

[82] N. S. Stoyanov, D. W. Ward, T. Feurer, and K. A. Nelson. Direct Visualization of Phonon-Polariton Focusing and Amplitude Enhancement. *J. Chem. Phys.*, 117(6):2897, 2002.

[83] N. S. Stoyanov, D. W. Ward, T. Feurer, and K. A. Nelson. Terahertz Polariton Propagation in Patterned Materials. *Nat. Mat.*, 1(2):95, 2002.

[84] Nikolay S. Stoyanov. *Phonon-Polaritons in Bulk and Patterned Materials.* Ph.d., Massachusetts Institute of Technology, 2004.

[85] Nikolay S. Stoyanov, T. Feurer, David W. Ward, Eric R. Statz, and Keith A. Nelson. Direct Visualization of a Polariton Resonator in the THz Regime. *Optics Express*, 12:2387–2396, 2004.

[86] M. A. Stroscio and M. Dutta. *Phonons in Nanostructures.* Cambridge University Press, Cambridge, 2001.

[87] A. Taflove and S. C. Hagness. *Computational Electrodynamics: The Finite-Difference-Time-Domain Method.* Artec House, Boston, 2 edition, 2000.

[88] H. F. Talbot. Facts Relating to Optical Science. *Philos. Mag.*, 9(4):401–407, 1836.

[89] V. Varadajan and R. Mittra. Finite-Difference Time-Domain Analysis using Distributed Computing. *IEEE Microwave and Guided Wave Letters*, 4:144–145, Jan. 1994.

[90] V. G. Veselago. The Electrodynamics of Substances with Simultaneously Negative Values of ϵ and μ. *Sov. Phys. Uspekhi*, 10(4):509–514, 1968.

[91] J. K. Wahlstrand and R. Merlin. Cherenkov Radiation Emitted by Ultrafast Laser Pulses and the Generation of Coherent Polaritons. *Phys. Rev. B*, 68:054301–1–054301–12, 2003.

[92] G. P. Wakeham. *Dual-Echelon Single-Shot Femtosecond Spectroscopy.* Ph.d., Massachusetts Institute of Technology, 2001.

[93] David W. Ward, Jaime D. Beers, T. Feurer, Eric R. Statz, Nikolay S. Stoyanov, and Keith A. Nelson. Coherent Control of Phonon-Polaritons in a Terahertz Resonator Fabricated with femtosecond Laser Machining. *Opt. Lett.*, 29(22):2671–2673, 2004.

[94] David W. Ward, Jaime D. Beers, and Keith A. Nelson. Measurement of the Differential Polarizability for Phonon-Polaritons in The A_1 Mode of $LiNbO_3$ By Impulsive Stimulated Raman Scattering. *App. Opt., submitted*, 2004.

[95] David W. Ward, Thomas Feurer, Joshua C. Vaughan, Nikolay S. Stoyanov, Eric R. Statz, and Keith A. Nelson. Polaritonics: Bridging the Gap Between Electronics and Photonics. *Manuscript in preparation*, 2004.

[96] David W. Ward, Keith A. Nelson, and Kevin J. Webb. On the Physical Origins of the Negative Index of Refraction. *Phys. Rev. Lett., submitted*, 2004.

[97] David W. Ward, Keith A. Nelson, and Kevin J. Webb. THz Negative Index Materials in the Polariton Regime. *Optics Express, Optics Express*, 2004.

[98] David W. Ward, Eric Statz, Jaime D. Beers, Nikolay Stoyanov, Thomas Feurer, Ryan M. Roth, Richard M. Osgood, and Keith A. Nelson. Phonon-Polariton Propagation, Guidance, and Control in Bulk and Patterned Thin Film Ferroelectric Crystals. In *2003 MRS Fall Meeting*, volume 797 of *Engineered Porosity for Microphotonics and Plasmonics*, Boston, MA, 2003. Materials Research Society.

[99] David W. Ward, Eric R. Statz, Jaime D. Beers, T. Feurer, John D. Joannopoulos, and Keith A. Nelson. Polaritonics in Complex Structures: Confinement, Bandgap Materials, and Coherent Control. In *Ultrafast Phenomenon XIV*, Toki Messe Convention Center, Niigata, Japan, 2004. Springer-Verlag. Also available as a preprint: ArXiv: physics/0409111.

[100] David W. Ward, Eric R. Statz, Zilong Chen, and Keith A. Nelson. Terahertz Reflective and Focusing Elements. *Optics Express, submitted*, 2004.

[101] David W. Ward, Eric R. Statz, Thomas Feurer, and Keith A. Nelson. Polaritonic Materials Fabricated and Tested with Ultrashort-Pulse Lasers. In *2004 MRS Fall Meeting*, volume 850 of *Ultrafast Lasers for Materials Science*, pages MM1.2.1–6, Hynes Convention Center, Boston, MA, 2004. Materials Research Society. Also Published as preprint: ArXiv:physics/0411196.

[102] David W. Ward, Eric R. Statz, and Keith A. Nelson. Direct Visualization of Electromagnetic Wave Propagation in Terahertz Photonic Bandgap Materials. *Manuscript in Preparation*, 2004.

[103] David W. Ward, Eric R. Statz, Keith A. Nelson, Ryan M. Roth, and Richard M. Osgood. Terahertz wave generation and propagation in thin-film lithium niobate produced by crystal ion slicing.

[104] David W. Ward, Eric R. Statz, Nikolay S. Stoyanov, Thomas Feurer, and Keith A. Nelson. Finite Difference Time Domain (FDTD) Simulations of Phonon-Polariton Generation and Propagation in Ferroelectric Crystals: A Comparison with Experiments. *Phys. Rev. B.*

[105] K. J. Webb, M. Yang, D. W. Ward, and K. A. Nelson. Metrics for Negative-Refrative-Index Materials. *Phys. Rev. E*, 70:035602(R)–1–4, 2004.

[106] Kevin J. Webb, Ming Yang, David W. Ward, and Keith A. Nelson. Resolution Limits of a Negative Refractive Index Lens. In *CLEO 2005, submitted*, Baltimore, MD, 2004.

[107] M. M. Wefers, H. Kawashima, and K. A. Nelson. Femtosecond Pulse Shaping and Multiple-Pulse Femtosecond Spectroscopy. *Ann. Rev. Phys. Chem.*, 46:627–656, 1995.

[108] A. M. Weiner, D. E. Leaird, J. S. Patel, and J. R. Wullert. Programmable Femtosecond Pulse Shaping by Using a Multielement Liquid Crystal Phase Modulator. *Opt. Lett.*, 15:326–328, 1990.

[109] R. S. Weis and T. K. Gaylord. Lithium niobate: Summary of physical properties and crystal structure. *Appl. Phys. A*, 16:191–205, 1985.

[110] K. S. Yee. Numerical Solution of Initial Boundary Value Problems Involving Maxwell's Equations in Isotropic Media. *IEEE Trans. Antennas and Propagation*, 14:302–307, 1966.

[111] T. J. Yen, W. J. Padilla, N. Fang, D. C. Vier, D. R. Smith, J. B. Pendry, D. N. Basov, and X. Zhang. Terahertz Magnetic Response from Artificial Materials. *Science*, 303:1494–1496, Mar. 2004.

[112] J. L. Young. Propagation in Linear Dispersive Media: Finite-Difference Time-Domain Methodologies. *IEEE Trans. Antennas and Propagation*, 43(4):422–426, 1995.

[113] J. L. Young and R. O. Nelson. A Summary and Systematic Analysis of FDTD Algorithms for Linearly Dispersive Media. *IEEE Antennas and Propagation Magazine*, 43:61–77, 2001.

[114] R. W. Ziolkowski and E. Heyman. Wave Propagation in Media Having Negative Permittivity and Permeability. *Phys. Rev. E*, 64:056625, Oct. 2001.

77 Massachusetts Ave. 6-026
Cambridge, MA 02139

(voice) 617-253-1956
(fax) 617-253-6295
(email) dward@mit.edu

David W. Ward

Education

Massachusetts Institute of Technology Cambridge, MA

Ph.D. Department of Chemistry. Research focuses on phonon-polariton propagation in thin films, confined structures and patterned materials. (1999 to present)

College of Charleston Charleston, SC

Bachelor of Science, Physics and Mathematics, Magna Cum Laude, May 1999.

- Quattrochi Merit Scholarship recipient, full-tuition, 1998-1999.
- Faculty Honors List-Highly distinguished category, 1997-1999.
- Inducted into Phi Kappa Phi honor society, Sigma Pi Sigma honor society, and the Mathematical Association of America, 1997.

Awards

Best student poster, *Ultrafast phenomena XII*, 2000. Quattrochi Merit Scholarship recipient, full-tuition, 1998-1999. Institutional merit scholarship, 1997.

Research Experience

Massachusetts Institute of Technology Cambridge, MA

Advisor: Keith A. Nelson

Developed integrated-platforms for THz signal processing, coherent control, and spectroscopy using phonon-polaritons. The results of this work **gave birth to the field of Polaritonics**, a regime intermediate to AC circuit theory and optics. Presently pursuing application of this field to semiconductor/ferroelectric hybrids, quantum nanostructures for quantum computing, ultra-thin film ferroelectrics, photonic bandgap materials, and near field scanning THz microscopy to study ferroelectric nanorods. Have supervised and trained five undergraduate researchers and maintained collaborations with principal investigators at the University of Cambridge (Prof. James F. Scott, Department of Earth Sciences), Columbia University (Prof. Richard M. Osgood, Department of Physics and Engineering), Purdue University (Prof. Kevin J. Webb, Department of Electrical Engineering), as well as MIT (Prof. John D. Joannopoulos, Department of Physics and Research Lab for electronics). Results have been published in Nature Materials, Physical Review Letters and other journals—see publication list below. (1999-present)

- Developed novel technique to design and test photonic bandgap materials in which electromagnetic waves can be directly imaged and time-resolved as they propagate through a photonic bandgap material. Note, also useful for design and testing of guided-wave and aperiodic structures.
- Developed **femtosecond laser machining** techniques for fabrication of guided-wave and photonic bandgap structures in

perovskites like $LiNbO_3$ and $LiTaO_3$, which are impervious to more traditional patterning techniques.

- Demonstrated and explained polariton dispersion in thin films, which made possible a host of new THz devices with novel functionalities that enjoy considerable benefit over similar devices in bulk crystals.
- Employed **impulsive stimulated Raman scattering**, Schlieren and Talbot imaging, optical Kerr effect, terahertz field induced second harmonic generation, and interferometry for novel characterization of optical materials in the THz band.
- Demonstrated the first direct visualization of the Gouy phase shift in focused THz radiation.
- Demonstrated one of the first non-trivial coherent control experiments in condensed matter using temporal pulse shaping and resonant THz cavities—combining the techniques of coherent control with patterned materials (a non-coherent control mechanism).
- Constructed a 24 processor Beowulf computer cluster and authored a novel **finite difference time domain (FDTD) simulation** architecture to model phonon-polariton propagation and generation as well as THz interactions with quantal systems (semiconductor nanostructures).
- Demonstrated the role of lattice anharmonicity in ferroelectric crystals, establishing the relation to normal mode potential energy surfaces by performing numerical experiments with the aforementioned simulation architecture. Efforts to experimentally demonstrate this are underway (see below).
- Extended the theory of negative refraction to condensed matter, putting it on equal footing with fundamental processes like attenuation and dispersion. Also demonstrated interesting nonlinear phenomena in hybrid phonon-polariton/magnon-polariton systems through numerical experiments.
- Participant and contributor to the early high-field THz experiments performed at Stanford's SLAC, which shows promise to corroborate the theoretical and numerical findings mentioned previously.
- 30 publications.

Rice Quantum Institute Houston, TX

Advisor: James L. Kinsey

Designed and constructed apparatus for conducting **UV resonance Raman spectroscopy** studies on particles and **nanoparticles** adsorbed on solid substrates. The device has since found application in spectroscopic applications in biology, where signal detection is plagued by parasitic Mie scattering. Became familiar with mechanical drawing, machining, glass working, welding, soldering, vacuum systems, electron microscopy, AFM and STM, spectrometers, Nd:Yag and dye lasers, electronics, and optics. Results were presented at the 216th American Chemical Society national meeting and the 12th annual Rice Quantum Institute Colloquium. (1998)

College of Charleston Charleston, SC

Advisors: Kristin Krantzman , Barbara Garrison, Jeff Wragg

Wrote and performed **molecular dynamics simulations** that determined the fundamental mechanism responsible for the nonlinear enhancement in secondary ion emission yield of surface adsorbed organic molecules using cluster projectiles. Work was performed in collaboration with the Pennsylvania State University. Results were presented at the 12th international conference on secondary ion mass spectrometry and published in the Journal of Physical Chemistry B. (1998-1999)

Proposed and developed a **logistic model of fermions**, which models a small system of weakly interacting fermions using discrete mathematics. Results were presented at the annual meeting of the South Carolina Academy of Science. (1997-1998)

Teaching Experience

Massachusetts Institute of Technology Cambridge, MA

Instructor for **Introduction to Simulation of Electromagnetic Wave Propagation using Finite Difference Time Domain Simulations** (FDTD) at MIT. (January, 2004)

Teaching assistant for **Applications of Technology**, a course addressing the role of government policy in technology development with an emphasis on energy and environmental policy. Duties included grading of assignments, preparing lectures and class handouts, and maintaining the course web site. (Fall 2001 and Fall 2002)

Teaching assistant for undergraduate thermodynamics. Led two 1-hour recitations a week for approximately 30 undergraduates. (1999-2000)

Supervised and trained five undergraduate students in Keith Nelson's lab. Over 80% of the junior graduate students in our lab spent some time under my instruction.

KC Academy Brookline, MA

Instructor in **abstract mathematics** at KC Academy, a private Korean High School in Brookline, MA. Duties included designing and implementing a curriculum in abstract mathematics, and lecturing a class of fifteen three hours a week. (2001-2002)

Other Experience

United States Navy Little Creek, VA

Boatswain's Mate, second class (E5), 1990-1996. Supervised and trained a division of over 100 men. Conducted operations in the Middle East, Eastern Europe, South America, and Western Africa.

- Responsible for the seizure of illegal drugs in excess of **$1M** street value.
- Provided **personal protection services** for key witnesses and plaintiffs; Naval Legal Service Offices, Mid Atlantic, Norfolk, VA.
- Recipient of over twenty personal, and unit citations, including the **humanitarian service medal** and a personal citation conferred by Johnny Young, US Ambassador, Lomé, Togo.